



HAL
open science

Computational modelling of cell mechanics: from osteogenesis down to collective and single cell migration

Rachele Allena

► **To cite this version:**

Rachele Allena. Computational modelling of cell mechanics: from osteogenesis down to collective and single cell migration. Biomechanics [physics.med-ph]. Université Pierre et Marie Curie, 2015. tel-01214057

HAL Id: tel-01214057

<https://hal.science/tel-01214057>

Submitted on 9 Oct 2015

HAL is a multi-disciplinary open access archive for the deposit and dissemination of scientific research documents, whether they are published or not. The documents may come from teaching and research institutions in France or abroad, or from public or private research centers.

L'archive ouverte pluridisciplinaire **HAL**, est destinée au dépôt et à la diffusion de documents scientifiques de niveau recherche, publiés ou non, émanant des établissements d'enseignement et de recherche français ou étrangers, des laboratoires publics ou privés.



Université Pierre et Marie Curie

Computational modelling of cell mechanics:
from osteogenesis down to collective and single cell
migration

Habilitation à Diriger des Recherches

présentée et soutenue publiquement le 25 Juin 2015

par

Rachele Allena

Composition du jury:

Mme K. Anselme	Rapporteur
M. D. Aubry	Examineur
M. A. Barakat	Rapporteur
M. D. Kondo	Examineur
M. Y. Rémond	Examineur
M. P. Rouch	Examineur
M. P. Swider	Rapporteur

*If we knew what we were doing,
it would not be called research,
would it?*

Albert Einstein

Acknowledgements

I would like to thank the Institut de Biomécanique Humaine Georges Charpak and all its members for welcoming me four years ago.

Thanks to Karine Anselme, Abdul Barakat and Pascal Swider for accepting to review this manuscript.

Thanks to Djimédo Kondo, Yves Rémond and Philippe Rouch to be part of my committee and for the time they spent reading these pages.

A special thank you to Denis Aubry who passed on to me his precious knowledge and transmitted me the passion for research.

I would like to thank the Chaire BiomecAM for funding part of my work.

Thank you to all the people that have been there for one reason or the other, for their support, their time and their advices.

Finally, thank you to myself.

Table of contents

Introduction (english)	1
Introduction (french)	5
Chapter 1: Curriculum Vitae	9
Chapter 2: Mechanical behaviour of cortical bone and osteogenesis	19
2.1 Osteogenesis and bone remodelling	20
2.2 Previous models of osteogenesis and bone remodelling	21
2.3 Development of a model for osteogenesis	23
2.4 Finite element model of osteogenesis within a titanium porous scaffold	25
2.5 Anisotropic behaviour of cortical bone under traction	36
2.6 Conclusions and perspectives	46
2.7 Bibliography	48
Chapter 3: Single cell migration	53
3.1 General overview on numerical modelling of single cell migration	54
3.2 Development of a finite element approach to single cell migration	55
3.3 Single cell migration over 2D flat substrates	57
3.4 Single cell migration with multiple pseudopodia	75
3.5 Confined migration	106
3.6 Influence of substrate stiffness	147
3.7 Conclusions and perspectives	148
3.8 Bibliography	151
Chapter 4: Collective cell migration	155
4.1 Previous works	155
4.2 Modelling collective cell migration	156
4.3 2D Finite element model of collective migration	159
4.4 2D Finite element model of lateral line primordium migration	186
4.5 Conclusion and perspectives	210
4.6 Bibliography	211

Introduction (english)

In medicine, when tackling disease, there are three principal scenarios. Firstly: the disease is unknown and therefore difficult or impossible to treat. Secondly: the disease is known to us but its origins cannot be traced and therefore the patient can only be treated *a posteriori*. Thirdly: the disease and its causes are familiar to us and so it can be detected and treated in time. Thanks to the scientific advancements made over the last few decades, the first-case scenario is, luckily, increasingly rare and most of the diseases can be successfully handled with specific drugs. Nevertheless there are some pathologies, such as tumorigenesis, where it is difficult to determine the causes. The grave consequences provoked by these pathologies have to be dealt with by surgeons and clinicians who have an urgent need to receive clear information as quickly as possible regarding pathological processes underway in bone, soft tissues or other organs.

Nowadays, it is evident that detection and prevention constitute the most arduous challenge and a huge effort is required in fundamental research at the level of the cells (or even smaller units), where everything originates. It is in this spirit that, since the completion of my PhD, the leitmotif of my research has been a top-down approach aimed at determining the basic principles at the microscale in control of specific biological phenomena occurring at the macroscale, sustained by the firm belief that mechanics is not a consequence of biology but rather its driving force.

When I joined the Institut de Biomécanique Humaine Georges Charpak almost four years ago, most of the studies performed in the institute focused on macro and mesoscale biomechanical problems and more specifically on the personalised geometrical and mechanical modelling of musculoskeletal structures. My background in cell and computational mechanics and my knowledge and expertise in this field meant that I was able to make a significant and new contribution at the microscale and could work towards integrating the team. In order to find a link with the activities of the institute, I decided to start working on the development of a computational model of osteogenesis, which entailed three main difficulties. Firstly, nobody in the laboratory had ever worked in this area, which made any technical exchange difficult, but enriching. Secondly, osteogenesis and bone remodelling have been the subject of several papers published over the last decades, and thus it was important to find the right approach and propose an original study. Last, but not least, my choice coincided with the arrival of Mary Schmitt, my first PhD student to enter into the team under the supervision of Philippe Rouch and myself.

The results that I have obtained have been more than encouraging and things have naturally fitted into what is now my research plan for the next few

years. My work, which is mostly based on the development of numerical tools, is organised in three main themes, which I shall subsequently present.

Mechanical behaviour of cortical bone and osteogenesis (Chapter 2)

The structure of cortical bone is based on the hierarchical assembly of lamellar materials in three forms: i) the osteons, constituted by circumferential lamellae and oriented along the longitudinal axis of the bone, ii) the interstices between the osteons and iii) the circumferential lamellae at the bone periphery. Such morphology results in transversely isotropic behaviour both for stiffness and strength, with mechanical properties which are different in the plane of the lamellae and perpendicular to them. Additionally, this structure can change and adapt itself to the stress and strain state of the environment during the remodelling process, which is intensified following fractures or implantation of prostheses. To explore these two aspects, I have developed two works in parallel.

The first study, in collaboration with Christophe Cluzel from the Ecole Normale Supérieure de Cachan, has consisted of setting up an original experimental protocol rarely employed before in biomechanics to test small bovine bone specimens in traction. Our main goal has been to verify that i) the microstructure of the bone promotes a diffuse highly anisotropic damaging whose degradation plans are parallel to the lamellae plane and that ii) the threshold of the brittle rupture for static loading perpendicular to the lamellae plan is lower than that in the lamellae plan.

The second study, which is the PhD topic of Mary Schmitt whom I co-supervise with Philippe Rouch at the Institut de Biomécanique Humaine Georges Charpak, is a mechanobiological model simulating the collective cell migration during bone osteogenesis within a titanium porous scaffold implanted in ewes' mandibles. We have coupled mechanics (i.e. cyclic loading and poroelastic behaviour of bone) and biology (i.e. cellular activities such as migration, proliferation and differentiation) via reaction-diffusion equations and have shown that mechanics may actually influence the intensity and the direction of cell colonisation. The numerical results have been consistently compared both qualitatively and quantitatively with histological and experimental data obtained after three months of scaffold implantation.

Although the outcomes to date are encouraging, two key questions remain open:

- how do cells sense and respond to their environment (i.e. mechanical properties, geometry, etc...)?
- how do cells coordinate their collective movement during colonisation of the porous implant?

In order to explore such aspects, further studies at the scale of the single cell and of the cell population need to be carried out. More specifically, it is necessary to understand how cells behave during single and collective migration, which leads to the next research axes.

Single cell migration (Chapter 3)

Single cell migration entails the displacement of the cell in response to an external signal within the extracellular matrix (ECM) showing specific heterogeneity (i.e. geometry, porosity, mechanical properties). In this context, I

have first developed a simplified three-dimensional (3D) model, based on continuum mechanics and using the finite element approach, which simulates free migration of a cell over a two-dimensional (2D) substrate, which can be either heterogeneous or homogeneous. Then, I have adapted such model in order to reproduce and analyse single cell migration in different configurations exhibiting specific constraints such as confinement or variation of mechanical properties within the cell's environment. In the former case, in collaboration with Matthieu Piel at the Institut Curie, we have been able to determine the necessary conditions for the cell to be invasive or not. Furthermore, we have confirmed the critical role of the nucleus, the stiffest component of the cell, during migration through sub-nuclear pores. In the latter case, in collaboration with Benoit Ladoux at the Institut Jacques Monod, we have established the link between the polarisation process of the cell and the substrate stiffness and more specifically the transition from an isotropic and non adhesive configuration over a soft substrate to an anisotropic and adherent state over a stiff substrate.

Collective cell migration (Chapter 4)

Collective cell migration is based on the same mechanical principles as single cell migration, but two additional key factors are necessary: i) synchronisation between cells comprising the population and ii) the presence within the cohort of leader cells able to pull the followers. In order to better understand such aspects, I have developed two models.

The first model, in collaboration with James Sharpe at the Center for Genomic Regulation at Barcelona, has allowed investigation of the relationship between the internal synchronisation of each cell of the population between the active strains of protrusion and contraction and the adhesive forces (i.e. intra-synchronisation) and the synchronisation between the cells (i.e. inter-synchronisation) in order for the cohort to be as efficient as possible.

The second model was developed with Philip Maini during my stay at the Mathematical Institute in Oxford and simulate the migration of the lateral line primordium in the zebrafish. Through the coupling via reaction-diffusion equations between the mechanical and the molecular framework we have been able to investigate the role and the influence of leader cells on the global efficiency of the population in terms of distance covered.

Introduction (french)

En médecine, quand on veut traiter une pathologie, trois scénarii sont possibles. Soit la maladie est inconnue et donc difficile ou impossible à traiter. Soit la maladie est connue, mais ses origines ne peuvent pas être tracées et le patient ne peut être soigné que *a posteriori*. Soit la maladie et ses causes sont connues et elle peut donc être détectée préventivement. Grâce aux avancées scientifiques des dernières décennies, le premier scénario est, heureusement, de plus en plus rare et la plus part des pathologies peuvent être traitées avec des médicaments spécifiques. Toutefois, il existe encore des maladies comme le cancer dont on ne connaît pas les origines. Les chirurgiens doivent donc faire face aux graves conséquences provoquées par ces maladies et ont besoin d'informations rapides et claires à l'échelle de l'os, des tissus et des organes.

Actuellement, la détection et la prévention constituent le défi majeur et un très grand effort est demandé dans le domaine de la recherche fondamentale à l'échelle de la cellule (ou à une échelle encore plus petite) où les causes de certaines pathologies sont à explorer. C'est dans cet esprit qu'à la suite de mon doctorat, le leitmotiv de ma recherche a été une approche descendante afin de déterminer les mécanismes à l'échelle microscopique contrôlant des phénomènes biologiques spécifiques à l'échelle macroscopique, soutenue par la ferme conviction que la mécanique n'est pas une conséquence de la biologie, mais aussi souvent le moteur.

Quand je suis arrivée à l'Institut de Biomécanique Humaine Georges Charpak il y a quatre ans, la plupart des études étaient focalisées sur des problèmes biomécaniques à l'échelle macro et mésoscopique et plus particulièrement sur la modélisation personnalisée de la géométrie et des propriétés mécaniques des structures musculosquelettiques. Mon expérience et mon expertise dans le domaine de la mécanique cellulaire et numérique m'ont permis de m'intégrer dans l'équipe en apportant une contribution significative et nouvelle à l'échelle microscopique. Afin de trouver un lien avec les activités de l'institut, j'ai décidé de développer un modèle d'ostéogenèse impliquant trois difficultés. D'une part, personne au laboratoire ne travaillait sur la même thématique, ce qui a parfois rendu difficiles, mais enrichissants les échanges techniques. D'autre part, l'ostéogenèse et le remodelage osseux ayant fait l'objet de très nombreux travaux au cours des dernières années, il a été nécessaire de proposer une étude pertinente et originale. Enfin, ce choix a coïncidé avec le démarrage de la thèse de Mary Schmitt, ma première doctorante que j'ai co-encadrée avec Philippe Rouch.

Les résultats que j'ai obtenus jusqu'à présent ont été plus qu'encourageants et m'ont permis de définir mon projet de recherche pour les prochaines années. Mon travail, qui consiste essentiellement à développer des

modèles numériques, est organisé en trois axes principaux que je présente brièvement dans la suite.

Comportement mécanique de l'os cortical et ostéogénèse (Chapitre 2)

La structure de l'os cortical repose sur l'assemblage hiérarchique de matériaux lamellaires selon trois formes: i) les ostéons, constitués par des lamelles circonférentielles et orientées selon l'axe longitudinal de l'os, ii) les interstices entre ostéons et iii) les lamelles circonférentielles à la périphérie de l'os.

Cette morphologie induit un comportement isotrope transverse aussi bien en rigidité qu'en résistance avec des propriétés mécaniques différentes dans le plan des lamelles et dans la direction perpendiculaire à celles-ci. De plus, cette structure peut évoluer et s'adapter à l'état de contraintes et déformations de l'environnement au cours du remodelage osseux, qui peut être intensifié suite à une fracture ou à l'implantation d'une prothèse. Afin d'évaluer ces deux aspects, j'ai développé deux études en parallèle.

La première, en collaboration avec Christophe Cluzel de l'Ecole Normale Supérieure de Cachan, a permis de mettre en place un protocole expérimental original, rarement utilisé dans le domaine de la biomécanique, permettant de tester en traction des éprouvettes d'os cortical de bœuf. Notre objectif a été de vérifier i) que la microstructure de l'os promeut la diffusion d'un endommagement anisotrope dont les plans de dégradation sont parallèles à celui des lamelles et ii) que le seuil de rupture fragile pour un chargement statique perpendiculaire au plan des lamelles est plus faible que celui dans le plan des lamelles.

La deuxième étude, qui fait l'objet de la thèse de Mary Schmitt que j'ai co-encadré avec Philippe Rouch à l'Institut de Biomécanique Humaine Georges Charpak, porte sur le développement d'un modèle mécanobiologique simulant la migration collective au cours de l'ostéogénèse au sein d'un scaffold poreux en titane implanté dans une mandibule de brebis. Dans ce modèle, on a couplé la mécanique (i.e. chargement cyclique et comportement poroélastique de l'os) et la biologie (i.e. activités cellulaires comme la migration, la prolifération et la différenciation) à travers des équations de diffusion-réaction et on a montré que la mécanique peut en fait influencer l'intensité et la direction de la colonisation cellulaire. Les résultats numériques ont été comparés qualitativement avec les examens histologiques et quantitativement avec les données expérimentales obtenues sur les brebis sacrifiées au bout de trois mois après l'implantation du scaffold.

Bien que les résultats soient prometteurs, deux questions principales sont encore ouvertes :

- comment les cellules et combien d'entre elles ressentent et répondent à leur environnement (i.e. propriétés mécaniques, géométrie, etc...) ?
- comment les cellules coordonnent leur mouvement collectif pendant la colonisation de l'implant poreux ?

Afin d'explorer ces aspects, des études ultérieures à l'échelle de la cellule et de la population cellulaire sont indispensables. Plus particulièrement, il est nécessaire de comprendre comment les cellules se comportent pendant la migration uni et pluricellulaire, ce qui conduit à mes deux autres axes de recherche présentés ci-dessous.

Migration unicellulaire (Chapitre 3)

La migration unicellulaire permet à la cellule de se déplacer en réponse à un signal externe au sein de la matrice extracellulaire (ECM) qui présente une certaine hétérogénéité (i.e. géométrie, porosité, propriétés mécaniques). Dans ce contexte, j'ai d'abord développé un modèle simplifié tridimensionnel (3D) de mécanique des milieux continus aux éléments finis pour simuler la migration d'une cellule sur un substrat bidimensionnel (2D) hétérogène ou homogène. Ensuite, j'ai adapté ce modèle afin de reproduire et analyser la migration unicellulaire dans différentes configurations comme le confinement ou la variation des propriétés mécanique de l'environnement. Dans le premier cas, en collaboration avec Matthieu Piel de l'Institut Curie, on a été capable de déterminer les conditions nécessaires pour qu'une cellule ait un comportement invasif ou pas. De plus, on a confirmé le rôle critique du noyau, la composante la plus rigide de la cellule, au cours de la migration à travers des pores à dimensions sub-nucléaires. Dans le deuxième cas, en collaboration avec Benoît Ladoux de l'Institut Jacques Monod, on a établi le lien entre le processus de polarisation cellulaire et la rigidité du substrat et plus particulièrement la transition d'une configuration isotrope non adhésive sur un substrat mou à une configuration anisotrope adhésive sur un substrat rigide.

Migration pluricellulaire (Chapitre 4)

La migration pluricellulaire se base sur les mêmes principes de la migration unicellulaire, mais deux facteurs supplémentaires sont nécessaires : i) la synchronisation entre la cellule au sein de la population et ii) la présence au sein de la cohorte de cellules leaders capables de tirer les autres. Pour mieux comprendre ces aspects, j'ai développé deux modèles.

Le premier, en collaboration avec James Sharpe du Center for Genomic Regulation de Barcelone, a permis d'étudier la relation entre la synchronisation dans chaque cellule entre les déformations actives et les forces d'adhésion (i.e. intra-synchronisation) et la synchronisation entre les cellules (i.e. inter-synchronisation) pour que la population soit la plus efficace possible.

Le deuxième modèle a été mis en place en collaboration avec Philip Maini pendant mon séjour au Mathematical Institute à l'Université d'Oxford et reproduit la migration du primordium latéral chez le poisson zèbre. Par un couplage entre la mécanique et le réseau moléculaire par des équations de diffusion-réaction on a analysé le rôle et l'influence des cellules leader sur l'efficacité globale de la cohorte.

Chapter 1

Curriculum Vitae

General information

Rachele Allena. Assistant professor at the Institut de Biomécanique Humaine Georges Charpak at the Ecole Nationale Supérieure des Arts et Métiers (ENSAM) Paris.

Born January 9th 1981 at Cuneo (Italy). Italian and french nationality. 34 years.

Professional address: Institut de Biomécanique Humaine Georges Charpak, ENSAM Paris, 151 Boulevard de l'hôpital, 75013 Paris, France.

Tel: +33 1 44 24 61 18

E-mail: rachele.allena@ensam.eu

Web page: racheleallena.altervista.org

Education

2009	PhD in Biomechanics at the Ecole Centrale Paris. Mention 'très honorable'.
2005	Master in mechanical engineering at Politecnico of Turin (Italy). Final grade 100/110.
2004-2005	Master project at the Biomechanics Laboratory at University of Illinois at Chicago (United States).
2003-2004	Erasmus at the Institut National Polytechnique of Grenoble.
1999	Baccalaureate at Lycée Giovanni Vasco of Mondovi (Cuneo, Italy).

Professional experience

2011-...	Assistant professor at the ENSAM Paris.
2010-2011	Marie Curie-INTERPOD Post doctoral fellow at the Center for Genomic Regulation of Barcelona (Spain).
2009-2010	CNRS Post doctoral fellow at the Laboratoire de Mécanique des Solides, Structures et Matériaux at the Ecole Centrale Paris.
2009-2010	Stand-in teacher at the Ecole Centrale Paris.
2006-2009	Teacher Assistant at the Ecole Centrale Paris.
2005-2006	Teacher Assistant at the University of Illinois at Chicago (United States).

2005-2006 Research engineer at the Cell and Tissue Laboratory at the University of Illinois at Chicago (United States).

Scientific supervision

PhD theses

- 09/2012-09/2015 Mary Schmitt (50%, co-supervision Pr Philippe Rouch).
Multiphysics and multiscale modelling of osteogenesis within a porous titanium scaffold.
Final defense scheduled for June, 16th 2015.
- 02/2012-12/2014 Sami Bendaya (30%, co-supervision Pr Wafa Skalli and Pr J.-Y. Lazenec).
Etude comparative des paramètres pelviens, acétabulaires et fémoraux proximaux des hanches natives asymptomatiques, chez les coxarthroses et après PTH. Analyse par système EOS.
Defended on December, 19th 2014.

Master

- 01/2015-06/2015 Solenne Devereaux (50%)
Quantitative evaluation of nucleus strains during confined cell migration.
- 10/2013-06/2014 Pierre-Antoine Rodesch (30%)
Hip arthroplasty and alteration of postural alignment.
- 10/2013-06/2014 Maxime Bourgain (30%)
Shell finite element model of the skull.
- 10/2012-06/2013 Andres Rondon (50%)
Prediction of fracture risk for patients affected by osteogenesis imperfecta.
- 10/2012-06/2013 Camille Hermann (30%)
Experimental validation of finite element model of human cranial vault.
- 10/2011-06/2012 Rafael Esprin (50%)
Prediction of the aortic response to an implantation of TAVI in order to optimize the therapeutic choice.
- 10/2011-06/2012 Caroline Perbos (50%)
Finite element modelling of femur drilling and restoration.
- 10/2011-06/2012 Erwan Barbier (30%)
A patient-specific finite element model of the human cranial vault.

10/2011-06/2012 Emeline Potevin (25%)
Mechanical property attribution from EOS images.

Teaching

Teaching for the BioMedical Engineering Master ParisTECH (2011 – ...):

Cell mechanics, adhesion and motility	25h/year	Master 2	English
Mechanical behaviour of biological tissues	34h/year	Master 2	English
Finite Elements	16h/year	Master 2	English

Teaching for the Unité d'Enseignement d'Expertise of Bioingénierie, ENSAM Paris (2011 – ...):

Comportement des biomatériaux	20h/year	Master 1	French
-------------------------------	----------	----------	--------

Teaching for the International Master 1, ENSAM Paris (2011 – ...):

Solid mechanics	25h/year	Master 1	English
-----------------	----------	----------	---------

Teaching at the Ecole Centrale Paris (2006 - 2010):

Mécanique	25h/year	Master 1	French
MicroElectroMechanicalSystem	20h/year	Master 1	French
Dimensionnement des structures composites	128h/year	Master 1	French

Teaching at the University of Illinois at Chicago (2005 - 2006):

Bioinstrumentation	32h/year	Master 1	English
Cell and tissue engineering	96h/year	Master 1	English

Administrative and collective activities

Reviewer for Bone, Physical Biology, Journal of the Royal Society of Interface, Journal of Biomechanics, Biomechanics and Modelling in Mechanobiology.

Member of the organizing committee of the Biomechanics Society Congress 2015.

Member of the organizing committee of the Rencontres Franciliennes de Mécanique 2015.

Sept 2013-...	Responsible for the Unité d'Enseignement 'Mechanical behaviour of biological tissues' of the BioMedical Engineering Master ParisTECH.
March 2013-...	Co-chair of the BioMAT track of the BioMedical Engineering Master ParisTECH.
Jan 2012-...	Representative of the teachers/researchers at the Institut de Biomécanique Humaine Georges Charpak.
Oct 2012-...	Responsible for the Unité d'Enseignement d'Expertise of Bioengineering at the ENSAM Paris.

Oct 2012-...	Responsible for the Unité d'Enseignement 'Cell mechanics, adhesion and motility' of the BioMedical Engineering Master ParisTECH.
Oct 2011-...	Responsible for the Unité d'Enseignement 'Biomaterials behavior' of the Unité d'Enseignement d'Expertise of Bioengineering at the ENSAM Paris.
Oct 2011-Sept 2014	Responsible for the Scientific Life at the Institut de Biomécanique Humaine Georges Charpak.

Grants

2015	Fellowship of the Isaac Newton Institut at the University of Cambridge (United Kingdom).
2015	Fellowship of the Gruppo Nazionale per la Fisica Matematica (Italy).
2013- 2017	Recipient of the Prime d'Excellence Scientifique.
2010-2011	Marie Curie-INTERPOD posto doctoral fellowship (Spain).
2009-2010	CNRS post doctoral fellowship.
2006-2009	French ministerial doctoral fellowship.
2006-2009	Teacher Assistant fellowship of the CIES de Versailles.
2005-2006	Teacher Assistant fellowship of the National Institute of Health (United States).
2004-2005	Master fellowship of the Politecnico of Turin (Italy).
2003-2004	Erasmus fellowship.

Appointments

August 2015	Long term visit, Isaac Newton Institute, University of Cambridge (United Kingdom).
11/01-07/02 2015	Long term visit, Mathematical Department, Politecnico of Turin (Italy).
26/07-02/08 2014	Short term visit, Mechanobiology Institute (Singapore).
11-17/08 2013	Short term visit, Mathematical Institute, University of Oxford (United Kingdom).
27/07-08/08 2013	Short term visit, Mechanobiology Institute (Singapore).
29/04-12/05 2013	Short term visit, Mathematical Institute, University of Oxford (United Kingdom).
6-10/12 2012	Short term visit, Universidad Politècnica de Catalunya, Barcelona (Spain).

Seminars

March 2015	Mathematics Department, University of Sussex (United Kingdom).
September 2014	Politecnico of Turin (Italy).
July 2014	Mechanobiology Institute (Singapore).
April 2014	Ecole Polytechnique de Lausanne (Switzerland).
July 2013	Mechanobiology Institute (Singapore).
May 2013	Mathematical Institute, University of Oxford (United Kingdom).
November 2012	Institut de Mécanique des Fluides de Toulouse.
April 2012	Institut Curie.
February 2012	MOX, Politecnico of Turin (Italy).

June 2011	Laboratoire de Biomécanique, ENSAM Paris.
March 2011	LADHYX, Ecole Polytechnique.
November 2010	Laboratoire de Mécanique des Solides, Ecole Polytechnique.
April 2010	Center for Genomic Regulation, Barcelona (Spain).
February 2010	INRIA, Rocquencourt.
February 2010	Laboratoire Matière et Systèmes Complexes, Paris 7.
April 2009	Laboratoire de Spéctométrie Physique, INP Grenoble.

Publications

14 Papers in peer reviewed international journals (1 Biomechanics and Modelling in Mechanobiology, 1 Molecular and Cellular Biomechanics, 1 Computational Mechanics, 1 Mechanical Engineering Research, 1 Clinical Biomechanics, 1 Journal of Theoretical Biology, 2 Journal of the Mechanical Behaviour of Biomedical Materials, 3 Computer Methods in Biomechanics and Biomedical Engineering, 3 Bulletin of Mathematical Biology).

19 International conferences.

2 Invited talks in international and national conferences.

Papers submitted to peer reviewed international journals

3) D. Aubry, M. Gupta, B. Ladoux, **R. Allena** *Mechanical link between durotaxis, cell polarization and anisotropy*. Submitted with minor revision to Physical Biology, 2015.

2) S. Bendaya, C. Anglin, J.-Y. Lazenec, **R. Allena**, C. Vergari, P. Thoumie, W. Skalli *Good VS Poor results after total hip arthroplasty A comparison of implant and anatomical parameters*. Submitted to Journal of arthroplasty, 2015.

1) M. Schmitt, **R. Allena**, P. Rouch *Poroelastic finite element model of an ewe's mandible to evaluate interstitial fluid pressure during cyclic mastication*. Submitted to Journal of the Mechanical Behavior of Biomedical Materials, 2014.

Papers accepted in peer reviewed international journals

14) M. Schmitt, **R. Allena**, T. Schouman, S. Frasca, J.M. Collombet, X. Holly, P. Rouch *Diffusion model to describe osteogenesis within a porous titanium scaffold*. Computer Methods in Biomechanics and Biomedical Engineering, 9: 1-9, 2015 (<http://www.ncbi.nlm.nih.gov/pubmed/25573031>).

13) **R. Allena** *Mechanical modelling of confined cell migration across constricted-curved micro-channels*. Molecular and Cellular Biomechanics, 11:185-208, 2014.

12) S. Bendaya, J.-Y. Lazenec, C. Anglin, **R. Allena**, N. Sellam, P. Thoumie, W. Skalli *Healthy vs. osteoarthritic hips: A comparison of hip, pelvis and femoral parameters and relationships using the EOS® system*. Clinical biomechanics, 2014 (<http://www.ncbi.nlm.nih.gov/pubmed/25532450>).

11) **R. Allena** and P. L. Maini *Reaction-diffusion finite element model of lateral*

line primordium migration to explore cell leadership. Bulletin of Mathematical Biology, 76: 3028-2050, 2014 (<http://www.ncbi.nlm.nih.gov/pubmed/25421149>).

10) **R. Allena** and C. Cluzel *Identification of anisotropic tensile strength of cortical bone using Brazilian test*. Journal of the Mechanical behaviour of Biomedical Materials, 38: 134-142, 2014 (<http://www.sciencedirect.com/science/article/pii/S1751616114001714>).

9) D. Aubry, H. Thiam, M. Piel, **R. Allena** *A computational mechanics approach to assess the link between cell morphology and forces during confined migration*. Biomechanics and Modelling in mechanobiology, 14: 143-157, 2014 (<http://www.ncbi.nlm.nih.gov/pubmed/24895016>).

8) **R. Allena**, D. Aubry, J. Sharpe *On the mechanical interplay between intra- and inter-synchronization during collective cell migration : a numerical investigation*. Bulletin of Mathematical Biology, 75: 2575-99, 2013 (<http://www.ncbi.nlm.nih.gov/pubmed/24135793>).

7) **R. Allena** *Cell migration with multiple pseudopodia: temporal and spatial sensing models*. Bulletin of Mathematical Biology, 75 : 288-316, 2013 (<http://link.springer.com/article/10.1007%2Fs11538-012-9806-1>).

6) **R. Allena**, J. Muñoz, D. Aubry *Diffusion-reaction model for Drosophila embryo development*. Computer methods in biomechanics and biomedical engineering, 16 : 235-248, 2013 (<http://www.ncbi.nlm.nih.gov/pubmed/21970322>).

5) **R. Allena** and D. Aubry *Run-and-tumble or look-and-run? A mechanical model to explore the behavior of a migrating amoeboid cell*. Journal of Theoretical Biology, 306 : 15-31, 2012 (<http://www.ncbi.nlm.nih.gov/pubmed/22726805>).

4) **R. Allena** and D. Aubry *Coupling ALE technique and harmonic parametrization to describe concurrent and successive elementary cell deformations*. Mechanical Engineering Research, 1 : 47-68, 2011 (<http://www.ccsenet.org/journal/index.php/mer/article/view/13969>).

3) **R. Allena** and D. Aubry *An extensive numerical simulation of cephalic furrow formation in Drosophila embryo*. Computer methods in biomechanics and biomedical engineering, 15 : 445-55, 2010 (<http://www.ncbi.nlm.nih.gov/pubmed/21331957>).

2) **R. Allena** and D. Aubry *A novel technique to parametrize shell-like deformations inside biological membranes*. Computational Mechanics, 47 : 409-423, 2010 (<http://link.springer.com/article/10.1007%2Fs00466-010-0551-8>).

1) **R. Allena**, A. -S. Mouronval, D. Aubry *Simulation of multiple morphogenetic movements in Drosophila embryo by a single 3D Finite Elements model*. Journal of the Mechanical Behavior of Biomedical Materials, 3 : 313-23, 2010 (<http://www.ncbi.nlm.nih.gov/pubmed/20346899>).

Invited communications

2) **R. Allena**, C. Cluzel *Towards a multiscale and multiphysics modelling of the mechanical behaviour of cortical bone*. Journée Scientifique de la Fédération de Médecine Translationnelle de Strasbourg, December 10th, 2014 October, Strasbourg (France), 2014.

1) **R. Allena**, E. Farge, D. Aubry *Finite element model to simulate multiple morphogenetic movements*. 3rd European meeting on Cell Mechanics, 19th – 21st October, Bad Honnef (Germany), 2009.

Other communications

19) S. Bendaya, C. Anglin, J.-Y. Lazennec, **R. Allena**, P. Thoumie, W. Skalli *Comparaison des paramètres acétabulaires chez les patients porteurs de PTH, assis-débout, étudiés par le système EOS*. 89^{ème} Congrès de la SOFCOT, November 8th – 13th, Paris (France), 2014.

18) S. Bendaya, C. Anglin, J.-Y. Lazennec, **R. Allena**, P. Thoumie, W. Skalli *HIP osteoarthritis vs healthy subjects: a comparison of hip, pelvis and lower limb parameters under weighbearing using the EOS imaging system*. CAOS – Computer Assisted Orthopaedic Sugery, June 18th – 21st, Milan (Italy), 2014.

17) D. Aubry, T.H. Racine, M. Piel, **R. Allena** *A computational mechanics approach to assess the link between cell morphology and forces during confined migration*. 5th European Conference on Computational Mechanics, July 20th – 25th, Barcelona (Spain), 2014.

16) M. Schmitt, P. Rouch, T. Schouman, **R. Allena** *Diffusion-reaction model to describe osteogenesis within a porous titanium scaffold*. 5th European Conference on Computational Mechanics, July 20th – 25th, Barcelona (Spain), 2014.

15) S. Bendaya, C. Anglin, J.-Y. Lazennec, **R. Allena**, P. Thoumie, W. Skalli *Coxométrie fonctionnelle en 3D en position debout avec le système EOS chez sujets sains et avec arthrose de hance*. 28^{ème} Congrès de la SOFMER, October 17th – 19th, Reims (France), 2013.

14) M. Schmitt, P. Rouch, Y. Tillier, T. Schouman, **R. Allena** *Diffusion-reaction model to describe osteogenesis within a porous titanium scaffold*. 38^{ème} Congrès de la Société de Biomécanique, September 3rd – 6th, Marseille (France), 2013.

13) M. Schmitt, P. Rouch, Y. Tillier, T. Schouman, **R. Allena** *Multiscale and multiphysics modeling of bone healing within a titanium scaffold*. 11th International Symposium on Computer Methods in Biomechanics and Biomedical Engineering, April 3rd – 7th, Salt Lake City (United States), 2013.

12) **R. Allena**, M. Schmitt, D. Aubry, P. Rouch *Two –time scale multiphysics model of osteogenesis within a 3D trabecular network*. 19th Congress of the European Society of Biomechanics, August 25th – 28th, Patras (Greece), 2013.

13) **R. Allena**, D. Aubry *A purely mechanical model to explore amoeboid cell migration*. 37^{ème} Congrès de la Société de Biomécanique, October 16th – 19th,

Toulouse (France), 2012 (Selected for the Prix de la Société de Biomécanique).

12) **R.Allena**, L. Duchemin, V. Bousson, D. Mitton, J.-D. Laredo, K. Engelke, W. Kalli *Evaluation of a subject specific finite element model of the proximal femur in a side load configuration*. Congress of the European Society of Biomechanics, July 1st – 4th, Lisbona (Portugal), 2012.

11) **R. Allena**, D. Aubry *Pseudopod controlled migration of an amoeboid cell : a realistic finite element model*. Congress of the European Society of Biomechanics, July 1st – 4th, Lisbona (Portugal), 2012.

10) **R. Allena**, D. Aubry *A mechanical model to explore the behavior of a migrating amoeboid cell*. Symposium ‘Frontiers in Biology’, March 7th – 9th, Barcelona (Spain), 2012.

9) **R. Allena**, J. Muñoz, D. Aubry *Viscoelastic model of Drosophila embryo*. 10th World Congress of Computational Mechanics, July 19th – 24th, Sydney (Australia), 2010.

8) **R. Allena**, J. Muñoz, D. Aubry *3D Mechano-diffusion model for Drosophila embryo development*. European Congress of Computational Mechanics, May 17th – 21st, Paris (France), 2010.

7) **R. Allena**, D. Aubry. *Modelling of regulated embryo morphogenesis*. 3rd International conference on Mechanics of Biomaterial and Tissue, December 13th – 17th, Clearwater Beach (United States), 2009.

6) A.-S. Mouronval, **R. Allena**, E. Farge, D. Aubry *Simulation numérique des mouvements morphogénétiques dans l’embryon de Drosophile : influence de la géométrie initiale*. 9^{ème} Colloque National en Calcul de Structures, May 25th – 29th, Giens (France), 2009.

5) **R. Allena**, E. Farge, A.-S. Mouronval, D. Aubry *Concurrent simulation of morphogenetic movements in Drosophila embryo*. Morphogenesis in Living Systems (Université Descartes), May 14th – 16th, Paris (France), 2009.

4) **R. Allena**, E. Farge, A.-S. Mouronval, D. Aubry *Concurrent simulation of morphogenetic movements in Drosophila embryo*. 13th International Conference on Biomedical Engineering, December 3rd – 8th, Singapore, 2008.

3) **R. Allena**, E. Farge, A.-S. Mouronval, D. Aubry *Concurrent simulation of morphogenetic movements in Drosophila embryo*. WCCM8 and ECCOMAS, June 30th – July 5th, Venice (Italy), 2008.

2) **R. Allena**, E. Farge, A.-S. Mouronval, D. Aubry *Numerical simulation of mechanotransduction in Drosophila embryo including mesoderm large strains*. Second International Conference on Mechanics of Biomaterials & Tissues, Marriot’s Kaua’i Resort and Beach Club, December 9th – 13th, Hawai’i (United States), 2007.

1) **R. Allena**, E. Farge, A.-S. Mouronval, D. Aubry *Numerical simulation of mechanotransduction in Drosophila embryo*. Workshop on Finite Elements Modelling in Biomechanics and Mechanobiology, European Society of Biomechanics, August 6th – 28th, Dublin (Ireland), 2007.

Chapter 2

Mechanical behaviour of cortical bone and osteogenesis

Bone is a porous material which is hierarchically organised at different levels (Fig. 2.1): i) the macrostructure (cortical and trabecular bone), ii) the mesostructure (haversian system, osteons and trabeculae), iii) the microstructure (lamellae and osteocytes), iv) the nanostructure (collagen and minerals) and v) the sub-nanostructure (molecules and proteins). Such a layered structure provides specific mechanical and failure behaviour at each level (1, 2). Several cell phenotypes including osteoblasts, responsible for the formation of new bone, and osteoclasts and osteocytes, responsible for the resorption of old and unhealthy bone (3), can be found in bone. These cells are embedded in a mineralized matrix mainly constituted of collagen and hydroxyapatite. Collagen (mostly Type I) consists of strands of repeated units providing tensile strength to the bone, whereas shear stress is resisted thanks to the overlapping arrangement of the strands. Additionally, as a poroelastic material, bone shows different types of porosity according to its hierarchical structure described above. More specifically, we find the vascular porosity (VP) (between 20 μ m and 40 μ m), the lacunacanalicular porosity (LCP) (around 100nm) and the collagen-apatite porosity (CAP) (about 1nm). Although the pore fluid may not carry a significant portion of the mechanical loading, its flow may play a critical role in most of the cellular sensing and signalling mechanisms such as those involved during the remodelling/osteogenesis processes (4–6). Actually, the osteocytes located in the lacunae sense the shear stress induced by the fluid flow and transmit specific signals to the osteoclasts and the osteoblasts.

It is possible to distinguish five types of bone in the human body:

- long bones composed of a diaphysis, much longer than its width, and an epiphysis, a rounded head at each end of the diaphysis (i.e. limbs, fingers and toes);
- short bones which are cube-shaped and show a thin layer of cortical bone surrounding the trabecular interior; (i.e. wrist and ankle);
- flat bones which are thin and curved, composed by two layers of cortical bone sandwiching the trabecular bone (i.e. skull);
- sesamoid bones which are embedded in tendons (i.e. patella);
- irregular bones such as spine and pelvis.

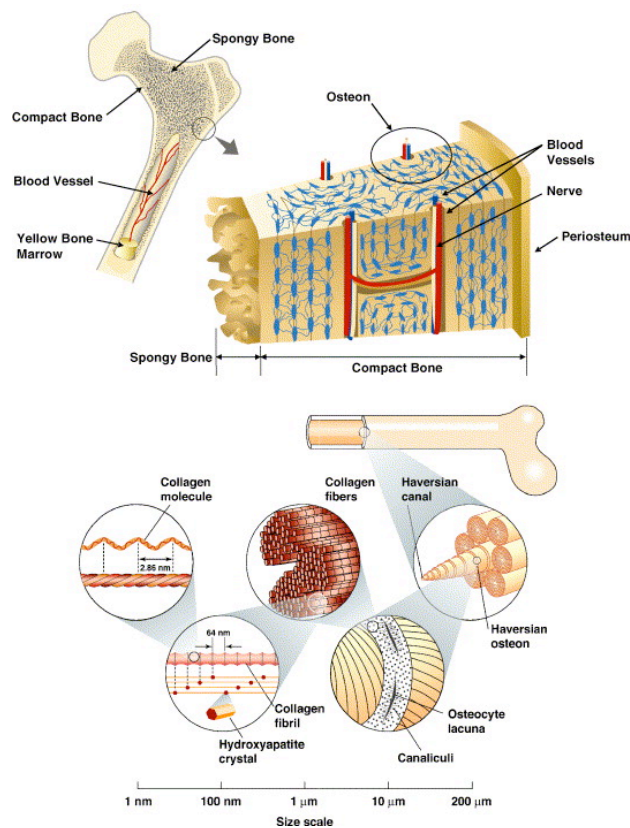


Fig. 2.1 Hierarchical structure of cortical bone (7).

2.1 Osteogenesis and bone remodelling

During embryogenesis, long bones are initially formed by cartilage, which is then gradually replaced by bone thanks to a process known as endochondral bone formation. However, flat bones are directly formed from mesenchymal condensation through a process called intramembranous ossification. During childhood, both osteogenesis (formation and shaping) and bone remodelling (replacing or renewing) occur, while in adulthood bone remodelling is the main process that maintains skeletal integrity (8, 9). Such phenomena are particularly intensified following injuries, micro-fractures or placement of implants which elicit a sequence of biomechanical and healing events. In the latter case, the short term mechanical stability of the implant is ensured by the direct contact and friction between the bone and the implant, whereas in the long term a biological attachment between the implant and the bone is required. Therefore, as bone is formed, its architecture must adapt to the functional loads and the modelling process is influenced by the induced strains and stresses.

Osteogenesis is a process that cooperates with bone growth and functions to alter the spatial distribution of accumulating tissue presented by growth (10–12). Since new tissue is deposited over existing bone undergoing an increased or altered loading environment, the positioning has to meet the rapid evolution of mechanical demands and the geometry has to be optimised. Osteogenesis may

occur in two different ways: i) osteoclast activation and resorption of bone or ii) osteoblast activation and formation of bone (11, 13).

While bone osteogenesis involves resorption or formation, but not both at the same time, bone remodelling always takes place in three phases: resorption, reversal and formation. Resorption (about 2 weeks) is induced by migration of preosteoclasts to the bone surface where osteoclasts are formed. Reversal (about 4 or 5 weeks) triggers appearance of mononuclear cells, which prepare the surface for osteoblasts and give the necessary signals for osteoblast migration and differentiation. Formation (up to 4 months) consists of the replacement of resorbed bone by new tissue, which results in a surface covered with flattened cells.

Mechanical loading may strongly influence osteogenesis and remodelling. On one hand, disuse, the lack of or low mechanical loading stimuli trigger a domination of bone resorption over bone formation. On the other hand, overuse of bone leads to damage of tissue and in turn remodelling, but, if damage accumulation occurs faster than its repair, one may observe larger microcracks and their propagation (10, 14). New bone formation is most effective if it takes place in bone regions where the stresses are highest, thus reducing the risk of structural failure. Furthermore, Wolff (15) observed that in many bones (i.e. proximal femur, vertebral bodies, proximal tibia) the trabecular trajectories were mainly aligned with the directions of maximum stress. Such alignment results in an anisotropic behaviour of the bone, so that the stiffness and strength are increased in the main direction without increasing bone mass.

2.2 Previous models of osteogenesis and bone remodelling

In recent decades several analytical (6, 16–21) and computational (22–25) works have been proposed in the literature to evaluate the fluid-structure interactions occurring during bone remodelling and osteogenesis. The common objective has been to understand the interaction between the cells and their mechanical environment in order to optimise the design of prostheses and other bone substitutes used in the tissue engineering field. Some of them (26–28) are based on the work of Weinbaum et al. (6) which aimed to elucidate the mechanotransduction phenomenon undergone by the osteocytes. Others have tried to take into account each type of porosity and their interconnection (22, 29–31) and they found that the fluid pressures in each domain are rather independent or not much reciprocally affected. Finally, some authors have employed the Biot theory to obtain the governing equations for bone samples undergoing simple mechanical loading such as step-loaded bending (32), transverse deflection (33) or cyclic bending and compression (20, 23).

In 1960, Pauwels (34) was the first to propose a model of bone cells differentiation during fracture healing. He stated that hydrostatic pressure promotes the formation of cartilage tissue, while shear strain enhances the formation of fibrous tissue. Consequently, bone formation only occurs once the stabilisation of the environment has been ensured by the fibrous tissue. Similarly, Carter et al. (35) developed a model based on the interaction between hydrostatic pressure and shear stress and defined the characteristic domains for the formation of bone, cartilage, fibrous and fibro-cartilage tissues. In the same spirit, Prendergast et al. (36) linearly coupled the distortion γ and the velocity of the

interstitial fluid v_f as follows

$$S = \frac{\gamma}{a} + \frac{v_f}{b} \quad (2.1)$$

where a and b are two constants respectively equal to 0.0375 and 3 $\mu\text{m/s}$ and S is the stimulus. This model was the first to consider the poroelastic behaviour of the bone and, thanks to specific animal tests, the authors have been able to determine a set of thresholds of S (Fig. 2.2) that has been widely used since (37, 38, 38–46).

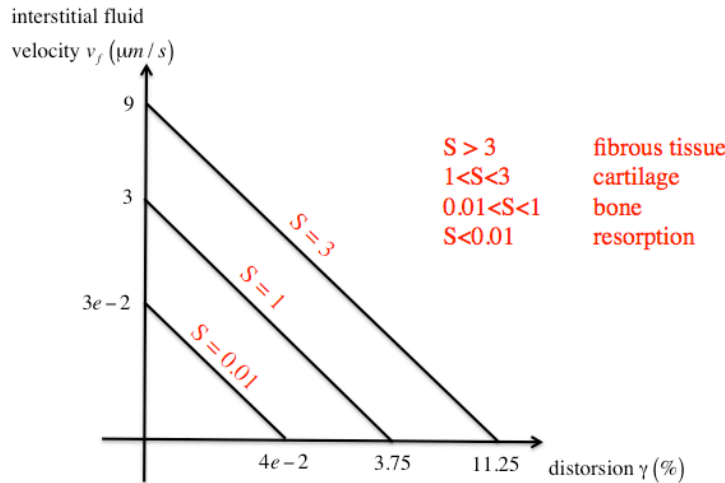


Fig. 2.2 Diagram of cell differentiation proposed by Prendergast et al. (36).

Nevertheless, this algorithm shows some limitations. Firstly, the cells only respond to mechanical stimuli (i.e. mechanotransduction), whereas bio-chemical signals may also influence cellular activity. Secondly, although the interstitial fluid is taken into account, the model neglects electrical potentials. Finally, Eq. 2.1 employs two constants that were deduced during an *in vivo* experiment, which may therefore circumscribe their applicability.

There exists a series of computational models that aim to simulate osteogenesis within porous materials or structures. Such works may be classified into two categories: the mechanobiological models that consider both the mechanics and the cellular activity (39, 47, 38, 44, 48, 37, 49) and the mechanical models that only take into account the mechanical framework (50–53).

Among the mechanobiological models, a further distinction must be made between the discrete (37, 38) and the continuum (38, 40, 44) models. The former allow modelling of the space occupied by each cell and both migration and proliferation are often regulated by a stochastic law. The latter instead use reaction-diffusion equations to describe migration, proliferation and differentiation. The main drawback of these models is their validation since they rely on a large number of parameters that are difficult to measure *in vivo*.

The mechanical models do not consider the formation of cartilage and fibrous tissue, but only bone. Therefore, they do not directly reproduce the cellular activity, but just the apposition or the resorption of the bone on or within the implant.

The previous models have certainly helped in better understanding the principal mechanisms regulating fluid-structure interactions during bone formation and remodelling, however they present two main drawbacks. Firstly, most of these works evaluate the behaviour of small bone specimens, thus they provide consistent results at the microscale, but may fail in capturing the global response of a whole bone structure. Secondly, the time dependent description of the evolution of the interstitial pressure coupled with the mechanics of the problem results in a significant computing time.

2.3 Development of a model for osteogenesis

When I joined the Institut de Biomécanique Georges Charpak four years ago, I started to develop a model of osteogenesis with the objective of bypassing the issues mentioned above. In order to do so, I made few assumptions:

- firstly, I consider the poroelastic behaviour of bone so that the total Cauchy stress $\boldsymbol{\sigma}$ in the mechanical structure is classically expressed as

$$\boldsymbol{\sigma} = \bar{\boldsymbol{\sigma}} - \alpha p_f \mathbf{I} \quad (2.2)$$

where $\bar{\boldsymbol{\sigma}}$ is the effective stress in the solid phase, whereas p_f is the interstitial pressure in the fluid phase. α and \mathbf{I} are the Biot-Willis coefficient (54) and the identity matrix respectively;

- secondly, four cell populations are involved: the mesenchymal cells, the osteoblasts, the fibroblasts and the chondrocytes whose activities are coupled as sketched in Fig. 2.3.

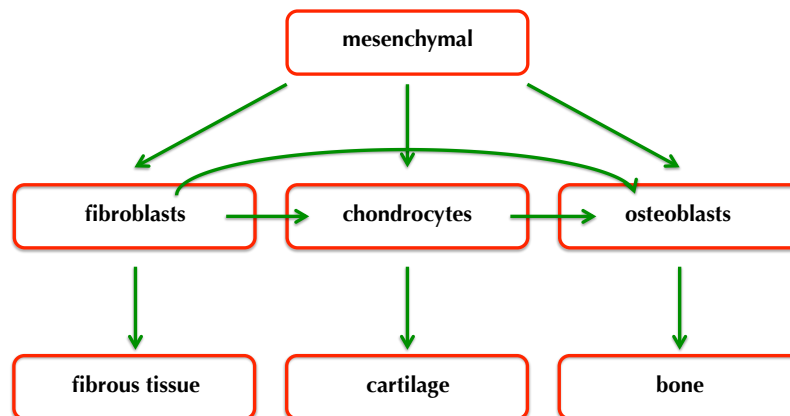


Fig. 2.3 Diagram showing the connections between the cell phenotypes. Arrows indicate potential differentiation processes.

Each cell population is described as a normalised concentration c_i (where the subscript i indicates the cell phenotype) through a reaction-diffusion equation which defines the main cellular functions and reads

$$\frac{\partial c_i}{\partial t} = \text{div}(\mathbf{D}_i \nabla c_i) + p(c_i) + d(c_i) \quad (2.3)$$

with t , Div and ∇ the time, the divergence and the gradient, respectively. The second ($p(c_i)$) and the third ($d(c_i)$) term on the right hand side characterise the proliferation and differentiation of the cells, whereas the first term defines the migration of the cells and is coupled with the mechanical framework of the problem through the tensor \mathbf{D}_i which is expressed as follows

$$\mathbf{D}_i = \alpha_i \mathbf{I} + \beta_i \left(\sqrt{|\sigma_I|} \phi_{\sigma_I} \otimes \phi_{\sigma_I} + \sqrt{|\sigma_{II}|} \phi_{\sigma_{II}} \otimes \phi_{\sigma_{II}} + \sqrt{|\sigma_{III}|} \phi_{\sigma_{III}} \otimes \phi_{\sigma_{III}} \right) \quad (2.4)$$

where α_i and β_i are constants, $|\sigma_I|$, $|\sigma_{II}|$ and $|\sigma_{III}|$ are the absolute values of the principal stresses and ϕ_{σ_I} , $\phi_{\sigma_{II}}$ and $\phi_{\sigma_{III}}$ are the principal directions. It has to be said that the migration term is computed for the mesenchymal cells and the fibroblasts only, since the migration velocity of osteoclasts and chondrocytes is negligible;

- thirdly, the cyclic loading to which the structure is submitted throughout the osteogenesis process is taken into account;
- finally, I employ the stimulus S introduced by Prendergast et al. (36) to determine the amount of cartilage, fibrous tissue and bone in the structure.

Therefore, the model includes the main aspects of both the mechanical (i.e. poroelastic behaviour of bone and cyclic loading) and the biological (i.e. cellular activity) framework and is able to simulate osteogenesis throughout twelve weeks in a reasonable computing time. In the next section I present the results for initial application of the approach.

2.4 Finite element model of osteogenesis within a titanium porous scaffold

When bone is injured and a fracture or defect exceeds a critical size, a support such as a scaffold is implanted in order to promote bone ingrowth and to ensure proper transmission of the mechanical loads. Such bone substitutes constitute a good compromise between autologous bone and distraction osteogenesis since they allow immediate re-establishment of the anatomical functions of the structure and avoidance of disease transmission. There exist two categories of scaffolds: the non resorbable (made of titanium or steel) and the resorbable ones (made of ceramics or polymers). On one hand, the main advantage of the resorbable scaffolds is that once implanted, bone progressively replaces the scaffold. Nevertheless, it is still difficult to find the proper adjustment between the mechanical properties and the resorbability (i.e. the interaction with the organism) in order to avoid the rejection of toxic substances. On the other hand, the non resorbable scaffolds show good mechanical strength and biocompatibility, but their mechanical properties are very different to those of bone and more specifically their Young's modulus is much higher than that of the bone. This results in a much stiffer structure which withstands nearly all the applied stresses with the consequence that the bone is under-loaded. One solution to this drawback is to design a porous scaffold to considerably reduce the effective Young's modulus and to enhance the osteointegration. Actually, it has been shown that porous implants promote cell anchorage and proliferation (55–58). One may distinguish between two porosities: the micro-porosity, responsible for the material roughness, and the macro-porosity, responsible for the structure of the scaffold. The former enables a better grip of the cells on the surface (59), whereas the latter allows the cells to migrate across the implant and to colonise it. Some studies have demonstrated that a coating of the implant (i.e. hydroxyapatite) may improve cell adhesion, corrosion resistance and bioactivity (56, 60, 61).

During the PhD of Mary Schmitt at the Institut de Biomécanique Humaine Georges Charpak, which I have co-supervised with Philippe Rouch, both experimental and numerical approaches have been used to investigate osteogenesis within a titanium porous scaffold designed and fabricated by OBL®, a French manufacturer of maxillofacial implants (www.oblparis.fr).

From an experimental point of view, a porous and a non porous scaffold were implanted after a symmetrical and bilateral resection of the non-toothed part of a series of 29 ewe's mandibles. The choice of a bigger animal such as the sheep is due to the similarities with human bone in terms of the remodeling process. Twelve weeks after implantation (characteristic time for osteogenesis), the animals were sacrificed and each hemi-mandible underwent a cantilever test to determine the stiffness at the bone-implant interfaces.

From a numerical point of view, the work has been organized in successive steps.

First, using poroelasticity theory (54, 62), we have evaluated the interstitial fluid pressure inside two three-dimensional (3D) beams (with dimensions of the hemimandible) with rectangular and elliptical sections, respectively and both submitted to cyclic loading. For the former, the results have been compared to those obtained by Manfredini et al. (23) to validate our computational approach. The latter has allowed us to determine the influence of

the geometry and the boundary conditions of the mechanical structure on the evolution of the interstitial pressure. A paper has been submitted to the Journal of Biomechanics.

Second, a preliminary two-dimensional (2D) finite element model has been developed which is partially based on the hypotheses described in Sec. 2.3. In fact, here we do not describe the poroelastic behaviour of the bone nor the cyclic boundary conditions and we only take into account the mesenchymal cells and their activity. Despite these simplifications, the numerical results at the end of the osteogenesis process are compared qualitatively with the data from the histological analysis and quantitatively with the data from the mechanical tests done on the sacrificed ewes. A paper has been published in Computer Methods for Biomechanical and Biomedical Engineering.

Third, a 3D realistic geometry of the hemimandible has been considered and all the hypotheses proposed in Sec. 2.3 have been included. Due to the complex coupling between mechanics and biology, a specific algorithm has been set up in order to update the mechanical properties according to the evolution of the cell populations and their differentiation. A paper on this part of the work is in progress.

Included Paper:

Schmitt M, et al. (2015) Diffusion model to describe osteogenesis within a porous titanium scaffold. *Comput Methods Biomech Biomed Engin* 0(0):1–9.

Submitted Paper:

Schmitt M, Allena R, Rouch P Poroelastic finite element model of a ewe's mandible to evaluate interstitial fluid pressure during cyclic mastication. *Submitted to Journal of Biomechanics*, 2015.

Diffusion model to describe osteogenesis within a porous titanium scaffold

M. Schmitt^{a*}, R. Allena^a, T. Schouman^{a,b}, S. Frasca^c, J.M. Collombet^c, X. Holy^c and P. Rouch^a

^aArts et Métiers ParisTech, LBM, 151 bd de l'hôpital, 75013 Paris, France; ^bDepartment of maxillofacial surgery, APHP – Pitié-Salpêtrière University Hospital, University of Paris 6, 75013 Paris, France; ^cInstitut de recherche biomédicale des armées, 91223 Brétigny sur Orge, France

(Received 10 March 2014; accepted 10 December 2014)

In this study, we develop a two-dimensional finite element model, which is derived from an animal experiment and allows simulating osteogenesis within a porous titanium scaffold implanted in ewe's hemi-mandible during 12 weeks. The cell activity is described through diffusion equations and regulated by the stress state of the structure. We compare our model to (i) histological observations and (ii) experimental data obtained from a mechanical test done on sacrificed animal. We show that our mechano-biological approach provides consistent numerical results and constitutes a useful tool to predict osteogenesis pattern.

Keywords: bone scaffold; osteogenesis; *in vivo* test; finite element method; mechanobiology

1. Introduction

Bone is a living tissue able to rebuild and restore its physical and geometrical properties when injured. Specifically, bone remodelling and bone ingrowth are two important biological phenomena that successively occur during fracture healing process, prosthesis osseointegration and distraction osteogenesis (Meyreuis and Cazenave 2004). Nevertheless, when a defect exceeds a critical size for spontaneous bone formation (Schmitz and Hollinger 1986), a structural support such as a porous implant (i.e. scaffold) is required to enhance bone ingrowth and to ensure the mechanical loads transmission.

During the last decades, many *in vivo* studies on rodents (i.e. rabbits or rats) have evaluated the osseointegration of porous implants (Karageorgiou and Kaplan 2005; Takemoto et al. 2005; St-Pierre et al. 2005; Otsuki et al. 2006; Lopez-Heredia et al. 2008). Nonetheless, besides the high cost of experimentations, osteogenesis is a long process with successive steps, which makes its experimental observation very difficult. Therefore, mathematical and numerical models have been proposed in the literature to better understand the complex process of osteogenesis and optimize the design of the scaffolds.

These models can be divided into two main categories: the multi-physics and the multi-scale models. The former consider the mechanoregulatory process that may take place during bone ingrowth and osteogenesis. Different theories emerged demonstrating that mechanics plays an important role on the cellular activity. Pauwels (1960) was the first to hypothesize that mechanical stresses and strains could determine the differentiation pathways of mesench-

ymal stem cells (MSCs). Specifically, he found that during bone fracture healing, bone formation only occurs once fracture stabilization is ensured by fibrous tissues. Carter et al. (1988) suggested that MSCs are more likely to become osteogenic if they are submitted to low shear strain and compressive hydrostatic stress. In Prendergast et al. (1997), the coupling between the fluid–solid velocity and the maximal shear strain is considered as a key factor for the regulation of cell differentiation. Such an approach has been widely used to predict tissue regeneration during fracture healing (Lacroix and Prendergast 2002; Isaksson et al. 2008), distraction osteogenesis (Isaksson et al. 2007) and also tissue ingrowth within scaffolds (Kelly and Prendergast 2006; Liu and Niebur 2008) or at bone–implant porous interface (Huiskes et al. 1997; Andreykiv et al. 2005; Andreykiv et al. 2008). Other mechanobiological models have been proposed using different techniques resulting in random walk models (Pérez and Prendergast 2007; Byrne et al. 2007), lattice-based models (Checa and Prendergast 2010; Sandino et al. 2010), biological model (Moreo et al. 2009) and voxel finite element (FE) models (Adachi et al. 2006; Sanz-Herrera et al. 2008, 2009).

The multi-scale models distinguish between two spatio-temporal scales at the tissue and at the pore-scaffold level. Among these works, we mention those from Prendergast et al. (1997), Kelly and Prendergast (2006) and Sanz-Herrera et al. (2008, 2009) in which the influence of both the cellular activity and the scaffold microstructure is considered. In addition, some homogenization approaches (Hollister et al. 2002, Taboas et al. 2003,

*Corresponding author. Email: mary.schmitt-8@etudiants.ensam.eu

Hutmacher et al. 2004) have been used to design and control the scaffold porosity and pores size.

Most of the previous works are defined by a large number of parameters, which are difficult to determine experimentally, and therefore the results are only qualitatively compared to the experimental observations. An alternative approach was proposed by Roshan-Ghias et al. (2011) according to which bone osteogenesis is regulated by a diffusion phenomenon and the few unknown variables of the model are identified through *in vivo* micro-computed tomography (micro-CT).

In the present paper, we introduce a two-dimensional (2D) FE model derived from a specific animal study. Our main goal is to propose a new numerical approach to describe osteogenesis within a titanium scaffold implanted in a ewe's hemi-mandible. The key feature of the model lays on the link between mechanics and biology, which is stronger than those proposed in previous works. In fact, the cellular activity (i.e. migration and proliferation) is defined through diffusion equations, which are coupled twice with the mechanical framework of the problem through (i) the principal stresses and (ii) the principal directions. At the end of the bone-remodelling process, which takes 12 weeks in our specific case (Den Boer et al. 1999), the numerical results are compared to the experimental ones in two different ways. First, we qualitatively correlate the cell density and colonization patterns to the histological data obtained on an implanted hemi-mandible. Secondly, we quantitatively assess the consistence of the same results by performing a cantilever bending simulation on the colonized hemi-mandible and comparing it to the corresponding experimental deflection.

2. Methods

2.1 Scaffold and experimental set up

In this present study, an 18-mm long titanium scaffold with a porosity of 53% was placed after resection of the non-toothed part of ewes' hemi-mandibles. To anchor the scaffold to the bone, 10 titanium screws were used (Figure 1(b)). The scaffold was designed and produced by OBL® using a selective laser melting (SLM) technique (Barbas et al. 2012).

Three ewes' hemi-mandibles were tested:

- a non-implanted (NI-0, Figure 1(a)) and an implanted (I-0, Figure 1(b)) hemi-mandibles coming from the same ewe sacrificed right after scaffold implantation ($t = 0$);
- an implanted (I-12, Figure 2(a)) hemi-mandible coming from a ewe sacrificed 12 weeks after scaffold implantation ($t = 12$ weeks).

Both ewes were approximately 2 years old. A cantilever bending test was performed on each hemi-mandible using a universal traction machine (INSTRON 5500-R).

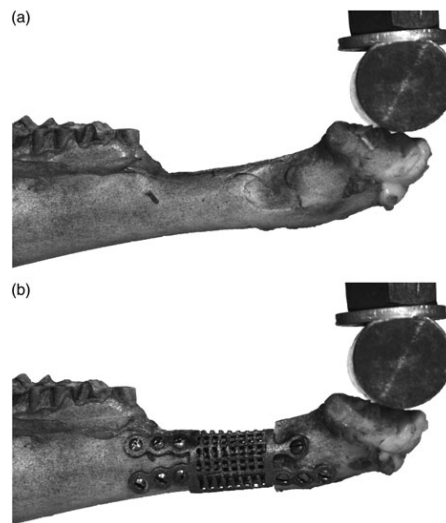


Figure 1. The NI-0 (a) and I-0 (b) hemi-mandible coming from the same ewe sacrificed right after scaffold implantation ($t = 0$). In (b), the 18-mm-long titanium scaffold placed after resection of the non-toothed part of the I-0 hemi-mandible and anchored to the bone with 10 titanium screws is noticeable.

Before the test, a black and white speckle pattern was painted on the hemi-mandible in order to perform digital images correlation (DIC). The proximal boundary of the hemi-mandible was embedded into polymethylmethacrylate (PMMA), while the distal boundary was submitted to a displacement of 2 mm/min, which was applied until failure through a cylinder load nose. The resultant force was measured using a load cell of 1 KN.

During the test, the hemi-mandible was kept wet to avoid the drying of the bone, which could have altered its mechanical properties (Evans and Lebow 1952; Blackburn et al. 1992). Finally, frontal images of the set-up were captured every 2 s using a digital camera.

2.2 Histological evaluation

After micro-CT, defect areas including a 5-mm edge of native bone at both the anterior and posterior margins were excised from the hemi-mandible I-12. The segments were fixed for at least 7 days in 10% phosphate-buffered formaldehyde solution.

Undecalcified segments were sectioned with a diamond saw (Secotom, Struers) along the antero-posterior direction thereafter dehydrated with methanol, and then embedded in methyl-methacrylate-based resin. The hardened specimen blocks were cut in the longitudinal

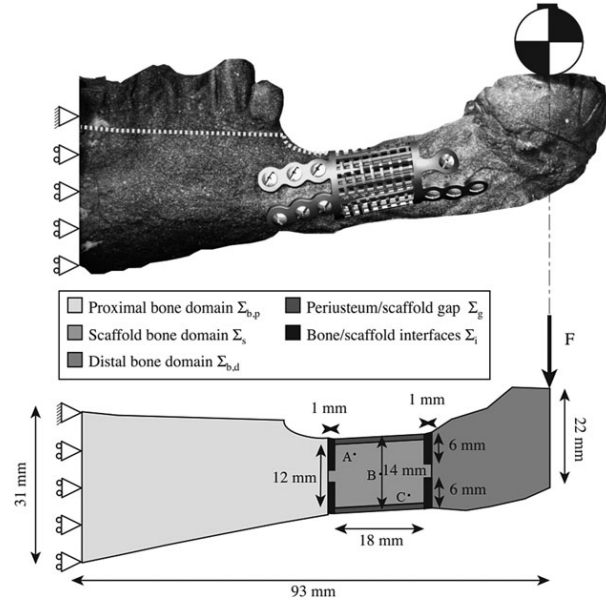


Figure 2. (a) The I-12 hemi-mandible. (b) The FE model geometry: dimensions, boundary conditions and subdomains of the implanted hemi-mandible. A, B and C indicate the three points used to evaluate c_m for the sensitivity analysis (see Appendix).

direction along the axis of the implant. Sections of interest were sawn off with the diamond saw, ground and finally polished up with a Buelher micro-grinding device to reach 100 μm thickness.

Finally, sections were stained with modified Masson–Goldner’s trichrome dye to evaluate bone healing efficiency by histomorphometry and examined under a light microscopy (DMRB Leica, DXC930 Camera Sony).

2.3 Mechano-biological FE model

The mechano-biological framework of the FE model allows simulating the bone ingrowth within the titanium scaffold implanted in the hemi-mandible. Because the mandible is considered as a flat bone, here we only take into account intramembranous ossification, which, in contrast to endochondral ossification, does not require cartilaginous tissue.

The 2D geometry representing a sagittal view of the hemi-mandible (Figure 2(b)) has been obtained from the frontal digital images through DIC. The hemi-mandible is constituted by a proximal and a distal bone domains, $\Sigma_{b,p}$ and $\Sigma_{b,d}$, respectively. In addition, it includes a central domain composed of the scaffold Σ_s , which is placed between the two gaps, Σ_g , between the periosteum and the

scaffold, and four interfaces Σ_{ij} (the subscript j indicates the interface number) between the scaffold and the bone. The domains Σ_s and Σ_{ij} have been represented through specific characteristic functions h_s and h_{ij} .

Here, we consider that each domain is made of an isotropic linear elastic material. For $\Sigma_{b,p}$ and $\Sigma_{b,d}$, homogenized Young’s moduli ($E_{b,p}$ and $E_{b,d}$, respectively) have been deduced from the experimental deflection curve of the neutral axis of the hemi-mandible. For Σ_s , Σ_{ij} and Σ_g , we assume that, at the initial configuration, they are filled with a granular tissue, which will be gradually replaced by bone during the 12 weeks. Consequently, E_s , E_{ij} and E_g vary with respect to time and bone mineralization and are defined as follows:

$$E_s = (E_{s,0}(1 - \varnothing_{s,0}) + \varnothing_{s,0}(E_t(1 - c_m h_{\tau_m}) + E_b c_m h_{\tau_m})) h_s, \quad (1)$$

$$E_{ij} = (E_t(1 - c_m h_{\tau_m}) + E_b c_m h_{\tau_m}) h_{ij}, \quad (2)$$

$$E_g = E_t(1 - c_m h_{\tau_m}) + E_b c_m h_{\tau_m}, \quad (3)$$

where $E_{s,0}$ is the initial Young’s modulus of the scaffold, E_t and E_b are the Young’s moduli of the granular tissue and the newly formed bone, respectively, $\varnothing_{s,0}$ is the scaffold initial porosity and c_m is the MSCs concentration, which is

defined as the fraction of MSCs inside the scaffold. h_{τ_m} is a characteristic function allowing to initiate the mineralization process. In fact, as the osteoblasts activity is not directly modelled, we assume that the mineralization starts after a maturation time τ_m of the MSCs of about 2 weeks (Malaval et al. 1999) and takes approximately 3 weeks to complete (Eriksen et al. 1986). Thus, the fraction of mineralized bone m_b inside the scaffold is defined as

$$m_b = c_m h_{\tau_m}. \quad (4)$$

We assume that both c_m and m_b are normalized and vary between 0 and 1.

During the simulation, the proximal boundary of the hemi-mandible is allowed to translate along the y -axis (except for the upper point which is completely blocked), while the distal boundary is submitted to a constant force to simulate the ewes' mastication (Thomason et al. 2001) (Figure 2(b)).

In the following, the diffusion equations used to describe the evolution of the MSCs concentration c_m within the different domains of the system are presented. Inside $\Sigma_{b,p}$ and $\Sigma_{b,d}$, we consider that c_m is constant with respect to time, while a Robin condition on $\partial\Sigma_{b,p}$ and $\partial\Sigma_{b,d}$ is applied to reproduce the cell proliferation outside the system. Thus, the diffusion equation reads

$$\frac{\partial c_m}{\partial t} = \text{div}(\mathbf{D}_{m,b} \text{grad } c_m) \quad \text{on } \Sigma_{b,p} \text{ and } \Sigma_{b,d}, \quad (5)$$

$$\begin{aligned} (\mathbf{D}_{m,b} \text{grad } c_m, \mathbf{n}) &= -\gamma(c_{m,0} - c_m) \\ &\quad \text{on } \partial\Sigma_{b,p} \text{ and } \partial\Sigma_{b,d}, \end{aligned} \quad (6)$$

where div and grad represent the divergence and the gradient, respectively, (\mathbf{a}, \mathbf{b}) defines the scalar product between two vectors, γ is a constant, $c_{m,0}$ is the initial concentration of the MSCs inside the domains and \mathbf{n} is the outward normal vector along the external boundaries. $\mathbf{D}_{m,b}$ is a tensor which couples the concentration c_m with the principal stresses and directions as follows:

$$\mathbf{D}_{m,b} = \alpha_b \mathbf{I} + \beta_b \left(\sqrt{|\sigma_I|} \mathcal{D}_{\sigma_I} \otimes \mathcal{D}_{\sigma_I} + \sqrt{|\sigma_{II}|} \mathcal{D}_{\sigma_{II}} \otimes \mathcal{D}_{\sigma_{II}} \right), \quad (7)$$

where α_b and β_b are specific constants, \mathbf{I} is the identity matrix and \mathcal{D}_{σ_I} and $\mathcal{D}_{\sigma_{II}}$ are the principal directions of the principal stresses σ_I and σ_{II} . $|\cdot|$ and \otimes indicate the absolute value and the tensorial product, respectively.

The evolution of c_m within the scaffold is also defined by a diffusion equation as follows:

$$\frac{\partial c_m}{\partial t} = \text{div}(\mathbf{D}_{m,s} \text{grad } c_m) + P_m, \quad (8)$$

where the first and the second terms on the right-hand side describe the migration and the proliferation processes,

respectively. As in Equation (6), $\mathbf{D}_{m,s}$ is coupled with the mechanics of the problem and reads

$$\mathbf{D}_{m,s} = \alpha_s \mathbf{I} + \beta_s \left(\sqrt{|\sigma_I|} \mathcal{D}_{\sigma_I} \otimes \mathcal{D}_{\sigma_I} + \sqrt{|\sigma_{II}|} \mathcal{D}_{\sigma_{II}} \otimes \mathcal{D}_{\sigma_{II}} \right), \quad (9)$$

where α_s and β_s are specific constants. The MSCs proliferation P_m is expressed as

$$P_m = P_{m,0}(1 - c_m)c_m, \quad (10)$$

with $P_{m,0}$ the MSCs production rate. MSCs migrate from the proximal and the distal bone domains but also from the periosteum. Thus, the previous diffusion equation is coupled with a Robin condition on the periosteum boundaries $\partial\Sigma_p$:

$$(\mathbf{D}_{m,s} \text{grad } c_m, \mathbf{n}) = -\gamma(c_{m,0} - c_m) \quad \text{on } \partial\Sigma_p. \quad (11)$$

3. Results

3.1 Experimental results

As mentioned in Section 2.1, a cantilever bending test was performed on three hemi-mandibles: NI-0, I-0 and I-12. The experimental deflection curves are represented in Figure 3.

First, it is possible to observe a clear difference between the two curves NI-0 and I-0. In fact, for NI-0 the curve is mostly straight, while for I-0 the curve presents two local changes in slope corresponding to the proximal and distal bone-scaffold interfaces, respectively.

Secondly, by comparing the curve of I-0 at $t = 0$ to the curve of I-12 at $t = 12$ weeks, it is possible to notice that the deflection is less important for the latter than for the former.

These outputs confirm that (i) the scaffold does not support the entire load and (ii) the cell colonization and mineralization do affect the global mechanical response of the system via the increase in the Young modulus inside the scaffold and at the interfaces of the scaffold with the proximal and distal bones.

3.2 Numerical osteogenesis

The numerical simulation has been run using the FE software COMSOL 3.5a. The main parameters associated with the constitutive behaviour of the system and the cellular activity are reported in Table 1.

In Figure 4, the results at the end of the process (i.e. 12 weeks) are represented. The MSCs concentration c_m varies between 0.3 and 1, respectively, at the centre and along the external boundaries of the scaffold (Figure 4(a)). More specifically, at points A, B and C (Figure 2(b)), c_m is equal to 0.61, 0.36 and 0.6, respectively. Because the

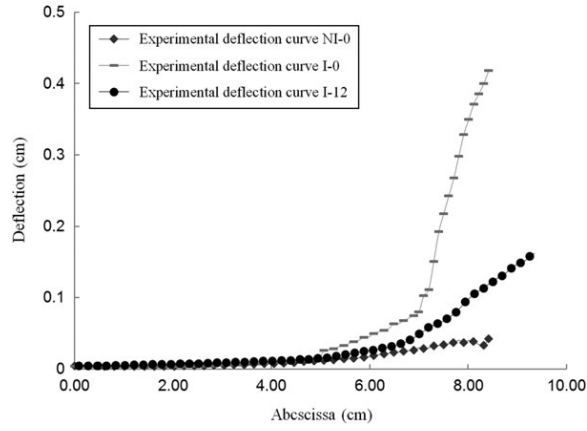


Figure 3. Experimental deflection curves of the neutral axis of NI-0 and I-0 at $t = 0$ and of I-12 at $t = 12$ weeks.

mineralization process starts after 2 weeks of maturation and takes approximately 3 weeks to complete (Section 2.3), we observe a complete cellular mineralization (i.e. equal to 1) at about 5 weeks after maturation (Figure 4(b)). We notice that the colonization and the mineralization patterns are very similar and occur from the outer boundaries towards the central region of the scaffold. In addition, the four interfaces Σ_{ij} , which were initially filled by a granular tissue, are now completely mineralized. Thus, according to Equation (1), the global stiffness of the scaffold is increased by the end of the simulation.

In Figure 5(a), a sagittal view of the middle section of the scaffold histological examination is reported. We distinguish between the mineralized bone (blue) and the fibrous tissue (purple), which are mostly

distributed at the periphery and at the centre of the scaffold, respectively. The histological analysis provided a ratio bone volume (BV)/total volume (TV) equal to 62%. The direct comparison with our numerical results is not possible due to the fact that (i) the FE model is 2D and (ii) the scaffold pores are not physically modelled here. Nevertheless, thanks to the specific in-house Matlab software, we have been able to evaluate the ratio bone surface (BS)/total surface (TS) on Figure 5(a) and a value of 27% was obtained. For the FE model, we considered that bone is mineralized when m_b (Equation 4) is higher than 0.8. Then, the numerical value of BS/TS after 12 weeks is equal to 29% (Figure 5(b)). Therefore, we may conclude that our numerical results are qualitatively and quantitatively in agreement with the histological data.

Table 1. Model parameters.

Variable	Symbol	Value	Unit	Reference
Young's modulus of the proximal bone	$E_{b,p}$	6500	MPa	Deduced from DIC
Young's modulus of the distal bone	$E_{b,d}$	300	MPa	Deduced from DIC
Initial Young's modulus of the scaffold	$E_{s,0}$	60	GPa	Deduced from Barbas et al. (2012)
Young's modulus of granular tissue	E_t	0.2	MPa	Andreykiv et al. (2008)
Young's modulus of newly formed bone	E_b	200	MPa	Deduced from Nafei et al. (2000)
Initial porosity of the titanium scaffold	$\varnothing_{s,0}$	0.53		Barbas et al. (2012)
Robin constant	γ	$1e^{-7}$	m^2/s	
The initial concentration of the MSCs	$c_{m,0}$	0.98		
Diffusion constant in the bone domain	α_b	$1e^{-20}$	m^2/s	
Diffusion constant in the bone domain	β_b	$3e^{-13}$	m^2/s	
Diffusion constant in the scaffold domain	α_s	$1e^{-20}$	m^2/s	
Diffusion constant in the scaffold domain	β_s	$3e^{-15}$	m^2/s	
The MSCs production rate	$P_{m,0}$	$2e^{-9}$	s^{-1}	
MSCs maturation time	τ_m	14	days	Malaval et al. (1999)

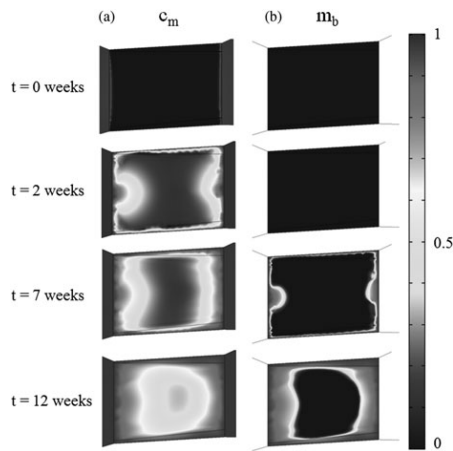


Figure 4. Time evolution of normalized MSCs concentration c_m (a) and of the fraction of mineralized bone m_b (b) within the scaffold predicted by the numerical simulation.

3.3 Comparison of the FE model to the experimental results

The cantilever bending test performed on the ewe's hemi-mandible 12 weeks after implantation (I-12) allows us to show the consistency of the FE model. In Figure 6, the experimental and the FE model deflection curves of the hemi-mandible's neutral axis at 12 weeks are represented. For both, the maximum deflection is reached at the distal boundary where the force is applied. Nevertheless, we obtained a maximal displacement of 1.62 mm for the former and of 1.46 mm for the latter. Furthermore, there are two local changes of the curve's slope which correspond to the proximal and distal bone-scaffold interfaces, respectively. Such a behaviour is mainly due to the low stiffness of the newly formed with respect to the proximal and distal bones.

Finally, in Figure 6, the FE model deflection curve of the hemi-mandible's neutral axis at the initial configuration is also represented. We notice that the maximum

deflection after osteogenesis is about four times lower than the one obtained at the initial configuration (1.46 mm versus 5.65 mm, respectively). Such a difference is mainly due to the bone ingrowth within the scaffold and also at the bone-scaffold interfaces, which increase the global stiffness of the structure.

4. Discussion

In the literature, most of the models have not been validated (Andreykiv et al. 2005; Adachi et al. 2006; Andreykiv et al. 2008; Byrne et al. 2007; Liu and Niebur 2008) or validated through experimental tests on small animals (i.e. rabbits or rats) because their size and cost make the experimental protocol easier (Sanz-Herrera et al. 2008, 2009; Roshan-Ghias et al. 2011). Nevertheless, their bone properties are quite different than human's (Pearce et al. 2007). For instance, their characteristic time for bone remodelling is four times shorter (Sanz-Herrera et al. 2008). Therefore, our model is directly derived from an animal experiment done on bigger animals such as ewes. Indeed, the ovine model has been widely used in bone defect repair, distraction osteogenesis, osteoporosis and osteoarthritis research (Willie et al. 2004), and has been indicated as a valid model for the study of human bone remodelling and turnover (Den Boer et al. 1999; Pearce et al. 2007). The 2D FE model we have proposed allows simulating osteogenesis within a porous titanium scaffold implanted in a ewe's hemi-mandible for 12 weeks.

Cells migration and bone ingrowth within the scaffold are described through diffusion equations as previous authors did (Andreykiv et al. 2005; Kelly and Prendergast 2006; Liu and Niebur 2008; Andreykiv et al. 2008; Sanz-Herrera et al. 2008, 2009; Roshan-Ghias et al. 2011). Furthermore, the cells activity is directly coupled to the mechanics of the problem because MSCs migration follows the principal stresses and principal directions. Such a hypothesis results in bone ingrowth occurring from the external boundaries to the centre of the scaffold, which is in agreement with a previous study (Fujibayashi et al. 2003). The model has been correlated to the experimental

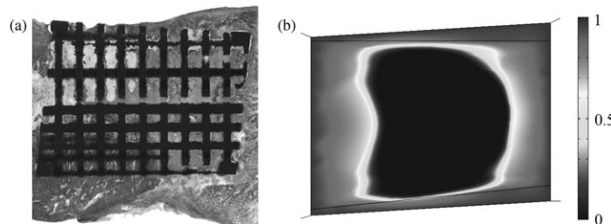


Figure 5. (a) Histological examination of the scaffold: stained middle section with modified Masson-Goldner's trichrome dye (mineralized bone in blue and fibrous tissues in purple). (b) Fraction of mineralized bone m_b at $t = 12$ weeks in the numerical model.

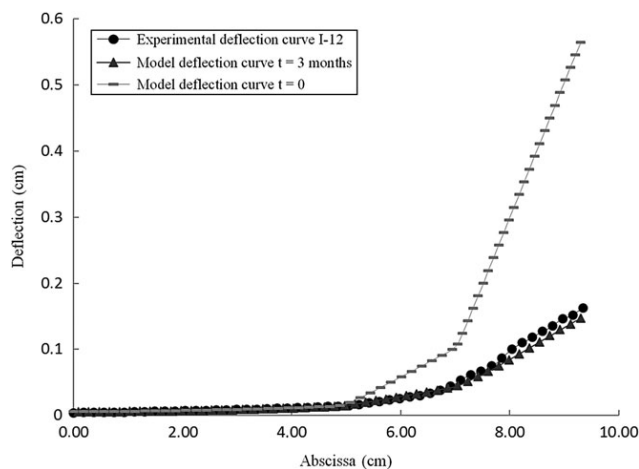


Figure 6. FE (at 0 and 12 weeks) and experimental (at 12 weeks) deflection curves of the neutral axis of the I-12 hemi-mandible.

data. For the former, a qualitative comparison between our numerical results and the histological observations has been done in terms of osteogenesis pattern. For the latter, the numerical and the experimental results obtained from a quasi-static bending test done on the 12 weeks ewe's hemi-mandible have been quantitatively compared. Although such a comparison has been done using the data from only one ewe and at a single time point, the FE model can still be considered as a useful and consistent tool to predict osteogenesis within the scaffold because the numerical results appear to be in agreement with the experimental ones.

Nevertheless, some assumptions have been done to develop the present work. First, a simplified 2D geometry has been employed to represent the implanted hemi-mandible. However, a 3D representation of the system may lead to a more realistic strain–stress distribution, which could influence the cells activity and thus the bone matrix distribution. Indeed, histological observations have pointed out that there might be more newly formed bone on the lingual region of the hemi-mandible than on the external region.

Second, the MSCs differentiation into either fibroblasts or osteoblasts is not regulated here by any biophysical stimulus derived from the interstitial flow and the shear strain (Prendergast et al. 1997) or the strain energy (Sanz-Herrera et al. 2008, 2009). Such stimulus would allow us to take into account all the cells types (i.e. fibroblasts and osteoblasts) involved in the intramembranous ossification.

Finally, we have not yet implemented the intrinsic properties of the implant such as its osteoconductive and osteoinductive characteristics.

Conflict of interest disclosure statement

No potential conflict of interest was reported by the authors.

Funding

This work has been funded by the Chaire BiomecAM, the Ministère de l'enseignement supérieur et de la recherche and OBL® Paris.

References

- Adachi T, Osako Y, Tanaka M, Hojo M, Hollister SJ. 2006. Framework for optimal design of porous scaffold microstructure by computational simulation of bone regeneration. *Biomaterials*. 27(21):3964–3972.
- Andreykiv A, Prendergast PJ, van Keulen F, Swieszkowski W, Rozing PM. 2005. Bone ingrowth simulation for a concept glenoid component design. *J Biomech*. 38(5):1023–1033.
- Andreykiv A, van Keulen F, Prendergast PJ. 2008. Computational mechanobiology to study the effect of surface geometry on peri-implant tissue differentiation. *J Biomech Eng*. 130(5):051015.
- Barbas A, Bonnet A-S, Lipinski P, Pesci R, Dubois G. 2012. Development and mechanical characterization of porous titanium bone substitutes. *J Mech Behav Biomed*. 9:34–44.
- Blackburn J, Hodgskinson R, Currey JD, Mason JE. 1992. Mechanical properties of microcallus in human cancellous bone. *J Orthop Res*. 10(2):237–246.
- Byrne DP, Lacroix D, Planell JA, Kelly DJ, Prendergast PJ. 2007. Simulation of tissue differentiation in a scaffold as a function of porosity, Young's modulus and dissolution rate: application of mechanobiological models in tissue engineering. *Biomaterials*. 28(36):5544–5554.
- Carter DR, Blenman PR, Beaupré GS. 1988. Correlations between mechanical stress history and tissue differentiation in initial fracture healing. *J Orthop Res*. 6(5):736–748.

- Checa S, Prendergast PJ. 2010. Effect of cell seeding and mechanical loading on vascularization and tissue formation inside a scaffold: A mechano-biological model using a lattice approach to simulate cell activity. *J Biomech.* 43(5): 961–968.
- Den Boer FC, Patka P, Bakker FC, Wippermann BW, van Lingen A, Vink GQM, Boshuizen K, Haarman HJT. 1999. New segmental long bone defect model in sheep: Quantitative analysis of healing with dual energy X-ray absorptiometry. *J Orthop Res.* 17(5):654–660.
- Eriksen EF, Mosekilde L, Melsen F. 1986. Trabecular bone remodeling and balance in primary hyperparathyroidism. *Bone.* 7(3):213–221.
- Evans FG, Lebow M. 1952. The strength of human compact bone as revealed by engineering technics. *AM J Surg.* 83(3):326–331.
- Fujibayashi S, Kim H-M, Neo M, Uchida M, Kokubo T, Nakamura T. 2003. Repair of segmental long bone defect in rabbit femur using bioactive titanium cylindrical mesh cage. *Biomaterials.* 24(20):3445–3451.
- Hollister SJ, Maddox RD, Taboas JM. 2002. Optimal design and fabrication of scaffolds to mimic tissue properties and satisfy biological constraints. *Biomaterials.* 23(20):4095–4103.
- Huiskes R, Driël WDV, Prendergast PJ, Søballe K. 1997. A biomechanical regulatory model for periprosthetic fibrous-tissue differentiation. *J Mater Sci Mater Med.* 8(12): 785–788.
- Hutmacher DW, Sittinger M, Risbud MV. 2004. Scaffold-based tissue engineering: rationale for computer-aided design and solid free-form fabrication systems. *Trends Biotechnol.* 22(7):354–362.
- Isaksson H, Comas O, van Donkelaar CC, Mediavilla J, Wilson W, Huiskes R, Ito K. 2007. Bone regeneration during distraction osteogenesis: Mechano-regulation by shear strain and fluid velocity. *J Biomech.* 40(9):2002–2011.
- Isaksson H, van Donkelaar CC, Huiskes R, Ito K. 2008. A mechano-regulatory bone-healing model incorporating cell-phenotype specific activity. *J Theor Biol.* 252(2):230–246.
- Karageorgiou V, Kaplan D. 2005. Porosity of 3D biomaterial scaffolds and osteogenesis. *Biomaterials.* 26(27): 5474–5491.
- Kelly DJ, Prendergast PJ. 2006. Prediction of the optimal mechanical properties for a scaffold used in osteochondral defect repair. *Tissue Eng.* 12(9):2509–2519.
- Lacroix D, Prendergast PJ. 2002. A mechano-regulation model for tissue differentiation during fracture healing: analysis of gap size and loading. *J Biomech.* 35(9):1163–1171.
- Liu X, Niebur GL. 2008. Bone ingrowth into a porous coated implant predicted by a mechano-regulatory tissue differentiation algorithm. *Biomech Model Mechanobiol.* 7(4):335–344.
- Lopez-Heredia MA, Sohier J, Gaillard C, Quillard S, Dorget M, Layrolle P. 2008. Rapid prototyped porous titanium coated with calcium phosphate as a scaffold for bone tissue engineering. *Biomaterials.* 29(17):2608–2615.
- Malaval L, Liu F, Roche P, Aubin JE. 1999. Kinetics of osteoprogenitor proliferation and osteoblast differentiation in vitro. *J Cell Biochem.* 74(4):616–627.
- Meyrueis J-P, Cazenave A. 2004. Consolidation des fractures [Fracture healing]. *EMC - Rhumatologie-Orthopédie.* 1(2):138–162. French.
- Moreo P, García-Aznar JM, Doblaré M. 2009. Bone ingrowth on the surface of endosseous implants. Part 1: Mathematical model. *J Theor Biol.* 260(1):1–12.
- Nafei A, Danielsen CC, Linde F, Hvid I. 2000. Properties of growing trabecular ovine bone. Part I: mechanical and physical properties. *J Bone Joint Surg Br.* 82(6):910–920.
- Otsuki B, Takemoto M, Fujibayashi S, Neo M, Kokubo T, Nakamura T. 2006. Pore throat size and connectivity determine bone and tissue ingrowth into porous implants: three-dimensional micro-CT based structural analyses of porous bioactive titanium implants. *Biomaterials.* 27(35):5892–5900.
- Pauwels F. 1960. Eine neue Theorie über den Einfluß mechanischer Reize auf die Differenzierung der Stützgewebe. *Z Anat Entwickl Gesch.* 121(6):478–515.
- Pearce AJ, Richards RG, Milz S, Schneider E, Pearce SG. 2007. Animal models for implant biomaterial research in bone: a review. *Eur Cell Mater.* 13:1–10.
- Pérez MA, Prendergast PJ. 2007. Random-walk models of cell dispersal included in mechanobiological simulations of tissue differentiation. *J Biomech.* 40(10):2244–2253.
- Prendergast PJ, Huiskes R, Søballe K. 1997. Biophysical stimuli on cells during tissue differentiation at implant interfaces. *J Biomech.* 30(6):539–548.
- Roshan-Ghias A, Vogel A, Rakotomanana L, Pioletti DP. 2011. Prediction of spatio-temporal bone formation in scaffold by diffusion equation. *Biomaterials.* 32(29):7006–7012.
- Sandino C, Checa S, Prendergast PJ, Lacroix D. 2010. Simulation of angiogenesis and cell differentiation in a CaP scaffold subjected to compressive strains using a lattice modeling approach. *Biomaterials.* 31(8):2446–2452.
- Sanz-Herrera JA, García-Aznar JM, Doblaré M. 2008. Micro-macro numerical modelling of bone regeneration in tissue engineering. *Comput Method Appl M.* 197(33–40): 3092–3107.
- Sanz-Herrera JA, García-Aznar JM, Doblaré M. 2009. On scaffold designing for bone regeneration: A computational multiscale approach. *Acta Biomater.* 5(1):219–229.
- Schmitz JP, Hollinger JO. 1986. The critical size defect as an experimental model for craniomandibulofacial nonunions. *Clin Orthop Relat Res.* 205:299–308.
- St-Pierre J-P, Gauthier M, Lefebvre L-P, Tabrizian M. 2005. Three-dimensional growth of differentiating MC3T3-E1 pre-osteoblasts on porous titanium scaffolds. *Biomaterials.* 26(35)–7328.
- Taboas J, Maddox R, Krebsbach P, Hollister S. 2003. Indirect solid free form fabrication of local and global porous, biomimetic and composite 3D polymer-ceramic scaffolds. *Biomaterials.* 24(1):181–194.
- Takemoto M, Fujibayashi S, Neo M, Suzuki J, Kokubo T, Nakamura T. 2005. Mechanical properties and osteoconductivity of porous bioactive titanium. *Biomaterials.* 26(30):6014–6023.
- Thomason JJ, Grovum LE, Deswysen AG, Bignell WW. 2001. In vivo surface strain and stereology of the frontal and maxillary bones of sheep: implications for the structural design of the mammalian skull. *Anat Rec.* 264(4):325–338.
- Willie BM, Bloebaum RD, Bireley WR, Bachus KN, Hofmann AA. 2004. Determining relevance of a weight-bearing ovine model for bone ingrowth assessment. *J Biomed Mater Res A.* 69(3):567–576.

Appendix

Sensitivity analysis

According to Table 1, the model presents 14 parameters. Among them, two have been determined from DIC ($E_{b,p}$ and $E_{b,d}$) and five have been found (E_t , $\mathcal{O}_{s,0}$ and τ_m) or deduced ($E_{s,0}$ and E_b) from the literature. As for $c_{m,0}$, since we have assumed that both the proximal and the distal bone regions are completely fulfilled of MSCs throughout the simulation, a value of 0.98 has been fixed.

Therefore, to determine which parameters most influence the results and in particular the final value of the MSCs concentration c_m , a sensitivity analysis has been performed by letting vary of $\pm 10\%$ the remaining six parameters: γ , α_b , β_b , α_s , β_s and $P_{m,0}$. The value of c_m at $t = 12$ weeks has been evaluated at points A, B and C (Figure 1) and has been compared to the value obtained at the same points for the standard simulation (Section 3.2). The results are reported in Table 2.

As expected, the most influencing parameter is the diffusion constant in the scaffold domain β_s . In fact, as β_s increases or decreases, c_m increases (between 3.9% and 10%) and decreases (between 6% and 12%), respectively. However, when γ , α_b , α_s , β_b and $P_{m,0}$ change, the final value of c_m only undergoes a variation between 0.23% and 1.1%.

Table 2. Numerical results for the sensitivity analysis.

Constant	Variation (%)	Value	Deviation of c_m with respect to the values in Section 3.2		
			Point A (%)	Point B (%)	Point C (%)
γ	+10	$1.1e^{-7} \text{ m}^2/\text{s}$	-1.0	-0.77	+0.52
	-10	$0.9e^{-7} \text{ m}^2/\text{s}$	-1.1	-0.83	+0.23
α_b	+10	$1.1e^{-20} \text{ m}^2/\text{s}$	-0.83	-0.71	+0.44
	-10	$0.9e^{-20} \text{ m}^2/\text{s}$	-0.89	-0.74	+0.51
β_b	+10	$3.3e^{-13} \text{ m}^2/\text{s}$	-0.77	-0.56	+0.55
	-10	$2.7e^{-13} \text{ m}^2/\text{s}$	-0.89	-0.78	+0.33
α_s	+10	$1.1e^{-20} \text{ m}^2/\text{s}$	-1.0	-0.83	+0.44
	-10	$0.9e^{-20} \text{ m}^2/\text{s}$	-0.69	-0.64	+0.49
β_s	+10	$3.3e^{-15} \text{ m}^2/\text{s}$	+3.9	+10	+6.0
	-10	$2.7e^{-15} \text{ m}^2/\text{s}$	-6.3	-12	-6.0
$P_{m,0}$	+10	$2.2e^{-9} \text{ s}^{-1}$	-0.78	-0.53	+0.45
	-10	$1.8e^{-9} \text{ s}^{-1}$	-0.85	-0.76	+0.56

Note: The value of c_m at $t = 12$ weeks has been evaluated at points A, B and C (Figure 1) and the deviations with respect to the reference values (Section 3.2) are reported.

2.5 Anisotropic behaviour of cortical bone under traction

As mentioned above, as bone forms and remodels, it adapts its architecture to the surrounding mechanical framework (i.e. stresses and strains). In order to better understand such a process, it is necessary to take into account both the mechanical properties of the bone and its failure behaviour, which highly depend on the hierarchical structure of cortical bone. In the last decades, several experimental tests have been employed toward this goal, but most of them focus on only one of the previous aspects and fail to depict the multiaxial behaviour of the bone.

In collaboration with Christophe Cluzel, Assistant Professor at the Laboratoire de Mécanique et Technologie de l'ENS Cachan, we have proposed the Brazilian test as an alternative experimental technique to study cortical bone behaviour. This technique is usually employed in the field of civil engineering to study the brittle behaviour of materials such as concrete, rock or ceramic, whereas it has rarely been adopted in the biomechanics field.

In the Brazilian test a cylindrical specimen is loaded in compression along its main axis until failure. Since compression triggers tensile stresses normal to the loading direction, a crack appears perpendicular to the maximum traction stress direction resulting in the splitting into two halves of the cylinder. This test shows some interesting features. First, it allows traction testing in brittle materials. Second, it enables the use of specimens whose dimensions may be smaller than those of the representative volume of the material. In the specific case of cortical bone this leads to three further advantages: i) it decreases the probability of finding large defect triggering macroscopic failure, ii) it provides a correlation between the specimen dimensions and the defect distribution and iii) it allows traction testing of the cortical bone along its three axes of anisotropy.

In this study, the Brazilian test was carried out on 29 specimens of bovine cortical bone with diameters from 4 mm to 10 mm. The cortical bone being an anisotropic material, the analytical solution used for an isotropic material is not adequate anymore, but a correction coefficient must be integrated. We have been able to find such coefficient for each failure stress and we have found a variation of about 14% of the maximum stress. Finally, we have assessed the scale influence on the failure mechanism.

Included Paper:

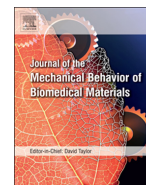
Allena R, Cluzel C (2014) Identification of anisotropic tensile strength of cortical bone using Brazilian test. *J Mech Behav Biomed Mater* 38:134–142.



ELSEVIER

Available online at www.sciencedirect.com

ScienceDirect

www.elsevier.com/locate/jmbbm

Research Paper

Identification of anisotropic tensile strength of cortical bone using Brazilian test

Rachele Allena^{a,*}, Christophe Cluzel^{a,b,c}^aArts et Métiers ParisTech, LBM, 151 Boulevard de l'hôpital, 75013 Paris, France^bLMT-Cachan, 61 av. du Président Wilson, 94235 Cachan, France^cIUT-SGM, rue du Pjarlan, 91025 Evry, France

ARTICLE INFO

Article history:

Received 7 April 2014

Received in revised form

12 June 2014

Accepted 14 June 2014

Available online 25 June 2014

Keywords:

Cortical bone

Anisotropy

Brazilian test

Brittle strength

ABSTRACT

For a proper analysis of cortical bone behaviour, it is essential to take into account both the elastic stiffness and the failure criteria. While ultrasound methods allow complete identification of the elastic orthotropic coefficients, tests used to characterise the various failure mechanisms and to identify the brittle tensile strength in all directions are currently inadequate. In the present work we propose the Brazilian test as a complement to conventional tensile tests. In fact, this experimental technique, rarely employed in the biomechanics field, has the potential to provide an accurate description of the anisotropic strength of cortical bone. Additionally, it allows us to assess the scale influence on failure behaviour which may be attributed to an intrinsic length in correlation with the cortical bone microstructure. In order to correctly set up the Brazilian test, several aspects such as the machining, the geometrical parameters of the specimen and the loading conditions were determined. The finite element method was used to evaluate the maximal tensile stress at the centre of a 2D anisotropic elastic specimen as a simple function of the loading. To validate the protocol, the Brazilian test was carried out on 29 cortical bovine cylindrical specimens with diameters ranging from 10 mm to 4 mm.

© 2014 Elsevier Ltd. All rights reserved.

1. Introduction

1.1. Bone's structure and behaviour

Bone presents a hierarchical structure (Currey, 2001; Rho et al., 1998; Vashishth, 2007) which is organised in different levels as follows: (i) the macrostructure: cancellous and cortical bones, (ii) the mesostructure (from 10 to 500 μm): haversian system, osteons, trabeculae (iii) the microstructure (1–10 μm): the

lamellae and the osteocytes, (iv) the nanostructure (from a few hundred nanometres to 1 μm): fibrillar collagen and embedded mineral, and (v) the sub-nanostructure (below a few hundred nanometres): collagen, molecules and proteins.

The complex structure of the bone has been the object of many studies during the last decades in order to decipher the influence of each level on both the mechanical and the failure behaviour (Currey, 2001). At the nanoscale, the orientation of the collagen fibrils and their degree of mineralisation

*Corresponding author. Tel.: +33 1 44 24 61 18; fax: +33 1 44 24 63 66.

E-mail address: rachele.allena@ensam.eu (R. Allena).

(Turner-Walker and Parry, 1995) may affect Young's modulus leading to a failure stress in the fibres direction. At the microscale, the stacking of successive lamellae, each composed of collagen fibres oriented in a single direction, provides an isotropic mechanical behaviour in the lamellae plan, while weak properties are observed along the perpendicular direction. At the mesoscale, the osteons structure supplies a transverse isotropy for both the stiffness and the failure stresses (Rho et al., 1998; Ascenzi et al., 2013). Such a behaviour is maintained at the macroscale due to the main orientation of the osteons along the longitudinal axis of the bone. Finally, at this level the interface between the osteons and the interstitial lamellae (the cement line) brings a further weakness to the failure behaviour.

Conventional mechanical tests in traction, compression and torsion on specimens obtained from cortical bone of the femur diaphysis were carried out by Reilly and Burstein (1975). They actually observed that Young's modulus along the longitudinal direction is double that measured along the circumferential or radial directions. Therefore, the anisotropy of the elastic behaviour is clearly marked and complies with the geometrical organisation of the bone at the mesoscopic scale.

Nevertheless, this anisotropy is not limited to stiffness, it also influences failure behaviour. As has been pointed out in Norman and Wang (1997), O'Brien et al. (2007), and Feerick et al. (2013), the cement line is a source of weakness that may enhance crack propagation. Similarly, the interface between two lamellae may reduce the failure threshold along their perpendicular direction when several of them are aligned in a circumferential direction as it is shown in Fig. 1 for cortical bone of a young bovine. In contrast, along the longitudinal direction, the lamellae and the osteons are continuous and, for longitudinal loading, rupture occurs with a very high stress. In parallel to the analysis of failure mechanisms, many studies have focused on the failure criterion and have shown that taking into account the failure anisotropy allows better predictive ability (Doblare et al., 2004). Nonetheless, these criteria are very complex to identify experimentally. Additionally, Hashin (1996) and Puck and Schürmann (1998) for fibre reinforced plastic (FRP) composite and Arramon et al. (2000) for bone have pointed out that a multicriterion approach in which each function is related to a specific failure mechanism is more suitable than a quadratic function defining an admissible rupture domain. Therefore,

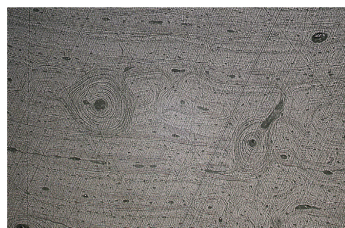


Fig. 1 – Bovine bone microstructure: sections perpendicular to the longitudinal axis.

it is essential to identify the failure mechanism in order to determine which stress triggers the rupture.

1.2. Mechanical tests

During mechanical tests on brittle material, two different sets of parameters can be measured: (i) those describing the elastic behaviour and (ii) those describing the failure thresholds for each loading condition.

In order to identify the orthotropic elastic coefficients of cortical bone, it is first necessary to perform traction or compression tests in the three main directions as presented in Reilly and Burstein (1975) for a bovine femoral cortical bone. Secondly, the shear elastic behaviour may be assessed through Iosipescu or Arcan tests as or by torsion tests like those employed by Reilly and Burstein (1975). Nonetheless, the ultrasonic method presented in Rho et al. (1998) on bovine cortical bone and the nanoindentation used in Hoc et al. (2006) and Vayron et al. (2012) may be very useful for a complete identification of the elastic parameters and for studying the spatial variations of the modulus, respectively. Additionally, resonant ultrasonic spectroscopy techniques (Bernard et al., 2013) have been recently employed for both human and bovine cortical bones and have confirmed the previous results with high accuracy. For bovine cortical bone, the values of Young's moduli along the circumferential and transverse directions are of the order of 12.8 GPa, while Young's modulus along the longitudinal direction is about 20.3 GPa.

Several experimental tests may be used to evaluate the strength for a brittle and anisotropic material like bone. Tensile testing is one of the classical methods to measure bone's mechanical properties. Nevertheless, specimens must have relatively large dimensions (15–20 mm in length, 4–8 mm in width) and they must be specifically designed to obtain the majority of the strain in the central region (Reilly and Burstein, 1974; Ashman et al., 1987). If one assumes that the external force is applied without inducing a bending moment, the tensile test provides a good assessment of bone's strength, but is limited in its ability to evaluate the effects of anisotropy due to the constraints on the dimensions of specimens.

Bending tests are usually employed for testing the bones of small animals for which a tensile test is difficult to set up. In such a test, the entire bone is loaded until failure leading to tensile stresses on one side of the bone and compressive stresses on the other side. Additionally, tensile or compressive stresses increase from the neutral axis to the external boundaries of the specimen. Thus, failure commonly occurs on the tensile side since bone is weaker in tension than in compression (Reilly and Burstein, 1975) and may also be highly sensitive to surface defects due to the machining of the specimens for instance. Bending may be applied to the bone through either a three-point or a four-point loading. The former is very simple to set up, but it may cause high shear stress around the middle section of the bone. The latter induces pure bending and ensures zero transverse shear stress between the two upper loading points. Nevertheless, if the specimen is rather small in length and the bending moment is maximum under the loading point, the stress

state is not easy to determine. Furthermore, in both three-point and four-point bending tests the total length of the specimen should be about 16 times the thickness of the specimen to guarantee that 85–90% of the bone flexion is actually due to bending. Unfortunately, this length–width ratio cannot be acquired in whole bones such as femora or tibias.

For compression testing, relatively small specimens (7–10 mm long) can be used and therefore machined along the three directions, but the measurement tends to be less accurate than those for tensile tests because of edge effects. In those regions in fact, the strain is likely to be higher than in the central region, possibly due to the misalignment of the specimen faces or other problems associated with specimen machining. Then, because of friction between the contact surfaces of the bone specimen and the plates of the testing machine, one may have a unidirectional strain at the boundaries and a stress static state in the central region, such that the specimen acquires a barrel-like shape. Although an extensometer is usually employed during tensile tests to determine the axial strain in the specimen, this is not possible in compression due to the small dimensions of the specimen. In this case image correlation represents an alternative method to evaluate the stress–strain relationship. Despite a lower accuracy of the results compared to tensile tests, compressive testing presents some major advantages. First, specimens do not have to be as large as tensile specimens. Second, machining of compressive specimens is easier than for tensile specimens and may be done in different directions to investigate the anisotropic behaviour of the bone. Nevertheless, compression tests do not initiate the same failure modes as tensile tests (for which failure mode and crack shape show a specific brittle mechanism).

In recent years, shear tests have been developed to determine the shear modulus of elasticity of the bone. Among them we mention the rail shear test, the torsion tube, cross-beam specimens and tension–compression of notched specimens, including the Iosipescu (ASTM D5379) (Iosipescu, 1967; Funk and Litsky, 1998; Sharma et al., 2011) and the Arcan tests (Arcan et al., 1978).

Although the previous resistance tests allow partial assessment of the anisotropic characteristics of cortical bone's behaviour and identification of some fracture modes, they fail in evaluating the anisotropy in traction. For this reason, here we propose the Brazilian test as an alternative experimental approach to characterise the bone failure responses along the longitudinal, circumferential and radial axes. Such a test presents interesting features, which appear to be decidedly appropriate to study bone's mechanical behaviour and to obtain a complete predictive model.

1.3. Brazilian test for brittle materials

The Brazilian test was first introduced by Carneiro (1943) and Akazawa (1943) to determine the tensile strength of brittle materials such as rock, concrete or ceramic, which is difficult to evaluate by performing a direct uniaxial tensile test. It is widely used in the field of civil engineering and has been the object of numerous works for both the calculation of stresses and the identification of material properties (Li et al., 2013). In

the biomechanics field, it has been employed to determine the tensile strength of archeological cortical bone (Turner-Walker and Parry, 1995) and artificially aged bone (Turner-Walker, 2011). Additionally, Huang et al. (2012) proposed a numerical analysis of the Brazilian test of heterogeneous specimens in order to analyse the tensile strength of dental amalgams.

In the Brazilian test, a cylindrical specimen is loaded in compression until failure over a short strip along the specimen length at each end of the vertical diameter. Compression induces tensile stresses normal to the loading direction, which are approximately constant within a region around the centre. Therefore, for a brittle material, a crack appears perpendicular to the maximum traction stress direction, leading to the splitting of the cylinder into two halves.

The Brazilian test has some interesting characteristics. Firstly, it greatly simplifies the traction loading of a brittle material. Secondly, it permits reduction of the size of the specimen down to that limited by testing a representative volume of the material. For the specific case of cortical bone, such a reduction in dimensions (e.g. some millimetres in diameter) leads to three further benefits: (i) it decreases the probability of finding very large defects that may induce macroscopic rupture, (ii) it provides information on the correlation between specimen size and defect distribution and (iii) it enables the analysis of the traction fracture along the three main axes of the bone. Therefore, the Brazilian test may be employed to provide an accurate identification of the anisotropic maximal traction stresses in cortical bone.

2. Materials and methods

2.1. Sample preparation

Specimens were obtained from a bovine tibia sourced from a local butcher and conserved at -18° . Once the tibia was defrosted, the internal marrow and the spongy bone were removed and the bone was cleaned with water. The three main local axes of the bone were chosen as follows (Fig. 2):

- the longitudinal axis x_1 corresponds to the main direction of the tibia;
- the circumferential axis x_2 coincides with the azimuthal direction;
- the radial axis x_3 is aligned with the outward radius of the bone's section.

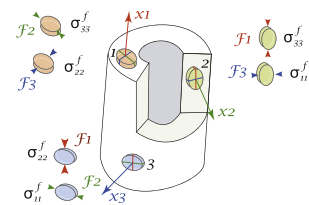


Fig. 2 – Coordinates system, traction stresses (σ_{ij}^f) and loading directions (F_j).

First, 25 bone cylinders were machined using diamond-tipped tubular drills of internal diameters ϕ 10, 8, 6 and 4 mm. For the sake of convenience, the machining was performed along the x_1 and x_3 directions, which maintains the ability to obtain the three fracture stresses σ_{11}^f , σ_{22}^f and σ_{33}^f (Fig. 2, the superscript f indicates failure). Second, the cylinders were sectioned perpendicular to the cylinder axis using a diamond disc saw. Furthermore, for those machined along the x_1 direction, more than one specimen was obtained. Finally, 29 specimens were acquired. The length L of the samples was set to 6.5 mm, 5.2 mm, 3.9 mm and 2.6 mm, respectively, for $\phi=10$ mm, $\phi=8$ mm, $\phi=6$ mm and $\phi=4$ mm (Fig. 3). Such values provide a minimal average ratio ϕ/L equal to 1.54. Before sectioning, the three main axes x_1 , x_2 and x_3 were identified on each specimen which allows us to classify the specimens as follows: x_i-F_j , with x_i and F_j indicating the cutting axis and the loading direction, respectively (Fig. 2). During cutting, water was used in order to reduce both friction and temperature rise.

2.2. Brazilian test for cortical bone

The Brazilian tests were performed at room temperature right after the cutting, using a universal traction-compression machine INSTRON 5500-R equipped with a 5 kN sensor. We have assumed that the room humidity does not influence the specimens behaviour. The machine was controlled by fixing the displacement rate of the upper plate at 0.2 mm/min. The positioning of the specimen between the two plates of the machine as shown in Fig. 4 must be done very carefully since it was necessary (i) to align the cylinder with respect to the mid-planes of the plates, (ii) to orient the cylinder along the main axis of the machine and (iii) to place the cylinder in the central region of the lower plate. Such conditions may not

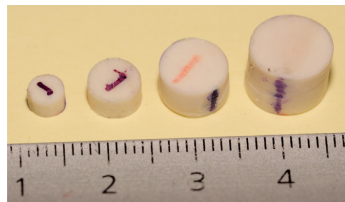


Fig. 3 - Specimens diameters: 4, 6, 8 and 10 mm.

been verified if, for instance, there exists a parallelism or a cylindricity defect of the specimen, which may influence the stress distribution.

During a regular test, the crack was generally initiated at the centre of the cylinder along the vertical axis (Fig. 5). Nevertheless, abnormal splitting might be observed due to (i) shear stress (Fig. 6a), (ii) crushing issues (Fig. 6b) or (iii) a non-centred crack. Defects such as those presented in Fig. 6a were mainly found during a preliminary series of tests with specimens having a ratio $\phi/L < 1.54$. To limit the crushing of the contact surface (Fig. 6b), a cushion can be inserted between the specimen and each load plate as described in the standard for Brazilian tests applied to rocks (ISRM 1978, ASTM 2008). In our case, a 0.52 mm thick square of cardboard was used (Fig. 4). The imprint was measured after each test to estimate the contact area and we found that it can actually be defined independent of the specimen diameter ϕ through the angle α (Fig. 4a) as described in Wang et al. (2004).

2.3. Structural analysis of Brazilian test for anisotropic elastic behaviour

Through a structural analysis, we may be able to evaluate the maximal tensile stress $\sigma_{xx,max}$ along the x direction at the centre of each specimen. For isotropic materials, an analytical solution was proposed by Peltier (1954) giving the tensile



Fig. 5 - Appearance of a vertical crack at the centre of a specimen x_1-F_3 with a 8.12 mm diameter.

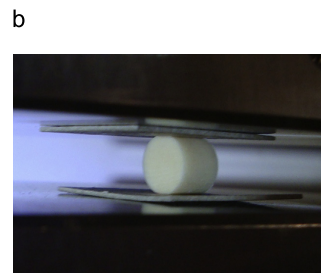
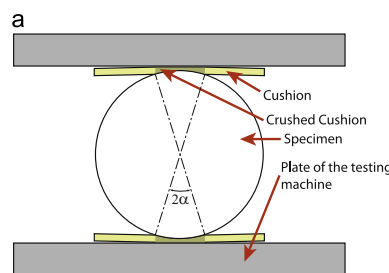


Fig. 4 - Schematic drawing of the Brazilian test (a) and positioning of a 4 mm diameter specimen (b).

stress in the centre of the disc as follows:

$$\sigma_{xx,max} = \frac{2F}{\phi L \pi} \tag{1}$$

where F is the applied load.

To account for the effect of a soft cushion between the specimen and the loading plates, a factor of correction k was introduced by [Hondros \(1959\)](#) and [Wang et al. \(2004\)](#) as a function of the angle α (Fig. 7). Thus, Eq. (1) becomes

$$\sigma_{xx,max} = k(\alpha) \frac{2F}{\phi L \pi} \tag{2}$$

Nonetheless, the previous relation is no longer valid for an anisotropic elastic behaviour as for the cortical bone. In [Exadaktylos and Kaklis \(2001\)](#), the authors propose an analytical approach in the form of a sum of Fourier series, which is validated for the isotropic case by comparing it with the results of [Hondros \(1959\)](#). In the present work, in order to have an extensive overview of anisotropy effects, the definition of the maximum tensile stresses (Fig. 2) is similar to that proposed in Eq. (2), but the coefficient of correction is now expressed as a function of both the direction of the failure stress and that of the loading. Thus, we have

$$\sigma_{ii,max} = \beta_{ii-j} \frac{2F_j}{\phi L \pi} \tag{3}$$

where β_{ii-j} is the correction factor and F_j is the applied vertical load. The subscripts ii and j indicate the principal stresses and the loading direction, respectively. The main objective of the structural analysis is to find the coefficient β_{ii-j} for the different directions independent of the specimen diameter ϕ .

In the present study, the analysis was performed using the finite elements (FE) method, which provides a better validation and simplify the management of various input and output data. The FE software COMSOL 3.5a was used to run two dimensional (2D) simulations and to evaluate the linear elastic stress field within the samples along x_1 , x_2 and x_3 with two loading directions each. The cylindrical specimens were represented as circles with an anisotropic elastic behaviour. The elastic material parameters were deduced from [Bernard et al. \(2013\)](#) (Table 1).

The problem was solved using the plane stress hypothesis. The displacement of the point A was constrained along the x direction while the point B was totally constrained to prevent rigid body motion (Fig. 7). Finally, the vertical load was applied along the upper and lower boundaries l (blue lines in Fig. 7), which, as previously explained (Section 2.2), have been calculated using the angle $\alpha = 14^\circ$. Thus, l is equal to 2.4 mm, 1.9 mm, 1.4 mm and 1 mm for $\phi = 10$ mm, $\phi = 8$ mm, $\phi = 6$ mm, and $\phi = 4$ mm, respectively.

2.4. Sensitivity analysis

The correction factor β_{ii-j} may change with respect to the elasticity coefficients. Therefore, a sensitivity analysis was performed for each specimen by varying Young's moduli and Poisson's ratios by $\pm 10\%$ relative to the 'benchmark' values.

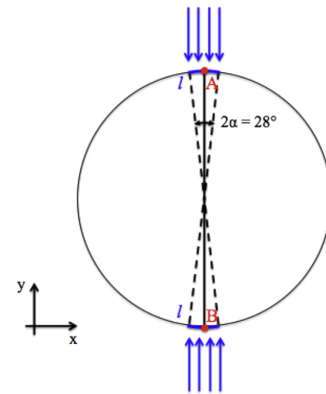


Fig. 7 – Boundary conditions for the simulation of the Brazilian test in COMSOL 3.5a. (For interpretation of the references to colour in this figure caption, the reader is referred to the web version of this paper.)

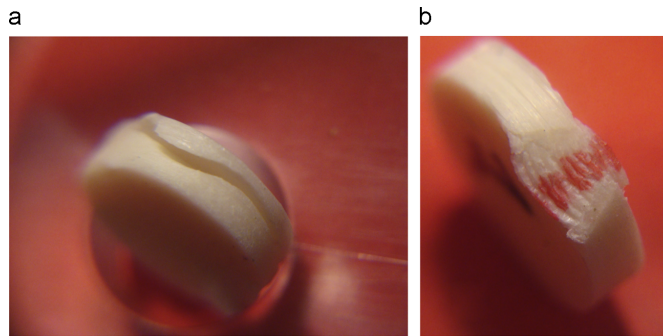


Fig. 6 – Examples of abnormal splitting due to shear stress (a) and matting (b).

Table 1 – Elastic parameters sourced and deduced from Bernard et al. (2013).

Modulus	Value	Reference or formula
E_1 (GPa)	20.3	Bernard et al. (2013)
E_2 (GPa)	12.8	Bernard et al. (2013)
E_3 (GPa)	12.8	Bernard et al. (2013)
G_{12} (GPa)	6.38	Bernard et al. (2013)
G_{13} (GPa)	6.32	Bernard et al. (2013)
G_{23} (GPa)	6.38	Bernard et al. (2013)
ν_{12}	0.421	Bernard et al. (2013)
ν_{13}	0.434	Bernard et al. (2013)
ν_{23}	0.348	Bernard et al. (2013)
ν_{21}	0.265	$\frac{\nu_{12}E_2}{E_1}$
ν_{31}	0.273	$\frac{\nu_{13}E_3}{E_1}$
ν_{32}	0.348	$\frac{\nu_{23}E_3}{E_2}$

3. Results

3.1. Stress state in the loaded specimen

In this section we present the numerical results and in particular we discuss the stress field inside the specimen. As it is possible to observe in Fig. 8a and b, for a load per length unit $F=1400$ N/mm (which is the same for each tested diameter), the compressive (σ_{yy}) and tensile (σ_{xx}) stresses are heterogeneously distributed. Their pattern is very similar to that of the isotropic case as reported in Wang et al. (2004) and specifically σ_{yy} and σ_{xx} are maximal along the loading surfaces and at the centre, respectively.

Actually, there exists a relationship between such stresses and the failure mechanism. In fact, as shown in Fig. 5, the crack is distinctly open at the centre of the disc ($(x,y)=(0,0)$) where the stress state is plane and given by

$$\underline{\underline{\sigma}} = \begin{pmatrix} \sigma_{xx} & 0 & 0 \\ 0 & \sigma_{yy} & 0 \\ 0 & 0 & 0 \end{pmatrix} \quad (4)$$

with $\sigma_{xx} = 55$ MPa and $\sigma_{yy} = -147$ MPa (blue line in Fig. 8d and b, respectively).

Let \underline{n} and \underline{t} be, respectively, the normal and the tangent vectors to the failure plane defined as

$$\underline{n} = \begin{pmatrix} \cos \theta \\ \sin \theta \\ 0 \end{pmatrix} \quad \text{and} \quad \underline{t} = \begin{pmatrix} -\sin \theta \\ \cos \theta \\ 0 \end{pmatrix} \quad (5)$$

where θ is the angle between the \underline{n} - and the \underline{x} -axis. Then, the normal (σ_n) and the shear (τ) stresses read

$$\sigma_n = \underline{n}^T \underline{\underline{\sigma}} \underline{n} \quad (6)$$

$$\tau = \underline{t}^T \underline{\underline{\sigma}} \underline{n} \quad (7)$$

with \underline{n}^T the transposition of \underline{n} .

It is interesting to evaluate the evolution of σ_n and τ for (i) θ varying between 0° and 180° and (ii) the axial coordinate x of the point of interest (x,y) varying between ± 0.73 mm from the centre of the disc (Fig. 9).

For $\theta = 0^\circ$, we find $\sigma_n = 55$ MPa and no shear stress, while τ is maximal (± 100 MPa) for $\theta = 45^\circ$ and 135° . Finally, for $\theta = 90^\circ$, σ_n is equal to -147 MPa showing a compressive stress state (Fig. 9). It can be noticed that for all these stresses, the maximal values are found at the centre of the disc (blue line in Figs. 8b, d, and 9). For a brittle material, the failure plane is a useful parameter to evaluate the cracking mechanism and the corresponding stress. Here, failure is neither activated at $\theta = 90^\circ$ nor at $\theta = 45^\circ$. On the contrary, the traction stress σ_{xx} is assumed to be responsible for the failure each time the crack occurs parallel to the loading axis.

The main objective of the numerical simulations was to evaluate the correction factor β_{ii-j} defined in Eq. (3), which is independent of the diameter ϕ of the disc. For an isotropic material, we found that such a coefficient is equal to 1 in the case of a concentrated load F_j and to 0.912 in the case of a distributed load as described in Section 2.3, which is very close to 0.92, the coefficient analytically calculated from Wang et al. (2004).

In order to use β_{ii-j} as a consistent indicator, the variation of the stress state must be low with respect to the cracking position. In Fig. 8b and d σ_{yy} and σ_{xx} are plotted for a plane placed at $x=0, 0.24, 0.48$ and 0.73 mm for a disc with a diameter of 6 mm. We notice that if the crack occurs between ± 0.4 mm from the vertical axis of the disc, the maximum stress only varies by about $\pm 5.5\%$. To keep such a low variability, the corresponding spatial tolerances for $\phi = 4, 8$ and 10 mm are $\pm 0.27, \pm 0.4$ and ± 0.67 mm, respectively. As an example, in Fig. 5, the diameter ϕ of the specimen is equal to 6 mm and the position of the crack is at 0.16 mm from the centre with an error of -1% for the coefficient β_{ii-j} .

Finally, as mentioned in Section 2.4, a source of uncertainty for the correction factor β_{ii-j} is related to the variations of the elastic coefficients. According to the sensitivity analysis that has been carried out, the results for the four loading cases are reported in Table 2.

3.2. Experimental data

The experimental tests were exploited to assess the failure force as well as the crack direction, which must be vertical, and shape, which must be sharp-cut. Furthermore, by using the correction coefficients β_{ii-j} derived from the numerical analysis (Table 2), the values of the tensile failure stress were determined depending on the specimen diameter ϕ for each direction of failure stress tested $\sigma_{11}^f, \sigma_{22}^f$ and σ_{33}^f (Fig. 10). Among the 29 tests carried out, 4 were stopped due to a crushing problem on the loading area (Section 2.2) and 4 presented a cracking mechanism outside the admissible region (Section 3.1) (hollow arrows in Fig. 10). For these specific cases, stress leading to failure was not usable as a value to rupture, but as an underestimation of the failure stress.

The brittle strength is anisotropic for all the tested diameters and significantly higher along the axial direction. According to Fig. 10, the size of the specimen may influence the failure stress. For instance, for specimens with a diameter of 4 mm we observe an increase of the failure stresses. However, for $\phi = 6, 8$ and 10 mm, failure stresses are in the same order of magnitude along each direction and the

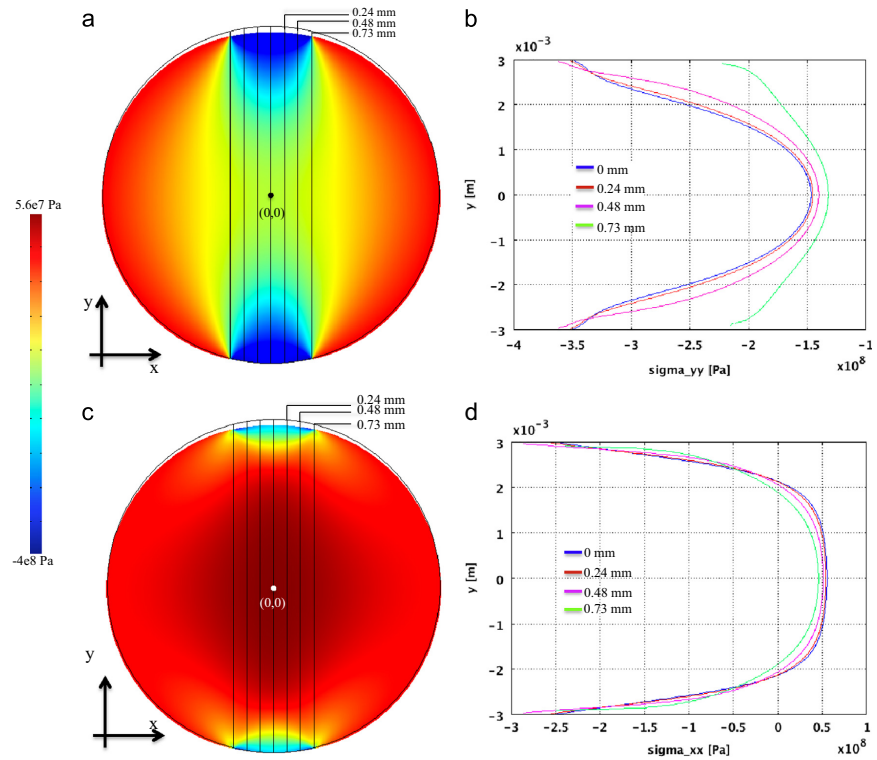


Fig. 8 – (a, c) Plot of σ_{yy} and σ_{xx} for a x_1-F_2 specimen of diameter 6 mm. (b, d) Outline of σ_{yy} and σ_{xx} respectively, along the vertical diameter (blue line, $x=0$) and along the vertical lines placed at $x=0.24$ mm (red line), $x=0.48$ mm (purple line) and $x=0.73$ mm (green line). (For interpretation of the references to colour in this figure caption, the reader is referred to the web version of this paper.)

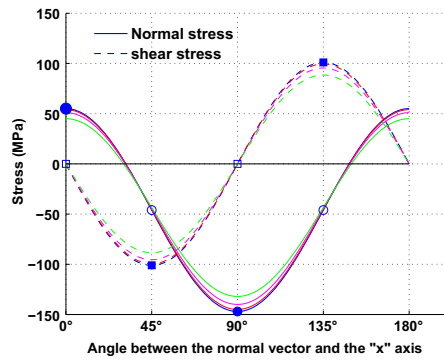


Fig. 9 – Normal and shear stress distributions at the centre and at 0.24 mm (red lines), 0.48 mm (purple lines) and 0.73 mm (green lines) from the centre along the x-axis. (For interpretation of the references to colour in this figure caption, the reader is referred to the web version of this paper.)

average values are equal to $\sigma_{11}^f = 62$ MPa, $\sigma_{22}^f = 41$ MPa and $\sigma_{33}^f = 34$ MPa.

As the traction stress σ_{xx} is not homogeneous within the sample (Fig. 8d), it may be of interest to identify a failure region for each specimen diameter rather than simply determining the relationship between the failure stress and the sample dimensions. Thus, a rectangular area $S_{failure}$ of height $h_{failure}$ and width $e_{failure}$ can be defined for each diameter ϕ such that $0.9\sigma_{xx,max} < \sigma_{xx} < \sigma_{xx,max}$. We notice that the dimensions and consequently the area of the failure region decrease with the specimen diameter (Table 3).

4. Discussion

The Brazilian test is suitable for brittle materials only, but the experimental validation of the failure mechanism is very easy to achieve because the crack must be unique and in a vertical plane as described in Tavallali and Vervoort (2010). Additionally, if the ϕ/L ratio is controlled and optimised, the rare faulty tests may be attributed to machining or

Table 2 – Results of the sensitivity analysis and values of correction factors β_{ii-j} for the four loading cases.

Specimen	σ_{11}^f	σ_{22}^f	σ_{33}^f
$x_1 F_2$	–	–	$\beta_{33-2} = 1.007 \pm 4\%$
$x_1 F_3$	–	$\beta_{22-3} = 1.007 \pm 4\%$	–
$x_2 F_1$	–	–	$\beta_{33-1} = 0.802 \pm 5\%$
$x_2 F_3$	$\beta_{11-3} = 1.044 \pm 3.5\%$	–	–
$x_3 F_1$	–	$\beta_{22-1} = 0.802 \pm 5\%$	–
$x_3 F_2$	$\beta_{11-2} = 1.045 \pm 3.5\%$	–	–

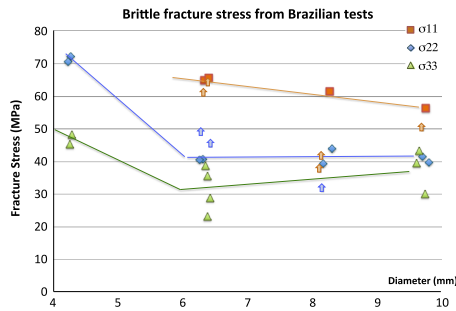


Fig. 10 – Maximum tensile stress versus diameter for three directions of loading.

Table 3 – Values of the failure region area according to the specimen diameter ϕ .

Specimen diameter ϕ (mm)	4	6	8	10
Failure region height $h_{failure}$ (mm)	1.5	2.2	2.9	3.7
Failure region width $e_{failure}$ (mm)	0.8	1.2	1.6	2
Failure region area $S_{failure} = h \cdot e$ (mm ²)	1.2	2.64	4.64	7.4

positioning defects. In the present work, although the bovine cortical bone we tested seemed rather young with a marked microstructure, the experimental dispersion was quite reasonable and the anisotropy of brittle fracture clearly appeared leading to a ratio $\sigma_{i,max}/\sigma_{i,min}$ of the order of 2.

For elastic isotropic materials, the fairly simple geometry of the specimen used for the Brazilian test allows the existence of analytical descriptions of the stress field either for a concentrated or a distributed load. In this case, the analytical solution and our numerical simulation were in very good agreement. Specifically, for a concentrated load, the correction coefficient β_{ii-j} defined in Eq. (3) is exactly equal to 1, while for a distributed load as described in Section 2.3, β_{ii-j} is equal to 0.912.

For an anisotropic material such as cortical bone, the elastic coefficients deduced from Bernard et al. (2013) were used to run the numerical simulations for specimens of different diameters. We were able to determine the correction factors β_{ii-j} associated with each failure stress and we found that all the coefficients are between 0.802 and 1.05 or in a range of $0.92 \pm 14\%$. This results in a variation of the maximum stress of the order of 14%. Furthermore, according to

the sensitivity analysis we performed, the uncertainties on β_{ii-j} due to the variation of the elastic parameters are not higher than 5%, which is quite low. Therefore, the coefficients can be directly used or, for better accuracy, recalculated after verification of the rigidity by, for example, an ultrasonic method.

The Brazilian test also allowed us to assess the scale influence on failure mechanism. The areas of the failure regions for the different specimens reported in Table 3 are very small for a tensile test on a brittle material, which results in failure stresses for specimens with a diameter of 4 mm higher than those for larger samples (Fig. 10). Previous works have focused on this specific aspect and have used either a Weibull distribution of the defect size (Fok et al., 2001) or a cohesive crack model (Guinea et al., 2000) to describe such a behaviour. In both cases, the size effect is attributed to an intrinsic length in correlation with the microstructure of the material below which the failure stress increases. This might also be the case for cortical bone. In fact, we can see that as the specimen diameter ϕ decreases, the dimensions $h_{failure}$ and $e_{failure}$ of the failure region decrease too (Table 3) and approach the dimensions of a portion of the cement line (Section 1.1), which may constitute a weakness for failure behaviour as mentioned in Norman and Wang (1997), O'Brien et al. (2007), and Feerick et al. (2013).

According to the previous remarks, it would be interesting to perform the Brazilian test on a large number of specimens within a range of small dimensions. In fact, this would allow us to consistently investigate the scale influence and the statistical dispersion and to characterise a suitable nonlocal model to be adopted for numerical simulations.

5. Conclusion

In this paper we have proposed the Brazilian test as an alternative technique to investigate both the anisotropic strength and the failure mechanism of cortical bone. In fact, although this test has rarely been employed in the field of bone biomechanics (Turner-Walker and Parry, 1995; Turner-Walker, 2011; Huang et al., 2012), it presents some interesting features. Firstly, it allows testing of brittle materials in traction through the use of a compressive load. Secondly, it allows us to reduce the specimen dimensions down to those of the representative volume of the material. Then, for specific case of cortical bone it has been possible to assess the tensile failure along its three main axes and its anisotropy.

REFERENCES

- Akazawa, T., 1943. A new test method for evaluating internal stress due to compression of concrete: the splitting tension test. *J. Jpn. Soc. Civil Eng.* 19, 777–787.
- Arcan, M., Hashin, Z., Voloshin, A., 1978. A method to produce uniform plane-stress states with applications to fiber-reinforced materials. *Exp. Mech.* 18, 141–146.
- Arramon, Y.P., Mehrabadi, M.M., Martin, D.W., Cowin, S.C., 2000. A multidimensional anisotropic strength criterion based on a multidimensional anisotropic strength criterion based on kelvin modes. *Int. J. Solids Struct.* 37, 2915–2935.
- Ascenzi, M.-G., Kawas, N.P., Lutz, A., Kardas, D., Nackenhorst, U., Keyak, J.H., 2013. Individual-specific multi-scale finite element simulation of cortical bone of human proximal femur. *J. Comput. Phys.* 244, 298–311.
- Ashman, R., Cowin, S., Buskirk, W.V., Rice, J., 1987. Elastic properties of cancellous bone: measurement by an ultrasonic technique. *J. Biomech.* 17, 349–361.
- Bernard, S., Grimal, Q., Laugier, P., 2013. Accurate measurement of cortical bone elasticity tensor with resonant ultrasound spectroscopy. *J. Mech. Behav. Biomed. Mater.* 18, 12–19.
- Carneiro, 1943. A new method to determine the tensile strength of concrete. In: *Proceedings of the Fifth meeting of the Brazilian Association for Technical Rules*, 3d. Section.
- Currey, J.D., 2001. *Bones: Structure and Mechanics*. Princeton University Press, Princeton, New Jersey.
- Doblare, M., Garcia, J., Gomez, M., 2004. Modelling bone tissue fracture and healing: a review. *Eng. Fract. Mech.* 71, 1809–1840.
- Exadaktylos, G., Kaklis, K., 2001. Applications of an explicit solution for the transversely isotropic circular disc compressed diametrically. *Int. J. Rock Mech. Min. Sci.* 38, 227–243.
- Fok, S., Mitchell, B., Smart, J., Marsden, B., 2001. A numerical study on the application of the Weibull theory to brittle materials. *Eng. Fract. Mech.* 68, 1171–1179.
- Funk, M., Litsky, A., 1998. Effect of cement modulus on the shear properties of the bone-cement interface. *Biomaterials* 19, 1561–1567.
- Guinea, G., Elices, M., Planas, J., 2000. Assessment of the tensile strength through size effect curves. *Eng. Fract. Mech.* 65, 189–207.
- Hashin, Z., 1996. Finite thermoelastic fracture criterion with application to laminate racking analysis. *J. Mech. Phys. Solids* 44 (7), 1129–1145.
- Hoc, T., Henry, L., Verdier, M., Aubry, D., Sedel, L., Meunier, A., 2006. Effect of microstructure on the mechanical properties of haversian cortical bone. *Bone* 38, 466–474.
- Hondros, G., 1959. The evaluation of Poisson's ratio and the modulus of materials of a low tensile resistance by the Brazilian (indirect tensile) test with particular reference to concrete. *J. Appl. Sci.* 10 (3), 243–268.
- Huang, S., Lin, L.S., Fok, A.S., Lin, C., 2012. Diametral compression test with composite disk for dentin bond strength measurement—finite element. *Dent. Mater.* 28, 1098–1104.
- Iosipescu, N., 1967. New accurate procedure for single shear testing of metals. *J. Mater.* 2, 537–566.
- Li, S., Demirci, E., Silberschmidt, V.V., 2013. Variability and anisotropy of mechanical behavior of cortical bone in tension and compression. *J. Mech. Behav. Biomed. Mater.* 21, 109–120.
- Feerick, E.M., Liu, X.C., McGarry, P., 2013. Anisotropic mode-dependent damage of cortical bone using the extended finite element method (XFEM). *J. Mech. Behav. Biomed. Mater.* 20, 77–89.
- Norman, T.L., Wang, Z., 1997. Microdamage of human cortical bone: incidence and morphology in long bones. *Bone* 20 (4), 375–379.
- O'Brien, F.J., Taylor, D., Lee, T.C., 2007. Bone as a composite material: the role of osteons as barriers to crack growth in compact bone. *Int. J. Fatigue* 29, 1051–1056.
- Peltier, R., 1954. Theoretical investigation of the Brazilian test. *Rilem Bull.* 19, 26–69.
- Puck, A., Schürmann, H., 1998. Failure analysis of FRP laminates by means of physically based phenomenological models. *Compos. Sci. Technol.* 58, 1045–1067.
- Reilly, D., Burnstein, A., 1974. The elastic modulus for bone. *J. Biomech.* 7, 271–275.
- Reilly, D., Burstein, A., 1975. The elastic and ultimate properties of compact bone tissue. *J. Biomech.* 8, 393–405.
- Rho, J.-Y., Kuhn-Spearing, L., Zioupos, P., 1998. Mechanical properties and the hierarchical structure of bone. *Med. Eng. Phys.* 20, 92–102.
- Sharma, N., Sehgal, D., Pandey, R., 2011. Studies on locational variation of shear properties in cortical bone with Iosipescu shear test. *Appl. Mech. Mater.* 148–149, 276–281.
- Tavallali, A., Vervoort, A., 2010. Behaviour of layered sandstone under Brazilian test conditions: layer orientation and shape effects. *Int. J. Rock Mech. Min. Sci.* 47, 313–322.
- Turner-Walker, G., 2011. The mechanical properties of artificially aged bone: probing the nature of the collagen-mineral bond. *Palaeogeogr. Palaeoclimatol. Palaeoecol.* 310, 17–22.
- Turner-Walker, G., Parry, T., 1995. The tensile strength of archaeological bone. *J. Archaeol. Sci.* 22, 185–191.
- Vashishth, D., 2007. Hierarchy of bone microdamage at multiple length scales. *Int. J. Fatigue* 29 (6), 1024–1033.
- Vayron, R., Barthel, E., Mathieu, V., Soffer, E., Anagnostou, F., Haiat, G., 2012. Nanoindentation measurements of biomechanical properties in mature and newly formed bone tissue surrounding an implant. *J. Biomech. Eng.* 134, 021007.
- Wang, Q., Jia, X., Kou, S., Zhang, Z., Lindqvist, P.-A., 2004. The flattened Brazilian disc specimen used for testing elastic modulus, tensile strength and fracture toughness of brittle rocks: analytical and numerical results. *Int. J. Rock Mech. Min. Sci.* 41, 245–253.

2.6 Conclusions and perspectives

The preliminary 2D finite elements model presented in Sec. 2.4 simulating osteogenesis within a titanium porous scaffold couples both an experimental and a computational approach. This model does not include all the hypotheses listed in Sec. 2.3 and more particularly does not consider the poroelastic behaviour of the bone nor the cyclic boundary conditions and only takes into account the activity of the mesenchymal cells. Despite such limitations, the primary objective has been to validate the numerical results by comparing them to histological observations and the data from mechanical tests on the sacrificed hemi mandibles. Unfortunately, this has been only partially possible. First, although the ovine animal model used compares favourably with human bone behaviour, the cost per animal is rather high, which limits the cohort and therefore the possibility to sacrifice animals at intermediate time steps. Another option would have been an *in vivo* study, but this is even more complicated to set up on such large animals. Second, some of the tests on the hemi mandibles have not worked correctly (i.e. breakage of the implant during the twelve weeks of implantation), which has reduced the number of usable specimens. Although the computational model was not validated since no statistical analysis was possible, a comparison of the numerical results with the empirical data was still feasible. On one side, histological examinations have been used to compare the colonisation pattern and we have found that in both cases (numerical and experimental) the cells migrate from the external boundaries towards the central region of the scaffold, which is never entirely filled with tissue. On the other side, the numerical geometry has been submitted to a quasi-static bending test at the end of the twelve week simulation and the deflection curve has been correlated with the experimental one showing a good agreement and confirming the recovery of the global stiffness of the structure.

To improve these outcomes, a 3D model has been developed which considers the assumptions presented in Sec. 2.3 and more specifically:

- the realistic geometry of the hemimandible which enables to provide consistent information at the macroscale;
- the description of the poroelastic behaviour of the bone;
- the applied cyclic loading, which realistically mimics the ewe's mastication;
- the coupling between the mechanics and the cellular activity;
- the reasonable computing time despite all the previous aspects taken into account.

Even though the numerical approach has been employed here for a specific anatomical site, it can be adapted to study further problems involving cellular colonisation in different contexts such as osteogenesis around prostheses. Actually, a PhD thesis is planned for commencement in September 2015 in collaboration with the Laboratoire de Mécanique et Technologie of the ENS Cachan, the ICube Laboratory at the Université de Strasbourg and NewClip Technics, a french company which designs and manufactures different osteosynthesis implants (www.newcliptechnics.com). The study will focus on analysis of the risk of fracture in the case of a femur equipped with two prostheses at the two extremities (knee and hip), which may affect the global elasticity as well as the stress field. The objective of the work is to decipher the mechanisms leading to failure and to evaluate the potential advantages of a periprosthetic diaphyseal plate to limit the risk of fracture. The thesis will rely on both numerical

modelling and the testing of human femurs. More specifically, the former will be based on simulation of the modelling process through the coupling between mechanics and cellular activity as previously performed ((46), Sec. 2.4), but also on a more accurate description of the morphology and the mechanical behaviour of the cortical bone. First, we will consider both the core of the cortical bone, which will be modelled as a volume, and the peripheral circumferential lamellae, which may play a critical role under specific loading such as torsion and will be described as a shell surface due to the thin thickness. Second, thanks to the results obtained in ((63), Sec. 2.5), we will introduce the anisotropic and damaging properties of both materials in different plans. Given the irregular shape of the femur, the main difficulty will consist in defining the principal axes of anisotropy. To do so, we will use a computational approach that I proposed few years ago in the context of the *Drosophila* morphogenesis (64, 65). Such technique allows to specify a curvilinear system of coordinates and to compute each of them using the relationship between the solution of the Laplace's equation on a given domain with appropriate boundary conditions and the proper geometry of the same domain (66).

To conclude, the works presented in this chapter have provided promising and consistent results at the macro- and mesoscale. Nonetheless, the bone modelling process as well as the hierarchical structure of cortical bone is initiated at the cellular scale. Therefore, my objective is to go down to the microscale to investigate specific mechanisms that may be at the origin of such processes. To do so, I have developed a series of computational models to analyse the behaviour of single cells or of populations of cells during their migration, which appear to be the principal cellular activity during several biological phenomena. In the former case, the goal is to evaluate how the cell senses and responds to its mechanical environment, which may change in terms of mechanical properties and geometry. In the latter case, I aim to understand how the cells communicate, synchronise and transmit the signals necessary to be as efficient as possible collectively. In the next chapters I present the results I have obtained so far and the new and fascinating questions that have consequently arisen.

2.7 Bibliography

1. Rho JY, Kuhn-Spearing L, Zioupos P (1998) Mechanical properties and the hierarchical structure of bone. *Med Eng Phys* 20(2):92–102.
2. Vashishth D (2007) Hierarchy of Bone Microdamage at Multiple Length Scales. *Int J Fatigue* 29(6):1024–1033.
3. Currey JD (2012) The structure and mechanics of bone. *J Mater Sci* 47(1):41–54.
4. Cowin SC, Moss-Salentijn L, Moss ML (1991) Candidates for the mechanosensory system in bone. *J Biomech Eng* 113(2):191–197.
5. Burger EH, Klein-Nulend J, van der Plas A, Nijweide PJ (1995) Function of osteocytes in bone--their role in mechanotransduction. *J Nutr* 125(7 Suppl):2020S–2023S.
6. Weinbaum S, Cowin SC, Zeng Y (1994) A model for the excitation of osteocytes by mechanical loading-induced bone fluid shear stresses. *J Biomech* 27(3):339–360.
7. Nalla RK, et al. (2006) Role of microstructure in the aging-related deterioration of the toughness of human cortical bone. *Mater Sci Eng C* 26(8):1251–1260.
8. Crockett JC, Rogers MJ, Coxon FP, Hocking LJ, Helfrich MH (2011) Bone remodelling at a glance. *J Cell Sci* 124(7):991–998.
9. Bone remodeling dynamics. By H. M. Frost, M.D. Springfield, Illinois, Charles C Thomas Company, 1963. 175 pp., 184 references, 12 appendices, 40 figures. \$8.50 (1964) *Arthritis Rheum* 7(5):545–545.
10. Robling AG, Castillo AB, Turner CH (2006) Biomechanical and Molecular Regulation of Bone Remodeling. *Annu Rev Biomed Eng* 8(1):455–498.
11. Frost HM (1983) The skeletal intermediary organization. *Metab Bone Dis Relat Res* 4(5):281–290.
12. Jee WS, Frost HM (1992) Skeletal adaptations during growth. *Triangle Sandoz J Med Sci* 31(2/3):77–88.
13. Hillam RA, Skerry TM (1995) Inhibition of bone resorption and stimulation of formation by mechanical loading of the modeling rat ulna in vivo. *J Bone Miner Res Off J Am Soc Bone Miner Res* 10(5):683–689.
14. Jacobs CR, Temiyasathit S, Castillo AB (2010) Osteocyte mechanobiology and pericellular mechanics. *Annu Rev Biomed Eng* 12:369–400.
15. Wolff J (1986) *The Law of Bone Remodelling* (Springer Berlin Heidelberg, Berlin, Heidelberg) Available at: <http://www.springer.com/us/book/9783642710339> [Accessed January 19, 2015].
16. Cowin SC, Weinbaum S, Zeng Y (1995) A case for bone canaliculi as the anatomical site of strain generated potentials. *J Biomech* 28(11):1281–1297.
17. Kameo Y, Adachi T, Hojo M (2009) Fluid pressure response in poroelastic materials subjected to cyclic loading. *J Mech Phys Solids* 57(11):1815–1827.
18. Rémond A, Naili S (2005) Transverse isotropic poroelastic osteon model under cyclic loading. *Mech Res Commun* 32(6):645–651.

19. Wang L, Fritton SP, Cowin SC, Weinbaum S (1999) Fluid pressure relaxation depends upon osteonal microstructure: modeling an oscillatory bending experiment. *J Biomech* 32(7):663–672.
20. Zhang D, Cowin SC (1994) Oscillatory bending of a poroelastic beam. *J Mech Phys Solids* 42(10):1575–1599.
21. Zhang D, Weinbaum S, Cowin SC (1998) Estimates of the peak pressures in bone pore water. *J Biomech Eng* 120(6):697–703.
22. Goulet GC, et al. (2008) Influence of vascular porosity on fluid flow and nutrient transport in loaded cortical bone. *J Biomech* 41(10):2169–2175.
23. Manfredini P, Cocchetti G, Maier G, Redaelli A, Montevecchi FM (1999) Poroelastic finite element analysis of a bone specimen under cyclic loading. *J Biomech* 32(2):135–144.
24. Nguyen V-H, Lemaire T, Naili S (2009) Numerical study of deformation-induced fluid flows in periodic osteonal matrix under harmonic axial loading. *Comptes Rendus Mécanique* 337(5):268–276.
25. Rémond A, Naili S, Lemaire T (2008) Interstitial fluid flow in the osteon with spatial gradients of mechanical properties: a finite element study. *Biomech Model Mechanobiol* 7(6):487–495.
26. You L, Cowin SC, Schaffler MB, Weinbaum S (2001) A model for strain amplification in the actin cytoskeleton of osteocytes due to fluid drag on pericellular matrix. *J Biomech* 34(11):1375–1386.
27. Han Y, Cowin SC, Schaffler MB, Weinbaum S (2004) Mechanotransduction and strain amplification in osteocyte cell processes. *Proc Natl Acad Sci U S A* 101(47):16689–16694.
28. Wang Y, McNamara LM, Schaffler MB, Weinbaum S (2007) A model for the role of integrins in flow induced mechanotransduction in osteocytes. *Proc Natl Acad Sci* 104(40):15941–15946.
29. Buechner PM, Lakes RS, Swan C, Brand RA (2001) A broadband viscoelastic spectroscopic study of bovine bone: implications for fluid flow. *Ann Biomed Eng* 29(8):719–728.
30. Fornells P, García-Aznar JM, Doblaré M (2007) A Finite Element Dual Porosity Approach to Model Deformation-Induced Fluid Flow in Cortical Bone. *Ann Biomed Eng* 35(10):1687–1698.
31. Cowin SC, Gailani G, Benalla M (2009) Hierarchical poroelasticity: movement of interstitial fluid between porosity levels in bones. *Philos Transact A Math Phys Eng Sci* 367(1902):3401–3444.
32. Nowinski JL, Davis CF (1972) The flexure and torsion of bones viewed as anisotropic poroelastic bodies. *Int J Eng Sci* 10(12):1063–1079.
33. Taber LA (1992) A Theory for Transverse Deflection of Poroelastic Plates. *J Appl Mech* 59(3):628–634.
34. Pauwels F (1960) Eine neue Theorie über den Einfluß mechanischer Reize auf die Differenzierung der Stützgewebe. *Anat Embryol (Berl)* 121(6):478–515.
35. Carter DR, Blenman PR, Beaupré GS (1988) Correlations between mechanical stress history and tissue differentiation in initial fracture healing. *J Orthop Res Off Publ Orthop Res Soc* 6(5):736–748.
36. Prendergast PJ, Huiskes R, Søballe K (1997) Biophysical stimuli on cells during tissue differentiation at implant interfaces. *J Biomech*

- 30(6):539–548.
37. Checa S, Prendergast PJ (2010) Effect of cell seeding and mechanical loading on vascularization and tissue formation inside a scaffold: A mechano-biological model using a lattice approach to simulate cell activity. *J Biomech* 43(5):961–968.
 38. Byrne DP, Lacroix D, Planell JA, Kelly DJ, Prendergast PJ (2007) Simulation of tissue differentiation in a scaffold as a function of porosity, Young's modulus and dissolution rate: application of mechanobiological models in tissue engineering. *Biomaterials* 28(36):5544–5554.
 39. Andreykiv A, Prendergast PJ, van Keulen F, Swieszkowski W, Rozing PM (2005) Bone ingrowth simulation for a concept glenoid component design. *J Biomech* 38(5):1023–1033.
 40. Andreykiv A, van Keulen F, Prendergast PJ (2008) Computational mechanobiology to study the effect of surface geometry on peri-implant tissue differentiation. *J Biomech Eng* 130(5):051015.
 41. Isaksson H, et al. (2007) Bone regeneration during distraction osteogenesis: mechano-regulation by shear strain and fluid velocity. *J Biomech* 40(9):2002–2011.
 42. Isaksson H, van Donkelaar CC, Huiskes R, Ito K (2008) A mechano-regulatory bone-healing model incorporating cell-phenotype specific activity. *J Theor Biol* 252(2):230–246.
 43. Lacroix D, Prendergast PJ (2002) A mechano-regulation model for tissue differentiation during fracture healing: analysis of gap size and loading. *J Biomech* 35(9):1163–1171.
 44. Liu X, Niebur GL (2008) Bone ingrowth into a porous coated implant predicted by a mechano-regulatory tissue differentiation algorithm. *Biomech Model Mechanobiol* 7(4):335–344.
 45. Huiskes R, Van Driel WD, Prendergast PJ, Søballe K (1997) A biomechanical regulatory model for periprosthetic fibrous-tissue differentiation. *J Mater Sci Mater Med* 8(12):785–788.
 46. Schmitt M, et al. (2015) Diffusion model to describe osteogenesis within a porous titanium scaffold. *Comput Methods Biomech Biomed Engin* 0(0):1–9.
 47. Ambard D, Swider P (2006) A predictive mechano-biological model of the bone-implant healing. *Eur J Mech ASolids* 25(6):927–937.
 48. Guérin G, Ambard D, Swider P (2009) Cells, growth factors and bioactive surface properties in a mechanobiological model of implant healing. *J Biomech* 42(15):2555–2561.
 49. Swider P, Ambard D, Guérin G, Søballe K, Bechtold JE (2011) Sensitivity analysis of periprosthetic healing to cell migration, growth factor and post-operative gap using a mechanobiological model. *Comput Methods Biomech Biomed Engin* 14(9):763–771.
 50. Adachi T, Osako Y, Tanaka M, Hojo M, Hollister SJ (2006) Framework for optimal design of porous scaffold microstructure by computational simulation of bone regeneration. *Biomaterials* 27(21):3964–3972.
 51. Roshan-Ghias A, Vogel A, Rakotomanana L, Pioletti DP (2011) Prediction of spatio-temporal bone formation in scaffold by diffusion equation. *Biomaterials* 32(29):7006–7012.

52. J. A. Sanz-Herrera JMG-A (2008) Micro–macro numerical modelling of bone regeneration in tissue engineering. *Comput Methods Appl Mech Eng* 197(s 33–40):3092–3107.
53. Sanz-Herrera JA, García-Aznar JM, Doblaré M (2009) On scaffold designing for bone regeneration: A computational multiscale approach. *Acta Biomater* 5(1):219–229.
54. Biot MA (1955) Theory of Elasticity and Consolidation for a Porous Anisotropic Solid. *J Appl Phys* 26(2):182–185.
55. Karageorgiou V, Kaplan D (2005) Porosity of 3D biomaterial scaffolds and osteogenesis. *Biomaterials* 26(27):5474–5491.
56. Lopez-Heredia MA, et al. (2008) Rapid prototyped porous titanium coated with calcium phosphate as a scaffold for bone tissue engineering. *Biomaterials* 29(17):2608–2615.
57. St-Pierre J-P, Gauthier M, Lefebvre L-P, Tabrizian M (2005) Three-dimensional growth of differentiating MC3T3-E1 pre-osteoblasts on porous titanium scaffolds. *Biomaterials* 26(35):7319–7328.
58. Xue W, Krishna BV, Bandyopadhyay A, Bose S (2007) Processing and biocompatibility evaluation of laser processed porous titanium. *Acta Biomater* 3(6):1007–1018.
59. Otsuki B, et al. (2006) Pore throat size and connectivity determine bone and tissue ingrowth into porous implants: three-dimensional micro-CT based structural analyses of porous bioactive titanium implants. *Biomaterials* 27(35):5892–5900.
60. Cachinho SCP, Correia RN (2008) Titanium scaffolds for osteointegration: mechanical, in vitro and corrosion behaviour. *J Mater Sci Mater Med* 19(1):451–457.
61. Weinans H, Prendergast PJ (1996) Tissue adaptation as a dynamical process far from equilibrium. *Bone* 19(2):143–149.
62. Biot MA (1941) General Theory of Three-Dimensional Consolidation. *J Appl Phys* 12(2):155.
63. Allena R, Cluzel C (2014) Identification of anisotropic tensile strength of cortical bone using Brazilian test. *J Mech Behav Biomed Mater* 38:134–142.
64. Allena R, Aubry D (2011) A novel technique to parametrize shell-like deformations inside biological membranes. *Comput Mech* 47(4):409–423.
65. Allena R, Aubry D (2012) An extensive numerical simulation of the cephalic furrow formation in *Drosophila* embryo. *Comput Methods Biomech Biomed Engin* 15(5):445–455.
66. Dimon KO (1929) *Foundations Of Potential Theory* (Berlin Verlag Von Julius Springer.) Available at: <http://archive.org/details/foundationsofpot033485mbp> [Accessed March 2, 2015].

Chapter 3

Single cell migration

Cell migration is a broad term used to refer to those processes involving the movement of cells from one location to another. This may occur in non-living environments, such as soil (e.g. the amoeba *Dictyostelium discoideum*) or on glass/plastic (common in vitro setups), or within complex, multicellular organisms. Cells migrate in response to multiple situations they encounter during their existence such as i) the need to feed (*Dictyostelium* again), ii) morphogenetic events that require the mobilisation of precursors to generate new structures/layers/organs, sometimes at distant locations (during embryogenesis, organogenesis and regeneration), or iii) the presence of environmental cues that inform the cells of the need for their movement to accomplish a larger goal (e.g. wound healing, the immune response or the bone remodelling). In pathology, production of abnormal migratory signals may induce the migration of the wrong cell type to the wrong place, which may have catastrophic effects on tissue homeostasis and overall health. Some examples include autoimmune syndromes in which immune cells travel to certain locations and destroy the supporting tissue, causing severe damage; or the process of metastasis, in which tumour cells abandon the primary tumour and migrate to distant tissues where they generate secondary tumours.

Cells differ in various ways (e.g. size, compactness or habitat), but during locomotion they all constantly change shape by rapidly protruding and retracting extensions that have been originally described as pseudopods or 'false feet'. The migration of a cell over a 2D surface is triggered by the forces of a polarized actomyosin cytoskeleton, while other cytoskeletal components have solely a regulatory or supportive function (1, 2). Network polymerisation (expansion) and network depolymerisation (contraction) are then the main forces that generate cell motion. Cells crawl in a cyclic manner like a worm, in a process that involves three main steps (3). Firstly, they extend their front end, the pseudopod. This term has been historically used to describe all cellular protrusions, but today it mostly indicates finger-like protrusions. Secondly, they grip the substrate. Actually, at the cell scale, the weight of the cell is not sufficient to maintain surface contact. Thus, adhesion receptors are necessary to anchor to the 2D surface. Surface anchoring is a prerequisite for migration in 2D, but it immobilizes the cell (4). However, membrane-parallel traction forces against the direction of movement are the ones that finally determine the locomotion by allowing the pulling forward of the rear end of the cell. Some authors suggest the presence of further steps such as release from contact sites and recycling of membrane receptors from the rear to the front of

the cell (5) as well as a relaxation phase (6).

3.1 General overview on numerical modelling of single cell migration

Abercrombie (7) was the first to propose a model of cell migration based on a series of isolated experimental observations. Although the model was not sustained by a mathematical approach, it has provided the necessary framework for almost all the quantitative and qualitative models of single cell migration to date. According to his approach, migration occurs in a cycle of four interconnected but separated steps and prerequisite to the cycle is cell polarization (8).

Since then, numerous mathematical and computational models have been developed. Among the first fairly complete models is a description of a cell as a chain of discrete viscoelastic and contractile elements connecting an adhesive pseudopod at the front to an adhesive uropod at the rear (9). The model postulated that there exists a dependency of migration efficiency on adhesiveness (i.e. too insufficient adhesion causes both the front and rear to slip, whereas too-strong adhesion stalls both the front and rear) and that, for optimal migration, a cell must sense the strength of its adhesion and adjust the level of acto-myosin activity accordingly. Concurrently to DiMilla (9), Dembo et al. (10, 11) developed a one-dimensional (1D) computational continuum model of the viscoelastic cytoplasm with moving boundaries including the dynamics of polymerisation and depolymerisation processes (12) whereas a series of models (13–19) proposed that growing of the actin filaments is translated by a ratchet mechanism into mechanical work pushing the leading edge of the cell membrane. In contrast to ratchet models that consider individual filaments and are therefore microscopic, elastic models (20, 21) are effectively macroscopic since they represent the actin network as a continuum gel, while mesoscopic models take into account forces from both the individual ratcheting filaments and viscoelastic deformations and the stresses of effective gel at the surface of which these filaments grow (22–24).

There are at least four main hypotheses that have been largely explored in recent decades: i) calcium concentration regulates expansion and contraction of the actin network through a sol/gel transition (25), ii) actin polymerisation triggered by random thermal fluctuations in the cell membrane or in the actin filaments is the main promoter of protrusion (26–28), iii) extension of the cellular membrane is regulated by specific mechanisms at the molecular scale (29–34) and iv) hydrostatic pressure generated by cytoplasmic flows inside the cell induces the protrusion of the membrane (29, 35–39). Finally, there are also models with a significant mechanical component (see review in (3, 40), even though most of these are one dimensional (1D) or 2D and only a few use a 3D finite element formulation (37, 41–43).

Most models are limited to migration in 2D, justified by the flatness of the cell-motile appendages, or even 1D. Some very challenging 3D models of cells moving on flat surfaces have begun to emerge (44–50). Nevertheless, it is still unclear how a 3D motile cell crawls through the extracellular matrix (ECM) and challenges include i) the additional modes of migration in 3D, ii) the fact that most of these modes are sensitive to ECM stiffness as well as its rheology and geometry and iii) the fact that the classic 2D polarisation process is not sufficient to describe efficient 3D migration.

3.2 Development of a finite element approach to single cell migration

Recently, I have developed a finite element model of single cell migration, which aims to depict the essential mechanical principles of the biological phenomenon. The core of the model rests on three main assumptions.

First, the cell is composed of many elements with specific mechanical properties and behaviours, which remain very difficult to quantify experimentally. Nevertheless, it is evident that the actin network and cytoplasm must be considered as the main actors during the migration process. In fact, the former is responsible for the protrusion-contraction movement of the cell whereas the latter holds together all the more or less deformable sub-structures of the cell. Therefore, the cell is essentially made of a biphasic material with a solid-like phase (the actin network) where the active strains take place and a fluid-like phase (the cytoplasm) which is itself comprised of two sub-phases - a suspension with solid particles (the organelles) embedded in a fluid (the cytosol). Such a configuration leads to a standard Maxwell model with elastic (including active strains) and viscoelastic components (Fig. 3.1). Since the cell may undergo large rotations and deformations, a fully non-linear approach to solution is required.

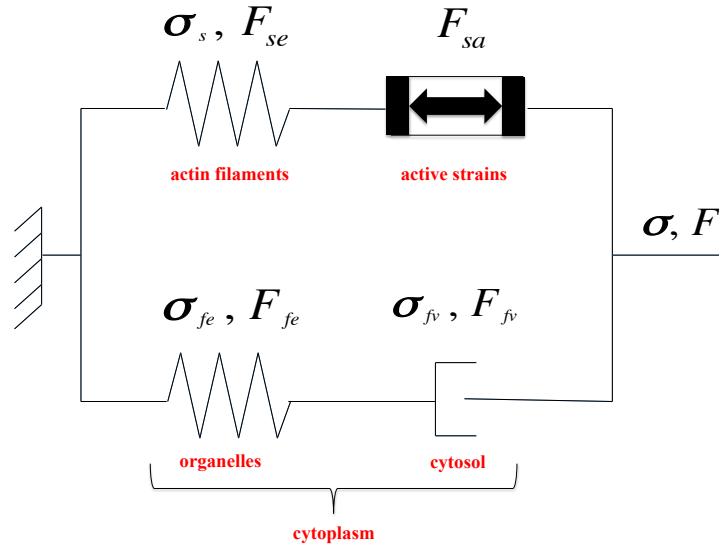


Fig. 3.1 The standard Maxwell model employed to describe the viscoelastic behaviour of the cell. F_{ij} and σ_{ij} indicate the deformation gradient and the Cauchy stress, respectively ($s = \text{solid}$, $e = \text{elastic}$, $f = \text{fluid}$, $v = \text{viscous}$, $a = \text{active}$).

Second, as previously mentioned, the migration process takes place in successive phases, which include protrusion at the front and contraction at the back of the cell. Such pulsatile movement is regulated by the alternating polymerisation and depolymerisation of the actin filaments embedded in the cytosol, respectively, which are in turn triggered by specific molecular processes intrinsic to the cell and not taken into account here. In the present work, both protrusion and contraction are considered as cyclic active strains and are treated analogously to thermal expansion in a material, such that stress-free dilations are generated when the cell is unconstrained. Thus, elastic deformations are generated when the cell is hindered

by boundary conditions provided by its environment. As has been proposed for other mechanobiological processes (51–53), active and elastic strains are computed through the decomposition of the deformation gradient (54) in order to solve for the global deformation of the cell which, according to the rheological model in Fig. 3.1, reads

$$\mathbf{F} = \mathbf{F}_f = \mathbf{F}_s = \mathbf{F}_{se} \mathbf{F}_{sa} \quad (3.1)$$

with \mathbf{F} , \mathbf{F}_f , \mathbf{F}_s , \mathbf{F}_{se} and \mathbf{F}_{sa} being the global, the fluid, the solid, the solid elastic and the solid active deformation tensors, respectively.

Third, cell migration occurs in four successive steps, which are not fully independent. For instance, during both protrusion and contraction some minimal amount of adhesion is necessary for the cell to migrate efficiently. Therefore, the four phases have been here reduced to two, namely i) protrusion at the front and adhesion at the back of the cell and ii) contraction at the back and adhesion at the front of the cell (Fig. 3.2). This schema is ensured by a tight synchronisation between the active strains and adhesive forces developed between the cell and the substrate and results in what I have termed the intra-synchronisation of the cell.

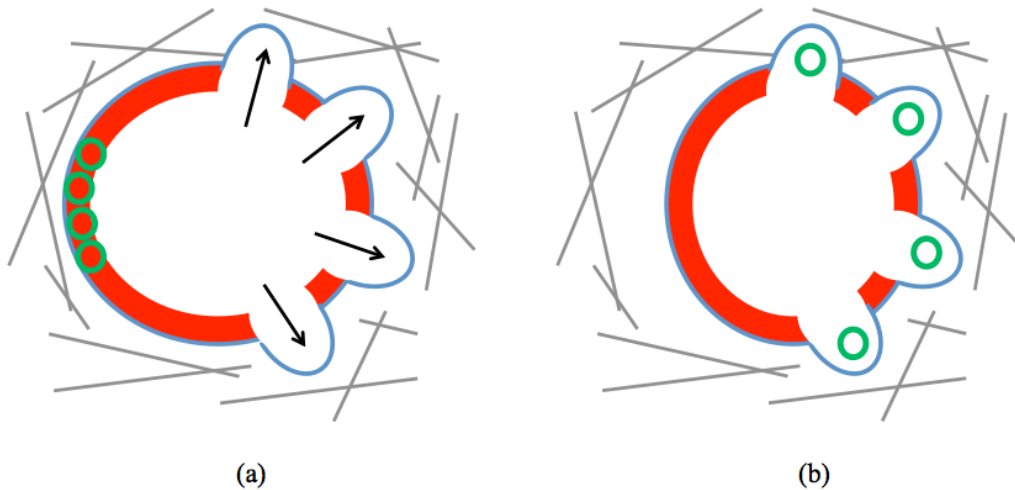


Fig. 3.2 The two main phases of the cell migration: (a) protrusion at the leading edge and adhesion at the back and (b) contraction at the rear edge and adhesion at the front.

Although the role of chemical and molecular mechanisms during single cell migration is clearly acknowledged, the model focuses on the mechanical aspects of the locomotion process. In fact, despite the complexity of the biological framework, the cell is still governed by the Newton's classical law of motion and must develop specific forces in order to move on or within its environment (55).

Additionally, the previous hypotheses make the model highly adaptable and powerful so that it has been possible to simulate single cell migration in different configurations of interest as described below.

3.3 Single cell migration over 2D flat substrates

As a first approach, the model has been used to simulate the migration of a 3D amoeboid cell over 2D homogeneous or heterogeneous flat substrates. This study naturally arose after my PhD thesis at the Laboratoire Mécanique des Sols, Structures et Matériaux at the Ecole Centrale Paris thanks to a profitable collaboration with my supervisor Denis Aubry. The objective has been to propose a finite element model able to realistically reproduce the migration process and to provide consistent quantitative results compared to the experimental data such as distance covered, migration velocity and forces exerted on the substrate.

Included Paper:

Allena R, Aubry D (2012) “Run-and-tumble” or “look-and-run”? A mechanical model to explore the behavior of a migrating amoeboid cell. *J Theor Biol* 306:15–31.



Contents lists available at SciVerse ScienceDirect

Journal of Theoretical Biology

journal homepage: www.elsevier.com/locate/jtbi

'Run-and-tumble' or 'look-and-run'? A mechanical model to explore the behavior of a migrating amoeboid cell

Rachele Allena*, Denis Aubry

Ecole Centrale Paris, Grande Voie des Vignes, 92295 Châtenay-Malabry, France

ARTICLE INFO

Article history:
Received 28 November 2011
Received in revised form
21 February 2012
Accepted 23 March 2012
Available online 17 April 2012

Keywords:
Single cell migration
Deformation gradient decomposition
Active strains
Adhesion forces
Viscoelastic model

ABSTRACT

Single cell migration constitutes a fundamental phenomenon involved in many biological events. Amoeboid cells are single cell organisms that migrate in a cyclic manner like worms. In this paper, we propose a 3D finite element model of an amoeboid cell migrating over a 2D surface. In particular, we focus on the mechanical aspect of the problem. The cell is able to generate cyclic active deformations, such as protrusion and contraction, in any direction. The progression of the cell is governed by a tight synchronization between the adhesion forces, which are alternatively applied at the front and at the rear edges of the cell, and the protrusion–contraction phases of the cell body. Finally, two important aspects have been taken into account: (1) the external stimuli in response to which the cell migrates (e.g. need to feed, morphogenetic events, normal or abnormal environment cues), (2) the heterogeneity of the 2D substrate (e.g. obstacles, rugosity, slippery regions) for which two distinct approaches have been evaluated: the 'run-and-tumble' strategy and the 'look-and-run' strategy. Overall, the results show a good agreement with respect to the experimental observations and the data from the literature (e.g. velocity and strains). Therefore, the present model helps, on one hand, to better understand the intimate relationship between the deformation modes of a cell and the adhesion strength that is required by the cell to crawl over a substrate, and, on the other hand, to put in evidence the crucial role played by mechanics during the migration process.

© 2012 Elsevier Ltd. All rights reserved.

1. Introduction

Cell migration is a broad term that we use to refer to those processes that involve the translation movements of cells from one location to another. This may occur in non-live environments, such as soil (e.g. the amoeba *Dictyostelium discoideum*) or on glass/plastic (common in vitro setups), or within complex, multicellular organisms. Cells migrate in response to multiple situations they encounter during their existence. Some examples include: the need to feed (*Dictyostelium* again); morphogenetic events that require the mobilization of precursors to generate new structures/layers/organs, sometimes at distant locations (during embryogenesis, organogenesis and regeneration); or the presence of environmental cues that inform the cells of the need for their movement to accomplish a larger goal (e.g. wound healing, the immune response or the bone remodeling). In pathology, production of abnormal migratory signals may induce the migration of the wrong cell type to the wrong place, which may have catastrophic effects on tissue homeostasis and overall

health. Some examples include autoimmune syndromes in which immune cells home to certain locations and destroy the supporting tissue, causing severe damage; or the process of metastasis, in which tumor cells abandon the primary tumor and migrate to distant tissues where they generate secondary tumors.

1.1. Amoeboid migration process

Amoeboid migrating cells are single cell organisms that rapidly crawl over surfaces or through spatial environments. These cells may be different in several ways (e.g. size, compactness or habitat), but during locomotion they all constantly change shape by rapidly protruding and retracting extensions that have been originally described as pseudopods or 'false feet'. Nevertheless, alternative strategies can be adopted by amoeboid cells during locomotion like contraction-based blebbing or entirely polymerization driven gliding (Lämmermann and Sixt, 2009).

The migration of an amoeboid cell over a 2D surface is triggered by the forces of a polarized actomyosin cytoskeleton, while other cytoskeletal components have just a regulatory or supportive function (Charest and Firtel, 2007; Krummel and Macara, 2006). Network polymerization (expansion) and network shrinkage (contraction) are then the main forces that allow the cell motion. Amoeboid cells crawl in a cyclic manner like a worm.

* Corresponding author. Tel.: +33 1 41 13 13 21; fax: +33 1 41 13 14 42.
E-mail addresses: racheleallena@gmail.com (R. Allena),
denis.aubry@ecp.fr (D. Aubry).

in a process that involves three main steps (Flaherty et al., 2007). Firstly, they extend their front end, the pseudopod. This term has been historically used to describe all cellular protrusions, but today it mostly indicates finger-like protrusions. Secondly, they grab the substrate. Actually, at the cell scale, the weight of the cell is not sufficient to maintain surface contact. Thus, adhesion receptors are necessary to anchor to the 2D surface. Although the adhesive forces generated by amoeboid cells are considered to be low compared to epithelial or mesenchymal cells, they allow for instance intravascularly crawling leukocytes to resist the shear forces of the blood stream (Auffray et al., 2007; Phillipson et al., 2006; Shulman et al., 2009). Surface anchoring is a prerequisite for migration in 2D, but it exclusively immobilizes the cell (Smith et al., 2005). However, membrane-parallel traction forces against the direction of movement are the ones that finally determine the locomotion by allowing the pulling of the rear end of the cell forward. Some authors suggest the presence of further steps such as release from contact sites and recycle of membrane receptors from the rear to the front of the cell (Sheetz et al., 1999) as well as relaxation phase (Meili et al., 2010).

The main objective of the present work is to show, as previously pointed out in (Gupton and Waterman-Storer, 2006), that the interplay between expansion and contraction of the actin network and the adhesive forces results in a perfect and essential synchronization.

In the next section, we review some of those models that have been developed to capture some of the features described above.

1.2. Previous models

During the last decades several mathematical and computational models have been proposed in literature in order to better understand and quantify the cell motility process. There exist essentially two types of models, one based on a micro/nano-structural approach, the other on a continuum approach (Lim et al., 2006). The former describes the cytoskeleton as the principal structural unit and it is developed to investigate cytoskeletal mechanics in adherent cells. The latter considers instead the cell as a continuum structure with specific mechanical properties identified from experimental observations. Although they provide less detail on the molecular events, the continuum models are easier and simpler to use in computing the large deformations of the cell. Moreover, such models may help understand how stresses and strains are distributed (Bottino et al., 2002; Mogilner and Verzi 2003; Rubinstein et al., 2005), which can be in turn very useful in investigating how these forces are then transmitted to the cytoskeleton components (Lim et al., 2006).

While earlier works have taken into account molecular motors and molecules (Alt and Tranquillo, 1995; Mogilner and Rubinstein, 2005; Stéphanou and Tracqui, 2002; Veksler and Gov, 2007) or diffusion–reaction equations to describe the kinetics and the reactions involved during migration, our model includes a significant mechanical component. On this topic, several 1D or 2D models have been presented in the literature (see reviews from (Carlsson and Sept, 2008; Flaherty et al., 2007)). Some of them consider the cytoskeleton as a viscoelastic material with contractile components that provide the necessary forces for locomotion (DiMilla et al., 1991; Larripa and Mogilner, 2006; Mogilner, 2009). Others describe the cytoplasm as a biphasic fluid material (Alt and Dembo, 1999; Kruse et al., 2006; Kuusela and Alt, 2009; Rubinstein et al., 2009): one phase contains the actin filaments, the other the actin monomers. The protrusion–contraction driving forces in this case are obtained through positive and negative pressures. Some models have been previously proposed that consider the hydrostatic pressure to be the principal driving force for extension of the pseudopods and contraction of the cell body

(Oster and Perelson, 1987; Young and Mitran, 2010). In other works instead (Taber et al., 2011; Zhu and Skalak, 1988), the hydrostatic pressure only regulates the rate of the actin polymerization that actually pushes the cell forwards and triggers fluid and actin monomers towards the back of the cell. Finally, we mention two 3D finite element models. The one of Stolarska et al. (2009) where an eukaryotic cell crawling on a surface is described as a viscoelastic solid and the focal adhesions are located at the boundary with the underneath substrate. The work of Sakamoto et al. (2011) where a viscoelastic gel-strip model of a single cell is proposed to investigate the migration in native-like environments.

Most of the previous works restrict their approach to analytical calculations, even if the equations are complex and strongly nonlinear. In engineering modeling, it is well known that numerical simulations allow overcoming the complexity of the equations.

However, to this date, only a few papers have been published on cellular motility using finite elements simulations, and even fewer have dealt with cellular crawling (Rubinstein et al., 2005; Sakamoto et al., 2011; Stolarska et al., 2009; Taber et al., 2011).

1.3. Objectives

In this paper, we propose a 3D viscoelastic continuum model of an amoeboid cell crawling on a 2D substrate. We have focused on the mechanical aspects of the locomotion process without considering the biochemistry and the molecular mechanisms although their important role during single cell migration is obviously acknowledged (Boulbitch et al., 2001; DiMilla et al., 1991; Schaub et al., 2007; Vicente-Manzanares et al., 2009; Yam et al., 2007). We believe in fact that despite the complex chemical reactions and the genetic functions that may rule its behavior, the cell is still governed by the classical Newton's law of mechanics with specific forces and deformations. Nevertheless, the chemical–mechanical coupling will be considered in the future following the diffusion–reaction model proposed in (Allena et al., 2011) for the *Drosophila* embryo.

Here, we show that

- the perfect synchronization between adhesion forces and cell shape changes is necessary for the cell to move forward. Errors in describing the cycling migration process or in choosing fundamental parameters provide inconsistent results;
- the heterogeneity of the 2D substrate (e.g. obstacles, rugosity, slippery regions) is to be considered and modeled in order to obtain a realistic simulation of the single cell migration;
- the external stimuli in response to which the cell migrates (e.g. need to feed, morphogenetic events, normal or abnormal environment cues) are essential to determine the direction of migration.

In the next sections, we focus on the main features of the work. The geometry and the dynamics of the model are presented together with the constitutive model implemented to describe the different cell actors during migration. As in our previous works (Allena et al., 2010; Allena et al., 2011), the decomposition of the deformation gradient is used to define the cyclic active cell deformations, which are strongly coupled with the adhesion forces. Finally, two essential features of cell locomotion are considered: an attracting source, that defines the direction of migration, and the presence of heterogeneities over the 2D underneath substrate.

2. The model

As mentioned above, our 3D numerical model of a crawling cell is based on pure mechanical considerations. By a top–down analysis it has been possible to investigate which sequence of microscale events regulate the cell locomotion over a 2D substrate.

Accordingly, the model relies on the following assumptions:

- the cell is able to generate cyclic internal deformations (protrusion and contraction) in any direction;
- the progression of the cell is governed by a tight synchronization between the adhesion forces, which are alternatively applied at the front and at the rear edge of the cell, and the protrusion–contraction phases of the cell body.

2.1. Geometry and dynamics

The migration of amoeboid cells is characterized by irregular deformations and the formation of pseudopods, which are actually bulges of the cytoplasm. Our objective has been here to simplify as much as possible the structure of the cell without loss of generality: the cell is thus described as the union of a cylinder and a spherical cap, as shown in Fig. 1a and b, and only one pseudopod, located along the frontal edge of the cell, is involved in the crawling process. Several false feet will be considered in the near future in order to achieve a more realistic representation of the biological system.

Let ρ be the cell density, \mathbf{a} the acceleration, $\boldsymbol{\sigma}$ the Cauchy stress, \mathbf{F} the deformation gradient and J its determinant, then conservation of momentum with respect to the initial configuration in the coordinates system \mathbf{X} is given by

$$\rho \mathbf{a} = \text{Div}_{\mathbf{X}}(J \boldsymbol{\sigma} \mathbf{F}^{-T}) \quad (1)$$

with $\text{Div}_{\mathbf{X}}$ the divergence with respect to the initial position and \mathbf{A}^{-T} the inverse transpose of the matrix \mathbf{A} (Holzapfel, 2000; Taber, 2004). Although we neglect all other body forces such as those due to gravity, we consider here the inertial effects that may play a major role especially during the protrusion phase where accelerations are significant (Gracheva and Othmer, 2004).

2.2. Constitutive model

We try here to build a simple macroscopic model based on typical materials inside the cell. Amoeboid cells are powered by flexible microfilaments (actin filaments) near the membrane. Their polymerization, which occurs mostly at the front of the cell (Schaub et al., 2007), generates the protrusive force at the leading edge and

their contraction due to binding of myosin generates the contractile stress at the rear of the cell (Mogilner, 2009). The actin network has to be considered then as the main actor during the migration process. Nevertheless, from a physical stand point, the cytoplasm, a thick liquid residing inside the cell membrane and holding all the more or less deformable cellular internal sub-structures (such as the organelles) plays also an important role (Fig. 1a). Therefore, the cell is essentially made of a biphasic material (see Fig. 1c) with a solid-like phase (actin network) where the active strain takes place and a fluid-like phase, which is made itself of two sub-phases like a suspension with solid particles (organelles) embedded into a fluid (cytoplasm). From a rheological point of view, this leads to a generalized viscoelastic Maxwell model with an elastic spring in parallel with a Maxwell viscoelastic fluid (Fig. 1c). Since the cell may undergo large rotations and deformations during its locomotion, a full nonlinear tensorial approach is required.

Consequently, the total Cauchy's stress $\boldsymbol{\sigma}$ is assumed to be the sum of the two contributions from the solid and the fluid phases

$$\boldsymbol{\sigma} = \boldsymbol{\sigma}_s + \boldsymbol{\sigma}_f \quad (2)$$

while the deformation gradients of each phase coincide so that $\mathbf{F}_s = \mathbf{F}_f = \mathbf{F}$. The equality between the deformation gradients results from the generalized Maxwell model. Then, the deformation gradient \mathbf{F}_s in the solid phase is the multiplicative decomposition (Allena et al., 2010; Lubarda, 2004; Muñoz et al., 2007; Rodriguez et al., 1994; Taber, 1995) of the active strain tensor \mathbf{F}_{sa} , responsible of the pulsating movement of the cell, and the elastic strain tensor \mathbf{F}_{se} , responsible of the stress generation

$$\mathbf{F}_s = \mathbf{F}_{sa} \mathbf{F}_{se} \quad (3)$$

The solid stress $\boldsymbol{\sigma}_s$ is computed as an isotropic hyperelastic Saint–Venant material as

$$\boldsymbol{\sigma}_s = \bar{\boldsymbol{\sigma}}_s(\mathbf{e}_{se}) \quad (4)$$

where \mathbf{e}_{se} is the Euler–Almansi strain tensor for the solid-elastic phase which is given by

$$\mathbf{e}_{se} = \frac{1}{2}(\mathbf{I} - \mathbf{F}_{se}^{-T} \mathbf{F}_{se}^{-1}) \quad (5)$$

where \mathbf{I} is the identity matrix.

By a classical tensors computation, it can be easily shown that the following decomposition generalizes the one defined for the

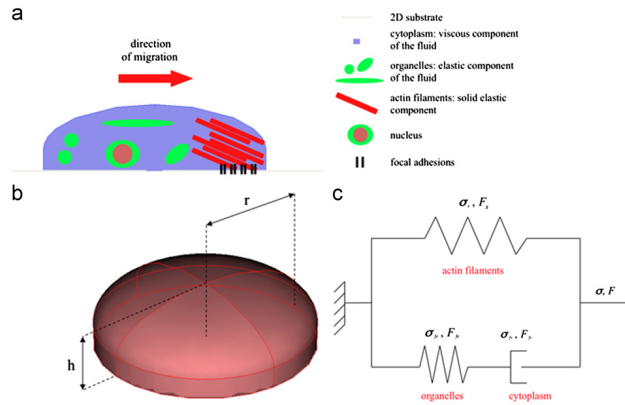


Fig. 1. (a) Sketch of an amoeboid cell and its components, (b) geometry of the cell for the numerical model and (c) representation of the biphasic material describing the cell.

small strains case

$$\mathbf{e}_{se} = \mathbf{F}_{sa}^T(\mathbf{e}_s - \mathbf{e}_{sa})\mathbf{F}_{sa} \quad (6)$$

with \mathbf{e}_s and \mathbf{e}_{sa} the Euler–Almansi strain tensors for the solid and the solid-active phases, respectively.

In the fluid phase, the Cauchy's stresses are assumed to be equal so that $\sigma_f = \sigma_{fe} = \sigma_{fv}$, but the deformation gradient \mathbf{F}_f is multiplicatively decomposed as follows:

$$\mathbf{F}_f = \mathbf{F}_{fv}\mathbf{F}_{fe} \quad (7)$$

where fe and fv stand for *fluid-elastic* and *fluid-viscoelastic*, respectively.

The Euler–Almansi strain tensor \mathbf{e}_{fe} can be computed as

$$\mathbf{e}_{fe} = \mathbf{F}_{fv}^T(\mathbf{e}_f - \mathbf{e}_{fv})\mathbf{F}_{fv} \quad (8)$$

where \mathbf{e}_f and \mathbf{e}_{fv} are the Euler–Almansi strain tensors for the fluid and the fluid-elastic parts, respectively. The fluid-elastic Cauchy's stress σ_{fe} is given by an isotropic hyperelastic model $\bar{\sigma}_{fe}(\mathbf{e}_{fe})$, similarly to the small-strain case. Nevertheless, given the multiplicative decomposition described above, σ_{fe} has to be expressed in the actual configuration as

$$\sigma_{fe} = \frac{1}{J_{fe}}\mathbf{F}_{fv}\bar{\sigma}_{fe}(\mathbf{e}_{fe})\mathbf{F}_{fv}^T \quad (9)$$

where J_{fe} is the determinant of the deformation gradient \mathbf{F}_{fe} for the fluid-elastic phase. Finally, the strain rate $\dot{\mathbf{e}}_{fv}$ is function of the deviator of the fluid-viscous stress σ_{fv}^D

$$\dot{\mathbf{e}}_{fv} = \frac{\sigma_{fv}^D}{\mu_{fv}} \quad (10)$$

where μ_{fv} is the viscosity.

In order to constantly update \mathbf{F}_{fv} , it is necessary to introduce an evolution law of such variable which relates it to $\dot{\mathbf{e}}_{fv}$. Thus, we write

$$\dot{\mathbf{e}}_{fv} = -\frac{1}{2}\mathbf{F}_{fv}^{-T}(\mathbf{F}_{fv}^T\mathbf{F}_{fv}^{-T} + \mathbf{F}_{fv}^{-1}\dot{\mathbf{F}}_{fv}^{-1})\mathbf{F}_{fv}^{-1} \quad (11)$$

As it is well known, the previous equation provides only the symmetric part of $\dot{\mathbf{F}}_{fv}$. Since here we have considered an isotropic material, the antisymmetric part of $\dot{\mathbf{F}}_{fv}$ can be obtained from the total spin (Lubarda, 2004).

To summarize, the independent variables of the problem are \mathbf{F} , \mathbf{F}_{sa} , \mathbf{F}_{fv} .

2.3. Cell active deformations

Although the amoeboid migration process is believed to take place in five steps (Section 1.1, (Sheetz et al., 1999)), we consider here only two main phases: (1) the protrusion at the front simultaneous with the adhesion at the back (2) the contraction at the back simultaneous with the adhesion at the front. The relaxation phase is not explicitly implemented in our model, but it could simply be a consequence of the inertial forces as well as the viscoelastic behavior of the cell.

The active deformations (protrusion and contraction), caused by the changes in configuration of the actin network, take place in the solid phase of the cell and are multiplicatively composed with the deformations responsible for mechanical stresses. They are similar here to thermal deformations, which do not produce any stress when the body is free but enforce dilatations. Thus, forces are generated when these deformations are hindered by boundary conditions.

According to this approach, the solid deformation gradient \mathbf{F}_s is decomposed into an elastic and an active part as described in Eq. (3).

\mathbf{F}_{sa} is considered as a uniaxial deformation and is chosen to be equal to

$$\mathbf{F}_{sa} = h_a e_a \mathbf{d}_a \otimes \mathbf{d}_a \quad (12)$$

with h_a being a characteristic function of the active domain $\{(x,y,z)/z \leq H_a\}$. Here in fact, we assume that the actin network is mostly localized over the cell surface in contact with the substrate. $e_a(t)$ is the cyclic component of the active strain and is simply chosen here as follows:

$$e_a(t) = e_{a0} \sin\left(2\pi \frac{t}{T_a}\right) \quad (13)$$

where t is the time, e_{a0} is the amplitude of the cyclic active strain and T_a is its period.

The direction of migration \mathbf{d}_a is given by

$$\mathbf{d}_a = \cos\theta(t)\mathbf{i}_x + \sin\theta(t)\mathbf{i}_y \quad (14)$$

where $\theta(t)$ will be defined more precisely in Section 2.6. The variability in $\theta(t)$ will allow the cell to reorient its crawling direction.

According to the cyclic nature of the deformation, \mathbf{F}_{sa} will alternatively correspond to the protrusion or contraction processes at the front and at the rear of the cell, respectively.

In summary, the cell model is submitted to a pulsating movement inside a viscoelastic material. Now, the locomotion of the cell is only possible through the adhesion to the 2D substrate at the anterior and posterior edges, otherwise the cell will only vibrate and slide in place without moving forward. In the next sections we describe how the boundary conditions and the attachment strengths are taken into account.

2.4. Boundary conditions

The boundary conditions are mainly associated with the 2D planar substrate underneath. The cell is assumed to be always in contact with the substrate (no flight and no penetration), but the adhesion forces are developed with a delicate phasing with respect to the active deformations. We introduce a frontal adhesion surface $\partial\Omega_{sf}$ in the direction \mathbf{d}_a defined inside the cell by a Heaviside function as follows:

$$h_{sf}(\mathbf{p}_s) = \begin{cases} 1 & (\mathbf{p}_s - \mathbf{p}_c, \mathbf{d}_a) > l_f \\ 0 & \text{otherwise} \end{cases} \quad (15)$$

and a rear adhesion surface $\partial\Omega_{sr}$ in the reverse direction of \mathbf{d}_a defined by

$$h_{sr}(\mathbf{p}_s) = \begin{cases} 1 & (\mathbf{p}_s - \mathbf{p}_c, \mathbf{d}_a) < -l_r \\ 0 & \text{otherwise} \end{cases} \quad (16)$$

where \mathbf{p}_s stands for a cell point in contact with the substrate, \mathbf{p}_c is the geometric center of the cell base, l_f and l_r are the distances of \mathbf{p}_c from the boundaries of the frontal and the rear adhesion surfaces respectively (Fig. 2a).

2.5. Adhesion forces

We consider first the case of a homogeneous 2D substrate. As in previous works (Friedl and Wolf, 2010; Holzapfel, 2000; Phillipson et al., 2006), the adhesion forces are assumed to be viscous forces and given by

$$\sigma_f(\mathbf{n}) = -\mu_{ff} h_e\left(-\frac{\partial \mathbf{u}_s}{\partial t}\right) h_{sf}(\mathbf{u}_s) \frac{\partial \mathbf{u}_s}{\partial t} \quad \text{on } \partial\Omega_{sf} \quad (17a)$$

$$\sigma_r(\mathbf{n}) = -\mu_{fr} h_e\left(\frac{\partial \mathbf{u}_s}{\partial t}\right) h_{sr}(\mathbf{u}_s) \frac{\partial \mathbf{u}_s}{\partial t} \quad \text{on } \partial\Omega_{sr} \quad (17b)$$

with μ_{ff} and μ_{fr} the friction coefficients for the frontal and rear surfaces, respectively, h_e the classical scalar Heaviside function and \mathbf{u}_s the tangential displacement of the cell with respect to the substrate. The two preceding equations (Eqs. (17a) and (17b)) are the key ingredients of the model because they link the adhesion forces with the pulsating movement of the cell. Furthermore, a small stabilizing viscous force is assumed to be applied along the whole interface

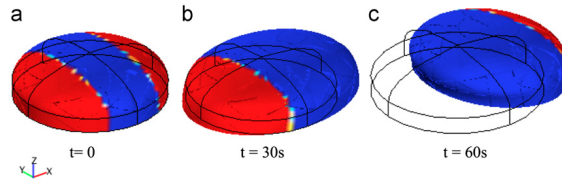


Fig. 2. First period of migration from $t=0$ to $t=60$ s. For sake of clarity, the anterior and the posterior adhesion regions (red) have been represented through the thickness of the cell although in reality they are placed on the cell surface in contact with the substrate. During the first 30 s, the posterior region grabs the substrate and the leading edge protrudes. From $t=30$ s to $t=60$ s, the anterior region adheres and the back of the cell is pulled forward. (For interpretation of the references to color in this figure legend, the reader is referred to the web version of this article.)

between the cell and the substrate to prevent negligible rigid body movements.

This approach allows one to reproduce the cyclic behavior of the cell as described in Section 1.1: first the protrusion occurs due to the expansion of the actin network in the frontal pseudopod and the adhesion forces are mobilized in the rear edge and relaxed in the front (step 1), then the cell adheres to the substrate at the frontal edge (step 2) and the cytoskeleton contracts and pulls the rear end of the cell forward (step 3).

As we have mentioned in the Introduction of this paper (see Section 1), the cell migrates in response to an external stimulus. In the next section, we describe how this particular aspect has been taken into account in the present model.

2.6. Chemotaxis

Any cellular motion or deformation is usually regulated by chemical events. For instance, as we showed in our previous work (Allena et al., 2011), elementary cell deformations in *Drosophila* embryo during morphogenetic movements are triggered by chemical reactions inside the cells.

This is also the case for single cell migration. Chemotaxis in fact is the phenomenon by which somatic cells, bacteria, and other single-cell or multicellular organisms direct their movements according to certain chemicals in their environment. This is important for bacteria to find food by swimming towards the highest concentration of food molecules, or to flee from poisons. In multicellular organisms, chemotaxis is critical to early development and subsequent phases of development as well as in normal function. In addition, it has been recognized that mechanisms that allow chemotaxis in animals can be subverted during cancer metastasis.

Here, we do not introduce any coupling between mechanics and chemicals, but we equip the model so that the cell migrates in the direction of an attracting source.

Thus, θ , the angle determining the direction \mathbf{d}_θ of migration, must satisfy a differential equation which includes an asymptotically attracting term as follows:

$$\theta' + \frac{\theta - \theta_\infty}{\tau_\infty} = 0 \quad (18)$$

where θ_∞ is the direction of the source, typically a concentration gradient vector. τ_∞ plays the role of the intensity of the source and controls how fast the cell can orient itself in the direction θ_∞ .

2.7. 'Obstacles' on the road

The cell actually migrates in response to many stimuli (see Section 1). Whatever the final destination and objective are, the cell tries to reach it as fast as possible. Nevertheless, the underneath 2D substrate is rarely homogeneous. Therefore, the cell needs to react when it encounters 'obstacles' on its way. Here,

we have simply assumed that such 'obstacles' coincide with regions where the sticking forces are increased. The cell is then led to avoid them as soon as it gets in their proximity, according to several strategies presented below.

The 'obstacles' are assumed to be circular, with a center \mathbf{p}_{obs} and a radius r_{obs} . They are defined by a level set function as follows:

$$h_{obs}(\mathbf{p}) = \begin{cases} 1 & \mathbf{p} \in \Omega_{obs} \\ 0 & \text{otherwise} \end{cases} \quad (19)$$

where Ω_{obs} represents the domain occupied by the 'obstacle' (Fig. 10).

As evocated by Erban and Othmer (2006) the cell can adopt two distinct strategies to avoid the 'obstacle': either it executes the 'bakery walk' ('run-and-tumble' strategy), which consists in taking a 'sniff' and judging the signal intensity at the present location, taking a step and another 'sniff', comparing the signals, and from the comparison deciding on the next step, or it uses sensors to measure the difference in the signal at the current location and uses this difference to decide on a direction, what we have called here the 'look-and-run' strategy.

Therefore, two hypotheses have been made for the two approaches:

- in the first case ('run-and-tumble' strategy), when approaching the 'obstacle', the cell slows down due to the larger sticking forces and tries to get away by changing the direction of migration. Therefore, the cell behaves as if it were equipped with a velocity sensor;
- in the second case ('look-and-run' strategy), the cell sees the 'obstacle' from far away and anticipates it by steering around the sticking region. In this case we assume that the cell has a distance sensor.

As mentioned above, the 'obstacles' act as an additional adhesion force over the contact surface between the cell and the underneath 2D substrate.

Such a force is expressed as

$$\boldsymbol{\sigma}_{obs}(\mathbf{n}) = -\mu_{obs} h_{obs} \frac{\partial \mathbf{u}_s}{\partial t} \quad \text{on } \partial\Omega_s \quad (20)$$

where μ_{obs} is the friction coefficient of the 'obstacle' and $\partial\Omega_s$ is the lower surface of the cell in contact with the substrate. This term is then added to Eqs. (17a) and (17b).

We describe now the main features of the two approaches.

2.7.1. Velocity sensor for a 'run-and-tumble' strategy

As the migration process leads to large deformations of the cell, the velocity is not uniform throughout its body. Here, we assume that the cell is able to sense its average velocity \mathbf{v}_c .

defined by

$$\mathbf{v}_c = \frac{1}{|\Omega_c|} \int_{\Omega_c} \mathbf{v} dV \quad (21)$$

where $|\Omega_c|$ is the cell volume.

The average velocity $\mathbf{v}_c(t)$ highly oscillates with respect to time between the protrusion and contraction phase. We further assume that the cell filters the signal in order to smooth such fluctuation and be able to change its direction of locomotion. Many theoretical filters do exist in the literature (Papoulis, 1977). Here, we choose a very simple one with a harmonic oscillator that tends to reduce the amplitude of high frequency oscillations.

The filtered velocity \mathbf{v}_{cf} is then defined as follows:

$$\frac{d^2 \mathbf{v}_{cf}}{dt^2} + 2\zeta_f \omega_f \frac{d\mathbf{v}_{cf}}{dt} + \omega_f^2 \mathbf{v}_{cf} = \mathbf{v}_c \quad (22)$$

where ζ_f is the critical damping ratio and ω_f is the undamped angular frequency of the filter.

The strategy by which the cell changes its direction in trying to avoid the 'obstacle' is then defined by three different configurations:

- (1) if there is no 'obstacle' on the substrate, the cell directly migrates towards the source with a direction of migration tending to θ_{sc} ;
- (2) if there is an 'obstacle', the velocity of the cell is decreased and two situations may occur:

- (2a) the cell slows down, but not so much. The magnitude of the average filtered velocity \mathbf{v}_{cf} is then intermediate between a maximal (v_{left}) and a minimal (v_{right}) value and the cell turns left. In this case, the Heaviside function reads

$$h_{obs_v_left}(\mathbf{v}_{cf}) = \begin{cases} 1 & v_{right} < \|\mathbf{v}_{cf}\| < v_{left} \\ 0 & \text{otherwise} \end{cases} \quad (23)$$

- (2b) the cell highly reduces its average filtered velocity \mathbf{v}_{cf} which is then smaller than a minimal value (v_{right}). According to such a signal, the cell deduces that the direction of migration employed in (2a) or in (1) must be inverted, and then it turns right. The associated Heaviside function can be written as

$$h_{obs_v_right}(\mathbf{v}_{cf}) = \begin{cases} 1 & \|\mathbf{v}_{cf}\| < v_{right} \\ 0 & \text{otherwise} \end{cases} \quad (24)$$

Consequently, the angle $\theta(t)$ of migration defined in Eq. (18) becomes equal to

$$\theta' = [h_{obs_v_left}(\mathbf{v}_{cf}) - h_{obs_v_right}(\mathbf{v}_{cf})] \omega_0 - \frac{\theta(t) - \theta_{sc}}{\tau} \quad (25)$$

where ω_0 is the angular velocity jump that the cell develops to avoid the 'obstacle'. Such a description is based on the assumption according to which the cell first turns left and eventually right when its average velocity is highly decreased. Of course the opposite as well as a random choice of direction could have been implemented in the model.

2.7.2. Distance sensor for a 'look-and-run' strategy

In the second case, with the minimal distance strategy, the distance cell-'obstacle' is described by

$$h_{obs_d}(\mathbf{u}_c) = \begin{cases} 1 & |\mathbf{x}_c - \mathbf{u}_c - \mathbf{p}_{obs}|^2 < r_{obs}^2 \\ 0 & \text{otherwise} \end{cases} \quad (26)$$

where \mathbf{x}_c is the present position of the cell center of inertia and \mathbf{u}_c its displacement.

Then, the direction of the pulsating movement of the cell changes according to the following differential equation:

$$\theta' = h_{obs_d}(\mathbf{u}_c) \omega_0 - \frac{\theta - \theta_{sc}}{\tau} \quad (27)$$

2.8. Numerics

In the preceding sections we have presented step by step the ingredients of our mechanical model of the cell. Here, we describe the numerical techniques that have been used to run the simulations. Let us summarize the main equations.

First, together with the dynamic equilibrium equation (Eq. (1)), we have the constitutive equation written in a symbolic manner as

$$\boldsymbol{\sigma} = \bar{\boldsymbol{\sigma}}_s(\mathbf{e}_{se}(\mathbf{u}, \mathbf{F}_{sa}(\theta))) + \bar{\boldsymbol{\sigma}}_f(\mathbf{e}_{fe}(\mathbf{u}, \mathbf{F}_{fv})) \quad (28)$$

which shows that the stress $\bar{\boldsymbol{\sigma}}_s$ in the solid phase is a function of the displacement \mathbf{u} and of the orientation angle θ . The stress $\bar{\boldsymbol{\sigma}}_f$ in the fluid elastic phase is instead a function of the displacement field \mathbf{u} and of the deformation gradient \mathbf{F}_{fv} , which satisfies Eq. (11).

Finally, the cell active deformation is defined by \mathbf{F}_{sa} which depends on the cyclic component of the active strain \mathbf{e}_a and the control variable θ . Recall that θ is computed according to the type of substrate the cell is migrating on, namely a homogeneous substrate (Eq. (18)) or a heterogeneous substrate. In the latter case, the cell avoids the 'obstacles' based on information provided by either a velocity sensor (Eq. (25)) or a distance sensor (Eq. (27)).

In the case of the velocity sensor, θ satisfies the differential equation Eq. (25) which we can be written now as follows:

$$\theta' = g_v(\mathbf{v}_{cf}) \omega_0 - \frac{\theta - \theta_{sc}}{\tau} \quad (29)$$

while in the case of the distance sensor (Eq. (27)), we have

$$\theta' = g_d(\mathbf{u}_c) \omega_0 - \frac{\theta - \theta_{sc}}{\tau} \quad (30)$$

where $g_v(\mathbf{v}_{cf})$ and $g_d(\mathbf{u}_c)$ stand for the Heaviside functions expressed in Eqs. (25) and (27) respectively.

Therefore, we have three unknowns: \mathbf{u} , \mathbf{F}_{fv} , and θ . Using a classical finite elements approximation, the displacements field \mathbf{u} is obtained by developing a weak form for Eq. (1) and Eqs. (17a and 17b), which reads then as follows:

$$\int_{\Omega} (\rho \mathbf{a}, \mathbf{w}) + \text{Tr}[\boldsymbol{\sigma}(\mathbf{D}_p \mathbf{w} \mathbf{F}^{-1})] dV = \int_{\Omega} \left[\left(\mu_{ff} h_e \left(-\frac{\partial \mathbf{u}_s}{\partial t} \right) h_g(\mathbf{p}_s) \frac{\partial \mathbf{u}_s}{\partial t} + \mu_{fv} h_e \left(\frac{\partial \mathbf{u}_s}{\partial t} \right) h_{sr}(\mathbf{p}_s) \frac{\partial \mathbf{u}_s}{\partial t} + \mu_{obs} h_{obs} \frac{\partial \mathbf{u}_s}{\partial t}, \mathbf{w} \right) \right] dS \quad (31)$$

where \mathbf{w} is any kinematically admissible displacement test function.

Since no spatial derivatives are involved in their definitions, both the fluid-viscous strain tensor \mathbf{F}_{fv} and the orientation angle θ are integrated by a simple weak form. Finally, the system of nonlinear differential equations (Belytschko et al., 2000) reads

$$\begin{cases} \mathbf{M} \mathbf{U}'' + \mathbf{F}^{\text{int}}(\mathbf{U}, \mathbf{U}) = \mathbf{0} \\ \mathbf{F}_{fv}' + \mathbf{A}_{fv}(\mathbf{F}_{fv}) = \mathbf{0} \\ \theta' + g_{\theta}(\theta) = 0 \end{cases} \quad (32)$$

where \mathbf{M} is the mass matrix, \mathbf{U} is the displacement vector and \mathbf{F}^{int} represents the internal forces vector (i.e. the stresses and adhesion forces). \mathbf{A}_{fv} is the matrix generated by the evolution law of the viscous gradient \mathbf{F}_{fv} , and g_{θ} describes the evolution equation of the direction of migration (Eqs. (18), (25) and (27)). A backward differentiation scheme of variable order (up to the 5th) is used to integrate the system. Such an implicit technique ensures better stability properties for the time integration allowing then to choose large enough time steps to simultaneously achieve good accuracy

and fast computations. Finally, a modified Newton method takes care of finding the updated displacement value at each time step.

3. Results

The simulations have been run using the finite element software COMSOL Multiphysics[®] 3.5a. The cell has a radius r of 5 μm and a maximal height h along the axis of symmetry of 3 μm . The underneath substrate has dimensions of $10 \times 10 \times 1 \mu\text{m}$. The Young modulus E_s and the Poisson's ratio ν_s for the solid phase of the model have been chosen uniformly equal to 10^4 Pa (Laurent et al., 2005) and 0.3 respectively. For the fluid phase, E_{fe} and ν_{fe} are equal to 10^2 Pa and 0.4, while the viscosity μ_{fv} is equal to $3 \times 10^5 \text{ Pa}\cdot\text{s}$ (Bausch et al., 1999; Drury and Dembo, 2001). The cell density has been set to 1000 kg/m^3 (Fukui et al., 2000). The main geometrical, material and mechanical parameters are listed in Table 1.

3.1. Symmetric migration

Firstly, we focus on the evolution of the shape, the displacement, the velocity of the cell and the adhesion forces to verify whether the proposed model realistically reproduce the cell behavior during migration on a 2D substrate. In order to do so, we propose a simulation where:

- the cyclic active strain e_{a0} is equal to 0.5;
- the rear and the frontal adhesion surfaces are spatially symmetric as represented in Fig. 2a. Each one of them has an area of $2 \times 10^{-11} \text{ m}^2$;
- the period T_{migr} of each migration cycle has been set equal to 60 s (Dong et al., 2002) in order to have an average cell velocity of some microns per minute;
- the underneath 2D substrate is considered homogeneous (therefore no 'obstacle' is introduced);
- an attracting source is simulated with direction $\theta_\infty = \pi/4$ and intensity $\tau = 100$. For clarity purposes, we have chosen here a specific value for both of these parameters. However, we show

in Fig. 3 how θ varies when one of these two parameters is differently chosen.

In Fig. 2, the very first period of the simulation from $t=0$ to $t=T_{migr}=60 \text{ s}$ is represented in detail so that the three main phases of the cyclic migration mode can be observed (Section 1.1): (i) initial phase (ii) rear adhesion and protrusion (iii) frontal adhesion and contraction. In Fig. 4 (also see Movie 1), the successive phases of the cell migration are plotted at different steps: $t=0 \text{ s}$, $t=300 \text{ s}$, $t=600 \text{ s}$ and $t=900 \text{ s}$. As soon as the cell senses the presence of the attracting force, it starts to rotate with an angular velocity ω_0 of 0.02 rad/s in order to keep migrating in the direction of θ_∞ (Fig. 5a). In 900 s, the cell is able to cover 100 μm as we can see in Fig. 5b, where the displacement of the cell center of inertia is reported. Since the rear and the frontal adhesion surfaces are here spatially symmetric, the displacements during the protrusion and the contraction phases are the same. Fig. 5c describes the trend of the cell velocity: each maximum corresponds to the cell velocity either during the protrusion or the contraction period. The average velocity is equal to 5.7 $\mu\text{m}/\text{mn}$ during the protrusion phase and to 5.2 $\mu\text{m}/\text{mn}$ during the contraction phase, which are in the range of reported values (3–12 $\mu\text{m}/\text{mn}$ (Adachi et al., 2009; Okeyo et al., 2009; Wilson et al., 2010)).

Supplementary material related to this article can be found online at doi:10.1016/j.jtbi.2012.03.041.

In order to evaluate the adhesion strength, we have calculated the projections along the direction of migration \mathbf{d}_0 of the resultant adhesion forces \mathbf{R}_f and \mathbf{R}_r over the contact surface between the cell and the 2D substrate, respectively for σ_f and σ_r . Their evolution over time is plotted in Fig. 5d. The two forces are almost identical given the symmetry of the adhesion surfaces ($R_{f,max} = 7.2 \times 10^{-13} \text{ N}$, $R_{r,max} = 7.6 \times 10^{-13} \text{ N}$). Also, they are mostly positive during each phase of the migration (protrusion or contraction), which is in agreement with the physical phenomenon according to which \mathbf{R}_f and \mathbf{R}_r are propulsion forces that allow the cell to move towards the attracting source.

Table 1

Parameter	Description	Value	Unit	Reference
r	Cell radius	5×10^{-6}	m	
h	Cell height	3×10^{-6}	m	
H_a	Height of the active domain	10^{-6}	m	
E_s	Young's modulus for the solid phase	10^4	Pa	(Laurent et al., 2005)
ν_s	Poisson's ratio for the solid phase	0.3		
E_{fe}	Young's modulus for the fluid-elastic phase	10^2	Pa	
ν_{fe}	Poisson's ratio for the fluid-elastic phase	0.4		
μ_{fv}	Viscosity for the fluid-viscous phase	3×10^5	Pa·s	(Bausch et al., 1999; Drury and Dembo, 2001)
ρ	Cell density	1000	Kg/m^3	(Fukui et al., 2000)
e_{a0}	Cyclic active strain	0.5		
S_f	Area of frontal region of adhesion	Symmetric case: 2×10^{-11} Asymmetric case: 2×10^{-11}	m^2	
S_r	Area of rear region of adhesion	Symmetric case: 2×10^{-11} Asymmetric case: 4.5×10^{-12}	m^2	
μ_{ff}	Friction coefficient at the frontal edge	10^8	Pa·s/m	
μ_{fr}	Friction coefficient at the rear edge	10^8	Pa·s/m	
T_{migr}	Period for migration cycle	60	s	(Dong et al., 2002)
ω_0	Angular velocity	0.02	rad/s	
θ_∞	Source direction	$\pi/4$		
τ_∞	Source intensity	100		
P_{obs}	Obstacle's position	$p_1 = (15 \times 10^{-6}, 0, 10^{-6})$ $p_2 = (8 \times 10^{-6}, 20 \times 10^{-6}, 10^{-6})$	m	
r_{obs}	Obstacle's radius	2×10^{-6}	m	
μ_{obs}	Friction coefficient at the slippery regions	10^8	Pa·s/m	
v_{right}	Minimal cell velocity	0.5×10^{-8}	m/s	
v_{left}	Maximal cell velocity	1.5×10^{-8}	m/s	
ξ_f	Damping ratio	10		(Papoulis, 1977)
ω_f	Undamped angular frequency	2	Rad/s	(Papoulis 1977)

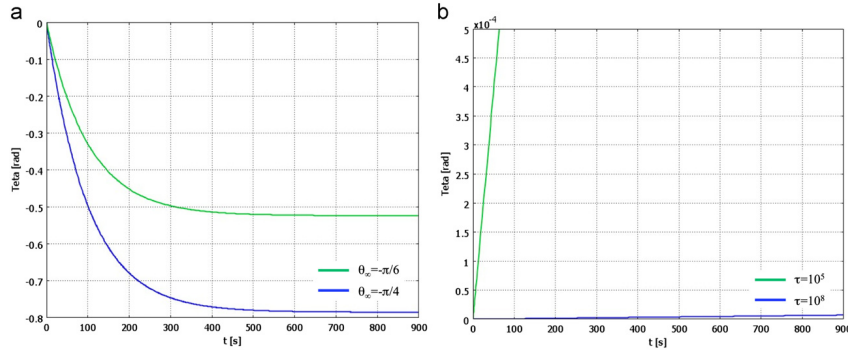


Fig. 3. (a) Plot of θ when $\tau = 10^2$ fe, $\theta_0 = -\pi/6$ (green) and $\theta_0 = -\pi/4$ (blue) and (b) plot of θ when $\theta_0 = \pi/4$, $\tau = 10^5$ (green) and $\tau = 10^8$ (blue). (For interpretation of the references to color in this figure legend, the reader is referred to the web version of this article).

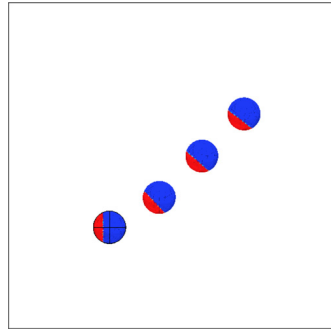


Fig. 4. Successive phases of the simulation for the symmetric migration at different steps: $t=0$, $t=300$ s, $t=600$ s and $t=900$ s. In red the anterior and the posterior adhesion regions. (For interpretation of the references to color in this figure legend, the reader is referred to the web version of this article).

Nevertheless, we can notice that during the initial phases of migration, the rear adhesion force R_r is actually bigger than the frontal adhesion force R_f . This occurs because, in order for the cell to start moving with an initial vanishing velocity, a bigger force is required. However, as long as the migration takes place, R_f is slightly higher than R_r . Such inversion is probably due to the small inertial forces in the system which make easier for the cell to protrude than contract. Such a result is in agreement with the experimental observations (Lämmermann and Sixt, 2009; Lauffenburger and Horwitz, 1996).

Consequently, our model allows us to realistically simulate the cyclic deformation mode and the associated adhesion forces necessary for the cell to move. However, slightly erroneous parameters can inhibit the cell locomotion. Particularly, we have analyzed the strength of the adhesion, which seems to play a determinant role during the migration process as pointed out by recent studies (Friedl and Wolf, 2010; Lämmermann and Sixt, 2009). In our model, the adhesion strength can be controlled by tuning the friction coefficients μ_{ff} and μ_{fr} , respectively at the front and at the rear of the cell. In both cases, we have decreased their values from 10^8 Pa-s/m to 10^2 Pa-s/m. We have plotted the

resultant adhesion forces R_f and R_r and the successive steps of the simulation for the low frontal adhesion case (Fig. 6a and c) and for the low rear adhesion case (Fig. 6b and d). While the resultant force for the unchanged adhesion force is in both cases similar in magnitude to the one found for the previous simulation, the resultant force for the adhesion force that has been decreased almost vanishes. From Fig. 7a and c, we observe that the total displacement of the cell over the same period is much smaller than the previous simulation. Here actually, the cell is able to cover only $55 \mu\text{m}$ due to the fact that the cyclic and synchronized modes of migration do not occur properly. When the adhesion force is low at the front, the cell does not have enough force to adhere to the 2D substrate and pull its back forward, so that the leading edge extends normally and at the same velocity as for the previous case (Fig. 7b vs. Fig. 5c), but the rear edge does not move much. When the adhesion force is low at the rear, the cell cannot protrude at the same rate because it slips at the back, so that its velocity during this phase vanishes (Fig. 7d) and it elongates almost symmetrically in both directions (front and back), while the contraction phase takes place properly.

3.2. Spatial asymmetry of cell adhesion surfaces

Recent works have suggested that, in order for the cell to stick to the 2D substrate and pull its back forward, the adhesion strength has to be stronger at the front than at the back, so that the contraction of the cell body can overwhelm the attachment of the leading edge (Lämmermann and Sixt, 2009; Lauffenburger and Horwitz, 1996). In order to confirm this hypothesis, we have introduced a spatial asymmetry between the frontal and the rear adhesion surfaces as represented in Fig. 8a. Their areas S_f and S_r are respectively equal to $2 \times 10^{-11} \text{ m}^2$ and $4.5 \times 10^{-12} \text{ m}^2$. Consequently, the resultant adhesion forces calculated at the front and the rear of the cell have different values compared to the ones obtained for the symmetric migration (Fig. 8d vs. Fig. 5d). In particular, R_f is bigger and has a maximal value of $5 \times 10^{-11} \text{ N}$, while R_r is in general smaller and reaches a maximum at $0.8 \times 10^{-11} \text{ N}$. In Fig. 9 (also see Movie 2) successive phases of the simulation are plotted. The total displacement (Fig. 8b) is bigger than the symmetric case. The cell in fact migrates for $130 \mu\text{m}$ in the direction d_0 to reach the attracting source during the same amount of time (900 s). Actually, the smaller the adhesion surface at the rear, the higher the protrusion at the front. Furthermore, the velocity plot (Fig. 8c) reveals that the cell

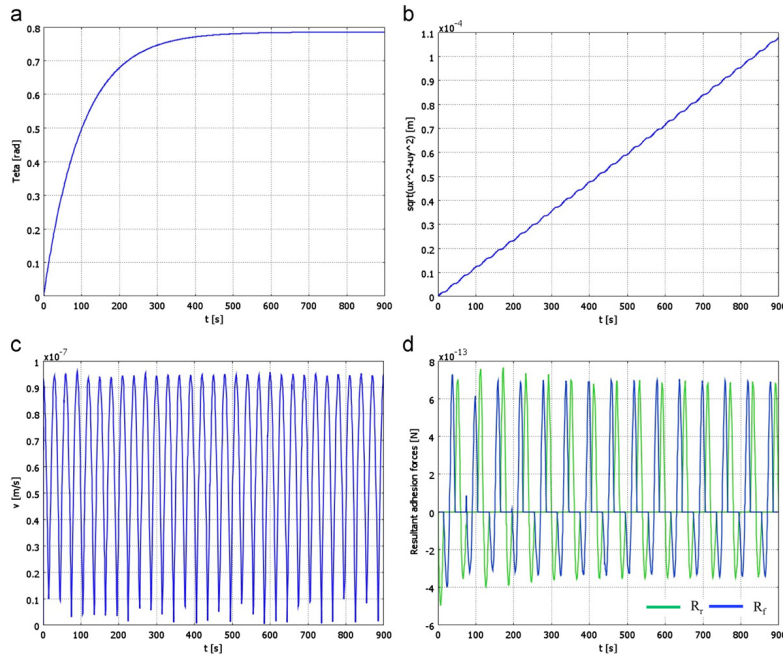


Fig. 5. Different plots for the simulation of the symmetric migration (Section 3.1): θ (a), cell displacement (b), cell velocity (c), adhesion forces at the front (blue) and at the rear (green) of the cell (d). (For interpretation of the references to color in this figure legend, the reader is referred to the web version of this article).

moves faster during the protrusion phase (8.2 $\mu\text{m}/\text{mn}$) and slower during the contraction phase (5.4 $\mu\text{m}/\text{mn}$). Therefore, the more spatially asymmetric the adhesion is, the faster the cell migrates. These results are consistent with previous experimental observations (Zaman et al., 2005) according to which asymmetry of adhesion may play a significant role during migration. Although the spatial asymmetry of the adhesion surfaces may look similar to the case where the rear adhesion forces are reduced (Section 3.1), it has to be noticed that in the former case the successive steps are preserved and correctly take place, while in the latter case they provide a somewhat abnormal migration process.

Supplementary material related to this article can be found online at doi:10.1016/j.jtbi.2012.03.041.

3.3. Substrate heterogeneity

The last simulation we propose allows one to take into account the heterogeneity of the underneath 2D substrate. In this case, we consider then

- symmetric frontal and rear adhesion surfaces, with $\mu_{ff} = \mu_{fr} = 10^8 \text{ Pa}\cdot\text{s}/\text{m}$;
- the attracting source always directed along $\theta_{\infty} = \pi/4$;
- two 'obstacles' are introduced on the 2D substrate. The first one \mathbf{p}_1 has coordinates $(15 \times 10^{-6}, 0, 10^{-6})$, while the second one \mathbf{p}_2 is placed at $(8 \times 10^{-6}, 20 \times 10^{-6}, 10^{-6})$. Both of them have a radius r_{obs} of $2 \times 10^{-6} \text{ m}$ (Fig. 10).

In these regions, that are obtained according to Eq. (19), the sticking force is increased so that an additional viscous component is added to the adhesion force over the whole surface of contact with the 2D substrate (Eq. (20)). The friction coefficient of the 'obstacles' μ_{obs} has been chosen equal to $10^8 \text{ Pa}\cdot\text{s}/\text{m}$. If μ_{obs} is higher ($10^{12} \text{ Pa}\cdot\text{s}/\text{m}$), the 'obstacle' becomes a 'wall' and the cell repeatedly beats against it.

Two main assumptions have been used to deal with such simulation, as described in Section 2.7. Here, we are going to present the results separately for each one of them.

3.3.1. 'Run-and-tumble' strategy

During migration over a homogeneous 2D substrate (see Section 3.1), the cell moves at an almost constant velocity during both the protrusion and the contraction phases. As soon as the cell approaches an 'obstacle', it starts to slow down because of the introduction of a bigger sticking force which inhibits its locomotion. Practically, the cell gropes the underneath 2D substrate little by little, slows down when the sticking force increases and turns left or right according to its speed.

To show such behavior, we first present here a simple case where the cell has a prescribed direction of locomotion. We have chosen in fact to fix $\mathbf{d}_a = \hat{\mathbf{i}}_x$, therefore $\theta(t)$ is constantly equal to 0° . The damping ratio ξ_f and the undamped angular frequency ω_f of the filtered velocity of the sensor are respectively equal to 10 and 2 rad/s (Papoulis, 1977). As represented in Fig. 10 (also see Movie 3), the cell starts to migrate and as soon as it approaches the 'obstacle' \mathbf{p}_1 ,

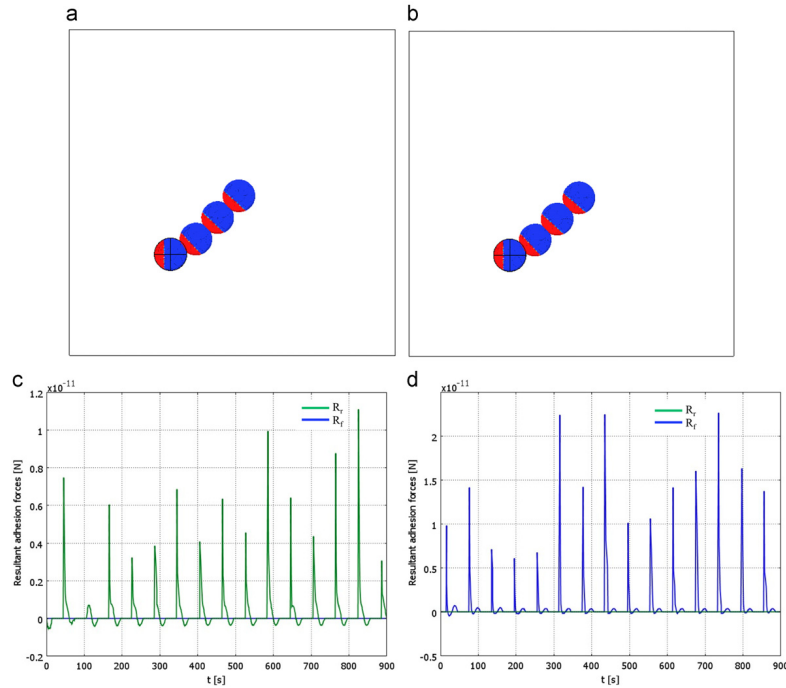


Fig. 6. Successive phases ($t=0$, $t=300$ s, $t=600$ s and $t=900$ s) for the simulations when the friction coefficients μ_{ff} at the front (a) and μ_{fr} at the rear (b) are decreased to 10^2 Pa-s/m. In red the anterior and the posterior regions of adhesion. When the friction coefficients μ_{ff} and μ_{fr} are decreased, the associated adhesion forces decreased too. Therefore, when $\mu_{ff}=10^2$ Pa-s/m, the adhesion force at the front of the cell (blue) is almost equal to 0 (c). When $\mu_{fr}=10^2$ Pa-s/m, the adhesion force at the back of cell is almost null (green) (d). (For interpretation of the references to color in this figure legend, the reader is referred to the web version of this article.)

its velocity \mathbf{v}_c decreases as well as \mathbf{v}_{cf} (Fig. 11a). Given the value of μ_{obs} , the cell is able to pass through the 'obstacle' although its velocity remains smaller when compared to the initial steps of the simulation and starts to increase again as soon as the frontal edge is away from it (Fig. 11a). The adhesion forces at the front and at the rear of the cell (Fig. 11b) are bigger than the ones found for the symmetric case (see Fig. 5d). Furthermore, the frontal adhesion force is much bigger than the rear adhesion force when the cell starts migrating through the 'obstacle', while the inverse occurs when the cell is leaving the 'obstacle' (Fig. 11b).

Supplementary material related to this article can be found online at doi:10.1016/j.jtbi.2012.03.041.

If we reconsider instead the definition of \mathbf{d}_q (Eq. (13)), the cell interprets the decrease of the velocity as a signal to rotate left or right in order to avoid the 'obstacle'. As described in Section 2.7.1, according to how much the cell slows down, three situations may occur. Here, we have fixed v_{right} and v_{left} equal to 0.5×10^{-8} m/s and 1.5×10^{-8} m/s, respectively. As observed in Fig. 12 (see also Movie 4), the cell immediately turns left and avoid \mathbf{p}_1 . However, as long as it migrates, it approaches \mathbf{p}_2 , but this time the cell does not completely avoid the 'obstacle': it just slows down and moves through it (Fig. 13b). As soon as the cell migrates across the sticking region, the resultant adhesion force at the front increases, while the opposite takes place when the cell leaves the 'obstacle'

and the resultant adhesion force at the back increases (Fig. 13d). In Fig. 13c, we have plotted the trend of θ according to Eq. (25). Given the variation of \mathbf{v}_{cf} and the values chosen for v_{right} and v_{left} , the cell changes direction of migration very often, even though overall it tends to reach the attracting source at θ_∞ . Due to the decrease in velocity and the oscillations of θ , the distance covered by the cell is smaller than for the cases of symmetric and asymmetric migration (Fig. 13a vs. Figs. 5b and 8b).

Supplementary material related to this article can be found online at doi:10.1016/j.jtbi.2012.03.041.

3.3.2. 'Look-and-run' strategy

For this approach, we have assumed that the cell is equipped with a distance sensor. Therefore, it can remotely detect the 'obstacle' and avoid it by modifying well in advance its path. As we can observe from Fig. 14 (also see Movie 5), the cell immediately turns left to avoid \mathbf{p}_1 and progresses until \mathbf{p}_2 is overtaken as well. At that moment, the cell smoothly changes its direction of migration in order to reach the source. The plot in Fig. 15c shows the trend of θ over time. In this case, θ vary more smoothly than in the previous case and the cell approaches more rapidly the attracting source than when it is equipped with a velocity sensor (Section 3.3.1), but the covered distance is still smaller compared to the previous symmetric and

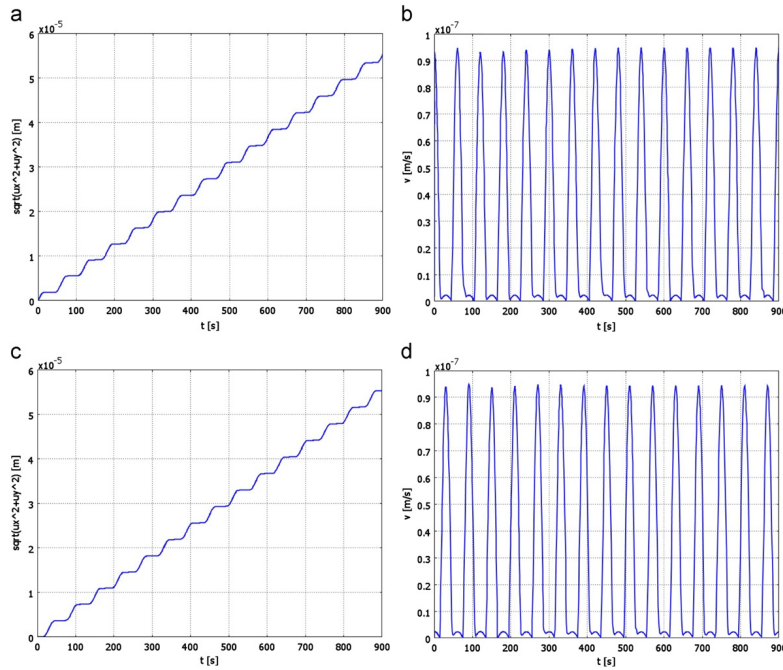


Fig. 7. Displacement (a) and velocity (b) plot for the simulation with $\mu_f=10^2$ Pa-s/m. Displacement (c) and velocity (d) plot for the simulation with $\mu_f=10^2$ Pa-s/m.

asymmetric cases (Fig. 15a vs. Figs. 5b and 8b). Overall, the velocity of the cell (Fig. 15b) and the adhesion forces at the front and at the rear of the cell (Fig. 15d) are much more regular than the previous case (Section 3.3.1).

Supplementary material related to this article can be found online at doi:10.1016/j.jtbi.2012.03.041.

3.3.3. Comparison

The two approaches presented here are efficient and let us achieve the main objective of the simulation, which is to consider the heterogeneities of the 2D substrate and to make the cell turn in order to avoid them. However, some remarks and differences between the two can be noticed.

- as a general conclusion, in both cases the total distance covered by the cell is smaller than the one for the previous simulation over the same amount of time (see Section 3.1). Of course this is mainly due to the fact that the cell encounters the heterogeneities of the 2D substrate and it tries to avoid them. This means that the cell will need more time to get to the attracting source;
- the variation of θ is much smoother for the case of a distance sensor than a velocity sensor. This is basically due to the fact that with a distance sensor, by seeing the 'obstacle' in the distance, the cell is able to adjust ahead of time its path. However, with a velocity sensor, the cell behaves as if it were

- blind. It gropes the underneath 2D substrate little by little and changes the direction of migration according to the value of v_c ;
- as a consequence of the previous consideration, in the case of a velocity sensor it is not guaranteed that the cell will completely avoid the 'obstacle'. Nevertheless, the average velocity will decrease and, unless μ_{obs} will be too high and the cell will repeatedly bang against the 'obstacle', the cell will slowly migrate through it;
- finally, from a numerical standpoint, the simulation with a distance sensor is more stable than the one with the velocity sensor. Even though the oscillations of the cell velocity v_c are attenuated by the one-dof oscillator, the range of values between the protrusion and the contraction phases is still large, which makes difficult the choice between v_{right} and v_{left} . However, the behavior of the cell in the case of a velocity sensor probably reproduces more closely the one observed in reality (Erban and Othmer, 2006).

3.4. Robustness of the model

Given the high number of input parameters of our model (25, Table 1), an exhaustive parametric study is not conceivable here. Additionally, not all the parameters have the same influence on the final results.

Nevertheless, to test the robustness of our model, we propose a sensitivity analysis. In order to do so, we first classify the parameters to determine those that may be of interest.

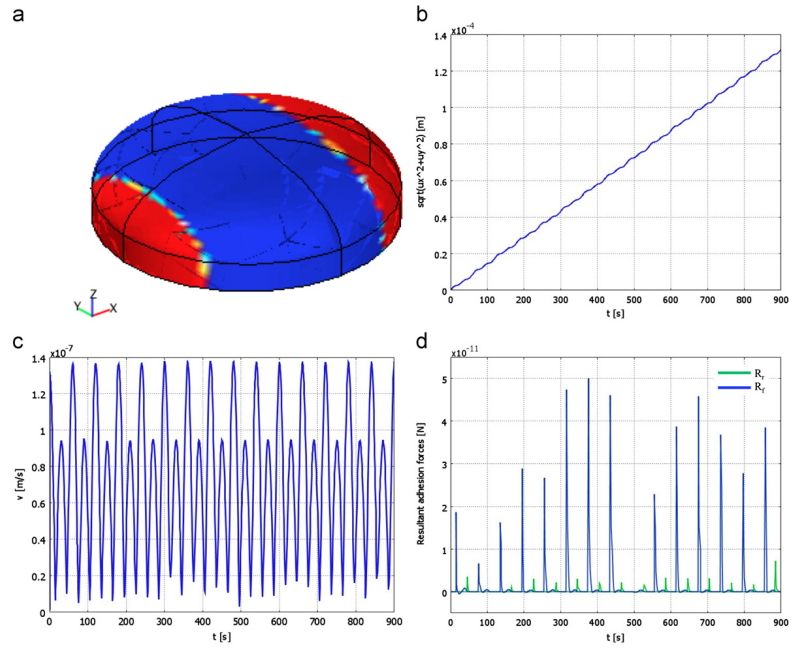


Fig. 8. Different plots for the simulation with spatial asymmetry (Section 3.2): the anterior and the posterior regions of adhesion (for sake of clarity the regions, in red, have been represented across the thickness of the cell) (a), cell displacement (b), cell velocity (c) and adhesion forces at the rear (green) and at the front (blue) of the cell (d). (For interpretation of the references to color in this figure legend, the reader is referred to the web version of this article).

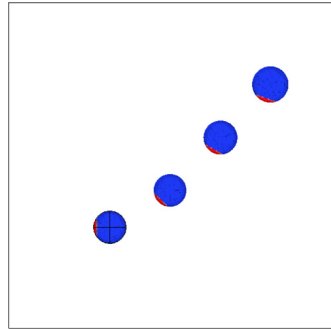


Fig. 9. Successive phases ($t=0$, $t=300$ s, $t=600$ s and $t=900$ s) for the simulation with spatial asymmetry between the anterior and the posterior regions of adhesion (red) (Section 3.2). (For interpretation of the references to color in this figure legend, the reader is referred to the web version of this article).

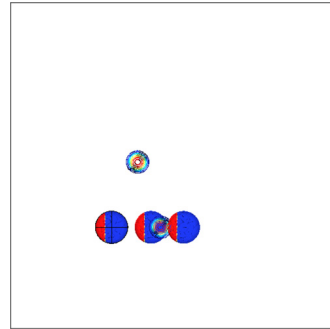


Fig. 10. Successive phases ($t=0$, $t=300$ s and $t=900$ s) for the simulation of symmetric migration and the cell equipped with a velocity sensor when $d_a[\theta(t)]=\bar{d}_a$ and $\theta(t)=0^\circ$ (Section 3.3.1). The two obstacles p_1 and p_2 are represented by their isovalues. In red the anterior and the posterior regions of adhesion. (For interpretation of the references to color in this figure legend, the reader is referred to the web version of this article).

Two main categories can be defined: (1) the parameters referenced in the literature (2) the parameters arbitrarily fixed. In the first set, we find: E_s , μ_{fs} , ρ , T_{migr} , ξ_f , ω_f . In the second set, a further division can be made: (2.1) the ones that have been chosen within a reasonable physical range (2.2) the ones that have been arbitrarily set.

Regarding the parameters of the former group, we try here to justify our choices. The cell radius r ($5 \mu\text{m}$) appears to be in agreement with the literature according to which the dimensions

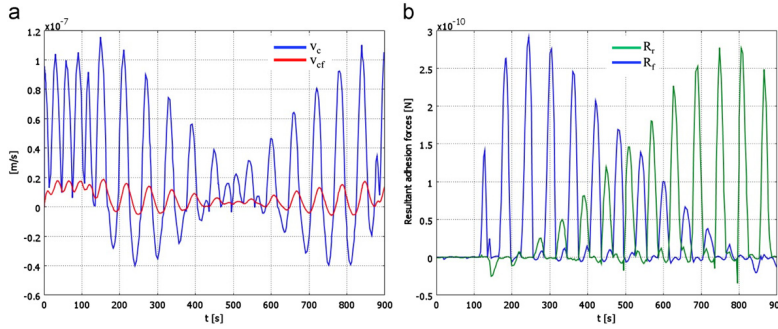


Fig. 11. Simulation of symmetric migration and the cell equipped with a velocity sensor when $d_d(\theta(t)) = \mathbf{i}$, and $\theta(t) = 0^\circ$ (Section 3.3.1). (a) Plot of the cell velocity $v_c(t)$ (blue) and the filter velocity $v_d(t)$ (red), which is supposed to reduce the oscillations of the cell velocity. Both $v_c(t)$ and $v_d(t)$ decrease when the cell migrates through the 'obstacle' (from $t = 100$ s to $t = 900$ s) and (b) plot of the adhesion forces at the rear (green) and the front (blue) of the cell. As soon as the cell approaches the 'obstacle', the adhesion force at the front of the cell highly increases ($t = 100$ s) while it starts decreasing when the cell leaves the 'obstacle' and the adhesion force at the rear of the cell starts increasing. (For interpretation of the references to color in this figure legend, the reader is referred to the web version of this article).

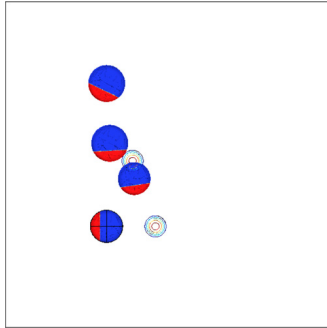


Fig. 12. Successive phases ($t = 0$, $t = 300$ s, $t = 600$ s and $t = 900$ s) for the simulation of symmetric migration and cell equipped with a velocity sensor (Section 3.3.1). The 'obstacles' p_1 and p_2 are represented by their isovalues. In red the anterior and the posterior regions of adhesion. (For interpretation of the references to color in this figure legend, the reader is referred to the web version of this article).

of a biological cell can vary between $10 \mu\text{m}$ and $100 \mu\text{m}$. The height of the active domain H_d ($1 \mu\text{m}$) has been introduced assuming that the actin filaments are mostly concentrated over the contact surface between the cell and the underneath substrate. The elastic contribution in the fluid phase is represented by the organelles which are considered to be rather solid, but less stiff than the actin filaments. For such a reason, the associated Young's modulus E_{fe} has been decreased by two orders of magnitude (100 Pa) with respect to the Young's modulus of the solid phase E_s (10^4 Pa). The Poisson's ratios ν_s and ν_{fe} for the solid and the fluid elastic phase respectively have been chosen according to the values that are commonly employed to describe the behavior of a solid (0.3) and a liquid (0.4).

The following parameters belong to the latter group: h , e_{a0} , S_f , S_r , μ_{ff} , μ_{fr} , ω_0 , θ_{∞} , τ_{∞} , p_{obs} , r_{obs} , μ_{obs} , ν_{right} , ν_{left} . The influence of some of these variables has been previously discussed in the paper. Specifically, Fig. 3 and Figs. 6 and 7 show the effects on the final results by changing the values of θ_{∞} , τ_{∞} and μ_{ff} , μ_{fr} respectively (Section 3.1). The area of the frontal adhesion region

S_f and consequently of the rear adhesion surface S_r , has been set assuming that only one pseudopod is involved in the migration process as previously described (Section 2.1). Nevertheless, the influence of the spatial asymmetry between S_f and S_r has been described in Section 3.2. Regarding the 'obstacles': (i) their position and shape (p_{obs} , r_{obs}) have been chosen here to show the ability of the cell to avoid them, although an open or a closed array of 'obstacles' could have been modeled (ii) the value of the friction coefficient μ_{obs} ($10^8 \text{ Pa}\cdot\text{s}/\text{m}$) has been fixed so that the cell is still able to slowly migrate through the sticking region. If such a value is increased (up to $10^{12} \text{ Pa}\cdot\text{s}/\text{m}$), the 'obstacle' behaves as a rigid wall against which the cell repeatedly beats as evocated in Section 3.3. Finally, h , ν_{right} , and ν_{left} have been arbitrarily chosen.

According to the previous remarks, the sensitivity analysis has been performed by letting vary of $\pm 10\%$ and one by one the following parameters for three specific simulations: (1) E_{fe} , μ_{fr} and e_{a0} for the symmetric migration (Section 3.1), (2) S_r for the asymmetric migration (Section 3.2), (3) ω_0 for the symmetric migration with distance sensor (Section 3.3.2) (Table 2).

When we compare the results with the ones obtained for the original simulations we can notice that

- in general, the total covered distance is not affected by the slight change of the parameters, except for the case of the cyclic active strain e_{a0} . Obviously, the higher e_{a0} , the higher the covered distance (up to $1.2 \times 10^{-4} \text{ m}$);
- for the symmetric migration
 - (1) E_{fe} and μ_{fr} slightly affect the values of the maximal velocities (maximal variation of $+0.02 \times 10^{-7} \text{ m/s}$ and of $+0.01 \times 10^{-7} \text{ m/s}$ for the frontal and the rear velocities respectively) and the maximal resultants of adhesion forces (maximal variation of $+0.3 \times 10^{-13} \text{ N}$ and of $\pm 0.2 \times 10^{-13} \text{ N}$ for the frontal and rear forces respectively);
 - (2) the maximal velocities and the resultants of the adhesion forces are rather affected by the slight change of e_{a0} (maximal variation of $+0.09 \times 10^{-7} \text{ m/s}$ and of $+0.11 \times 10^{-7} \text{ m/s}$ for the frontal and rear adhesion respectively; maximal variation of $+1.7 \times 10^{-13} \text{ N}$ and of $+1.8 \times 10^{-13} \text{ N}$ for the frontal and rear adhesion forces respectively);
- for the asymmetric migration: reducing the rear adhesion surface S_r mostly influences the maximal resultants of the adhesion forces (maximal variation of $+0.9 \times 10^{-13} \text{ N}$ and of $+0.4 \times 10^{-13} \text{ N}$ for the frontal and the rear forces respectively),

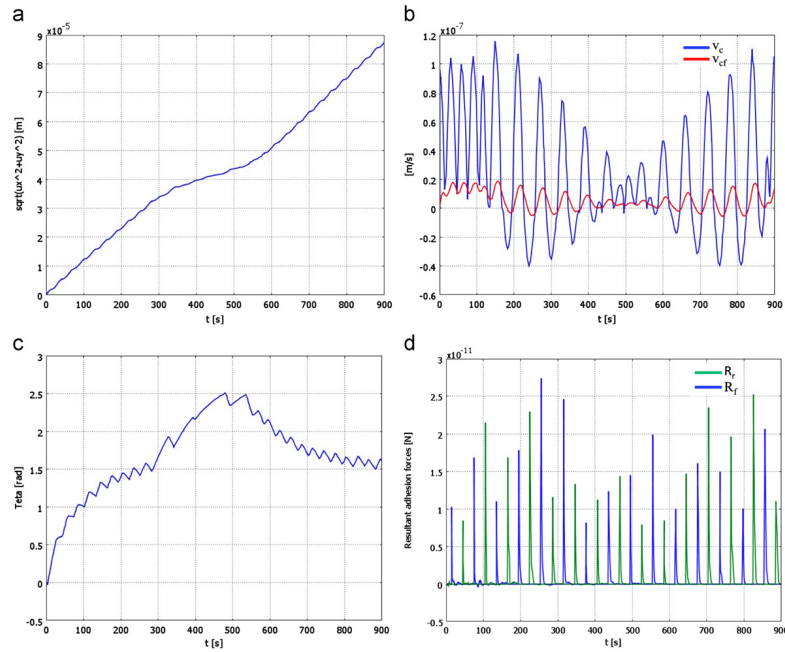


Fig. 13. Different plots for the simulation of symmetric migration and the cell equipped with a velocity sensor (Section 3.3.1): cell displacement (a), cell velocity (b), θ (c) and adhesion forces at the rear (green) and at the front of the cell (blue) (d). (For interpretation of the references to color in this figure legend, the reader is referred to the web version of this article).

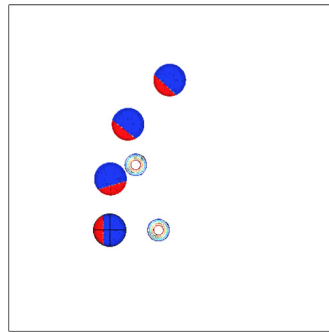


Fig. 14. Successive phases ($t=0$, $t=300$ s, $t=600$ s and $t=900$ s) for the simulation of symmetric migration and cell equipped with a distance sensor (Section 3.3.2). The 'obstacles' p_1 and p_2 are represented by their isovalues. In red the anterior and the posterior regions of adhesion. (For interpretation of the references to color in this figure legend, the reader is referred to the web version of this article).

but not so much the maximal velocities (-0.02×10^{-7} m/s and $+0.03 \times 10^{-7}$ m/s for the frontal and rear adhesion respectively),

– for the symmetric migration with a distance sensor: the variation of ω_0 has a major impact on the resultant of the frontal adhesion force ($+1.05 \times 10^{-13}$ N), while a smaller change is observed for the maximal frontal and rear velocities.

To conclude, the sensitivity analysis shows that the variation of specific parameters may slightly influence the results, but it does not affect the fundamental principles of the mechanical model.

4. Discussion

In this paper, we have proposed a 3D continuum finite element model of an amoeboid cell migrating over a plane surface. We have mainly focused on the mechanical aspects of the problem, without considering the chemical, molecular or genetic functions that may regulate the behavior of the cell. Then, the movement of the cell takes place according to force and torque balances only.

The migration process occurs in a cyclic manner as in the amoeboid cells. In this work, the geometry of the cell has been simplified with respect to the reality so that there is only one pseudopod that triggers the protrusion of the whole body. The model is equipped with a pulsating movement inside a viscoelastic material (Sections 2.2 and 2.3). In order for the cell to move forward, an intricate synchronization between the adhesion forces at the anterior and the posterior edge of the cell and the protrusion–contraction phases is necessary. Furthermore, if the strength of the adhesion at

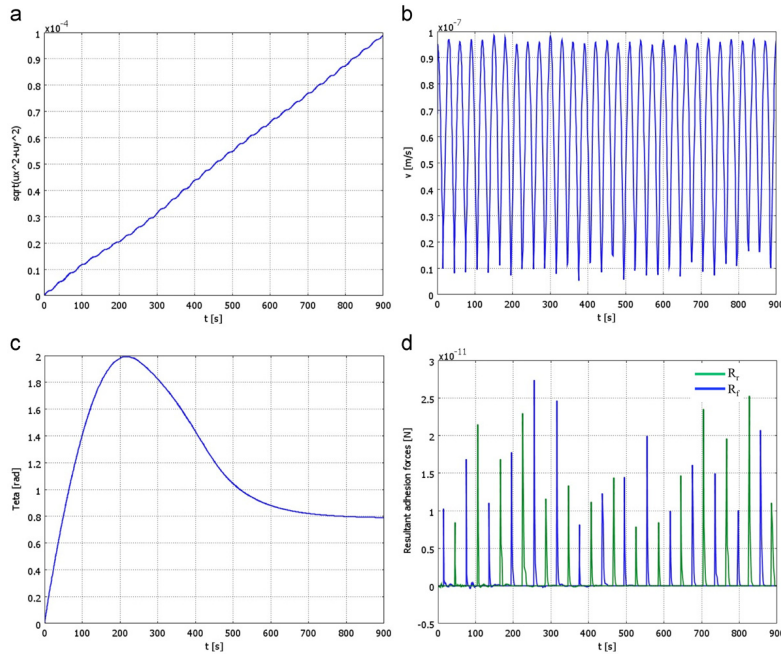


Fig. 15. Different plots for the simulation of symmetric migration and the cell equipped with a distance sensor (Section 3.3.2): cell displacement (a), cell velocity (b), θ (c) and adhesion forces at the rear (green) and at the front of the cell (blue) (d). (For interpretation of the references to color in this figure legend, the reader is referred to the web version of this article.)

Table 2

Parameter	Value	Covered distance	Maximal protrusion velocity	Maximal contraction velocity	Maximal resultant of the frontal adhesion forces	Maximal resultant of the rear adhesion forces
E_c (symmetric migration)	90 Pa	1.09×10^{-4} m	0.95×10^{-7} m/s	0.96×10^{-7} m/s	7.3×10^{-13} N	7.6×10^{-13} N
	100 Pa (original value)	1.09×10^{-4} m	0.94×10^{-7} m/s	0.96×10^{-7} m/s	7.3×10^{-13} N	7.7×10^{-13} N
	110 Pa	1.09×10^{-4} m	0.95×10^{-7} m/s	0.95×10^{-7} m/s	7.6×10^{-13} N	7.8×10^{-13} N
μ_p (symmetric migration)	2.7×10^5 Pa-s	1.09×10^{-4} m	0.95×10^{-7} m/s	0.96×10^{-7} m/s	7.2×10^{-13} N	7.5×10^{-13} N
	3×10^5 Pa-s (original value)	1.09×10^{-4} m	0.94×10^{-7} m/s	0.96×10^{-7} m/s	7.3×10^{-13} N	7.7×10^{-13} N
	3.3×10^5 Pa-s	1.09×10^{-4} m	0.96×10^{-7} m/s	0.97×10^{-7} m/s	7.3×10^{-13} N	7.6×10^{-13} N
ϵ_{a0} (symmetric migration)	0.45	0.98×10^{-4} m	0.86×10^{-7} m/s	0.85×10^{-7} m/s	5.7×10^{-13} N	6×10^{-13} N
	0.5 (original value)	1.09×10^{-4} m	0.94×10^{-7} m/s	0.96×10^{-7} m/s	7.3×10^{-13} N	7.7×10^{-13} N
	0.55	1.2×10^{-4} m	1.05×10^{-7} m/s	1.04×10^{-7} m/s	9×10^{-13} N	9.5×10^{-13} N
S_c (asymmetric migration)	4.05×10^{-12} m ²	1.3×10^{-4} m	1.37×10^{-7} m/s	0.94×10^{-7} m/s	5.9×10^{-11} N	5.7×10^{-11} N
	4.5×10^{-12} m ² (original value)	1.3×10^{-4} m	1.38×10^{-7} m/s	0.92×10^{-7} m/s	5×10^{-11} N	5.3×10^{-11} N
	4.95×10^{-12} m ²	1.3×10^{-4} m	1.35×10^{-7} m/s	0.95×10^{-7} m/s	5.3×10^{-11} N	5.2×10^{-11} N
ω_0 (symmetric migration with distance sensor)	0.018 rad/s	1.02×10^{-4} m	0.98×10^{-7} m/s	0.97×10^{-7} m/s	2.35×10^{11} N	2.5×10^{11} N
	0.02 rad/s (original value)	10^{-4} m	10^{-7} m/s	10^{-7} m/s	2.75×10^{11} N	2.52×10^{11} N
	0.022 rad/s	0.98×10^{-4} m	0.99×10^{-7} m/s	0.99×10^{-7} m/s	3.8×10^{11} N	2.9×10^{11} N

the front or at the rear of the cell is not high enough to let the cell adhere to the underneath 2D surface, the cell only vibrates in place without progressing much (Sections 2.4 and 2.5). Additionally, chemotaxis effects are taken into account, without introducing any coupling between mechanics and chemicals, so that the cell directs its movement towards an attracting source (Section 2.6).

As a first attempt, the anterior and the posterior regions of adhesion have been considered spatially symmetric (Section 3.1), but in Section 3.2 we show that when the rear surface is smaller than the frontal one, the cell is able to cover a larger distance than in the previous case. This simulation confirms the experimental observations according to which the adhesion strength has to be stronger at the front and weaker at the back.

Finally, we have considered heterogeneous 2D substrates (Section 2.7) characterized by 'obstacles' that the cell needs to avoid in order to reach the attracting source in the shortest time possible. These 'obstacles' are defined by regions in which the sticking force is greater than in the rest of the substrate. Therefore, we have introduced two regions where the sticking force is increased with respect to the rest of the substrate. Two different methods have been used to test this type of simulation. In the first approach, we have equipped the cell with a velocity sensor so that as soon as its velocity of migration decreases, it interprets such signal as an input to turn left or right in order to avoid the 'obstacle' (Section 3.3.1). In the second approach, the cell is equipped with a distance sensor (Section 3.3.2). Therefore, it is able to see the 'obstacle' from far and to plan its path in advance. From a numerical point of view the second technique is more stable than the first one. However, from a biological standpoint, the velocity sensor probably allows one to successfully reproduce the behavior of the cell, which in fact blindly gropes the substrate little by little and suddenly changes its direction of migration.

The numerical model allows to successfully simulate the migration of the 3D cell over a 2D surface. The cyclic phenomenon of locomotion is reproduced and the results obtained from the simulations seem to concur with the experimental observations and data from the literature. Therefore, we may conclude that cell mechanics constitutes an important, if not essential, factor in cell migration. At this stage, the robustness of the model and the numerical approach have been highly tested so that further improvements can be considered.

As a perspective, we would like in fact to consider new aspects such as

- (1) the presence of several pseudopods which will allow us to take into account the randomness in the direction of migration;
- (2) a more proper topology of the biological system which will include the nucleus as well as the actin filaments and the cytoskeleton. The mechanical properties of the cell will then change according to these constitutive elements;
- (3) chemical reactions can be implemented in the model to regulate the active deformations of the cell, as we have already presented in our previous work (Allena et al., 2011). We will explore the coupling between mechanics and chemicals and how the physico-chemical signals inside the cell regulate the protrusion–contraction deformations;
- (4) finally, we would like to simulate the migration of the 3D cell through a 3D extracellular matrix.

References

Adachi, T., Okeyo, K.O., Shitagawa, Y., Hojo, M., 2009. Strain field in actin filament network in lamellipodia of migrating cells: implication for network reorganization. *J. Biomech.* 42, 297–302.

Allena, R., Mourouval, A.-S., Aubry, D., 2010. Simulation of multiple morphogenetic movements in the *Drosophila* embryo by a single 3D finite element model. *JMBBM* 3, 313–323.

Allena, R., Muñoz, J., Aubry, D., 2011. Diffusion–Reaction Model For *Drosophila* Embryo Development. *CMBBE*.

Alt, W., Tranquillo, R., 1995. Basic morphogenetic system modeling shape changes of migrating cells: how to explain fluctuating lamellipodial dynamics. *J. Biol. Syst.* 3, 905–916.

Alt, W., Dembo, M., 1999. Cytoplasm dynamics and cell motion: two-phase flow models. *Math. Biosci.* 156, 207–228.

Auffray, C., Fogg, D., Garfa, M., Elain, G., Join-Lambert, O., Kaval, S., Sarnacki, S., Cumano, A., Lauvau, G., Geissmann, F., 2007. Monitoring of blood vessels and tissues by a population of monocytes with patrolling behavior. *Science* 317, 666–670.

Bausch, A., Möller, W., Sackmann, E., 1999. Measurement of local viscoelasticity and forces in living cells by magnetic tweezers. *Biophys. J.* 76, 573–579.

Belytschko, T., Liu, W.K., Moran, B., 2000. *Nonlinear Finite Elements for Continua and Structures*. Wiley.

Bottino, D., Mogilner, A., Roberts, T., Stewart, M., Oster, G., 2002. How nematode sperm crawl. *J. Cell Sci.* 115, 367–384.

Boulbitch, A., Guttenberg, Z., Sackmann, E., 2001. Kinetics of membrane adhesion mediated by ligand–receptor interaction studied with a biomimetic system. *Biophys. J.* 81, 2743–2751.

Carlsson, A.E., Sept, D., 2008. Mathematical modeling of cell migration. *Methods Cell Biol.* 84, 911–937.

Charest, P.G., Firtel, R.A., 2007. Big roles for small GTPases in the control of directed cell movement. *Biochem. J.* 401, 377–390.

DiMilla, P.A., Barbee, K., Lauffenburger, D.A., 1991. Mathematical model for the effects of adhesion and mechanics on cell migration speed. *Biophys. J.* 60, 15–37.

Dong, C., Slattery, M.J., Rank, B.M., You, J., 2002. In vitro characterization and micromechanics of tumor cell chemotactic protrusion, locomotion and extravasation. *Ann. Biomed. Eng.* 30, 344–355.

Drury, J., Dembo, M., 2001. Aspiration of human neutrophils: effects of shear thinning and cortical dissipation. *Biophys. J.* 81, 3166–3177.

Erban, R., Othmer, H.G., 2006. Taxis equations for amoeboid cells. *J. Math. Biol.* 54, 847–885.

Flaherty, B., McGarry, J.P., McHug, P.E., 2007. Mathematical models of cell motility. *Cell Biochem. Biophys.* 49, 14–28.

Friedl, P., Wolf, K., 2010. Plasticity of cell migration: a multiscale tuning model. *J. Cell Biol.* 188, 11–19.

Fukui, Y., Uyeda, T.Q.P., Kitayama, C., Inoue, S., 2000. How well can an amoeba climb? *PNAS* 97, 10020–10025.

Gracheva, M.E., Othmer, H.G., 2004. A continuum model of motility in amoeboid cells. *Bull. Math. Biol.* 66, 167–193.

Gupton, S.L., Waterman-Storer, C.M., 2006. Spatiotemporal feedback between actomyosin and focal-adhesion systems optimizes rapid cell migration. *Cell* 125, 1361–1374.

Holzappel, G.A., 2000. *Nonlinear Solid Mechanics. A Continuum Approach for Engineers*. Wiley Sons Ltd.

Krummel, M.F., Macara, I., 2006. Maintenance and modulation of T cell polarity. *Nat. Immunol.* 7, 1143–1149.

Kruse, K., Joanny, J.F., Julicher, F., Prost, J., 2006. Contractility and retrograde flow in lamellipodium motion. *Phys. Biol.* 3, 130–137.

Kuusela, E., Alt, W., 2009. Continuum model of cell adhesion and migration. *J. Math. Biol.* 58, 135–161.

Lämmermann, T., Sixt, M., 2009. Mechanical modes of 'amoeboid' cell migration. *Curr. Opin. Cell Biol.* 21, 636–644.

Larripa, K., Mogilner, A., 2006. Transport of a 1D viscoelastic actin–myosin strip of gel as a model of a crawling cell. *Phys. A: Stat. Mech. Applications* 372, 113–123.

Lauffenburger, D.A., Horwitz, A.F., 1996. Cell migration: a physically integrated molecular process. *Cell* 84, 359–369.

Laurent, V.M., Kasas, S., Yersin, A., Schäffer, T.E., Catsicas, S., Dieter, G., Verkhovsky, A.B., Meister, J.J., 2005. Gradient of rigidity in the lamellipodia of migrating cells revealed by atomic force microscopy. *Biophys. J.* 89, 667–675.

Lim, C.H., Zhou, E.H., Quek, S.T., 2006. Mechanical models for living cells. A review. *J. Biomech.* 39, 195–216.

Lubarda, V.A., 2004. Constitutive theories based on the multiplicative decomposition of deformation gradient: Thermoelasticity, elastoplasticity, and biomechanics. *Appl. Mech. Rev.* 57, 95–108.

Meili, R., Alonso-Latorre, B., del Alamo, J.C., Firtel, R.A., Lasheras, J.C., 2010. Myosin II is essential for the spatiotemporal organization of traction forces during cell motility. *Mol. Cell Biol.* 21, 405–417.

Mogilner, A., Verzi, D.W., 2003. A simple 1-D physical model for the crawling nematode sperm cell. *J. Stat. Phys.* 110, 1169–1189.

Mogilner, A., Rubinstein, B., 2005. The physics of filopodial protrusion. *Biophys. J.* 89, 782–795.

Mogilner, A., 2009. Mathematics of cell motility: have we got its number? *J. Math. Biol.* 58, 105–134.

Muñoz, J., et al., 2007. A deformation gradient decomposition method for the analysis of the mechanics of morphogenesis. *J. Biomech.* 40, 1372–1380.

Okeyo, K.O., Adachi, T., Sunaga, J., Hojo, M., 2009. Actomyosin contractility spatiotemporally regulates actin network dynamics in migrating cells. *J. Biomech.* 42, 2540–2548.

Oster, G.F., Perelson, A.S., 1987. The physics of cell motility. *J. Cell Sci. Suppl.* 8, 35–54.

- Papoulis, A., 1977. *Signal Analysis*. Mc Graw Hill, New York.
- Phillipson, M., Heit, B., Colarusso, P., Liu, L., Ballantyne, C.M., Kubes, P., 2006. Intraluminal crawling of neutrophils to emigration sites: a molecularly distinct process from adhesion in the recruitment cascade. *J. Exp. Med.* 203, 2569–2575.
- Rodriguez, E.K., Hoger, A., McCulloch, A.D., 1994. Stress-dependent finite growth in soft elastic tissues. *J. Biomech.* 27, 455–46.
- Rubinstein, B., Jacobson, K., Mogilner, A., 2005. Multiscale two-dimensional modeling of a motile simple-shaped cell. *Multiscale Model. Simulation* 3, 413–439.
- Rubinstein, B., Fournier, M.F., Jacobson, K., Verkhovsky, A.B., Mogilner, A., 2009. Actin-myosin viscoelastic flow in the keratocyte lamellipod. *Biophys. J.* 97, 1853–1863.
- Sakamoto, Y., Prudhomme, S., Zaman Viscoelastic, M.H., 2011. Gel-Strip model for the simulation of migrating cells. *Ann. Biomed. Eng.* 39, 2735–2749.
- Schaub, S., Bohnet, S., Laurent, V.M., Meister, J.J., Verkhovsky, A.B., 2007. Comparative maps of motion and assembly of filamentous actin and myosin II in migrating cells. *Mol. Biol. Cell* 18, 3723–3732.
- Sheetz, M.P., Felsenfeld, D., Galbraith, C.G., Choquet, D., 1999. Cell migration as a five-step cycle. *Biochem. Soc. Symp.* 65, 233–243.
- Shulman, Z., Shinde, V., Klein, E., Grabovsky, V., Yeger, O., Geron, E., Montresor, A., Bolomini-Vittori, M., Feigelson, S.W., Kirchhausen, T., et al., 2009. Lymphocyte crawling and transendothelial migration require chemokine triggering of high-affinity LFA-1 integrin. *Immunity* 30, 384–396.
- Smith, A., Carrasco, Y.R., Stanley, P., Kieffer, N., Batista, F.D., Hogg, N., 2005. A talin-dependent LFA-1 focal zone is formed by rapidly migrating T lymphocytes. *J. Cell Biol.* 170, 141–151.
- Stéphanou, A., Tracqui, P., 2002. Cytomechanics of cell deformations and migration: from models to experiments. *C. R. Biol.* 325, 295–308.
- Stolarska, M.A., Kim, Y., Othmer, H.G., 2009. Multi-scale models of cell and tissue dynamics. *Philos. Trans. R. Soc. A-Math. Phys. Eng. Sci.* 367, 3525–3553.
- Taber, L.A., 1995. Biomechanics of growth, remodeling and morphogenesis. *Appl. Mech. Rev.* 48, 487–545.
- Taber, L.A., 2004. *Nonlinear Elasticity: Applications in Biomechanics*. World Scientific Publ.
- Taber, L.A., Shi, Y., Yang, L., Bayly, P.V., 2011. A poroelastic model for cell crawling including mechanical coupling between cytoskeletal contraction and actin polymerization. *J. Mech. Mater. Struct.* 6, 569–589.
- Veksler, A., Gov, N.S., 2007. Phase transitions of the coupled membrane-cytoskeleton modify cellular shape. *Biophys. J.* 93, 3798–3810.
- Vicente-Manzanares, M., Ma, X.F., Adelstein, R.S., Horwitz, A.R., 2009. Non-muscle myosin II takes centre stage in cell adhesion and migration. *Nat. Rev. Mol. Cell Biol.* 10, 778–790.
- Wilson, C.A., Tsuchida, M.A., Allen, G.M., Barnhart, E.L., Applegate, K.T., Yam, P.T., Ji, L., Keren, K., Danuser, G., Theriot, J.A., 2010. Myosin II contributes to cell-scale actin network treadmilling through network disassembly. *Nature* 465, 373–U137.
- Yam, P.T., Wilson, C.A., Ji, L., Hebert, B., Barnhart, E.L., Dye, N.A., Wiseman, P.W., Danuser, G., Theriot, J.A., 2007. Actin-myosin network reorganization breaks symmetry at the cell rear to spontaneously initiate polarized cell motility. *J. Cell Biol.* 178, 1207–1221.
- Young, J., Mitran, S.A., 2010. Numerical model of cellular blebbing: a volume-conserving, fluidstructure interaction model of the entire cell. *J. Biomech.* 43, 210–220.
- Zaman, M.H., Kamm, R.D., Matsudaira, P., Lauffenburger, D.A., 2005. Computational model for cell migration in three-dimensional matrices. *Biophys. J.* 89, 1389–1397.
- Zhu, C., Skalak, R., 1988. A continuum model of protrusion of pseudopod in leukocytes. *Biophys. J.* 54, 1115–1137.

3.4 Single cell migration with multiple pseudopodia

In the initial model presented above, the cell migrates by protruding its entire leading edge towards the attractant source. However, most real cells protrude several pseudopodia (or ‘false feet’), which are temporary and spontaneous projections of the cytoplasm that form at random sites of the cell. Pseudopodia are essential for cell movement since they determine the trajectory, the direction and the speed of the cell. Also, adjacent cells may coordinate pseudopodia extensions to contribute to collective cell migration (56) or contact guidance (57). Pseudopodia can be classified as lobopodia, lamellipodia or filipodia according to their size, shape, structure and mode of working. External cues may then control the time and the position on the cell boundary where the pseudopod will form, but growth time and length of the pseudopodia are independent properties of the false feet (58–60). In general, the cells may employ two strategies to protrude their pseudopodia: i) the ‘temporal sensing’ strategy by which the cell ‘sniffs’ the surroundings by extending different pseudopodia and only the one that receives a positive input will become the new leading edge (61) or ii) the ‘spatial sensing’ strategy by which the cell senses the simultaneous external signals introduced in its environment and, as a result, only one pseudopod is formed on the side that corresponds to the higher concentration of chemoattractant or in the direction of the most attractive signal. In this case, the cell adopts a polarized shape, with one false foot and a tail (62).

Despite the interesting and encouraging results presented in Sec. 3.3, I propose here an improvement on the previous model in order to have an even more realistic simulation of single cell migration and to be able to reproduce the behaviour of different types of cells. The main assumptions presented in Sec. 3.2 are maintained, but now the cell produces multiple pseudopodia to move forward on the substrate.

Included Paper:

Allena R (2013) Cell migration with multiple pseudopodia: temporal and spatial sensing models. *Bull Math Biol* 75(2):288–316.

Cell Migration with Multiple Pseudopodia: Temporal and Spatial Sensing Models

Rachele Allena

Received: 29 June 2012 / Accepted: 20 December 2012
© Society for Mathematical Biology 2013

Abstract Cell migration triggered by pseudopodia (or “false feet”) is the most used method of locomotion. A 3D finite element model of a cell migrating over a 2D substrate is proposed, with a particular focus on the mechanical aspects of the biological phenomenon. The decomposition of the deformation gradient is used to reproduce the cyclic phases of protrusion and contraction of the cell, which are tightly synchronized with the adhesion forces at the back and at the front of the cell, respectively. First, a steady active deformation is considered to show the ability of the cell to simultaneously initiate multiple pseudopodia. Here, randomness is considered as a key aspect, which controls both the direction and the amplitude of the false feet. Second, the migration process is described through two different strategies: the temporal and the spatial sensing models. In the temporal model, the cell “sniffs” the surroundings by extending several pseudopodia and only the one that receives a positive input will become the new leading edge, while the others retract. In the spatial model instead, the cell senses the external sources at different spots of the membrane and only protrudes one pseudopod in the direction of the most attractive one.

Keywords Cell migration · Pseudopodia · Computational mechanics · Temporal and spatial model

1 Introduction

Many biological phenomena such as embryonic development, wound healing, and immune responses require the orchestrated movement of cells in particular direc-

Electronic supplementary material The online version of this article (doi:[10.1007/s11538-012-9806-1](https://doi.org/10.1007/s11538-012-9806-1)) contains supplementary material, which is available to authorized users.

R. Allena (✉)
Arts et Metiers ParisTech, LBM, 151 bd de l'hôpital, 75013 Paris, France
e-mail: rachele.allena@ensam.eu

Published online: 15 January 2013

 Springer

tions and to specific locations. Errors during these processes may have serious consequences like vascular diseases, tumorigenesis, or metastasis. Nowadays, it is still unclear how exactly cell motility occurs. Therefore, a complete understanding of the mechanisms governing cell migration may lead to the development of novel therapeutic strategies for controlling, for example, invasive tumor cells.

1.1 Pseudopodia Characteristics

The most primitive and most used type of locomotion is the one occurring with the support of pseudopodia (or “false feet”), which are a temporary and spontaneous projection of the cytoplasm that form at random sites of the cell’s surface by structural reorganization of the actin-myosin network.

The protrusion and the contraction of the pseudopodia are triggered by the polymerization of actin gels (Borisy and Svitkina 2000) and the depolymerization of actin-myosin motors, respectively (Jay et al. 1995; Merkel et al. 2000). Pseudopodia are essential for cell movement since they determine the trajectory, the direction, and the speed of the cell. Also, adjacent cells may coordinate pseudopodia extensions to contribute to collective cell migration (Van Haastert 2010) or contact guidance (Weijer 2009).

There is a considerable variability in size, shape, structure, and mode of working of pseudopodia, on the basis of which they can be grouped into three main categories as follows:

- (1) lobopodia: these are blunt relatively short or finger-like, rarely branched pseudopodia;
- (2) lamellipodia: these are broad and flat appendages mainly made of cytoplasm;
- (3) filipodia: these are rod-like and filamentous extensions often with rounded ends.

Pseudopodia formation is triggered by different types of external signals: chemicals (chemotaxis) (Hoeller and Kay 2007; Weiner 2002) or temperature (thermotaxis) gradients, electric fields (Bahat and Eisenbach 2006; Zhao 2009), or surface heterogeneity (durotaxis). Such external cues may then control the time and the position at the cell boundary where the pseudopod will form, but growth time and length of the pseudopodia are instead independent properties of the false feet (Andrew and Insall 2007; Bosgraaf and Van Haastert 2009a; Karsenti 2008). In order to elucidate how the cell senses the external attractants, two models are generally used. In the temporal sensing model, the cell “sniffs” the surroundings by extending different pseudopodia and only the one that receives a positive input will become the new leading edge (Gerish et al. 1974). In the spatial sensing model instead, the cell senses at different points along the membrane the chemical gradient or the simultaneous external signals introduced in its environment. As a result, only one pseudopod is formed on the side that corresponds to the higher concentration of chemoattractant or in the direction of the most attractive signal. In this case, the cell adopts a polarized shape, with one false foot and a tail (Zigmond et al. 1981).

It has been shown that from an energetical point of view the pseudopodia are more likely to extend perpendicular to the cell membrane (Mogilner and Oster 1996). Therefore, when migration occurs in chemotactic gradients, pseudopodia do not bend

in the direction of the gradient. To move toward a gradient, the cell needs to develop further pseudopodia at the side closest to the gradient. Additionally, chemotaxis properly occurs when the cell presents a smooth ellipsoid shape. Cells with very irregular shapes show, in fact, poor chemotaxis since pseudopodia form in many different directions (Van Haastert and Bosgraaf 2009).

In general, cells may extend the pseudopodia in two different ways (Andrew and Insall 2007): either by splitting an existing pseudopod or by extending the membrane from areas of the cells not previously active (often referred to as “lateral” or *de novo* pseudopodia because they appear at the side and in the rear of the cell, Bosgraaf and Van Haastert 2009a). In the first case, few ruffles appear at the base of the existing pseudopod that successively becomes a major pseudopod to which the cell body flows (one way split). Rarely, such a division leads to two equivalent extensions resulting in a Y-shape, one of which can remain active while the other retracts. In the second case, the new pseudopodia start as very lean protrusions that dilate as soon as they include the cell body. Previous studies have shown that the angle between two splitting pseudopodia is approximately 55° and that very often a split to the right is followed by a split to the left and vice versa, which leads to a zig-zag trajectory (Bosgraaf and Van Haastert 2009a). On the contrary, pseudopodia that form *de novo* may protrude in any direction without any preference relative to the left or right previous or next pseudopod, which induces a random trajectory.

As it has been observed (Gail and Boone 1970; Patlak 1953; Potel and Mackay 1979), the cell tends to robustly preserve the orientation of motion under perturbations of the external signal. Thus, it migrates with persistence in a given direction and the persistence time depends on the ratio of splitting and formation of new pseudopodia. Weak chemical gradients do not significantly affect the frequency, the dimensions, and the lifetime of the pseudopodia, which mostly follow a self-organization (Andrew and Insall 2007; Bosgraaf and Van Haastert 2009a). The external signals have then three main consequences on the cell behavior:

- (1) selective retraction: the cell usually migrates using only one pseudopod at the time. Thus, in the presence of more than one false foot, they all retract but the one which is the best oriented toward the attractant;
- (2) oriented extension: in general, more pseudopodia are initialized in the direction of the external cue, which results then in the formation of successive pseudopodia that may be closer or farther according to the position of the cue;
- (3) suppression of *de novo* pseudopodia by which the persistence time is increased.

1.2 Experimental and Numerical Approaches

From an experimental point of view, two different strategies have been used in the last decades to better understand how cells respond and behave in the presence of chemical gradients. The first approach (signal based approach) consists in exposing the cell to a gradient of chemoattractant and subsequently identifying and analyzing the signaling pathways and molecules involved in the migration process and that are in control of the oriented movement of the cell (Franca-Koh et al. 2006; Insall 2010; King and Insall 2009; Merlot and Firtel 2003; Schneider and Haugh 2006). The second and more recent approach (pseudopod based approach) focuses on how

cells form and extend the pseudopodia and the acquired information are afterward related to what is already known about the established signaling patterns (Andrew and Insall 2007; Arrieumerlou and Meyer 2005; Bosgraaf and Van Haastert 2009a; Insall 2010; Li et al. 2008; Takagi et al. 2008).

From a numerical point of view, several studies have been proposed in the literature in order to decipher the mechanism by which the cell membrane protrude and extend. Two main approaches have been used to model cell migration: micro/nanostructural and continuum approaches (Lim et al. 2006). While the former considers the cytoskeleton as the principle actor of cell motility and try to investigate the mechanical processes which regulate it, the latter mostly focuses on a macroscale description of the cellular structure to take into account the large deformations of the membrane and understand how stresses and strains are distributed (Bottino et al. 2002; Mogilner and Verzi 2003; Rubinstein et al. 2005).

There exist at least four main hypotheses that have been largely explored in the last decades: (i) calcium concentration regulates the expansion and the contraction of the actin network through a sol/gel transition (Oster 1984), (ii) actin polymerization triggered by random thermal fluctuations in the cell membrane or in the actin filaments is the main promoter of protrusion (Carlier and Pantaloni 1997; Mogilner and Oster 1996; Theriot and Mitchison 1991), (iii) the extension of the cellular membrane is regulated by specific mechanisms at the molecular scale (Alt and Tranquillo 1995; Lee et al. 1993; Mogilner and Rubinstein 2005; Small et al. 1993; Stéphanou et al. 2004; Veksler and Gov 2007), and (iv) hydrostatic pressure generated by cytoplasmic flows inside the cell induces the protrusion of the membrane (Alt and Tranquillo 1995; Bereiter-Hahn and Lüers 1998; Oster and Perelson 1987; Taber et al. 2011; Young and Mitran 2010; Zhu and Skalak 1988). Finally, there are also those models with a significant mechanical component (see review in Carlsson and Sept (2008), Flaherty et al. (2007)), even though most of them are 1D or 2D and only few use a 3D finite element formulation (Rubinstein et al. 2005; Sakamoto et al. 2011; Stolarska et al. 2009; Taber et al. 2011).

The general conclusion is that the protrusion-contraction deformations of the cell are strongly connected to the polymerization-depolymerization processes of the actin network inside the cytoskeleton (Borisy and Svitkina 2000; Carlier and Pantaloni 1997; Condeelis 1993). Additionally, in the last decades, it has been experimentally demonstrated that the existence of the recurring pattern of deformation could be related to a self-organization of spontaneous deformation dynamics inside the cell (Alt 1990; Alt and Tranquillo 1995; Killich et al. 1993; Stéphanou et al. 2004) rather than to significant stimuli from the environment. Although so far very poorly explored, this is a fundamental aspect to consider, which may affect the response of the cell to external signals.

In this paper, a finite element model of a 3D cell migrating over a 2D substrate using pseudopodia is proposed, which is based on the following hypotheses:

- as in previous works (Borisy and Svitkina 2000; Carlier and Pantaloni 1997; Condeelis 1993; Mogilner and Oster 1996; Theriot and Mitchison 1991), the oscillating protrusion-contraction movement of the cell is assumed to be controlled by the cyclic polymerization/depolymerization of the actin network, which may occur at any site along the cell membrane where the actin filaments are concentrated;

- a purely mechanical approach is used to describe the cell behavior as it has been proposed in previous models (Carlsson and Sept 2008; Flaherty et al. 2007; Rubinstein et al. 2005; Sakamoto et al. 2011; Taber et al. 2011). Nevertheless, a different mathematical method is applied. In fact, the decomposition of the deformation gradient is employed to take into account the active elementary strains undergone by the cell (i.e., protrusion and contraction) as well as the elastic deformations generated by the interaction of the cell with the underneath substrate;
- as in Stéphanou et al. (2004), large deformations of the cell membrane are considered which trigger the formation of multiple pseudopodia in response to external attractive sources. Additionally, in the present model, the cell may adopt two different strategies: whether it initiates several simultaneous pseudopodia and then it chooses the one which is the best oriented toward the chemoattractant (temporal sensing model) or it only protrudes one pseudopod in the direction of the external signal (spatial sensing model);
- finally, the protrusion of the pseudopodia and the contraction of the cell body are tightly synchronized with the adhesion forces at the back and at the front, respectively, which actually allow the forward movement of the cell over the substrate.

As similarly as in Allena and Aubry (2012), the main objective is to show that although the chemical, molecular, or genetic functions may play an important role during the biological phenomenon, the cell is strongly governed by fundamental mechanical principles that need to be taken into account (Murray 2003). Furthermore, the model is much more realistic with respect to the previous one (Allena and Aubry 2012) and the adaptability of the numerical formulation allows to reproduce the behavior of different types of cells, which could be a powerful feature for further applications.

2 Modeling of Multiple Pseudopodia

In this section, the main characteristics of the model are described. First, the cell and the pseudopodia geometry together with the constitutive model and the general mechanical framework are described. Second, a pseudopod centered approach in a steady active configuration is used to show the ability of the cell to initiate more than one false foot. Different forms of protrusion are then proposed, which allow obtaining morphologies that are typical of various animal cells.

2.1 Cell and Pseudopodia Geometry

As in Allena and Aubry (2012), the global geometry of the cell is obtained by superposing a cylinder and a spherical cap (Fig. 1a). As mentioned in Sect. 1.2, the protrusion and the contraction of the cell are regulated by the polymerization and depolymerization of the actin filaments, respectively, which are mostly located toward the outmost region of the cell (Schaub et al. 2007) and radially organized (Cramer et al. 1997). Accordingly, the actin network is here represented by an annulus of inner radius r_{annulus} equal to $3 \mu\text{m}$ (Fig. 1b), which is analytically given by

$$\Omega_{\text{annulus}}(\mathbf{p}) = h \circ l_{\text{annulus}}(\mathbf{p}) \quad (1)$$

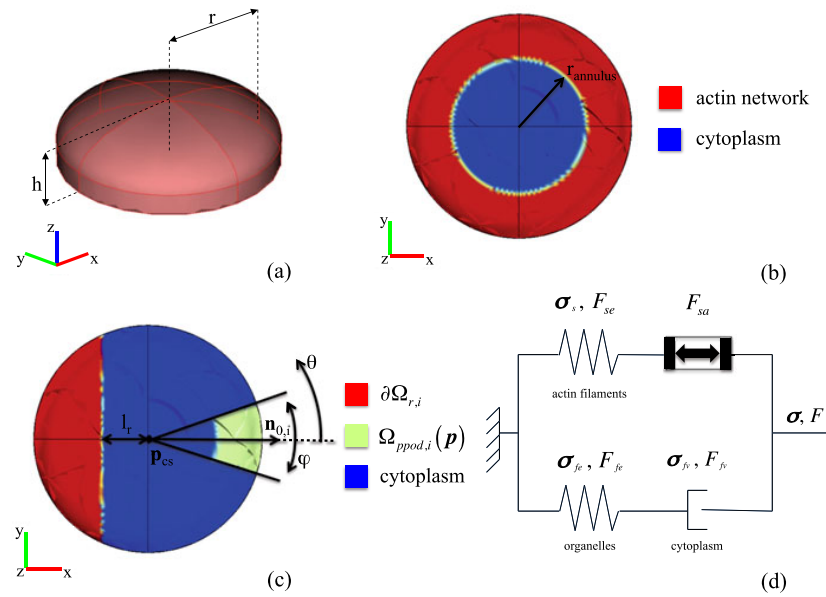


Fig. 1 (a) Geometry of the cell. (b) Top view of the cell at $z = 0$. In red the actin network, which is defined by an annulus of inner radius r_{annulus} , and in blue the cytoplasm. (c) Top view of the cell at $z = 0$. In green the pseudopod domain $\Omega_{\text{ppod},i}(\mathbf{p})$, in red the rear adhesion surface $\partial\Omega_{r,i}$ and in blue the cytoplasm. (d) Sketch of the generalized Maxwell model used to the described the mechanical behavior of the system (Color figure online)

where h is the classical Heaviside function (Eq. (29)) and $l_{\text{annulus}}(\mathbf{p})$ is the level set function of the annulus (Eq. (32)), with \mathbf{p} the initial position of any particle of the cell.

Then a pseudopod can be initiated in any direction and its position is at the intersection between the annulus and a cone of action defined in the x, y plane as

$$\Omega_{\text{cone}}(\mathbf{p}) = h \circ l_{\text{cone},i}(\mathbf{p}) \tag{2}$$

where $l_{\text{cone},i}(\mathbf{p})$ is the level set function of the cone (Eq. (33)) and $i \in \{1, 2, \dots, N\}$ while N is the number of pseudopodia. The cone has an apex angle φ fixed here to $\frac{\pi}{10}$ (Fig. 1c).

Therefore, the pseudopod active domain $\Omega_{\text{ppod},i}(\mathbf{p})$ can be expressed as

$$\Omega_{\text{ppod},i}(\mathbf{p}) = \Omega_{\text{cone},i}(\mathbf{p}) \cdot \Omega_{\text{annulus}}(\mathbf{p}) \tag{3}$$

and it has an initial volume and length along the pseudopod axis $\mathbf{n}_{0,i}$ (Eq. (35), Fig. 1c) of about $10 \mu\text{m}^3$ and $2 \mu\text{m}$, respectively. For the present model, only *de novo* pseudopodia are considered.

2.2 Constitutive Model

As described in Allena and Aubry (2012), all the body forces are neglected, but the inertial effects, which may play an important role, especially during protrusion (Gracheva and Othmer 2004). Thus, the global equilibrium of the system reads

$$\rho \mathbf{a} = \mathbf{Div}_p (J \boldsymbol{\sigma} \mathbf{F}^{-T}) \quad (4)$$

where ρ is the cell density, \mathbf{a} is the acceleration, \mathbf{Div}_p is the divergence with respect to the initial position \mathbf{p} , J is the determinant of the deformation gradient \mathbf{F} and \mathbf{A}^{-T} denotes the inverse transpose of the matrix \mathbf{A} (Holzapfel 2000; Taber 2004). A generalized Maxwell model (Larson 1998) (Fig. 1d) is used to describe the Cauchy stress $\boldsymbol{\sigma}$ and the deformation gradient \mathbf{F} as follows:

$$\begin{aligned} \boldsymbol{\sigma} &= \boldsymbol{\sigma}_s + \boldsymbol{\sigma}_f \\ \mathbf{F} &= \mathbf{D}_p \mathbf{u} + \mathbf{I} = \mathbf{F}_s = \mathbf{F}_f \end{aligned} \quad (5)$$

where $\mathbf{D}_p \mathbf{u} = \sum_{m=1}^3 \frac{\partial \mathbf{u}}{\partial p_m} \otimes \mathbf{i}_m$, with \mathbf{u} the displacement and \mathbf{I} the identity matrix, respectively (Holzapfel 2000; Taber 2004). The indices s and f indicate the solid (actin filaments) and the fluid viscoelastic (cytoplasm with embedded organelles) phase, respectively.

As in previous works (Allena et al. 2010; Balan and Tsakmakis 2002; Bonet 2001; Lubarda 2004; Muñoz et al. 2007), the decomposition of the deformation gradient is employed to define both \mathbf{F}_s and \mathbf{F}_f as follows:

$$\begin{aligned} \mathbf{F}_s &= \mathbf{F}_{se} \mathbf{F}_{sa} \\ \mathbf{F}_f &= \mathbf{F}_{fe} \mathbf{F}_{fv} \end{aligned} \quad (6)$$

In the solid phase, \mathbf{F}_{sa} regulates the active protrusion-contraction movement of the cell and \mathbf{F}_{se} controls the stress generation inside the mechanical system. In the fluid phase, \mathbf{F}_{fe} and \mathbf{F}_{fv} represent the fluid elastic and the viscoelastic deformation, respectively.

The solid stress $\boldsymbol{\sigma}_s$ is computed as an isotropic hyperelastic Saint-Venant material and it reads

$$\boldsymbol{\sigma}_s = \frac{1}{J_{se}} \mathbf{F}_{se} \mathbf{S}_{se} \mathbf{F}_{se}^T \quad (7)$$

where J_{se} is the determinant of \mathbf{F}_{se} and \mathbf{S}_{se} is the second Piola–Kirchhoff stress tensor of the solid elastic phase, which is defined as

$$\mathbf{S}_{se} = \lambda_s \text{Tr}(\mathbf{E}_{se}) \mathbf{I} + 2\mu_s \mathbf{E}_{se} \quad (8)$$

with λ_s , μ_s , and \mathbf{E}_{se} are the Lamé's coefficients and the Green–Lagrange strain tensor of the solid elastic phase, respectively.

In the fluid phase, the Cauchy stresses are assumed to be equal so that $\boldsymbol{\sigma}_f = \boldsymbol{\sigma}_{fe} = \boldsymbol{\sigma}_{fv}$. The fluid elastic Cauchy stress $\boldsymbol{\sigma}_{fe}$ is given by an isotropic hyperelastic Saint-Venant model as follows:

$$\boldsymbol{\sigma}_{fe} = \frac{1}{J_{fe}} \mathbf{F}_{fe} \mathbf{S}_{fe} \mathbf{F}_{fe}^T \quad (9)$$

with J_{fe} the determinant of \mathbf{F}_{fe} and \mathbf{S}_{fe} is the second Piola–Kirchhoff stress tensor of the fluid elastic phase and it is given by

$$\mathbf{S}_{fe} = \lambda_{fe} \text{Tr}(\mathbf{E}_{fe})\mathbf{I} + 2\mu_{fe}\mathbf{E}_{fe} \quad (10)$$

where λ_{fe} and μ_{fe} and \mathbf{E}_{fe} are the Lamé's coefficients and the Green–Lagrange strain tensor of the fluid elastic phase, respectively.

Additionally, the deviator of the second Piola–Kirchhoff stress tensor \mathbf{S}_{fe}^D is given by

$$\mathbf{S}_{fe}^D = 2\mu_{fv}\mathbf{D}_{fv} \quad (11)$$

with μ_{fv} the viscosity of the fluid viscous phase and the Eulerian strain rate \mathbf{D}_{fv} expressed as

$$2\mathbf{D}_{fv} = \dot{\mathbf{F}}_{fv}\mathbf{F}_{fv}^{-1} + \mathbf{F}_{fv}^{-T}\dot{\mathbf{F}}_{fv}^T \quad (12)$$

The preceding equation allows determining the evolution law of \mathbf{F}_{fv} , which is numerically integrated.

2.3 Steady Active Protrusion

The active part of the solid deformation gradient \mathbf{F}_s usually defines the protrusion and the contraction of the cell (Allena and Aubry 2012). In this first part of the work, instead only the protrusion phase is taken into account to describe a steady active configuration during which the cell is able to form and extend multiple pseudopodia. As in Allena and Aubry (2012), \mathbf{F}_{sa} is modeled as a uniaxial deformation as

$$\mathbf{F}_{sa} = \sum_{i=1}^N (e_{ap,i}(t)\mathbf{n}_i \otimes \mathbf{n}_i) \quad (13)$$

where \mathbf{n}_i is the normal vector in the actual configuration expressed as Holzzapfel (2000)

$$\mathbf{n}_i = \frac{\mathbf{F}^{-T} \cdot \mathbf{n}_{0,i}}{\|\mathbf{F}^{-T} \cdot \mathbf{n}_{0,i}\|} \quad (14)$$

with $\|\cdot\|$ defining the norm of a vector.

The cyclic component of the protrusion $e_{ap,i}$ can assume here three different forms as follows:

- (1) the active deformation is applied everywhere through a gradient along the axis of the pseudopod $\mathbf{n}_{0,i}$ as follows:

$$e_{ap,i}(t) = e_{ap0}T_p(t)(1 + \alpha p_{d,i}) \quad (15)$$

where t is the time, e_{ap0} is the amplitude of the cyclic active strain, which can be either constant or random, $p_{d,i}$ is defined in Eq. (34) and α is a constant that determines the amplitude of the gradient and it is equal here to 0.8. The duration of the protrusion phase is given by $T_p(t) = h \circ l_p(t)$, where $l_p(t)$ is the level set function defined in Eq. (36), and is equal to half the duration of a migration cycle T_{migr} , which has been fixed here to 60 s (Allena and Aubry 2012; Dong et al. 2002);

- (2) the protrusion is applied only in the pseudopod active domain $\Omega_{\text{ppod},i}(\mathbf{p})$, thus the uniform elongation is expressed as

$$e_{ap,i}(t) = e_{ap0}T_p(t)\Omega_{\text{ppod},i}(\mathbf{p}) \quad (16)$$

- (3) finally a combination of the two previous modes of deformation modes is considered

$$e_{ap,i}(t) = e_{ap0}T_p(t)(1 + \alpha p_{d,i})\Omega_{\text{ppod},i}(\mathbf{p}) \quad (17)$$

As it will be shown later on, each one of these patterns of the active deformation will lead to different final shapes of the cell. This is an interesting aspect of the present work, which simultaneously points out the flexibility of the mechanical formulation and the ability of the model to describe the behavior of various kinds of cell.

3 Migration

In this section, a signal centered approach is employed to describe the migration process of the cell over a 2D substrate. One or more external sources are introduced in the system in response to which the cell initiates one or multiple pseudopodia according to the strategy employed to move forward: the spatial or the temporal sensing model, respectively.

3.1 Temporal Sensing Model

In the temporal sensing model, the cell first explores the environment by simultaneously protruding several pseudopodia. Then the cell adheres to the substrate using only one pseudopod, the best oriented toward the external source, retract the other pseudopodia, and contract the entire body in the direction of the selected pseudopod. Therefore, the solid active deformation gradient \mathbf{F}_{sa} can be expressed as

$$\mathbf{F}_{sa} = \sum_{i=1}^N [\Theta_{\text{crit1},i}(\theta_i)e_{ap,i}(t) + \Theta_{\text{crit1},i}(\theta_i)\Theta_{\text{crit2},i}(\theta_i)\Theta_{\text{crit3},i}(\theta_i)e_{ac,i}(t)]\mathbf{n}_i \otimes \mathbf{n}_i \quad (18)$$

with θ_i the angle of the pseudopod $\Omega_{\text{ppod},i}$ and $e_{ac,i}$ the cyclic deformation for the uniform contraction of the body cell which is defined as

$$e_{ac,i}(t) = e_{ac0}T_c(t) \quad (19)$$

where $T_c(t) = h \circ l_c(t)$ and $l_c(t)$ is the level set function defined in Eq. (36).

During the protrusion phase, the cell may extend multiple pseudopodia, but as experimentally observed (Bosgraaf and Van Haastert 2009a), there has to be a minimal distance between them equal to $\frac{\pi}{36}$. The function $\Theta_{\text{crit1},i}(\theta_i) = h \circ l_{\text{crit1},i}(\theta_i)$, where $l_{\text{crit1},i}(\theta_i)$ is defined in Eq. (37), takes into account such a condition for each pseudopod.

For the contraction to occur, three conditions have to be satisfied:

- (1) $\Theta_{\text{crit1},i}(\theta_i)$ has to be equal to one for at least one pseudopod;

- (2) if $\Theta_{\text{crit}1,i}(\theta_i) = 1$ for more than one pseudopod, then the cell has to evaluate which one among the extended pseudopodia is the best oriented toward the external source, which is defined by its direction $\theta_{\text{source},i}$. Such a criterion has been implemented in the model through the function $\Theta_{\text{crit}2,i}(\theta_i) = h \circ l_{\text{crit}2,i}(\theta_i)$, with $l_{\text{crit}2,i}(\theta_i)$ defined in Eq. (38).
- (3) finally, the direction θ_i of the pseudopod i satisfying conditions (1) and (2) has to be in the same quadrant of $\theta_{\text{source},i}$. The function $\Theta_{\text{crit}3,i}(\theta_i) = h \circ l_{\text{crit}3,i}(\theta_i)$, with $l_{\text{crit}3,i}(\theta_i)$ expressed as in Eq. (39), allows taking into account such an aspect.

If no one of the previous criteria is satisfied for any pseudopod, then the cell will not contract and, therefore, not move forward.

3.2 Spatial Sensing Model

In the spatial sensing model, the cell senses the surroundings at different points of the membrane, but it only protrudes one pseudopod at the time in the direction of the most attractive source.

Let $\tau_{\text{source},i}(t)$ and $\theta_{\text{source},i}$ being the intensity and the direction of each source respectively. Then, $\theta_i = \theta_{\text{source},i \text{ max}}$ with

$$i \text{ max} = \text{Arg} \left\{ \max_i \{ \tau_{\text{source},i} \} \right\} \quad (20)$$

where $i = 1, \dots, N_{\text{source}}$, with N_{source} the total number of external sources.

Thus, the solid active deformation gradient \mathbf{F}_{sa} reads now

$$\mathbf{F}_{sa} = [e_{ap,i}(t) + e_{ac,i}(t)] \mathbf{n}_{i \text{ max}} \otimes \mathbf{n}_{i \text{ max}} \quad (21)$$

3.3 Adhesion Forces

In order for the cell to move forward, some forces are necessary to adhere to the underneath 2D substrate at the leading and at the rear edge of the cell alternatively. The frontal adhesion surface $\partial\Omega_{f,i}$ always coincides with the contact surface between the substrate and the pseudopod selected for the migration in the direction \mathbf{n}_i (area of $5.5 \mu\text{m}^2$, Fig. 1c) and is then defined by

$$\partial\Omega_{f,i}(\mathbf{p}_s) = \partial\Omega_{\text{ppod},i}(\mathbf{p}_s) = \partial\Omega_{\text{cone},i}(\mathbf{p}_s) \cdot \partial\Omega_{\text{annulus}}(\mathbf{p}_s) \quad (22)$$

where

$$\begin{aligned} \partial\Omega_{\text{annulus}}(\mathbf{p}_s) &= h \circ l_{\text{annulus}}(\mathbf{p}_s) \\ \partial\Omega_{\text{cone},i}(\mathbf{p}_s) &= h \circ l_{\text{cone},i}(\mathbf{p}_s) \end{aligned} \quad (23)$$

with $l_{\text{annulus}}(\mathbf{p}_s)$ and $l_{\text{cone},i}(\mathbf{p}_s)$ defined in Eq. (40).

Similarly, for each pseudopod, there exists a rear adhesion surface $\partial\Omega_{r,i}$ (area of $25 \mu\text{m}^2$, Fig. 1c), which reads

$$\partial\Omega_{r,i}(\mathbf{p}_s) = h \circ l_{r,i}(\mathbf{p}_s) \quad (24)$$

with $l_{r,i}(\mathbf{p}_s)$ defined in Eq. (41).

As in Allena and Aubry (2012) and in previous works (Friedl and Gilmour 2009; Phillipson et al. 2006), the adhesion forces are assumed to be viscous forces and they read differently according to the strategy adopted by the cell to migrate.

In the temporal sensing model, they are expressed as follows:

$$\sigma_{f,\text{temp}}(\mathbf{n}_{0,i}) = -\mu_{ff} T_{af}(t) \frac{\partial \mathbf{u}_s}{\partial t} \sum_{i=1}^N [\partial \Omega_{f,i}(\mathbf{u}_s) \Theta_{\text{crit1},i}(\theta_i) \Theta_{\text{crit2},i}(\theta_i) \Theta_{\text{crit3},i}(\theta_i)]$$

on $\partial \Omega_{f,i}$ (25)

$$\sigma_{r,\text{temp}}(\mathbf{n}_{0,i}) = -\mu_{fr} T_{ar}(t) \frac{\partial \mathbf{u}_s}{\partial t} \sum_{i=1}^N [\partial \Omega_{r,i}(\mathbf{u}_s) \Theta_{\text{crit1},i}(\theta_i) \Theta_{\text{crit2},i}(\theta_i) \Theta_{\text{crit3},i}(\theta_i)]$$

on $\partial \Omega_{r,i}$ (26)

with μ_{ff} and μ_{fr} the friction coefficients for the frontal and rear surfaces equal to 10^8 Pa s, respectively, and \mathbf{u}_s the tangential displacement of the cell with respect to the substrate. In this case, the viscous forces are only activated in the pseudopodia for which the three conditions $\Theta_{\text{crit1},i}(\theta_i)$, $\Theta_{\text{crit2},i}(\theta_i)$, and $\Theta_{\text{crit3},i}(\theta_i)$ are simultaneously equal to one.

In the spatial sensing model instead, only one pseudopod is formed at each migration cycle, thus the viscous forces are activated in this selected false foot and in the associated rear region as follows:

$$\sigma_{f,\text{spat}}(\mathbf{n}_{0,i \text{ max}}) = -\mu_{ff} T_{af}(t) \frac{\partial \mathbf{u}_s}{\partial t} \partial \Omega_{f,i \text{ max}}(\mathbf{u}_s) \quad \text{on } \partial \Omega_{f,i \text{ max}} \quad (27)$$

$$\sigma_{r,\text{spat}}(\mathbf{n}_{0,i \text{ max}}) = -\mu_{fr} T_{ar}(t) \frac{\partial \mathbf{u}_s}{\partial t} \partial \Omega_{r,i \text{ max}}(\mathbf{u}_s) \quad \text{on } \partial \Omega_{r,i \text{ max}} \quad (28)$$

As amply discussed and demonstrated in Allena and Aubry (2012), such forces play a fundamental role during the migration process. In fact, the cell would only deform on place if no adhesion force were activated. Therefore, $\sigma_{f,\text{temp}}(\mathbf{n}_{0,i})$, $\sigma_{f,\text{spat}}(\mathbf{n}_{0,i \text{ max}})$, and $\sigma_{r,\text{temp}}(\mathbf{n}_{0,i})$, $\sigma_{r,\text{spat}}(\mathbf{n}_{0,i \text{ max}})$ are perfectly synchronized with the contraction and the protrusion phases through the functions $T_{af}(t) = h \circ l_{af}(t)$ and $T_{ar}(t) = h \circ l_{ar}(t)$, respectively, with $l_{af}(t)$ and $l_{ar}(t)$ defined in Eq. (42). Additionally, a small viscous force is applied over the whole contact surface between the cell and the substrate as the cell constantly lies on the substrate.

4 Results

The numerical simulations have been run using the finite element software COMSOL Multiphysics[®] 3.5a. The cell has an initial geometry with a radius r of 5 μm and a maximal height h along the axis of symmetry of 3 μm . The Young's modulus E_s and the Poisson's ratio ν_s for the solid phase of the model have been chosen uniformly equal to 10^4 Pa (Laurent et al. 2005) and 0.3, respectively. For the fluid phase, E_{fe} and ν_{fe} are equal to 10^2 Pa and 0.4, respectively, while the viscosity μ_{fv} is equal to 3×10^5 Pa s (Bausch et al. 1999; Drury and Dembo 2001). The cell density ρ has been set to 1000 kg/m^3 (Fukui et al. 2000). The main geometrical, material, and mechanical parameters are listed in Table 1.

Table 1 Main geometrical, material, and mechanical parameters

Parameter	Description	Value	Unit	Reference
r	Cell radius	5×10^{-6}	m	
h	Cell height	3×10^{-6}	m	
r_{annulus}	Annulus radius	3×10^{-6}	m	
φ	Cone apex angle	$\frac{\pi}{10}$	rad	
E_s	Young's modulus for the solid phase	10^4	Pa	Laurent et al. (2005)
ν_s	Poisson's ratio for the solid phase	0.3		
E_{fe}	Young's modulus for the fluid-elastic phase	10^2	Pa	
ν_{fe}	Poisson's ratio for the fluid-elastic phase	0.4		
μ_{fv}	Viscosity for the fluid-viscous phase	3×10^5	Pa s	Bausch et al. (1999), Drury and Dembo (2001)
ρ	Cell density	1000	kg/m ³	Fukui et al. (2000)
e_{ap0}	Cyclic active protrusion	0.5		
e_{ac0}	Cyclic active contraction	0.2		
α	Gradient amplitude	0.8		
$\partial\Omega_{f,i}$	Area of frontal region of adhesion	5.5×10^{-6}	m ²	
$\partial\Omega_{r,i}$	Area of rear region of adhesion	25×10^{-6}	m ²	
μ_{ff}	Friction coefficient at the frontal edge	10^8	Pa s/m	
μ_{fr}	Friction coefficient at the rear edge	10^8	Pa s/m	
T_{migr}	Period for migration cycle	60	s	Allena and Aubry (2012), Dong et al. (2002)
	Minimal distance between pseudopodia	$\pm \frac{\pi}{36}$		Bosgraaf and Van Haastert (2009a)
$\theta_{\sigma\text{ov}\rho\chi\varepsilon,t}$	Source direction	Temporal sensing model: $\theta_{\text{source},1} = \frac{\pi}{4}$ Spatial sensing model: $\theta_{\text{source},1} = 0$, $\theta_{\text{source},2} = \frac{2\pi}{3}$, $\theta_{\text{source},3} = \frac{4\pi}{3}$		

4.1 Multiple Pseudopodia

The objective here is to show the ability of the cell to initiate and extend multiple pseudopodia, up to $N = 8$, even though in reality configurations with more than four pseudopodia are rare because very unstable (Stéphanou et al. 2004). In this first series of simulations then, only the protrusion is implemented in the model and the cell does

not migrate but only deforms on place. The cyclic component of the active strain e_{ap0} has been fixed equal to 0.5. As described in Sect. 2.3, several forms of protrusion have been tested.

In the very first row (a:e) of Fig. 2, five different initial configurations are presented at $t = 0$: (a) only one pseudopod ($\theta_1 = 0$), (b) two pseudopodia ($\theta_1 = 0, \theta_2 = \pi$), (c) three pseudopodia ($\theta_1 = 0, \theta_2 = \frac{2\pi}{3}, \theta_3 = \frac{4\pi}{3}$), (d) four pseudopodia ($\theta_1 = 0, \theta_2 = \frac{\pi}{2}, \theta_3 = \pi, \theta_4 = \frac{3\pi}{2}$), and (e) eight pseudopodia ($\theta_1 = 0, \theta_2 = \frac{\pi}{4}, \theta_3 = \frac{\pi}{2}, \theta_4 = \frac{3\pi}{4}, \theta_5 = \pi, \theta_6 = \frac{5\pi}{4}, \theta_7 = \frac{3\pi}{2}, \theta_8 = \frac{7\pi}{4}$). The successive rows (f:j, k:o, p:t) of Fig. 2 represent the magnitude of the deformation at the end of the first protrusion phase (30 s) of the pseudopodia. In Fig. 2 f:j, a gradient of the active deformation is implemented in the whole cell domain along the directions θ_i of the pseudopodia (Eq. (15)). In the case of two (f), four (i), and eight (j) pseudopodia, such a pattern of deformation does not produce realistic false feet, but rather a uniform ellipsoidal (f) or radial (i and j) deformation, and thus an extension of about 5 μm (f), 5 μm (i), and 10 μm (j), respectively. In the case of one pseudopod (f), there is actually a protrusion of the frontal edge of the cell with a maximal elongation of 6 μm , while the rear end seems to contract of about 1 μm . Finally, in the case of three pseudopodia (h), the final protrusion leads to a star-shape configuration very similar to the one observed in fibroblasts (Fig. 3). This type of cell in fact usually exhibits between two or four long and narrow membrane extensions (filipodia) in opposite directions around the cell body (Stéphanou et al. 2004). The maximal elongation of the pseudopodia in this case is 7 μm . The third row (k:o) of Fig. 2 shows the morphology of the cell when a uniform active deformation is implemented only in the pseudopod domain (Eq. (16)). This pattern leads then to a maximal elongation of 1 μm for each pseudopod in all the cases.

Finally, Fig. 2 p:t represents the deformation as described in Eq. (17) according to which a gradient of the active deformation along the direction $\mathbf{n}_{0,i}$ is implemented in the pseudopod domain. Although the smaller extension undergone by each pseudopod (4 μm) and the more rounded shape (typical of the lobopodia in amoeboid cells), here the final morphologies (Fig. 2q, r, and s) are again very similar to the ones observed in Stéphanou et al. (2004) (Fig. 3). These preliminary results point out the ability of the model to reproduce different patterns of deformation and, therefore, the behavior of different types of cells. Since our previous study (Allena and Aubry 2012) was focused on amoeboid cells, the same will be done here and the third mode of deformation (gradient of the active strain along the direction $\mathbf{n}_{0,i}$, applied in the pseudopod domain) will be adopted in the other simulations.

4.2 Randomness

In reality, it is very unusual to observe regular and symmetric shapes as described in the previous section. Randomness, in fact, plays a significant role during the migration process. In this section, it will be shown how the magnitude of the cyclic active strain e_{ap0} and the direction θ_i of the pseudopodia can randomly vary throughout the time. For this purpose, the four pseudopodia cells (Fig. 2d) will be taken as an example.

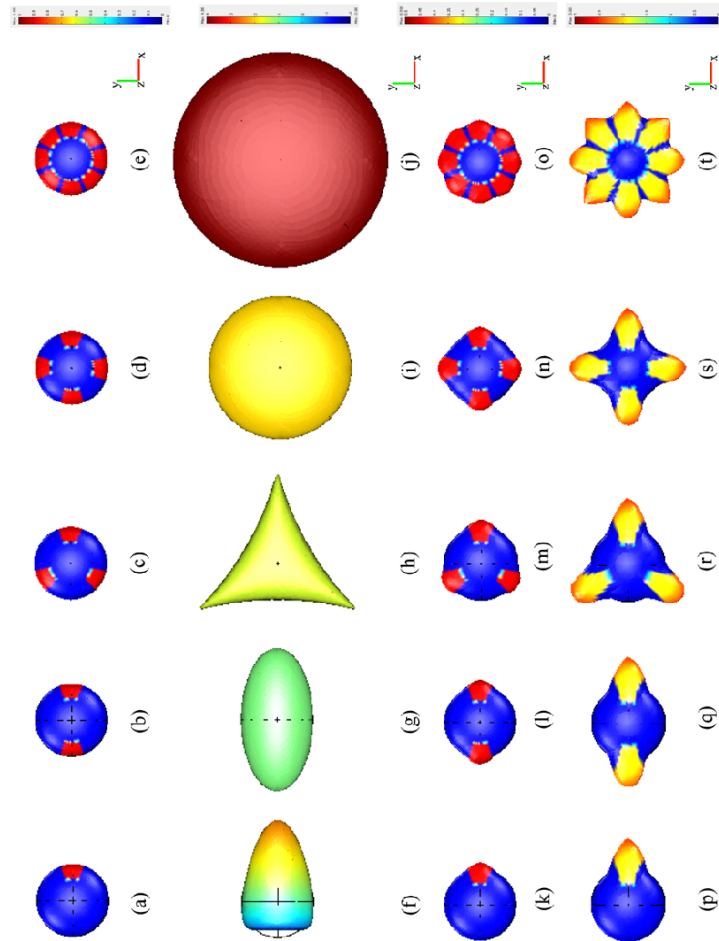


Fig. 2 Steady active protrusion (all views from the top) (a-e) Initial configuration ($t = 0$) for the cell with one, two, three, four, and eight pseudopodia (red). Cell morphology at $t = 30$ s when: the active deformation is applied everywhere through a gradient along the axis $\theta_{0,i}$ of the pseudopodia (f-j); the protrusion is applied only in the pseudopod active domain $\mathcal{Q}_{ppod,i}$ (k-o); a combination of the two previous modes of deformation is considered (p-t) (Color figure online)

Fig. 3 Images originally appeared in Stéphanou et al. (2004), used by the permission of A. Stéphanou. (a) Typical morphologies of nonmigrating L929 fibroblasts observed with phase contrast microscopy. (b) From the top to the bottom, videomicroscopy sequence of a L929 pulsating fibroblast

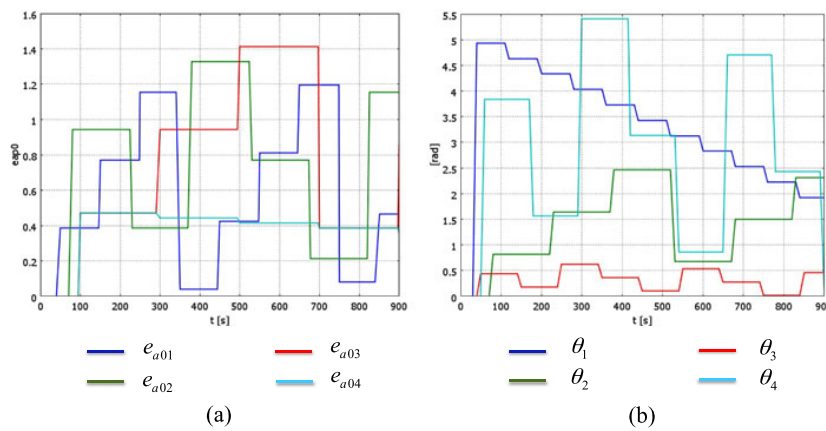
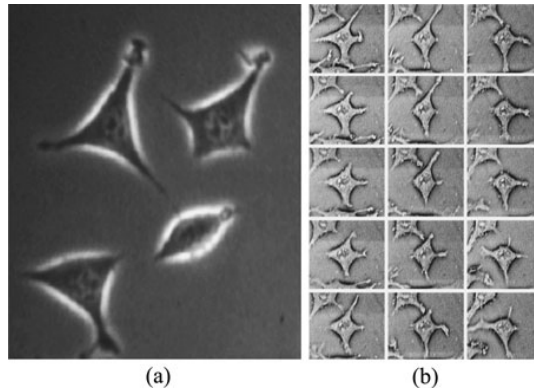


Fig. 4 Steady active protrusion for a cell with four pseudopodia. (a) and (b) Variation of the cyclic component $e_{a0,i}$ and of the direction θ_i over time for each pseudopod, respectively (Color figure online)

First, the cyclic components e_{ap0} of the active deformation for each pseudopod randomly vary between 0 and 1.5 (Fig. 4a). Such a variation occurs over different periods, which have been set equal to $T_{e_{a0,1}} = 100$ s, $T_{e_{a0,2}} = 150$ s, $T_{e_{a0,3}} = 200$ s, $T_{e_{a0,4}} = 200$ s for each pseudopod, respectively. Thus, the value of e_{ap0} changes for each false foot at different time steps, which adds a further random component. In Fig. 5, snapshots at different time steps are presented ($t = 0, 150, 320, 500, 680, 870$ s). The maximal and the minimal extensions observed are respectively of 9.5 μm and 1 μm .

Second, the amplitude e_{ap0} of the active deformation is restored to 0.5 and the directions θ_i of each pseudopod randomly vary between 0 and 2π over different periods for each pseudopod ($T_{\theta,1} = 180$ s, $T_{\theta,2} = 150$ s, $T_{\theta,3} = 100$ s, $T_{\theta,4} = 120$ s, Fig. 4b). In Fig. 6, snapshots at time steps $t = 0, 150, 320, 500, 680, 870$ s are presented. As the direction of each pseudopod randomly changes, it may happen that two or more

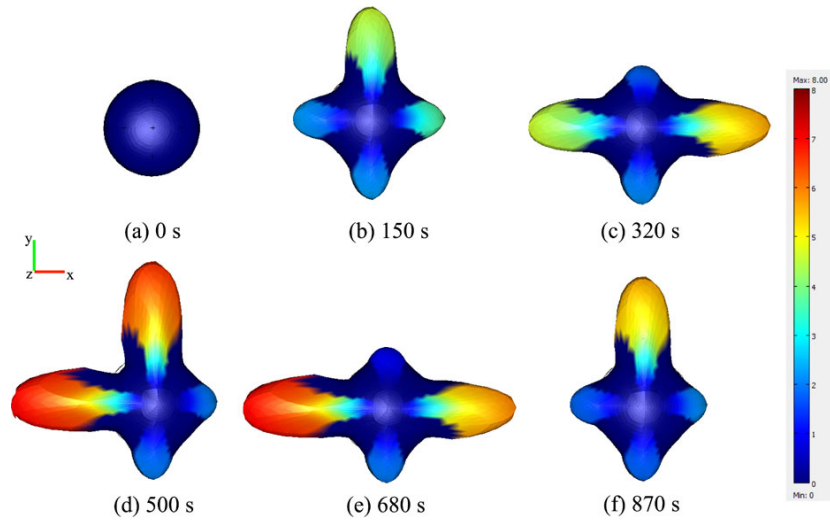


Fig. 5 Snapshots from the top at successive time steps for the steady active protrusion of a cell with four pseudopodia when the cyclic component e_{ap0} randomly varies over time for each false foot (colors: final deformation) (Color figure online)

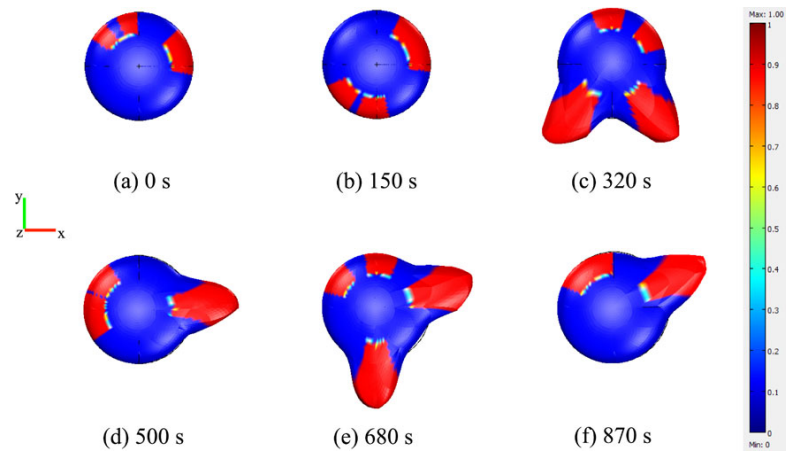


Fig. 6 Snapshots at successive time steps for the steady active protrusion of a cell with four pseudopodia when the direction θ_i randomly varies over time for each false foot (in red the pseudopodia) (Color figure online)

false feet totally or partially superpose. In this case, the pseudopodia cannot extend since, according to the literature (Bosgraaf and Van Haastert 2009b), the protrusion is only possible if the false foot is at a minimal distance of $\frac{\pi}{36}$ with respect to the very next pseudopodia. Therefore, when such a condition is not verified for two or

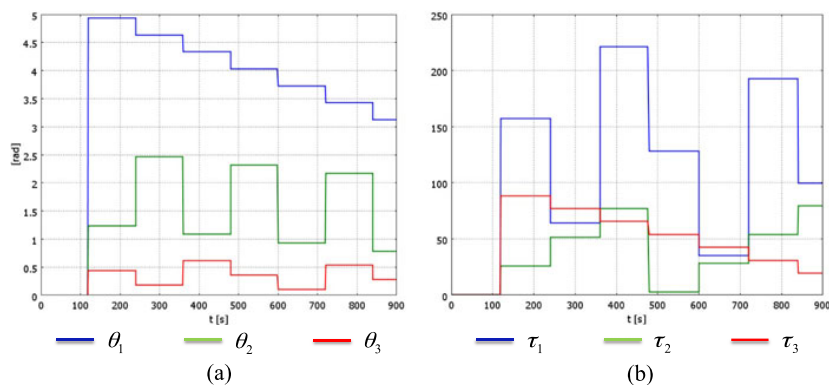


Fig. 7 (a) and (b) Variation of the direction θ_i and of the sources intensities $\tau_{source,i}$ over time for each pseudopod in the temporal and the spatial sensing model, respectively (Color figure online)

more pseudopodia ($h_{crit1,i} = 0$, see Sect. 3.1), these are not initiated as it is possible to observe in Fig. 6 at different time steps.

4.3 Migration

When the cell forms multiple pseudopodia, the migration can occur in two different ways: either the cell simultaneously extends several pseudopodia and then chooses the best oriented toward the external signal to move forward (temporal sensing model) or it only initiates one pseudopod in the direction of the most attractive source (spatial sensing model). In any case, only one pseudopod is employed by the cell to migrate. Here, the results obtained for the simulations of the two strategies are described. In both cases, a cell able to protrude up to three pseudopodia ($N = 3$) has been used as an example. The cyclic components of the active protrusion e_{ap0} and contraction e_{ac0} have been set equal to 0.5 and 0.2, respectively. Such a difference in magnitude has been introduced in agreement with the literature according to which the deformation during the protrusion phase is larger than the one observed during the contraction phase (Gracheva and Othmer 2004).

4.3.1 Temporal Sensing Model

In the temporal sensing model, the directions θ_1 , θ_2 , and θ_3 of the pseudopodia, perpendicular to the cell membrane, vary with respect to time (Fig. 7a) and the periods $T_{\theta,1}$, $T_{\theta,2}$, $T_{\theta,3}$ are all equal to 120 s, which corresponds to two migration cycles. An external source is introduced in the system and $\theta_{source,1} = \frac{\pi}{4}$. As amply discussed and demonstrated in Allena and Aubry (2012), the cell needs to adhere to the underneath substrate in order to move forward. Thus, according to Eq. (26), during the protrusion phase the rear adhesion force is activated in the rear regions associated to the pseudopodia for which $\Theta_{crit1,i}(\theta_i)$, $\Theta_{crit2,i}(\theta_i)$ and $\Theta_{crit3,i}(\theta_i)$ are simultaneously satisfied. During the contraction phase, the same conditions have to be verified and the region of adhesion coincides with the contact surface between the substrate and

the pseudopod selected for the migration. Movie 1 shows the successive steps of the migration over 900 s. The cell is able to extend three pseudopodia in different directions if there is a minimal distance of $\frac{\pi}{36}$ between each other according to $\Theta_{\text{crit}1,i}(\theta_i)$. If a superposition of two or more pseudopodia occurs, the cell does not protrude them. The contraction phase only takes place if $\Theta_{\text{crit}1,i}(\theta_i)$, $\Theta_{\text{crit}2,i}(\theta_i)$, and $\Theta_{\text{crit}3,i}(\theta_i)$ are simultaneously equal to one for at least one false foot, otherwise the cell does not move forward. In Figs. 8a and b, the trajectory over the substrate and the displacement of the cell center of mass are represented. As it can be observed (Fig. 8b), there is an initial phase (0–120 s) during which nothing happens because the three directions θ_1 , θ_2 , and θ_3 are all equal to zero, thus $\Theta_{\text{crit}1,i}(\theta_i)$ is not verified. Between 120–240 s, the cell only extends one pseudopod since the other two coincide, but it does not move forward because the direction θ_1 of this false foot is not in the same quadrant of the external source $\theta_{\text{source},1}$, thus $\Theta_{\text{crit}3,i}(\theta_i)$ is different than one. Therefore, no displacement is observed and the cell only deforms on place (steady active phase). A similar situation takes place between 360–480 s, 600–720 s, and 840–900 s (Fig. 8b). The cell starts moving at $t = 240$ s until $t = 360$ s in the direction θ_3 of the pseudopod, which is the best oriented with respect to the attractant and for which then the three conditions $\Theta_{\text{crit}1,i}(\theta_i)$, $\Theta_{\text{crit}2,i}(\theta_i)$, $\Theta_{\text{crit}3,i}(\theta_i)$ are simultaneously verified. Two other phases of migration take place between 480–600 s and 720–840 s. The overall displacement of the cell center of mass is of about 28 μm (Fig. 8b). In Fig. 8c, the trend of the velocity of the cell center of mass can be observed. During the steady active phases, the cell center of mass actually moves due to the protrusion of the pseudopodia, but its velocity is very small (~ 0.2 $\mu\text{m}/\text{min}$). During the migration phases, the velocity increases and it is bigger during the contraction (~ 8.1 $\mu\text{m}/\text{min}$, green line Fig. 8c) than the protrusion (~ 4.2 $\mu\text{m}/\text{min}$, blue line Fig. 8c) phase. Although such values are in agreement with the ones experimentally found (Adachi et al. 2009; Okeyo et al. 2009; Wilson et al. 2010), some remarks may be done. First, a smaller velocity during the protrusion phase is due to the fact that the extension mainly occurs locally at the pseudopod domain $\Omega_{\text{ppod},i}(\mathbf{p})$, according to the chosen mode of deformation (Eq. (17)). Thus, the cell center of mass is not much perturbed during this period. However, the contraction phase involves the whole cell body, which is pushed forward, then the velocity of the cell center of mass increases.

Second, by plotting the velocity of the center of mass of the pseudopod selected to migrate (Fig. 9a), it is possible to observe that the exact opposite situation takes place. In fact, the velocity is larger during the protrusion phase (~ 11.4 $\mu\text{m}/\text{min}$, blue line Fig. 9a), while it decreases to 2.4 $\mu\text{m}/\text{min}$ during the contraction phase (green line Fig. 9a) since the pseudopod adheres to the underneath substrate.

Finally, experimental observations (Lämmermann and Sixt 2009; Lauffenburger and Horwitz 1996) and previous computational models (Allena and Aubry 2012; Zaman et al. 2005) have shown that the migration process as well as the velocity of the cell are enhanced if a spatial asymmetry between the frontal and the rear adhesion regions exists (i.e., rear adhesion surface smaller with respect to the frontal one). Here, the frontal region coincides with the contact surface between the pseudopod and the substrate, which is smaller (5.5 μm^2) than the rear adhesion surface (25 μm^2). Thus, the asymmetry is inverted. In order to reestablish the correct spatial asymmetry, the rear boundary should be reduced to very few square microns, which could lead to slipping effects during the protrusion phase as discussed in Allena and Aubry (2012).

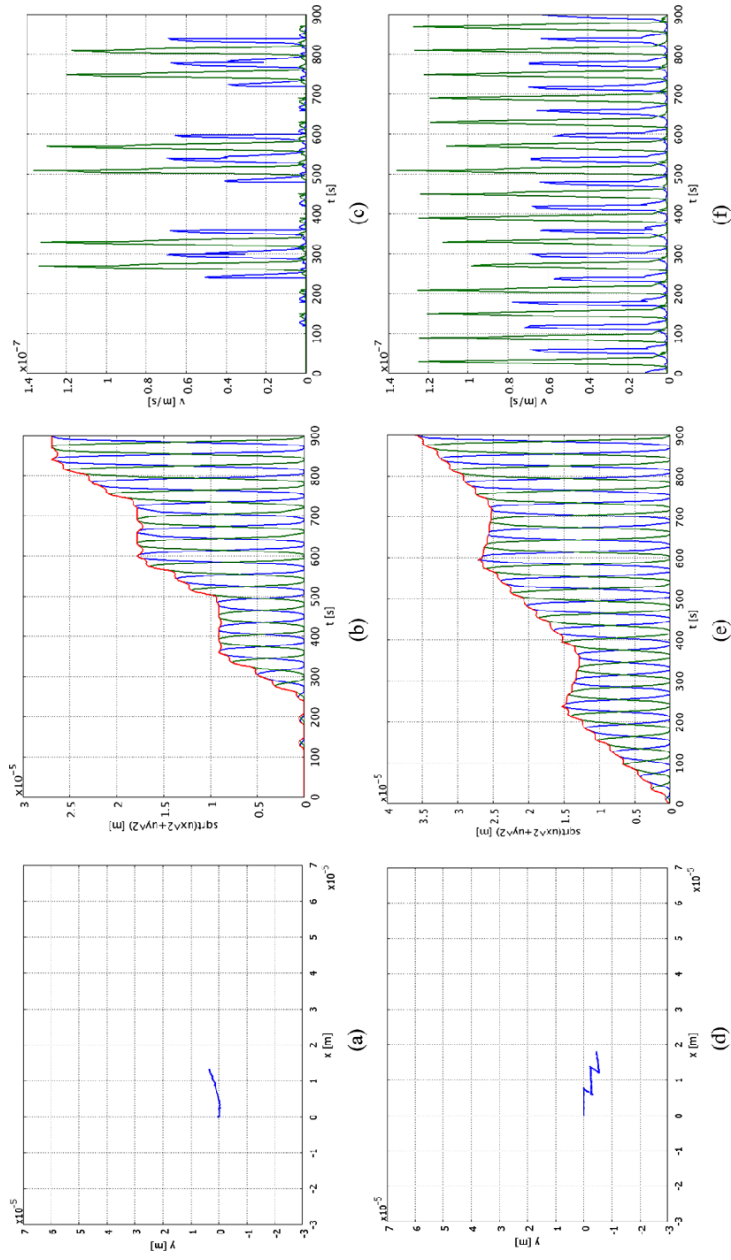


Fig. 8 Results for the temporal (a,c) and the spatial (d,f) sensing model. (a) and (d) Trajectories of the cell over the substrate. (b) and (e) Total displacement (red line) and relative displacements during protrusion (blue line) and contraction (green line). (c) and (f) Velocity of the cell center of mass during protrusion (blue line) and contraction (green line) (Color figure online)

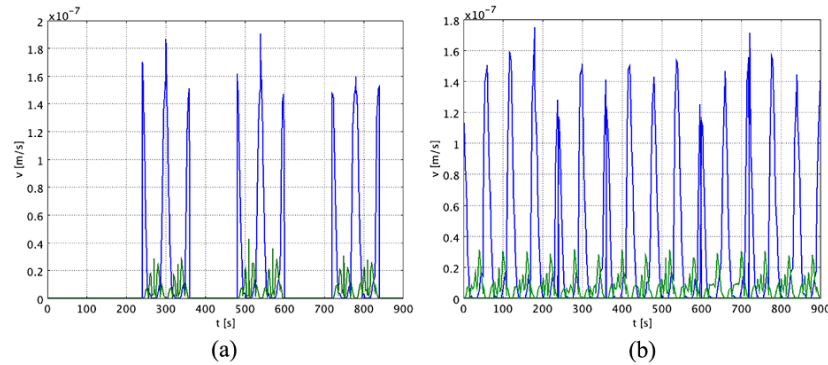


Fig. 9 Velocity of the center of mass of the pseudopod selected to migrate in the temporal (a) and the spatial (b) sensing model during the protrusion (blue line) and the contraction (green line) phase (Color figure online)

4.3.2 Spatial Sensing Model

In the spatial sensing model, the cell “sniffs” the environment at different points of the cell membrane and then only protrudes one pseudopod in the direction of the most attractive source (Eq. (20)), so that $\theta_i = \theta_{\text{source},i \text{ max}}$. This is possible because the actin filaments that trigger the initiation of the false feet are distributed toward the membrane along the whole cell perimeter, thus each particle of this region is “potentially” active.

To describe this strategy of migration, three external sources have been introduced in the system. Their directions have been fixed equal to $\theta_{\text{source},1} = 0$, $\theta_{\text{source},2} = \frac{2\pi}{3}$ and $\theta_{\text{source},3} = \frac{4\pi}{3}$ while their intensities $\tau_{\text{source},1}(t)$, $\tau_{\text{source},2}(t)$, $\tau_{\text{source},3}(t)$ vary with respect to time (Fig. 7b).

In Movie 2, it is possible to observe the different phases of the migration and in Fig. 8d the trajectory of the cell center of mass over the substrate. The cell moves toward the first source ($\theta_{\text{source},1} = 0$) between 0–240 s, 360–600 s, and 720–900 s, while it migrates toward the second source ($\theta_{\text{source},3} = \frac{4\pi}{3}$) between 240–360 s and 600–720 s (Fig. 8e). The cell covers a distance of about 37 μm , which is larger than the distance covered for the temporal sensing model (Fig. 8e). This is due to the fact that in the spatial sensing model no steady active phases occur and there are no conditions to be satisfied. The cell in fact does not lose time, but always moves by protruding one pseudopod in the direction $\theta_{\text{source},i \text{ max}}$ of the most attractive source at that precise instant. Therefore, the velocity of the cell center of mass is always around some microns per minute in agreement with the literature (Adachi et al. 2009; Okeyo et al. 2009; Wilson et al. 2010), and similarly to the temporal sensing model, it is larger during the contraction ($\sim 7.8 \mu\text{m}/\text{min}$, green line Fig. 8f) than the protrusion ($\sim 4.8 \mu\text{m}/\text{min}$, blue line Fig. 8f). Similar remarks to the temporal sensing model to explain the difference in velocity between the protrusion and the contraction phases may be done. Additionally, Fig. 9b shows the velocity of the center of mass of the pseudopod selected to migrate. In this case, the velocity is actually larger during the

protrusion phase ($\sim 10.5 \mu\text{m}/\text{min}$, blue line Fig. 9b) and much smaller ($\sim 2.3 \mu\text{m}/\text{min}$, green line Fig. 9b) during the contraction phase.

5 Conclusions

In this paper, a 3D continuum model to simulate cell migration on 2D substrate in presence of multiple pseudopodia has been presented. As in a previous work (Allena and Aubry 2012), the present model focuses on the mechanical principles regulating the biological phenomenon, specifically the synchronization between the active deformations (protrusion-contraction) of the cell and the adhesion forces necessary to move forward on the underneath substrate. Although the mechanical and numerical formulations are very similar to the ones employed in Allena and Aubry (2012), here the pulsating movement of the cell is controlled by the formation of multiple pseudopodia at different sites of the cell membrane. The main characteristics (Van Haastert 2010) of the false feet are taken into account and reproduced by the model: (i) external signals such as chemoattractants initiate the formation of the pseudopodia, (ii) the cell always forms pseudopodia perpendicular to the membrane, (iii) there has to be a minimal distance of $\frac{\pi}{36}$ between two pseudopodia, (iv) pseudopodia are formed *de novo* in random directions and in regions of the cell that could be previously inactive, and (v) to migrate, the cell only uses one pseudopod.

In the first part of the paper (Sects. 2.3 and 4.1), the ability of the cell to protrude several pseudopodia (up to 8) in a steady configuration has been explored. In particular, three types of active strains (protrusion) have been tested, which allow reproducing various kinds of pseudopodia (lamellipodia, filipodia, etc.) and, therefore, the behavior of various cells. Furthermore, since rarely the cell presents a perfect symmetric morphology, randomness has been introduced in the model to control both the direction and the amplitude of the pseudopodia (Sect. 4.2).

In the second part of the paper (Sects. 3 and 4.3), the migration process is described. As previously mentioned, the cell only uses one pseudopod to move forward, thus two approaches may be adopted: the temporal (Gerish et al. 1974) or the spatial (Zigmond et al. 1981) sensing model. In the temporal sensing model (Sects. 3.1 and 4.3.1), the cell simultaneously initiates several pseudopodia at different spots of the membrane. Then it chooses the one which is the best oriented toward the external source to migrate and retracts the others.

In the spatial sensing model instead (Sects. 3.2 and 4.3.2), the cell only protrudes one pseudopod in the direction of the most attractive source and uses it to move.

While in the first approach the cell behaves as if it was “blind,” and spies on the environment with multiple false feet and later selects the right one, in the second approach, the cell seems to see from far away the external source and it therefore does not lose too much energy and only forms one pseudopod, which is already oriented in the direction of the attractant. These two techniques show two distinct behaviors of the cell very similar to the ones described in the previous paper (Allena and Aubry 2012), where the cell avoided the “obstacles” on the substrate by adopting the “run-and-tumble” or the “look-and-run” approach.

The new model allows having a more realistic representation of the migration process, although there are still further improvements that may be done. First, a more proper description of the cell structure including, for instance, the nucleus and the actin filaments should be used with specific mechanical properties. Second, as already proposed in Allena et al. (2011), a diffusion–reaction equation should be implemented in order to regulate the active strains (protrusion and contraction) that are now directly introduced into the mechanical formulation. Third, the migration process should be reproduced in a 3D environment constituted by more or less dense network of fibers that trigger then the direction of the cell.

Acknowledgements I am grateful to Professor Denis Aubry for discussions and critical comments on the manuscript, and to A. Stéphanou for the permission to use experimental figures.

Appendix A: Heaviside and Level Set Functions

Let $h(\psi)$ be the classical Heaviside function defined as

$$h(\psi) = \begin{cases} 1 & \psi > 0 \\ 0 & \text{otherwise} \end{cases} \quad (29)$$

and $l(\phi)$ the level set function which reads

$$l(\phi) = c \quad (30)$$

where ψ is a real variable, ϕ is a set of real variables and c is a constant value.

Then, by composing the Heaviside and the level set function, three different applications are obtained as follows:

$$\begin{aligned} \Omega_i(\mathbf{p}) &= h \circ l_i(\mathbf{p}) \\ T_i(t) &= h \circ l_i(t) \\ \Theta_i(\theta) &= h \circ l_i(\theta) \end{aligned} \quad (31)$$

which allow to determine whether a spatial particle with initial position \mathbf{p} , a time instant t or an angle θ belong or not to a geometrical domain, a time interval or a range of directions, respectively.

Appendix B: Geometrical Level Set Functions

The annulus describing the actin network is defined by a characteristic function as follows:

$$l_{\text{annulus}}(\mathbf{p}) = \|\mathbf{p}\|^2 - r_{\text{annulus}}^2 \quad (32)$$

The cone of action is defined by

$$l_{\text{cone},i}(\mathbf{p}) = \|\mathbf{p}_{s,i} - p_{d,i}\mathbf{n}_{0,i}\| - tg(\varphi)p_{d,i} \quad (33)$$

where $p_{d,i}$ is the horizontal distance of a particle $\mathbf{p}_{s,i} = (p_x, p_y, 0)$ of the pseudopod i from $\mathbf{p}_{cs} = (p_{cx}, p_{cy}, 0)$ (Fig. 1c), which is the projection of the cell center of mass

\mathbf{p}_c on the x, y plane along the axis of the pseudopod $\mathbf{n}_{0,i}$ (Fig. 1c). Thus, $p_{d,i}$ is given by

$$p_{d,i} = (\mathbf{p}_s - \mathbf{p}_{cs}, \mathbf{n}_{0,i}) \quad (34)$$

where $\mathbf{n}_{0,i}$, which is always perpendicular to the cell membrane (Sect. 1.1), reads

$$\mathbf{n}_{0,i} = \cos \theta_i(t) \mathbf{i}_x + \sin \theta_i(t) \mathbf{i}_y \quad (35)$$

with θ_i the angle of the pseudopod i .

Appendix C: Temporal Level Set Functions

The level set function $l_p(t)$ and $l_c(t)$ for the protrusion and the contraction phase are defined as follows:

$$\begin{aligned} l_p(t) &= \sin\left(2\pi \frac{t}{T_{\text{migr}}}\right) \\ l_c(t) &= -\sin\left(2\pi \frac{t}{T_{\text{migr}}}\right) \end{aligned} \quad (36)$$

Appendix D: Temporal Sensing Model Level Set Functions

In order for the cell to be able to simultaneously extend multiple pseudopodia, three criteria need to be satisfied (Sect. 3.1). Each one of them is expressed through a specific analytical function $\Theta_i(\theta) = h \circ l_i(\theta)$ and allows determining the admissibility of the angle θ_i of each pseudopod. Here, the level set functions associated to each criterion are defined.

Let θ_i being the direction of a pseudopod i and θ_{i+1} and θ_{i-1} the directions of its anticlockwise and clockwise nearest pseudopod, then $l_{\text{crit1},i}(\theta_i)$ reads

$$l_{\text{crit1},i}(\theta_i) = \begin{cases} \theta_i - (\theta_{i+1} + \frac{\pi}{36}) \\ -\theta_i + (\theta_{i+1} - \frac{\pi}{36}) \\ \theta_i - (\theta_{i-1} + \frac{\pi}{36}) \\ -\theta_i + (\theta_{i-1} - \frac{\pi}{36}) \end{cases} \quad (37)$$

To contract and migrate, the cell must choose the pseudopod which is the best oriented in the direction $\theta_{\text{source},i}$, thus $\Theta_{\text{crit2},i}(\theta_i)$ need to be verified. The associated level set function $l_{\text{crit2},i}(\theta_i)$ reads

$$l_{\text{crit2},i}(\theta_i) = \begin{cases} -|\theta_i - \theta_{\text{source},i}| + |\theta_{i+1} - \theta_{\text{source},i}| \\ -|\theta_i - \theta_{\text{source},i}| + |\theta_{i-1} - \theta_{\text{source},i}| \end{cases} \quad (38)$$

Finally, the angle θ_i of the pseudopod $\Omega_{\text{ppod},i}$ chosen to migrate has to be in the same quadrant of $\theta_{\text{source},i}$. Thus, $\Theta_{\text{crit3},i}(\theta_i)$ is implemented in the model and the associated

level set function $l_{\text{crit}3,i}(\theta_i)$ is defined as

$$l_{\text{crit}3,i}(\theta_i) = \begin{cases} \theta_i & \text{if } 0 < \theta_{\text{source},i} < \frac{\pi}{2} \\ -\theta_i + \frac{\pi}{2} & \text{if } 0 < \theta_{\text{source},i} < \frac{\pi}{2} \\ \theta_i - \frac{\pi}{2} & \text{if } \frac{\pi}{2} < \theta_{\text{source},i} < \pi \\ -\theta_i + \pi & \text{if } \frac{\pi}{2} < \theta_{\text{source},i} < \pi \\ \theta_i - \pi & \text{if } \pi < \theta_{\text{source},i} < \frac{3\pi}{2} \\ -\theta_i + \frac{3\pi}{2} & \text{if } \pi < \theta_{\text{source},i} < \frac{3\pi}{2} \\ \theta_i - \frac{3\pi}{2} & \text{if } \frac{3\pi}{2} < \theta_{\text{source},i} < 2\pi \\ -\theta_i + 2\pi & \text{if } \frac{3\pi}{2} < \theta_{\text{source},i} < 2\pi \end{cases} \quad (39)$$

Appendix E: Adhesion Surfaces and Forces

Similarly to the pseudopod domain $\Omega_{\text{ppod},i}(p)$, the frontal adhesion surface results from the intersection between the annulus and the cone at $z = 0$. Thus, $l_{\text{annulus}}(\mathbf{p}_s)$ and $l_{\text{cone},i}(\mathbf{p}_s)$ are now expressed as follows:

$$\begin{aligned} l_{\text{annulus}}(\mathbf{p}_s) &= \|\mathbf{p}_s\|^2 - r_{\text{annulus}}^2 \\ l_{\text{cone},i}(\mathbf{p}_s) &= \|\mathbf{p}_{s,i} - p_{d,i}\mathbf{n}_{0,i}\| - tg(\varphi)p_{d,i} \end{aligned} \quad (40)$$

The level set function $l_{r,i}(\mathbf{p}_s)$, which allows defining the rear adhesion surface $\partial\Omega_{r,i}(\mathbf{p}_s)$, reads

$$l_{r,i}(\mathbf{p}_s) = -(\mathbf{p}_s - \mathbf{p}_{cs}, \mathbf{n}_{0,i}) - l_r(24) \quad (41)$$

where l_r is the distance of \mathbf{p}_{cs} from the boundary of the rear adhesion surface and is here equal to $2 \mu\text{m}$ (Fig. 1c).

The level set functions $l_{af}(t)$ and $l_{ar}(t)$, which synchronize the adhesion forces with the active deformations (Sect. 3.3), are expressed as

$$\begin{aligned} l_{af}(t) &= -\frac{\partial(\sin(2\pi \frac{t}{T_{\text{migr}}}))}{\partial t} \\ l_{ar}(t) &= \frac{\partial(\sin(2\pi \frac{t}{T_{\text{migr}}}))}{\partial t} \end{aligned} \quad (42)$$

Appendix F: Sensitivity Analysis

The high number of parameters in the model (20, Table 1) does not allow performing an exhaustive sensitivity study. Nevertheless, the parameters can be classified in four categories:

- (1) the parameters referenced in the literature: E_s (Laurent et al. 2005), μ_{fv} (Bausch et al. 1999; Drury and Dembo 2001), ρ (Fukui et al. 2000), T_{migr} (Allena and Aubry 2012; Dong et al. 2002), and the minimal distance between the pseudopodia ($\pm \frac{\pi}{36}$) (Bosgraaf and Van Haastert 2009a);

Table 2 Results for the sensitivity analysis

Parameter	Value	Covered distance		Maximal protrusion velocity		Maximal contraction velocity	
		Temporal sensing model	Spatial sensing model	Temporal sensing model	Spatial sensing model	Temporal sensing model	Spatial sensing model
$r_{annulus}$	3.3×10^{-6}	2.56×10^{-5} m	3.57×10^{-5} m	6.85×10^{-8} m/s	7.32×10^{-8} m/s	1.19×10^{-7} m/s	1.18×10^{-7} m/s
	3×10^{-6}	2.69×10^{-5} m	3.60×10^{-5} m	6.93×10^{-8} m/s	7.84×10^{-8} m/s	1.37×10^{-7} m/s	1.36×10^{-7} m/s
	(original value)	2.8×10^{-5} m	3.68×10^{-5} m	7.23×10^{-8} m/s	7.83×10^{-8} m/s	1.43×10^{-7} m/s	1.34×10^{-7} m/s
φ	$\frac{7}{9}$	2.73×10^{-5} m	3.91×10^{-5} m	6.82×10^{-8} m/s	6.97×10^{-8} m/s	1.48×10^{-7} m/s	1.58×10^{-7} m/s
	$\frac{7}{10}$	2.69×10^{-5} m	3.60×10^{-5} m	6.93×10^{-8} m/s	7.81×10^{-8} m/s	1.37×10^{-7} m/s	1.36×10^{-7} m/s
	(original value)	2.29×10^{-5} m	3.46×10^{-5} m	8.05×10^{-8} m/s	7.95×10^{-8} m/s	1.71×10^{-7} m/s	1.54×10^{-7} m/s
	$\frac{7}{11}$	2.79×10^{-5} m	3.85×10^{-5} m	7.6×10^{-8} m/s	8.28×10^{-8} m/s	1.46×10^{-7} m/s	1.29×10^{-7} m/s
ϵ_{acc0}	0.22	2.69×10^{-5} m	3.60×10^{-5} m	6.93×10^{-8} m/s	7.80×10^{-8} m/s	1.37×10^{-7} m/s	1.36×10^{-7} m/s
	0.2 (original value)	2.56×10^{-5} m	3.51×10^{-5} m	6.34×10^{-8} m/s	6.93×10^{-8} m/s	1.33×10^{-7} m/s	1.28×10^{-7} m/s
	0.18	2.60×10^{-5} m	3.81×10^{-5} m	6.93×10^{-8} m/s	7.65×10^{-8} m/s	1.39×10^{-7} m/s	1.54×10^{-7} m/s
α	0.88	2.69×10^{-5} m	3.60×10^{-5} m	6.93×10^{-8} m/s	7.86×10^{-8} m/s	1.37×10^{-7} m/s	1.36×10^{-7} m/s
	0.8 (original value)	2.43×10^{-5} m	3.58×10^{-5} m	7.45×10^{-8} m/s	7.75×10^{-8} m/s	1.22×10^{-7} m/s	1.21×10^{-7} m/s
	0.72	2.43×10^{-5} m	3.58×10^{-5} m	7.45×10^{-8} m/s	7.75×10^{-8} m/s	1.22×10^{-7} m/s	1.21×10^{-7} m/s

- (2) the parameters that have been chosen within a reasonable physical range (Allena and Aubry 2012): r, E_{fe}, ν_s, ν_f ;
- (3) the parameters that have been arbitrarily chosen and for which a sensitivity analysis has been proposed in Allena and Aubry (2012), showing a slight influence on the final results: $h, e_{ap0}, \partial\Omega_{r,i}, \mu_{ff}, \mu_{fr}$;
- (4) the parameters that have been arbitrarily chosen and for which a sensitivity analysis is proposed here: $r_{annulus}, \varphi, e_{ac0}, \alpha$.

Each parameter has been allowed a variance of $\pm 10\%$ in both the temporal and the spatial sensing models. The values of the source directions $\theta_{source,i}$ are assumed to not affect the mechanical behavior of the cell, but just the path over the 2D substrate in both the temporal and spatial sensing models.

As a general remark, for both the temporal and the spatial sensing models, the variation of the parameters do not highly affect the final results in terms of the covered distance and maximal velocities of the cell center of inertia during the protrusion and contraction phase (Table 2). More importantly, such a variation does not affect the fundamental principles of the mechanical model. Nevertheless, we can notice that higher values of the cone apex angle φ , the cyclic active contraction e_{ac0} , the gradient amplitude α , as expected, enhance the movement forward in both the temporal and the spatial sensing models, thus the cell is able to migrate over a longer distance. On the contrary, a higher value of $r_{annulus}$, which reduces the volume of the actin network and, therefore, the volume of the pseudopod also (Eq. (32)) leads to a smaller covered distance.

References

- Adachi, T., Okeyo, K. O., Shitagawa, Y., & Hojo, M. (2009). Strain field in actin filament network in lamellipodia of migrating cells: implication for network reorganization. *J. Biomech.*, *42*, 297–302.
- Allena, R., & Aubry, D. (2012). “Run-and-tumble” or “look-and-run”? A mechanical model to explore the behavior of a migrating amoeboid cell. *J. Theor. Biol.*, *306*, 15–31.
- Allena, R., Mouronval, A.-S., & Aubry, D. (2010). Simulation of multiple morphogenetic movements in the *Drosophila* embryo by a single 3D finite element model. *J. Mech. Behav. Biomed. Mater.*, *3*, 313–323.
- Allena, R., Muñoz, J. J., & Aubry, D. (2011). Diffusion–reaction model for *Drosophila* embryo development. *Comput. Methods Biomech. Biomed. Eng.* doi:10.1080/10255842.2011.616944.
- Alt, W. (1990). Mathematical models and analysing methods for the lamellipodial activity of leukocytes. In N. Akkas (Ed.), *Nato ASI series H: Vol. 42. Biomechanics of active movement and deformation of cells* (pp. 403–422).
- Alt, W., & Tranquillo, R. T. (1995). Basic morphogenetic system modeling shape changes of migrating cells: How to explain fluctuating lamellipodial dynamics. *J. Biol. Syst.*, *3*, 905–916.
- Andrew, N., & Insall, R. H. (2007). Chemotaxis in shallow gradients is mediated independently of PtdIns 3-kinase by biased choices between random protrusions. *Nat. Cell Biol.*, *9*, 193–200.
- Arrieumerlou, C., & Meyer, T. (2005). A local coupling model and compass parameter for eukaryotic chemotaxis. *Dev. Cell*, *8*, 215–227.
- Bahat, A., & Eisenbach, M. (2006). Sperm Thermotaxis. *Mol. Cell. Endocrinol.*, *252*, 115–119.
- Balan, C., & Tsakmakis, C. (2002). A finite deformation formulation of the 3-parameter viscoelastic fluid. *J. Non-Newton. Fluid Mech.*, *103*, 45–64.
- Bausch, A. R., Möller, W., & Sackmann, E. (1999). Measurement of local viscoelasticity and forces in living cells by magnetic tweezers. *Biophys. J.*, *76*, 573–579.
- Bereiter-Hahn, J., & Lüers, H. (1998). Subcellular tension fields and mechanical resistance of the lamella front related to the direction of locomotion. *Cell Biochem. Biophys.*, *29*, 243–262.

- Bonet, J. (2001). Large strain viscoelastic constitutive models. *Int. J. Solids Struct.*, *38*, 2953–2968.
- Borisy, G. G., & Svitkina, T. M. (2000). Acting machinery: pushing the envelope. *Curr. Opin. Cell Biol.*, *12*, 104–112.
- Bosgraaf, L., & Van Haastert, P. J. M. (2009a). Navigation of chemotactic cells by parallel signaling to pseudopod persistence and orientation. *PLoS ONE*, *4*, e6842.
- Bosgraaf, L., & Van Haastert, P. J. M. (2009b). The ordered extension of pseudopodia by amoeboid cells in the absence of external cues. *PLoS ONE*, *4*, e5253.
- Bottino, D., Mogilner, A., Roberts, T., Stewart, M., & Oster, G. (2002). How nematode sperm crawl. *J. Cell Sci.*, *115*, 367–384.
- Carlier, M. F., & Pantaloni, D. (1997). Control of actin dynamics in cell motility. *J. Mol. Biol.*, *269*, 459–467.
- Carlsson, A. E., & Sept, D. (2008). Mathematical modeling of cell migration. *Methods Cell Biol.*, *84*, 911–937.
- Condeelis, J. (1993). Life at the leading edge: the formation of cell protrusions. *Annu. Rev. Cell Biol.*, *9*, 411–444.
- Cramer, L. P., Siebert, M., & Mitchison, T. J. (1997). Identification of novel graded polarity actin filament bundles in locomoting heart fibroblasts: implications for the generation of motile force. *J. Cell Biol.*, *136*, 1287–1305.
- Dong, C., Slattery, M. J., Rank, B. M., & You, J. (2002). In vitro characterization and micromechanics of tumor cell chemotactic protrusion, locomotion, and extravasation. *Ann. Biomed. Eng.*, *30*, 344–355.
- Drury, J. L., & Dembo, M. (2001). Aspiration of human neutrophils: effects of shear thinning and cortical dissipation. *Biophys. J.*, *81*, 3166–3177.
- Flaherty, B., McGarry, J. P., & McHugh, P. E. (2007). Mathematical models of cell motility. *Cell Biochem. Biophys.*, *49*, 14–28.
- Franca-Koh, J., Kamimura, Y., & Devreotes, P. (2006). Navigating signaling networks: chemotaxis in *Dictyostelium discoideum*. *Curr. Opin. Genet. Dev.*, *16*, 333–338.
- Friedl, P., & Gilmour, D. (2009). Collective cell migration in morphogenesis, regeneration and cancer. *Nat. Rev. Mol. Cell Biol.*, *10*, 445–457.
- Fukui, Y., Uyeda, T. Q. P., Kitayama, C., & Inoué, S. (2000). How well can an amoeba climb? *Proc. Natl. Acad. Sci. USA*, *97*, 10020–10025.
- Gail, M. H., & Boone, C. W. (1970). The locomotion of mouse fibroblasts in tissue culture. *Biophys. J.*, *10*, 980–993.
- Gerish, G., Malchow, D., & Hess, B. (1974). Cell communication and cyclic-amp regulation during aggregation of the slime mold, *dictyostelium discoideum*. In L. Jaenicke (Ed.), *Biochemistry of sensory functions* (pp. 279–298). New York: Springer.
- Gracheva, M. E., & Othmer, H. G. (2004). A continuum model of motility in amoeboid cells. *Bull. Math. Biol.*, *66*, 167–193.
- Hoeller, O., & Kay, R. R. (2007). Chemotaxis in the absence of PIP3 gradients. *Curr. Biol.*, *17*, 813–817.
- Holzappel, G. A. (2000). *Nonlinear solid mechanics: a continuum approach for engineering* (1st ed.). New York: Wiley.
- Insall, R. H. (2010). Understanding eukaryotic chemotaxis: a pseudopod-centred view. *Nat. Rev. Mol. Cell Biol.*, *11*, 453–458.
- Jay, P. Y., Pham, P. A., Wong, S. A., & Elson, E. L. (1995). A mechanical function of myosin II in cell motility. *J. Cell Sci.*, *108*, 387–393.
- Karsenti, E. (2008). Self-organization in cell biology: a brief history. *Nat. Rev. Mol. Cell Biol.*, *9*, 255–262.
- Killich, T., et al. (1993). The locomotion, shape and pseudopodial dynamics of unstimulated *Dictyostelium* cells are not random. *J. Cell Sci.*, *106*(Pt 4), 1005–1013.
- King, J. S., & Insall, R. H. (2009). Chemotaxis: finding the way forward with *Dictyostelium*. *Trends Cell Biol.*, *19*, 523–530.
- Lämmermann, T., & Sixt, M. (2009). Mechanical modes of “amoeboid” cell migration. *Curr. Opin. Cell Biol.*, *21*, 636–644.
- Larson, R. G. (1998). *The structure and rheology of complex fluids*. Oxford: Oxford University Press.
- Lauffenburger, D. A., & Horwitz, A. F. (1996). Cell migration: a physically integrated molecular process. *Cell*, *84*, 359–369.
- Laurent, V. M., et al. (2005). Gradient of rigidity in the lamellipodia of migrating cells revealed by atomic force microscopy. *Biophys. J.*, *89*, 667–675.
- Lee, J., Ishihara, A., & Jacobson, K. (1993). How do cells move along surfaces? *Trends Cell Biol.*, *3*, 366–370.

- Li, L., Nørrelykke, S. F., & Cox, E. C. (2008). Persistent cell motion in the absence of external signals: a search strategy for eukaryotic cells. *PLoS ONE*, *3*, e2093.
- Lim, C. T., Zhou, E. H., & Quek, S. T. (2006). Mechanical models for living cells—a review. *J. Biomech.*, *39*, 195–216.
- Lubarda, V. (2004). Constitutive theories based on the multiplicative decomposition of deformation gradient: thermoelasticity, elastoplasticity, and biomechanics. *Appl. Mech. Rev.*, *57*, 95–109.
- Merkel, R., et al. (2000). A micromechanic study of cell polarity and plasma membrane cell body coupling in Dictyostelium. *Biophys. J.*, *79*, 707–719.
- Merlot, S., & Firtel, R. A. (2003). Leading the way: directional sensing through phosphatidylinositol 3-kinase and other signaling pathways. *J. Cell Sci.*, *116*, 3471–3478.
- Mogilner, A., & Oster, G. (1996). The physics of lamellipodial protrusion. *Eur. Biophys. J.*, *25*, 47–53.
- Mogilner, A., & Rubinstein, B. (2005). The physics of filopodial protrusion. *Biophys. J.*, *89*, 782–795.
- Mogilner, A., & Verzi, D. W. (2003). A simple 1-D physical model for the crawling nematode sperm cell. *J. Stat. Phys.*, *110*, 1169–1189.
- Muñoz, J. J., Barrett, K., & Miodownik, M. (2007). A deformation gradient decomposition method for the analysis of the mechanics of morphogenesis. *J. Biomech.*, *40*, 1372–1380.
- Murray, J. D. (2003). *Mathematical biology II: spatial models and biomedical applications*. Berlin: Springer.
- Okeyo, K. O., Adachi, T., Sunaga, J., & Hojo, M. (2009). Actomyosin contractility spatiotemporally regulates actin network dynamics in migrating cells. *J. Biomech.*, *42*, 2540–2548.
- Oster, G. F. (1984). On the crawling of cells. *J. Embryol. Exp. Morphol.*, *83*, 329–364.
- Oster, G. F., & Perelson, A. S. (1987). The physics of cell motility. *J. Cell Sci., Suppl.*, *8*, 35–54.
- Patlak, C. (1953). Random walk with persistence and external bias. *Bull. Math. Biol.*, *15*, 311–338.
- Phillipson, M., et al. (2006). Intraluminal crawling of neutrophils to emigration sites: a molecularly distinct process from adhesion in the recruitment cascade. *J. Exp. Med.*, *203*, 2569–2575.
- Potel, M. J., & Mackay, S. A. (1979). Preaggregative cell motion in Dictyostelium. *J. Cell Sci.*, *36*, 281–309.
- Rubinstein, B., Jacobson, K., & Mogilner, A. (2005). Multiscale two-dimensional modeling of a motile simple-shaped cell. *Multiscale Model. Simul.*, *3*, 413–439.
- Sakamoto, Y., Prudhomme, S., & Zaman, M. H. (2011). Viscoelastic gel-strip model for the simulation of migrating cells. *Ann. Biomed. Eng.*, *39*, 2735–2749.
- Schaub, S., Bohnet, S., Laurent, V. M., Meister, J.-J., & Verkhovskiy, A. B. (2007). Comparative maps of motion and assembly of filamentous actin and myosin II in migrating cells. *Mol. Biol. Cell*, *18*, 3723–3732.
- Schneider, I. C., & Haugh, J. M. (2006). Mechanisms of gradient sensing and chemotaxis: conserved pathways, diverse regulation. *Cell Cycle*, *5*, 1130–1134.
- Small, J. V., Rohlf, A., & Mogilner, A. (1993). In G. Jones, C. Wigley, & R. Warn (Eds.), *Actin and cell movement. Cell behaviour: adhesion and motility* (pp. 57–71). London: The Society of Experimental Biology.
- Stéphanou, A., Chaplain, M. A. J., & Tracqui, P. (2004). A mathematical model for the dynamics of large membrane deformations of isolated fibroblasts. *Bull. Math. Biol.*, *66*, 1119–1154.
- Stolarska, M. A., Kim, Y., & Othmer, H. G. (2009). Multi-scale models of cell and tissue dynamics. *Philos. Trans. R. Soc., Math. Phys. Eng. Sci.*, *367*, 3525–3553.
- Taber, L. A. (2004). *Nonlinear theory of elasticity: applications in biomechanics*. Singapore: World Scientific.
- Taber, L. A., Shi, Y., Yang, L., & Bayly, P. V. (2011). A poroelastic model for cell crawling including mechanical coupling between cytoskeletal contraction and actin polymerization. *J. Mech. Mater. Struct.*, *6*, 569–589.
- Takagi, H., Sato, M. J., Yanagida, T., & Ueda, M. (2008). Functional analysis of spontaneous cell movement under different physiological conditions. *PLoS ONE*, *3*, e2648.
- Theriot, J. A., & Mitchison, T. J. (1991). Actin microfilament dynamics in locomoting cells. *Nature*, *352*, 126–131.
- Van Haastert, P. J. M. (2010). Chemotaxis: insights from the extending pseudopod. *J. Cell Sci.*, *123*, 3031–3037.
- Van Haastert, P. J. M., & Bosgraaf, L. (2009). The local cell curvature guides pseudopodia towards chemoattractants. *HFSP J.*, *3*, 282–286.
- Veksler, A., & Gov, N. S. (2007). Phase transitions of the coupled membrane-cytoskeleton modify cellular shape. *Biophys. J.*, *93*, 3798–3810.

- Weijer, C. J. (2009). Collective cell migration in development. *J. Cell Sci.*, *122*, 3215–3223.
- Weiner, O. D. (2002). Regulation of cell polarity during eukaryotic chemotaxis: the chemotactic compass. *Curr. Opin. Cell Biol.*, *14*, 196–202.
- Wilson, C. A., et al. (2010). Myosin II contributes to cell-scale actin network treadmilling through network disassembly. *Nature*, *465*, 373–377.
- Young, J., & Mitran, S. (2010). A numerical model of cellular blebbing: a volume-conserving, fluid-structure interaction model of the entire cell. *J. Biomech.*, *43*, 210–220.
- Zaman, M. H., Kamm, R. D., Matsudaira, P., & Lauffenburger, D. A. (2005). Computational model for cell migration in three-dimensional matrices. *Biophys. J.*, *89*, 1389–1397.
- Zhao, M. (2009). Electrical fields in wound healing—an overriding signal that directs cell migration. *Semin. Cell Dev. Biol.*, *20*, 674–682.
- Zhu, C., & Skalak, R. (1988). A continuum model of protrusion of pseudopod in leukocytes. *Biophys. J.*, *54*, 1115–1137.
- Zigmond, S. H., Levitsky, H. I., & Kreel, B. J. (1981). Cell polarity: an examination of its behavioral expression and its consequences for polymorphonuclear leukocyte chemotaxis. *J. Cell Biol.*, *89*, 585–592.

\mathbf{p}_c on the x, y plane along the axis of the pseudopod $\mathbf{n}_{0,i}$ (Fig. 1c). Thus, $p_{d,i}$ is given by

$$p_{d,i} = (\mathbf{p}_s - \mathbf{p}_{cs}, \mathbf{n}_{0,i}) \quad (34)$$

where $\mathbf{n}_{0,i}$, which is always perpendicular to the cell membrane (Sect. 1.1), reads

$$\mathbf{n}_{0,i} = \cos \theta_i(t) \mathbf{i}_x + \sin \theta_i(t) \mathbf{i}_y \quad (35)$$

with θ_i the angle of the pseudopod i .

Appendix C: Temporal Level Set Functions

The level set function $l_p(t)$ and $l_c(t)$ for the protrusion and the contraction phase are defined as follows:

$$\begin{aligned} l_p(t) &= \sin\left(2\pi \frac{t}{T_{\text{migr}}}\right) \\ l_c(t) &= -\sin\left(2\pi \frac{t}{T_{\text{migr}}}\right) \end{aligned} \quad (36)$$

Appendix D: Temporal Sensing Model Level Set Functions

In order for the cell to be able to simultaneously extend multiple pseudopodia, three criteria need to be satisfied (Sect. 3.1). Each one of them is expressed through a specific analytical function $\Theta_i(\theta) = h \circ l_i(\theta)$ and allows determining the admissibility of the angle θ_i of each pseudopod. Here, the level set functions associated to each criterion are defined.

Let θ_i being the direction of a pseudopod i and θ_{i+1} and θ_{i-1} the directions of its anticlockwise and clockwise nearest pseudopod, then $l_{\text{crit1},i}(\theta_i)$ reads

$$l_{\text{crit1},i}(\theta_i) = \begin{cases} \theta_i - (\theta_{i+1} + \frac{\pi}{36}) \\ -\theta_i + (\theta_{i+1} - \frac{\pi}{36}) \\ \theta_i - (\theta_{i-1} + \frac{\pi}{36}) \\ -\theta_i + (\theta_{i-1} - \frac{\pi}{36}) \end{cases} \quad (37)$$

To contract and migrate, the cell must choose the pseudopod which is the best oriented in the direction $\theta_{\text{source},i}$, thus $\Theta_{\text{crit2},i}(\theta_i)$ need to be verified. The associated level set function $l_{\text{crit2},i}(\theta_i)$ reads

$$l_{\text{crit2},i}(\theta_i) = \begin{cases} -|\theta_i - \theta_{\text{source},i}| + |\theta_{i+1} - \theta_{\text{source},i}| \\ -|\theta_i - \theta_{\text{source},i}| + |\theta_{i-1} - \theta_{\text{source},i}| \end{cases} \quad (38)$$

Finally, the angle θ_i of the pseudopod $\Omega_{\text{ppod},i}$ chosen to migrate has to be in the same quadrant of $\theta_{\text{source},i}$. Thus, $\Theta_{\text{crit3},i}(\theta_i)$ is implemented in the model and the associated

3.5 Confined migration

As the modelling of single cell migration progressed, I happened to meet Matthieu Piel who is the Principal Investigator of the Systems cell biology of cell polarity and cell division team at the Institut Curie and who is interested in investigating cell migration during confinement.

In fact, during many biological processes such as embryogenesis, immunity response and tumorigenesis, cell migration takes place within the confined environment of tissues (63). In these cases, cell motility is influenced by the morphology of the ECM, which may vary in terms of heterogeneity, fibre density and organization. In fact, the width of the ECM pores, the degree of ECM alignment and the ECM stiffness are all fundamental parameters determining the mechanism and extent to which the ECM steers or inhibits the cell movement. Thus, the cell must continuously adapt its shape and consequently its migratory behaviour.

Therefore, an extension of the models presented in (49, 50) has been proposed to reproduce the experimental set up used in (64) where HeLa cells migrate across microchannels of different width and shape. Although the main hypotheses are still valid, here the geometry and the constitutive behaviour of the cell are more precisely described in order to consider specific components such as the nucleus and the nuclear lamina, which seem to play a critical role during confined migration.

Included Papers:

Aubry D, Thiam H, Piel M, Allena R (2015) A computational mechanics approach to assess the link between cell morphology and forces during confined migration. *Biomech Model Mechanobiol* 14(1):143–157.

Allena R (2014) Mechanical modelling of confined cell migration across constricted-curved microchannels. *Molecular and Cellular Biomechanics*, 11:185-208.

A computational mechanics approach to assess the link between cell morphology and forces during confined migration

D. Aubry · H. Thiam · M. Piel · R. Allena

Received: 12 December 2013 / Accepted: 12 May 2014
© Springer-Verlag Berlin Heidelberg 2014

Abstract Confined migration plays a fundamental role during several biological phenomena such as embryogenesis, immunity and tumorigenesis. Here, we propose a two-dimensional mechanical model to simulate the migration of a HeLa cell through a micro-channel. As in our previous works, the cell is modelled as a continuum and a standard Maxwell model is used to describe the mechanical behaviour of both the cytoplasm (including active strains) and the nucleus. The cell cyclically protrudes and contracts and develops viscous forces to adhere to the substrate. The micro-channel is represented by two rigid walls, and it exerts an additional viscous force on the cell boundaries. We test four channels whose dimensions in terms of width are i) larger than the cell diameter, ii) sub-cellular, iii) sub-nuclear and iv) much smaller than the nucleus diameter. The main objective of the work is to assess the necessary conditions for the cell to enter into the channel and migrate through it. Therefore, we evaluate both the evolution of the cell morphology and the cell-channel and cell-substrate surface forces, and we show that there exists a link between the two, which is the essential parameter deter-

mining whether the cell is permeative, invasive or penetrating.

Keywords Confined cell migration · Continuum mechanics · Computational mechanics · Forces

1 Introduction

In our previous works (Allena and Aubry 2012; Allena 2013), we have presented numerical models which helped to understand the mechanisms controlling cell motility on two-dimensional (2D) flat surfaces. Nevertheless, during many biological processes such as embryogenesis, immunity and tumorigenesis, cell migration takes place in confined environments of tissues (Friedl and Wolf 2010). In these cases, cell locomotion is influenced by the presence of attractant molecules, but also by the morphology of the extracellular matrix (ECM). In fact, the surrounding tissues may vary in terms of heterogeneity, fibres density and organization. As shown both experimentally (Erler and Weaver 2009; Wolf et al. 2009; Egeblad et al. 2010; Friedl and Wolf 2010) and theoretically (Zaman et al. 2005, 2006, 2007; Scianna et al. 2013), the width of the ECM pores, the degree of ECM alignment as well as the ECM stiffness are fundamental parameters, which determine how and how much the ECM steers or inhibits the cell movement. Therefore, the cell needs to continuously adapt its shape and consequently its migratory behaviour. In tumorigenesis for instance, cancer cells develop an invasive behaviour, which allows them to enter and progressively invade healthy tissue as they are constantly exposed to biomechanical and biophysical stimuli. Such adaptation requires an internal reorganization of both the cytoskeleton and the embedded organelles, among which the nucleus is the stiffest and the most voluminous. Consequently, it has become essen-

Electronic supplementary material The online version of this article (doi:10.1007/s10237-014-0595-3) contains supplementary material, which is available to authorized users.

D. Aubry
Laboratoire MSSMat UMR CNRS 8579, Ecole Centrale Paris,
92295 Châtenay-Malabry, France

H. Thiam · M. Piel
Biologie systémique de la division et de la polarité cellulaire,
Institut Curie UMR 144, 12 Rue Lhomond, 75005 Paris, France

R. Allena (✉)
Arts et Métiers ParisTech, LBM, 151 Bd de l'hôpital,
75013 Paris, France
e-mail: Rachele.allena@ensam.eu

Published online: 04 June 2014

 Springer

tial to quantitatively assess the cell ability to deform as well as which mechanical forces the cell has to develop in order to move forward within a confined micro-structure.

In the last few years, several experimental studies have tried to provide such data. Systems like collagen gels or lattices are commonly used to simulate cell migration in confined connective tissues (Wolf et al. 2009). Although very simplified, such systems are highly complex and difficult to control since many physical parameters (i.e. gel density and elasticity, local constrictions) may affect the global mobility of the cell and furthermore fail to reproduce spatial tracks or obstacles (Provenzano et al. 2008; Wolf et al. 2009; Egeblad et al. 2010). More recently, it has been possible to better control, vary and tune the geometrical characteristics of the patterned micro-structure using micro-laser techniques (Irina et al. 2011) or photolithography (Heuzé et al. 2011). In the latter work, cells migrate through straight micro-channels made of silicone rubber (i.e. polydimethylsiloxane, PDMS), whose sub-cellular dimensions vary between 2 and 10 μm in width and highly depend on cell type. Such an approach has provided interesting results for cancer cells (Irimia and Toner 2009; Ronot et al. 2000), immune cells (Irimia et al. 2007; Faure-André et al. 2008) and neurons (Taylor et al. 2005). Micro-channels may be modulated in order to investigate specific biological problems such as trans-migration ability within a well-defined geometry or the influence of the substrate stiffness by letting channel material vary. Additionally, more complex geometries can be obtained to force the cell to take turns and explore its 2D confined environment.

From a numerical point of view, many models have been proposed to simulate single cell migration on 2D flat surfaces or in three-dimensional (3D) environment (Rangarajan and Zaman 2008). Such models have used different approaches resulting in force-based dynamics models (Zaman et al. 2005, 2006), stochastic models to simulate persistent random walks (Tranquillo and Lauffenburger 1987; Tranquillo et al. 1988; Stokes et al. 1991; Stokes and Lauffenburger 1991), models reproducing the movement of cancer cell spheroids (McElwain and Ponzio 1977; McElwain 1978; McElwain et al. 1979), Monte Carlo models (Zaman et al. 2007; Scianna and Preziosi 2013; Scianna et al. 2013) or purely mechanical models (Allena and Aubry 2012; Allena 2013). Active gel layers submitted to external forces have been used to represent actomyosin cells migrating in a free (Recho and Truskivsky 2013; Recho et al. 2013) or confined (Hawkins et al. 2009; Hawkins and Voituriez 2010) environment. Scianna and Preziosi (Scianna and Preziosi 2013) have presented a cellular potts model (CPM), which reproduces an experimental assay very similar to those used in (Taylor et al. 2005; Irimia et al. 2007; Faure-André et al. 2008; Irimia and Toner 2009; Rolli et al. 2010; Heuzé et al. 2011). In this model, the cell is modelled as a discrete physical unit, including the cytosol and the nucleus, while channels of different

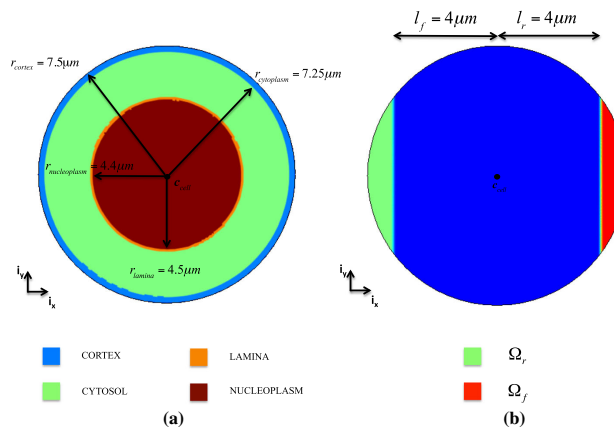
widths constitute the migration chamber. The authors have investigated the invasiveness of tumour cells by evaluating their displacement and velocity as well as their deformability, which seems to be strongly linked to the deformability of the nucleus. In (Tozluoğlu et al. 2013), a hybrid agent-based finite element model is proposed to evaluate the migration strategy of the cell in different environments such as confinement. The model is able to simulate both the protrusion–contraction and the membrane blebbing modes of migration. Therefore, the authors estimate the effects of the ECM geometry on the relationship between cell velocity, contractility and adhesion, and they also find interesting effects of membrane blebbing on cell velocity and morphology. Finally, in (Givero et al.), an energetic continuum approach is employed to investigate the necessary condition for which a cell migrate through a cylindrical channel. They consider the nucleus either as an elastic membrane surrounding a liquid droplet or as an incompressible elastic material. By taking into account and balancing different forces exerted by and on the cell during confined movement, they are able to determine the minimal size of the cylindrical structure and they observe that cell ability to migrate through it depends on both nucleus stiffness and adhesion to ECM.

1.1 Objective of the present work

In the present paper, a finite element model that reproduces the experimental set-up used in (Heuzé et al. 2011) for HeLa cells is proposed, which is based on the following hypotheses:

- the 2D geometry represents a top view of the global structure, and a plane stress hypothesis has been made;
- as in (Givero et al.), a purely mechanical approach is used to describe the cell behaviour. However, a different mathematical method is applied. In fact, the decomposition of the deformation gradient is employed to consider both the active (i.e. protrusion and contraction) and the elastic (i.e. strains generated by the interaction with the environment) strains undergone by the cell;
- contrary to previous works (Scianna and Preziosi 2013; Scianna et al. 2013; Tozluoğlu et al. 2013), the cell is modelled as a continuum. Nonetheless, both the cytoplasm and the nucleus have been originally represented through two characteristic functions, and a standard Maxwell model has been used to describe their viscoelastic behaviour (Allena and Aubry 2012; Allena 2013; Tozluoğlu et al. 2013);
- the cell is able to cyclically protrude and contract. Such active strains are triggered respectively by the polymerization and depolymerization of the actin filaments and are synchronized with the viscous adhesion forces between the cell and the substrate (Allena and Aubry 2012; Allena 2013);

Fig. 1 Geometry of the cell (a) and frontal and rear adhesion surfaces (b)



- the micro-channel is represented by two rigid walls, which are described by two characteristic functions, and exerts an additional normal viscous force on the cell boundaries when contact condition is fulfilled.

The main objective of our work is to assess the necessary conditions for the cell to enter into the channel and migrate through it. In order to do so, we test four different channels whose dimensions in width are i) larger than the cell diameter, ii) sub-cellular, iii) sub-nuclear and iv) much smaller than the nucleus diameter. We analyse the evolution of the cell morphology by consistently comparing it with experimental observations, and we classify the cell behaviour according to the covered distance inside the channel. Additionally, we evaluate both the cell-substrate and the cell-channel surface forces during migration, and we find that there exists a link between such forces and the changes in cell shape, which may be essential in determining the invasive behaviour of the cell.

The paper is organized as follows: in Sect. 2, the geometry of the cell, the constitutive model and the mechanical approach are described. In Sect. 3, the results of the numerical simulations are presented. First, we analyse the cell behaviour (Sect. 3.1). Second, we evaluate the mechanical cell-substrate and cell-channel surface forces (Sect. 3.2), and we find the necessary conditions determining whether the cell is penetrating, invasive or permeative.

2 The model

In this section, we provide the general framework of the model. First, we describe the geometry of the cell includ-

ing the cytoplasm and the nucleus. Second, we focus on the mechanics of the system. Specifically, we introduce the standard Maxwell models, which are used to reproduce the viscoelastic behaviour of the nucleus and the cytoplasm. Third, the intra-synchronization is presented. As in our previous works (Allena and Aubry 2012; Allena 2013), this represents the key ingredient of the cell movement. In fact, we show how the cyclic active strains (i.e. protrusion and contraction) are strongly coupled with the viscous forces generated by the cell to adhere to the substrate and necessary to efficiently move forward. Finally, we describe the geometry of the micro-channel and the associated viscous force exerted on the cell boundaries, which allows the cell to squeeze and pass (or not) through it.

2.1 Cell geometry

HeLa cells are human cells with a rather rounded initial shape and a diameter of about $15 \mu\text{m}$ (Ronot et al. 2000; Ngali et al. 2013). For the numerical model, the geometry of the cell has been simplified by a circular domain Ω_{cell} of radius r_{cell} (Fig. 1a). Here, we consider two main components of the cell: the cytoplasm ($\Omega_{\text{cytoplasm}}$) and the nucleus (Ω_{nucleus}) (Fig. 1a, Sect. 5.1). Additionally, the cell cyclically generates a frontal (Ω_f) and a rear (Ω_r) adhesion region in order to move forward (Allena and Aubry 2012; Allena 2013) (Fig. 1b, Sect. 5.1).

2.2 Constitutive model and mechanics of the cell

Both the nucleus and the cytoplasm are assumed to be viscoelastic materials, and their behaviour is described by two

standard Maxwell models (Larson 1998) (Sect. 5.2). On one hand, the nucleus is composed by the nuclear lamina Ω_{lamina} (the solid phase, Sects. 5.1 and 5.2), which surrounds the viscoelastic nucleoplasm $\Omega_{\text{nucleoplasm}}$ (the fluid phase, Sects. 5.1 and 5.2). On the other hand, the cytoplasm is essentially made of a solid phase represented by the cell cortex Ω_{cortex} (Sects. 5.1 and 5.3) and a fluid-like phase, the cytosol Ω_{cytosol} (Sects. 5.1 and 5.3) in which the organelles such as the actin filaments are embedded. As in our previous works (Allena and Aubry 2012; Allena 2013), we assume that the polymerization of the actin filaments inside the cytosol, which mostly occurs at the front of the cell (Schaub et al. 2007), generates the protrusive force at the leading edge, and their contraction due to binding of myosin generates the contractile stress at the rear of the cell (Mogilner 2009). Such active strains triggering the deformability of the cell are then described through a deformation tensor $\mathbf{F}_{\text{cytosol},a}$ (Sects. 2.3 and 5.3) in the fluid-like branch of the symbolic standard Maxwell model of the cytoplasm.

As described in (Allena and Aubry 2012; Allena 2013), the global equilibrium of the system is expressed as

$$\rho \mathbf{a} = \text{Div}_p \left(\mathbf{J} \boldsymbol{\sigma} \mathbf{F}^{-T} \right) + \mathbf{f}_{\text{adh}} + \mathbf{f}_{\text{channel}} \quad (1)$$

where ρ is the cell density, \mathbf{a} is the acceleration, Div_p is the divergence with respect to the initial position \mathbf{p} , \mathbf{J} is the determinant of the deformation gradient \mathbf{F} and \mathbf{A}^{-T} denotes the inverse transpose of the matrix \mathbf{A} (Holzapfel 2000; Taber 2004). \mathbf{f}_{adh} and $\mathbf{f}_{\text{channel}}$ indicate, respectively, the viscous adhesion forces between the cell and the substrate (Sect. 2.3) and the viscous force exerted by the channel on the cell boundaries (Sect. 2.4). Here, all the body forces but the inertial effects are neglected (Gracheva and Othmer 2004; Allena and Aubry 2012; Allena 2013).

2.3 Intra-synchronization

To describe the oscillating movement of the cell, two main assumptions have been made:

- 1) the active strains of protrusion and contraction are only applied in the cytosol. In fact, as in our previous works (Allena and Aubry 2012; Allena 2013), we assume that the oscillatory movement of the cell is triggered by the periodic polymerization and depolymerization of the actin filaments, which are embedded in the cytosol. The former only occurs at the front of the cell, while the latter takes place from the front towards the rear of the cell. Therefore, although the nucleus does not undergo any active strain, it will interact with the surrounding cytosol apart from the protrusion phase (Friedl et al. 2011);
- 2) although the cell may form multiple pseudopodia (Allena 2013), here only one is generated in the direction of

migration, which, to reproduce the experimental set-up where the cell is constrained into a micro-channel (Heuzé et al. 2011), corresponds to the horizontal axis i_x .

Therefore, the solid active deformation tensor $\mathbf{F}_{\text{cytosol},a}$ reads

$$\mathbf{F}_{\text{cytosol},a} = \begin{cases} e_{a0} \sin \left(2\pi \frac{t}{T} \right) h_{\text{cytosol,front}} i_x \otimes i_x & \text{if } \sin \left(2\pi \frac{t}{T} \right) > 0 \\ \frac{e_{a0}}{2} \sin \left(2\pi \frac{t}{T} \right) h_{\text{cytosol}} i_x \otimes i_x & \text{if } \sin \left(2\pi \frac{t}{T} \right) < 0 \end{cases} \quad (2)$$

where e_{a0} is the amplitude of the active strain, t is time, T is the migration period, h_{cytosol} and $h_{\text{cytosol,front}}$ are two characteristic functions (Sect. 5.1) and \otimes indicates the tensorial product.

As shown in (Allena and Aubry 2012), in order to be able to effectively migrate, the cell must adhere on the substrate otherwise it would only deform on place. Thus, an intra-synchronization is required which coordinates the cyclic protrusion–contraction deformations with the adhesion forces \mathbf{f}_{adh} (Eq. 1) generated between the cell frontal and rear adhesion surfaces and the underneath substrate. As in previous works (Phillipson et al. 2006; Sakamoto et al. 2011; Allena and Aubry 2012; Allena 2013), such forces are assumed to be viscous and may be distinguished into a frontal ($\mathbf{f}_{\text{adh},f}$) and a rear ($\mathbf{f}_{\text{adh},r}$) force as follows

$$\begin{aligned} \mathbf{f}_{\text{adh},f}(\mathbf{n}_{\text{cell}}) &= -\mu_{\text{adh}} h_{\text{sync}} \left(-\frac{\partial e_a}{\partial t} \right) \mathbf{v} \quad \text{on } \Omega_f \\ \mathbf{f}_{\text{adh},r}(\mathbf{n}_{\text{cell}}) &= -\mu_{\text{adh}} h_{\text{sync}} \left(\frac{\partial e_a}{\partial t} \right) \mathbf{v} \quad \text{on } \Omega_r \end{aligned} \quad (3)$$

with \mathbf{n}_{cell} the outward normal to the cell boundary, μ_{adh} the friction coefficient and \mathbf{v} the velocity. The characteristic function h_{sync} is the key ingredient of the preceding equations since it couples the adhesion forces with the active strains, which results in the intra-synchronization mentioned above. Thus, we observe two main phases during the migratory movement of the cell: i) the protrusion and the adhesion at the rear edge; ii) the contraction and the adhesion at the frontal edge.

2.4 Micro-channel

Here, we want to reproduce the micro-channel-based assay presented in (Heuzé et al. 2011). Thus, the micro-channel domain Ω_{channel} is represented by two pseudo-elliptical rigid walls with no top roof (Sect. 5.4).

When the cell enters into the micro-channel, it is then submitted to a viscous force $\mathbf{f}_{\text{channel}}$ (Eq. 1), which can be distinguished into an upper ($\mathbf{f}_{\text{channel},u w_i}$) and a lower ($\mathbf{f}_{\text{channel},l w_i}$) force as follows

$$\begin{aligned}
 & f_{\text{channel},uw_i}(\mathbf{n}_{uw,i}) \\
 &= -\mu_{\text{channel}} \frac{1}{(l_{w,i} + 1)^8 + \alpha} \left(\frac{\partial \mathbf{u}}{\partial t}, \mathbf{n}_{uw,i} \right) \mathbf{n}_{uw,i} \quad \text{on } \partial\Omega_{uw,i} \\
 & f_{\text{channel},lw_i}(\mathbf{n}_{lw,i}) \\
 &= -\mu_{\text{channel}} \frac{1}{(l_{w,i} + 1)^8 + \alpha} \left(\frac{\partial \mathbf{u}}{\partial t}, \mathbf{n}_{lw,i} \right) \mathbf{n}_{lw,i} \quad \text{on } \partial\Omega_{lw,i}
 \end{aligned} \tag{4}$$

where μ_{channel} is the viscosity of the micro-channel, $l_{w,i}$ and $l_{l,i}$ are two level set functions (Sect. 5.4), α is a constant and $\mathbf{n}_{uw,i}$ and $\mathbf{n}_{lw,i}$ are the outward normal to the boundaries $\partial\Omega_{uw,i}$ and $\partial\Omega_{lw,i}$ of the upper and lower wall, respectively, which are here originally calculated (Sect. 5.4) (the subscript 'i' indicates the channel number as explained in Sect. 3.1 and 5.4). Finally, (\mathbf{a}, \mathbf{b}) defines the scalar product between two vectors.

3 Results

The numerical simulations have been run using the finite element software COMSOL Multiphysics® 3.5a. As described in Sect. 2.2, the viscoelastic behaviour of the cell has been taken into account. The components of the cytoplasm and the nucleus have been implicitly described by specific characteristic functions (Sect. 5.1) in order to be able to define the parameters of the standard Maxwell models. The radius r_{cortex} , r_{cytosol} , r_{lamina} and $r_{\text{nucleoplasm}}$ of the HeLa cell have been fixed to 7.5, 7.25, 4.5 and 4.4 μm , respectively. Then, the cell cortex and the nuclear lamina have a thickness t_{cortex} and t_{lamina} of 0.25 μm (Pesens and Hoh 2005; Tinevez et al. 2009; Jiang and Sun 2013) and 0.1 μm (Righolt et al. 2010), respectively. The nominal values of the Young moduli $E_{\text{cortex},0}$ of the cell cortex and $E_{\text{cytosol},0}$ of the cytosol have been chosen equal to 100 and 10 Pa (Crick and Hughes 1950). For the nucleus, assuming that its stiffness is mostly provided by the nuclear lamina, we have set $E_{\text{lamina},0}$ and $E_{\text{nucleoplasm},0}$ to 3,000 Pa (Caille et al. 2002; Dahl et al. 2008) and 25 Pa (Vaziri et al. 2006), respectively. According to a simple spatial homogenization approach (Christensen 1991; Larson 1998), such moduli have then been recalculated according to the surface occupied by each component in the cell to obtain E_{cortex} , E_{cytosol} , E_{lamina} and $E_{\text{nucleoplasm}}$ (Table 1). Since we consider here that the cell cortex and the nuclear lamina are rather elastic, while the cytosol and the nucleoplasm are rather viscoelastic, the Poisson's ratios ν_{cortex} and ν_{lamina} have been set to 0.3, while ν_{cytosol} and $\nu_{\text{nucleoplasm}}$ to 0.4. The viscosities μ_{cytosol} and $\mu_{\text{nucleoplasm}}$ are equal to 3×10^5 Pa-s (Bausch et al. 1999; Drury and Dembo 2001). The cell density ρ has been set to 1,000 kg/m^3 (Fukui et al. 2000), and the viscous friction coefficient μ_{adh} is equal 10⁸ Pa-s/m. Finally, the intensity of the active strain e_{a0} and

the migration period T have been chosen equal to 0.2 and 600 s, respectively, in order to obtain an average migration velocity of the order of magnitude of the one experimentally observed for HeLa cells (Ronot et al. 2000; Ngalmim et al. 2013).

All the parameters of the model have been reported in Table 1.

3.1 Cell behaviour and morphology

As described in Sect. 2.4, the channel is represented by two pseudo-elliptical walls ($l_{uw,i}$ and $l_{lw,i}$), whose semi-axes a and b are 30 and 2 μm long, respectively.

For the simulations, only two-thirds of the total length of the channel are considered, which corresponds to 40 μm .

By letting the position of the upper and lower walls centres $\mathbf{c}_{uw,i}$ and $\mathbf{c}_{lw,i}$ vary, we have tested four channels with different width as follows:

- *channel 16* has a width $W_{c,1}$ of 16 μm , which is larger than the cell diameter with $\mathbf{c}_{uw,16}$ (42.5, 10 μm) and $\mathbf{c}_{lw,16}$ (42.5 μm , –10 μm);
- *channel 12* has an intermediate width $W_{c,2}$ of 12 μm , which is smaller than the cell diameter and bigger than the nucleus diameter, with $\mathbf{c}_{uw,12}$ (42.5, 8 μm) and $\mathbf{c}_{lw,12}$ (42.5, –8 μm);
- *channel 7* has a width $W_{c,3}$ of 7 μm , which is slightly smaller than the nucleus diameter with $\mathbf{c}_{uw,7}$ (42.5, 5.5 μm) and $\mathbf{c}_{lw,7}$ (42.5, –5.5 μm);
- *channel 4* has a width $W_{c,4}$ of 4 μm , which is much smaller than the nucleus diameter with $\mathbf{c}_{uw,4}$ (42.5, 4 μm) and $\mathbf{c}_{lw,4}$ (42, –4 μm).

For the first set of simulations, the viscous friction coefficient μ_{channel} and the constant α have been set equal to 10¹⁰ Pa-s/m and 0.1, respectively.

We have studied the cell behaviour for each of the previous configurations by analysing specific aspects of the confined movement, and the main results are listed in Table 2.

First, we have evaluated the efficiency of the migration in terms of covered distance. In Fig. 3, the total displacement of the frontal edge of the cell is reported for the four simulations. Then, as previously proposed by (Rolli et al. 2010; Scianna et al. 2013), we can classify the cell as permeative, invasive or penetrating. The permeative behaviour is observable for *channel 16* and *channel 12* (Fig. 2a, b) where the cell reaches the other side of the channel by covering a distance of 38 μm in 9,000 s (blue and red lines in Fig. 3, and Movie 1 and Movie 2, respectively). The invasive behaviour occurs when the cell enters into the channel, but it is not able to achieve the other side (Fig. 2c). This is the case of *channel 7* where the cell only migrates over 25 μm in 6,000 s (green line in Fig. 3 and Movie 3). Finally, the cell is penetrating (Fig. 2d)

Table 1 Main geometrical and material parameters of the model

Parameter	Description	Value (unit)	References
r_{cell}	Cell radius	$7.5 \mu\text{m}$	
r_{cortex}	Cortex radius	$7.5 \mu\text{m}$	
r_{cytosol}	Cytosol radius	$7.25 \mu\text{m}$	
r_{lamina}	Lamina radius	$4.5 \mu\text{m}$	
$r_{\text{nucleoplasm}}$	Nucleoplasm radius	$4.4 \mu\text{m}$	
t_{cortex}	Cortex thickness	$0.25 \mu\text{m}$	Pesen and Hoh (2005), Tinevez et al. (2009), Jiang and Sun (2013)
t_{lamina}	Lamina thickness	$0.1 \mu\text{m}$	Righolt et al. (2010)
l_f	Distance cell centre— boundary of frontal adhesion region	$4 \mu\text{m}$	
l_r	Distance cell centre— boundary of rear adhesion region	$4 \mu\text{m}$	
Ω_{cell}	Initial cell area	$176.6 \mu\text{m}^2$	
Ω_{cortex}	Initial cortex area	$11.6 \mu\text{m}^2$	
Ω_{cytosol}	Initial cytosol area	$101.4 \mu\text{m}^2$	
$\Omega_{\text{cytoplasm}}$	Initial cytoplasm area	$113 \mu\text{m}^2$	
Ω_{lamina}	Initial lamina area	$2.8 \mu\text{m}^2$	
$\Omega_{\text{nucleoplasm}}$	Initial nucleoplasm area	$60.8 \mu\text{m}^2$	
Ω_{nucleus}	Initial nucleus area	$63.6 \mu\text{m}^2$	
Ω_f	Initial frontal adhesion region area	$31 \mu\text{m}^2$	
Ω_r	Initial rear adhesion region area	$31 \mu\text{m}^2$	
$E_{\text{cortex},0}$	Nominal cortex Young modulus	100 Pa	
$E_{\text{cytosol},0}$	Nominal cytosol Young modulus	10 Pa	Crick and Hughes (1950)
$E_{\text{lamina},0}$	Nominal lamina Young modulus	3,000 Pa	
$E_{\text{nucleoplasm},0}$	Nominal nucleoplasm Young modulus	25 Pa	Caille et al. (2002), Dahl et al. (2008)
E_{cortex}	Equivalent cortex Young modulus	15 Pa	Vaziri et al. (2006)
E_{cytosol}	Equivalent cytosol Young modulus	8 Pa	
E_{lamina}	Equivalent lamina Young modulus	196 Pa	
$E_{\text{nucleoplasm}}$	Equivalent nucleoplasm Young modulus	23 Pa	
ν_{cortex}	Cortex Poisson ratio	0.3	
ν_{cytosol}	Cytosol Poisson ratio	0.4	
ν_{lamina}	Lamina Poisson ratio	0.3	
$\nu_{\text{nucleoplasm}}$	Nucleoplasm Poisson ratio	0.4	
μ_{cytosol}	Cytosol viscosity	$3 \times 10^5 \text{ Pa}\cdot\text{s}$	Bausch et al. (1999), Drury and Dembo (2001)
$\mu_{\text{nucleoplasm}}$	Nucleoplasm viscosity	$3 \times 10^5 \text{ Pa}\cdot\text{s}$	Bausch et al. (1999), Drury and Dembo (2001)
ρ	Cell density	$1,000 \text{ kg/m}^3$	Fukui et al. (2000)
e_{a0}	Amplitude of the active strain	0.8	
T	Migration period	600 s	
μ_{adh}	Cell friction coefficient	$10^8 \text{ Pa}\cdot\text{s/m}$	
a	Semi-axis of the pseudo-elliptical walls	$30 \mu\text{m}$	

Table 1 continued

Parameter	Description	Value (unit)	References
b	Semi-axis of the pseudo-elliptical walls	$2\mu\text{m}$	
x_0	x-coordinate of the pseudo-elliptical walls centre	$42.5\mu\text{m}$	
$y_{uw0,i}$	y-coordinate of the upper pseudo-elliptical wall centre	$y_{uw0,1}: 10$ $y_{uw0,2}: 8$ $y_{uw0,3}: 6$ $y_{uw0,4}: 4\mu\text{m}$	
$y_{lw0,i}$	y-coordinate of the lower pseudo-elliptical wall centre	$y_{lw0,1}: -10$ $y_{lw0,2}: -8$ $y_{lw0,3}: -6$ $y_{lw0,4}: -4\mu\text{m}$	
μ_{channel}	Channel viscous friction coefficient	$10^{10}\text{Pa}\cdot\text{s}/\text{m}$	
α		0.1	
$W_{c,16}$	Width of channel 1	$16\mu\text{m}$	
$W_{c,12}$	Width of channel 3	$12\mu\text{m}$	
$W_{c,7}$	Width of channel 3	$8\mu\text{m}$	
$W_{c,4}$	Width of channel 4	$4\mu\text{m}$	

Table 2 Main numerical results for the different channels

	Channel 16	Channel 12	Channel 7	Channel 4
Displacement (μm)	38	38	25	7.5
Protrusion average velocity ($\mu\text{m}/\text{s}$)	0.0055	0.0051	0.0055	0.0053
Contraction average velocity ($\mu\text{m}/\text{s}$)	0.0102	0.0122	0.0118	0.0115
t_{contact} (s)	–	1,950	1,250	1,220
$t_{\text{penetration}}$ (s)	3,900	4,600	4,610	–
T_{entry} (s)	–	2,650	3,360	–
Maximal ratio cell area/nucleus area	3.29	2.89	2.25	3.29
Minimal ratio cell area/nucleus area	2.11	1.93	1.35	2.11
t_{regime1} (s)	–	1,800	1,250	1,230
t_{regime2} (s)	–	2,450	1,350	1,250
t_{regime3} (s)	–	2,600	1,850	–

when only part of the body (or nothing) penetrates within the channel as it takes place for *channel 4* (purple line in Fig. 3 and Movie 4) where the total displacement is only equal to $7.5\mu\text{m}$.

In Fig. 4, the trend of the cell average velocity is represented. As a general remark, the velocity during the contraction phase is slightly higher than during the protrusion phase, since the former only involves the frontal portion of the cytoplasm (see Sect. 2.3). While the average protrusion velocity remains rather constant for all the channels (roughly $5 \cdot 10^{-3}\mu\text{m}/\text{s}$), the average contraction velocity varies between a minimal value of about $10^{-2}\mu\text{m}/\text{s}$ for channel 16 (blue line Fig. 4) and a maximal value of $1.2 \cdot 10^{-2}\mu\text{m}/\text{s}$ for channel 12 (red line Fig. 4). Additionally, for *channel 7* (green line Fig. 4), we observe a peak of the velocity up to $1.3 \cdot 10^{-2}\mu\text{m}/\text{s}$ at the entrance of the channel, while afterwards the cell acquires again a constant

velocity. Such values are of the same order of magnitude of those experimentally observed for HeLa cells (Ronot et al. 2000; Ngali et al. 2013).

Second, for each configuration, we have quantified the entry time (T_{entry}), which has been defined by Lautenschläger et al. (Lautenschläger et al. 2009) as the time interval between the first contact of the cell with the channel walls (t_{contact}) and the complete penetration of the cell body within the channel ($t_{\text{penetration}}$). For *channel 16* and *channel 4*, such a parameter cannot be evaluated since the cell either does not enter in contact with the channel (*channel 16*) or does not migrate through it (*channel 4*). For *channel 12* and *channel 7*, we found 2,650 and 3,360s respectively, which confirms that the smaller the channel, the more difficult is for the cell to get in. In fact, the contact cell channel occurs earlier for *channel 7* than for *channel 12* ($t_{\text{contact}} = 1,250\text{s}$ versus $t_{\text{contact}} = 1,950\text{s}$), while $t_{\text{penetration}}$ is almost the same

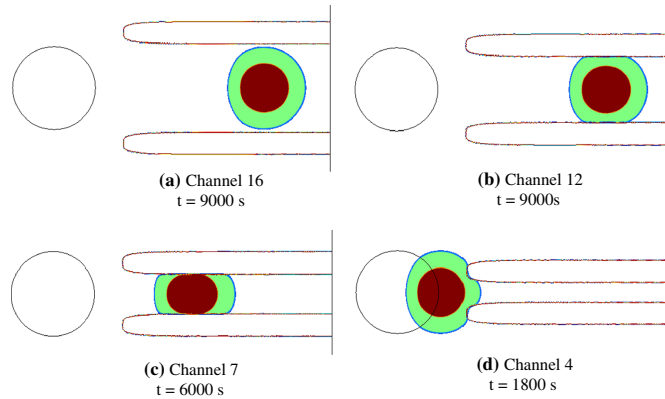


Fig. 2 Snapshots of the permeative (a and b), invasive (c) and penetrating (d) cell

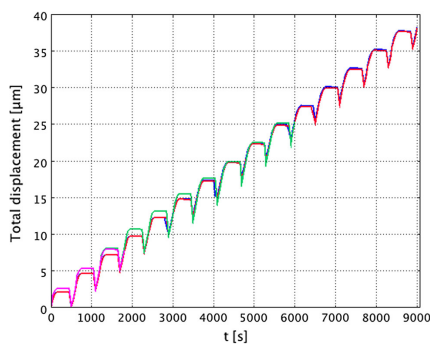


Fig. 3 Total displacement of the cell for channel 16 (blue line), channel 12 (red line), channel 7 (green line) and channel 4 (purple line)

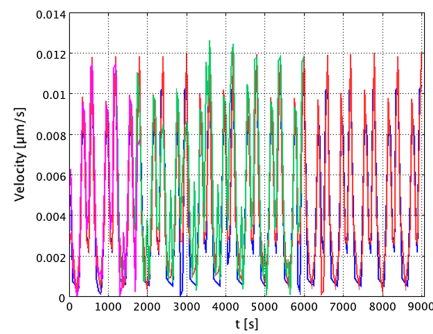


Fig. 4 Migration average velocity of the cell for channel 16 (blue line), channel 12 (red line), channel 7 (green line) and channel 4 (purple line)

for both channels ($t_{\text{penetration}} = 4,610$ s versus $t_{\text{penetration}} = 4,600$ s).

Third, we have evaluated the ratio between the total cell area and the nucleus area. At the initial configuration, such ratio is equal to 2.8, but it undergoes an oscillatory variation due to the protrusion–contraction movement of the cell. In the case of *channel 16* (Fig. 5, blue line), it varies between a maximal value of 3.3 during protrusion and a minimal value of 2.1 during contraction. Here, such values are the same at the end of each phase during the whole simulation since the cell overall deformation is not perturbed by the contact with channel. For *channel 12* instead, we observe a decrease of the maximal value of the ratio to 2.9 once the cell has completely

entered the channel ($t_{\text{penetration}} = 4,600$ s, Fig. 5, red line), while the minimal value decreases to 1.9. Such drop is mainly due to a bigger shrinkage of the cell cytoplasm rather than of the nucleus due to the subcellular dimensions of the channel. However, in the case of *channel 7* (Fig. 5, green line), both cytoplasm and nucleus contribute to the progressive decrease of the ratio. In fact, the nucleus must squeeze too to move forward since the channel has sub-nuclear dimensions. Then, the maximal and minimal values of the ratio at $t_{\text{penetration}} = 4,610$ s decrease down to 2.25 and 1.35, respectively. For *channel 4* (Fig. 5, purple line), the ratio evolution is the same as for *channel 16* since the cell is not able to penetrate the channel and neither cytoplasm nor nucleus do not undergo large deformation.

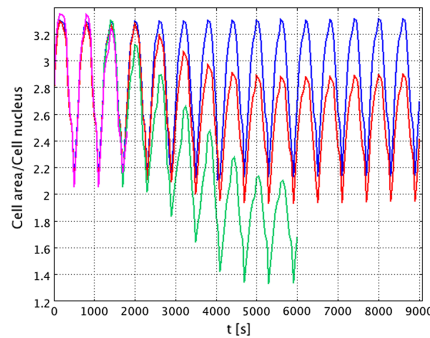


Fig. 5 Ratio between the cell area and the nucleus area for *channel 16* (blue line), *channel 12* (red line), *channel 7* (green line) and *channel 4* (purple line)

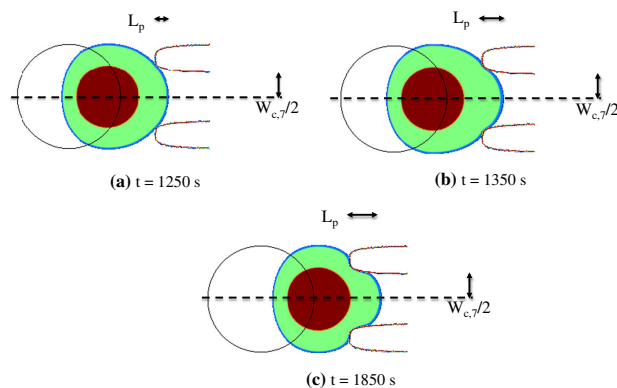
Finally, we have analysed the morphology of the cell relative to the channel, which can actually be divided into three regimes. The first regime is observed when the length L_p of the cell protrusion into the channel is smaller than half the width of the channel $W_{c,i}$ ($2L_p/W_{c,i} < 1$), and it has been indicated as t_{regime1} . The second regime occurs when $2L_p/W_{c,i} = 1$, and the protrusion is hemicircular with radius equal to $W_{c,i}$ (t_{regime2}). Finally, the third regime is obtained when $2L_p/W_{c,i} > 1$ (t_{regime3}). At this point, the first half of the protrusion is rectangular of length $W_{c,i}$ and the second half is hemicircular of radius L_c .

In the case of *channel 16*, the migration mode and the morphology of the cell do not change and are very similar to those observed for cell migrating over flat surfaces (Allena and Aubry 2012; Allena 2013). In fact, there is no contact

between the cell cortex and the channel walls, and thus, the cell body is not perturbed during its movement. This is not the case for *channel 12* and *channel 7* where the cell needs to squeeze in order to enter the channel. For *channel 12*, regime 1 is observed at $t_{\text{regime1}} = 1,800$ s, while L_p becomes equal to $W_{c,2}/2$ at $t_{\text{regime2}} = 2,450$ s. Starting from $t_{\text{regime3}} = 2,600$ s, regime 3 is achieved and the protrusion is clearly half rectangular and half hemicircular. For *channel 7* (Fig. 6), steps occur earlier. In fact, regime 1 and regime 2 are reached at $t_{\text{regime1}} = 1,250$ s and $t_{\text{regime2}} = 1,350$ s, respectively, while regime 3 starts at $t_{\text{regime3}} = 1,850$ s. For *channel 4* instead, only regime 1 and 2 observed at $t_{\text{regime1}} = 1,230$ s and $t_{\text{regime2}} = 1,250$ s, respectively. The reason why regime 3 is not achieved is mainly due to the fact that, despite the cell tries to enter the channel by protruding and contracting, the force f_{channel} exerted by the channel walls on the cell boundaries is too high. This means that reaching regime 3 is a necessary, but not sufficient condition for the cell to be invasive. In fact, a second necessary condition need to be satisfied, that is, the cell-channel surface force f_{channel} at t_{regime3} must be low enough for the cell to enter.

We have also been able to experimentally observe such changes in morphology for two types of cells using a micro-channel-based assay as proposed in (Heuzé et al. 2011). Figure 7a–d shows the successive steps (top view) of bone marrow-derived dendritic cells (BDMCs) migration through a $5\mu\text{m}$ (Fig. 7a–b) and $1.5\mu\text{m}$ (Fig. 7c, d) wide micro-channel. It is possible to clearly distinguish the three regimes undergone by the whole cell body (Fig. 7b, d) and by the stained nucleus (Fig. 7a, c). Figure 7e shows instead a sagittal view of the successive steps of a HeLa cell migrating through a $20\mu\text{m}$ wide micro-channel. We observe the deformation undergone by the stained nucleus along the z axis. In fact, in this specific case, the cell is confined in the x – y plane,

Fig. 6 The three regimes of the cell morphology during the migration through *channel 7*



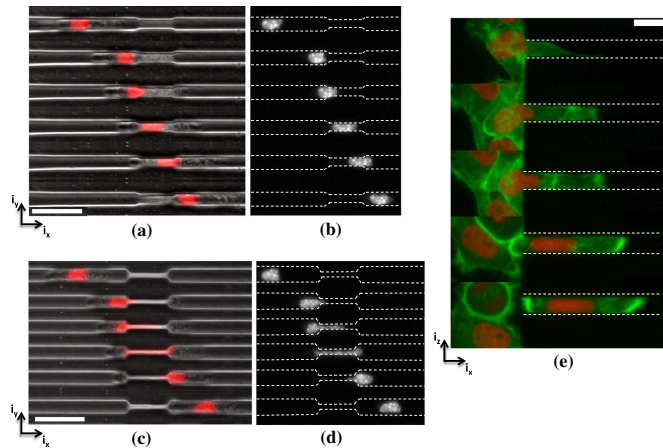


Fig. 7 (a-d) Top view of successive steps of a bone marrow-derived dendritic cell (BMDC) migration (from the *left* to the *right*) through a $5\mu\text{m}$ a-b and $1.5\mu\text{m}$ c-d wide micro-channels. Nuclear staining with Hoechst (a and c) (scale bar: $30\mu\text{m}$) e Sagittal view of successive steps

of a HeLa cell entering (from the *left* to the *right*) a $20\mu\text{m}$ wide micro-channel (HeLa Histone2B-mcherry (nucleus), MyrPalm-GFP (plasma membrane), scale bar: $15\mu\text{m}$)

Table 3 Values of the mechanical forces for the different channels

	Channel 16	Channel 12	Channel 7	Channel 4
Maximal frontal cell-substrate surface force (Pa)	10	10	10	10
Maximal rear cell-substrate surface force (Pa)	4	4	4	4
Maximal cell-channel surface force at t_{contact} (Pa)	–	3.3	3.1	7.2
Maximal cell-channel surface force at $t_{\text{penetration}}$ (Pa)	–	3.3	3.9	–
Average cell-substrate surface force between t_{contact} and $t_{\text{penetration}}$ (Pa)	–	3.3	3.3	3.3
Average cell-channel surface force between t_{contact} and $t_{\text{penetration}}$ (Pa)	–	2.5	3.2	$t_{\text{contact}} - t_{\text{regime2}}$ 4.5
Absolute maximal cell-channel surface force (Pa)	–	4.2	6.2	8.6

but also in the x - z plane. Although such an aspect has not been numerically considered so far, we are currently working to improve the model in order to have a three-dimensional representation of the cell and the micro-channel and therefore being able to implement this further confinement

3.2 Mechanical forces

In this section, we try to evaluate the cell-substrate and cell-channel surface forces, in particular during the time interval

between t_{contact} and $t_{\text{penetration}}$ in which t_{regime3} is included. The main values are summarized in Table 3.

Some general remarks may be pointed out:

- given the asymmetry of the active strain (Sect. 2.3) and the equation expressing the cell-substrate surface forces (Eq. 3), we found 10 and 4 Pa, respectively, at the front and rear edge of the cell. Additionally, such values do not change from one configuration;
- the cell-channel surface force increases as the channel width $W_{c,i}$ decreases (maximal absolute value of 4.25,

6.25 and 8.5 Pa for *channel 12*, *channel 7* and *channel 4*, respectively);

- as mentioned in Sect. 3.1, the necessary condition for the cell to be invasive is that the average cell-channel surface force at t_{regime3} must be lower than the average cell-substrate surface force at the same time point. This allows the cell to pull enough to penetrate within the channel without being obstructed by the channel. Since t_{regime3} is included in the time interval between t_{contact} and $t_{\text{penetration}}$, we have calculated the average cell-channel surface force during this period. For *channel 12* and *channel 7*, we have found an average value for the cell-channel surface force of about 2.5 Pa and 3.2, respectively, which is lower than the average cell-substrate surface force of 3.3 Pa. As a result, the cell is able to enter the channel. For *channel 4*, since the cell-channel surface force between t_{contact} and $t_{\text{penetration}}$ cannot be calculated, we have evaluated it between t_{contact} and t_{regime2} finding an average value of 4.5 Pa and a maximal value of 8.6 Pa, which is twice the cell-substrate surface force. Therefore, the cell is stuck at the entrance of the channel and shows a penetrating behaviour;
- once the cell has completely penetrated into the channel, the upper and lower central boundaries of the cell come very close or directly in contact with the nucleus, which is the stiffest component of the system. Then, a higher cell-channel surface force is necessary at this specific region to maintain the cell squeezing during the whole migration process and in order for the cell to be permeative. This is the case for *channel 12* for which the cell is able to reach the opposite end of the channel (Movie 5). However, for *channel 7*, the cell-channel surface force is slightly higher at the rear of the cell. Thus, the cell is slowed down and shows a penetrating behaviour (Movie 6).

For *channel 16*, only the cell-substrate surface force can be evaluated while the cell-channel surface force is null since no contact between the cell boundaries and the channel walls occurs.

4 Conclusions

In this paper, we have proposed a 2D mechanical model to simulate the migration of HeLa cell under confinement. The model reproduces the set-up used in a micro-channel assay as presented in (Heuzé et al. 2011). As in our previous works (Allena and Aubry 2012; Allena 2013), the cell is modelled as continuum and a standard Maxwell model is used to describe the mechanical behaviour of the cytoplasm (including active strains) and the nucleus. The cell is able to cyclically develop protrusion–contraction strains, which are synchronized with

the adhesion forces between the cell and the substrate. By approaching the channel, which is represented here by two pseudo-elliptical rigid walls, the cell is submitted to an additional viscous force. We have tested four channels whose dimensions in terms of width are larger than the cell diameter (*channel 16*), sub-cellular (*channel 12*), sub-nuclear (*channel 7*) and much smaller than the nucleus diameter (*channel 4*). We have analysed the cell behaviour and classified it as permeative (*channel 16* and *channel 12*), invasive (*channel 7*) or penetrating (*channel 4*) according to the distance covered by the cell inside the channel. From a morphological point of view, we have identified three different regimes in relation to the ratio between the cell protrusion length in the channel and the width of the channel. Additionally, we have evaluated the evolution of the cell shape and the cell-substrate and cell-channel surface forces between the first contact between the cell and the channel (t_{contact}) and the complete penetration of the cell body within the channel ($t_{\text{penetration}}$).

Therefore, we have been able to define the necessary conditions in order for the cell to be invasive or permeative. In the first case, two main conditions must be satisfied: i) regime 3 (i.e. cell protrusion length in the channel larger than half the channel width) has to be achieved, and ii) simultaneously, the cell-substrate surface force must be higher than the cell-channel surface force so that the cell is able to pull on the substrate and enter into the channel. For the second behaviour to occur, a further condition must be satisfied, that is, the cell-channel surface force during the whole migration has to be maximal along the upper and lower central boundaries of the cell. Those boundaries may come very close or directly in contact with the cell nucleus, which is the stiffest component of the system. Then, a larger force is required to maintain the squeezed cell shape.

Despite the consistent results shown in the present paper, our model still presents some limitations. Firstly, the geometry is 2D, which does not allow considering a top-roofed micro-channel and the cell deformation in the third direction. Secondly, the active strains of protrusion and contraction have been defined through a sinusoidal function, which may lead to a rather stable periodic deformation of the cytoplasm and consequently of the nucleus. In order to control the effects of such a phenomenon, some stochastic active input close to cell perception may be introduced and improve the global movement. Finally, so far all the cell components have been considered as viscoelastic materials. However, the nucleus may be able to adapt its deformation to the forces exerted by the micro-channel on the cell boundaries. Therefore, a viscoplastic behaviour with restoration (Mandel 1972; Lubliner 2008) would probably be more appropriate. We are currently working on this aspect in order to be able to investigate the ability of the cell to penetrate micro-channels with significant sub-nuclear dimensions.

5 Appendix

5.1 Geometry of the cell

For any spatial point \mathbf{p} , the four components of the cell body (the cortex Ω_{cortex} , the cytosol Ω_{cytosol} , the lamina Ω_{lamina} and the nucleoplasm $\Omega_{\text{nucleoplasm}}$) are described through characteristic functions (i.e. composition of a Heaviside and a level set function (Allena 2013)) as follows

$$h_{\text{cortex}}(\mathbf{p}) = \begin{cases} 1 & \text{if } r_{\text{cytoplasm}}^2 < \|\mathbf{p} - \mathbf{c}_{\text{cell}}\| < r_{\text{cortex}}^2 \\ 0 & \text{otherwise} \end{cases} \quad (5)$$

$$h_{\text{cytosol}}(\mathbf{p}) = \begin{cases} 1 & \text{if } r_{\text{lamina}}^2 < \|\mathbf{p} - \mathbf{c}_{\text{cell}}\| < r_{\text{cytosol}}^2 \\ 0 & \text{otherwise} \end{cases} \quad (6)$$

$$h_{\text{lamina}}(\mathbf{p}) = \begin{cases} 1 & \text{if } r_{\text{nucleoplasm}}^2 < \|\mathbf{p} - \mathbf{c}_{\text{cell}}\| < r_{\text{lamina}}^2 \\ 0 & \text{otherwise} \end{cases} \quad (7)$$

$$h_{\text{nucleoplasm}}(\mathbf{p}) = \begin{cases} 1 & \text{if } \|\mathbf{p} - \mathbf{c}_{\text{cell}}\| < r_{\text{nucleoplasm}}^2 \\ 0 & \text{otherwise} \end{cases} \quad (8)$$

where $\mathbf{p} = \mathbf{x} - \mathbf{u}$, with \mathbf{x} and \mathbf{u} being, respectively, the actual position and the displacement, \mathbf{c}_{cell} is the cell centre and r_{cortex} , r_{cytosol} , r_{lamina} and $r_{\text{nucleoplasm}}$ are the external radius of the cell cortex, the cytosol, the nuclear lamina and nucleoplasm, respectively (Fig. 1a). Therefore, the cytoplasm $\Omega_{\text{cytoplasm}}$ and the nucleus Ω_{nucleus} domains are defined by the following characteristic functions

$$\begin{aligned} h_{\text{cytoplasm}}(\mathbf{p}) &= h_{\text{cortex}}(\mathbf{p}) + h_{\text{cytosol}}(\mathbf{p}) \\ h_{\text{nucleus}}(\mathbf{p}) &= h_{\text{lamina}}(\mathbf{p}) + h_{\text{nucleoplasm}}(\mathbf{p}) \end{aligned} \quad (9)$$

The frontal portion of cytosol where the polymerization of the actin filaments takes place is described as follows

$$h_{\text{cytosol,front}}(\mathbf{p}) = \begin{cases} h_{\text{cytosol}} & \text{if } \mathbf{p} > \mathbf{c}_{\text{cell}} \\ 0 & \text{otherwise} \end{cases} \quad (10)$$

The frontal (Ω_f) and rear (Ω_r) adhesion regions are also defined by two characteristic functions as

$$\begin{aligned} h_f(\mathbf{p}) &= \begin{cases} 1 & (\mathbf{p} - \mathbf{c}_{\text{cell}}, \mathbf{i}_x) > l_f \\ 0 & \text{otherwise} \end{cases} \\ h_r(\mathbf{p}) &= \begin{cases} 1 & (\mathbf{p} - \mathbf{c}_{\text{cell}}, \mathbf{i}_x) < -l_r \\ 0 & \text{otherwise} \end{cases} \end{aligned} \quad (11)$$

with l_f and l_r the distances of \mathbf{c}_{cell} from the boundaries of Ω_f and Ω_r , respectively, (Fig. 1b). As soon as the cell moves, the argument \mathbf{p} is replaced by $\mathbf{x} - \mathbf{u}$, with \mathbf{x} the actual spatial position and \mathbf{u} the displacement.

5.2 Nucleus constitutive law

As mentioned in Sect. 2.2, the nucleus is described through a viscoelastic constitutive equation based on a standard

Maxwell model including a solid phase (i.e. the lamina) and a fluid phase (i.e. the nucleoplasm) (Fig. 8).

The Cauchy stress $\boldsymbol{\sigma}_{\text{nucleus}}$ and the deformation tensor $\mathbf{F}_{\text{nucleus}}$ in the nucleus are defined by

$$\begin{aligned} \boldsymbol{\sigma}_{\text{nucleus}} &= \boldsymbol{\sigma}_{\text{lamina}} + \boldsymbol{\sigma}_{\text{nucleoplasm}} \\ \mathbf{F}_{\text{nucleus}} &= \mathbf{D}_p \mathbf{u} + \mathbf{I} = \mathbf{F}_{\text{lamina}} = \mathbf{F}_{\text{nucleoplasm}} \end{aligned} \quad (12)$$

where $\mathbf{D}_p \mathbf{u} = \sum_{m=1}^3 \frac{\partial \mathbf{u}}{\partial p_m} \otimes \mathbf{i}_m$, with \mathbf{u} the displacement and \mathbf{I} the identity matrix (Holzapfel 2000; Taber 2004), and $\mathbf{F}_{\text{nucleoplasm}} = \mathbf{F}_{\text{nucleoplasm},e} \mathbf{F}_{\text{nucleoplasm},v}$. The solid part of the stress $\boldsymbol{\sigma}_{\text{lamina}}$ in the lamina reads

$$\boldsymbol{\sigma}_{\text{lamina}} = \frac{1}{J_{\text{lamina}}} \mathbf{F}_{\text{lamina}} \mathbf{S}_{\text{lamina}} \mathbf{F}_{\text{lamina}}^T \quad (13)$$

where J_{lamina} is the determinant of $\mathbf{F}_{\text{lamina}}$ and $\mathbf{S}_{\text{lamina}}$ is the second Piola–Kirchhoff stress tensor, which is computed as an isotropic hyperelastic Saint Venant material as follows

$$\mathbf{S}_{\text{lamina}} = \lambda_{\text{lamina}} \text{Tr}(\mathbf{E}_{\text{lamina}}) \mathbf{I} + 2\mu_{\text{lamina}} \mathbf{E}_{\text{lamina}} \quad (14)$$

with λ_{lamina} , μ_{lamina} and $\mathbf{E}_{\text{lamina}}$ the Lamé's coefficients and the Green-Lagrange strain tensor of the solid phase, respectively.

The fluid part of the stress $\boldsymbol{\sigma}_{\text{nucleoplasm}}$ in the nucleoplasm can be expressed as

$$\boldsymbol{\sigma}_{\text{nucleoplasm}} = 2\mu_{\text{nucleoplasm}} \mathbf{D}_{\text{nucleoplasm},v} \quad (15)$$

with $\mu_{\text{nucleoplasm}}$, the viscosity of the nucleoplasm and the eulerian strain rate $\mathbf{D}_{\text{nucleoplasm},v}$ is computed from the strain gradient velocity as

$$\begin{aligned} 2\mathbf{D}_{\text{nucleoplasm},v} &= \dot{\mathbf{F}}_{\text{nucleoplasm},v} \mathbf{F}_{\text{nucleoplasm},v}^{-1} \\ &\quad + \mathbf{F}_{\text{nucleoplasm},v}^{-T} \dot{\mathbf{F}}_{\text{nucleoplasm},v}^T \end{aligned} \quad (16)$$

5.3 Cytoplasm constitutive law

The cytoplasm is composed by two phases: i) a solid phase represented by the cell cortex and ii) a fluid phase represented by the viscous cytosol with the embedded organelles such as the actin filaments that undergo the active strains (Fig. 8). It is assumed that the Cauchy stress $\boldsymbol{\sigma}_{\text{cytoplasm}}$ and the deformation tensor $\mathbf{F}_{\text{cytoplasm}}$ read

$$\begin{aligned} \boldsymbol{\sigma}_{\text{cytoplasm}} &= \boldsymbol{\sigma}_{\text{cortex}} + \boldsymbol{\sigma}_{\text{cytosol}} \\ \mathbf{F}_{\text{cytoplasm}} &= \mathbf{F}_{\text{cortex}} = \mathbf{F}_{\text{cytosol}} \end{aligned} \quad (17)$$

Additionally, the fluid deformation tensor $\mathbf{F}_{\text{cytosol}}$ is multiplicatively decomposed as follows

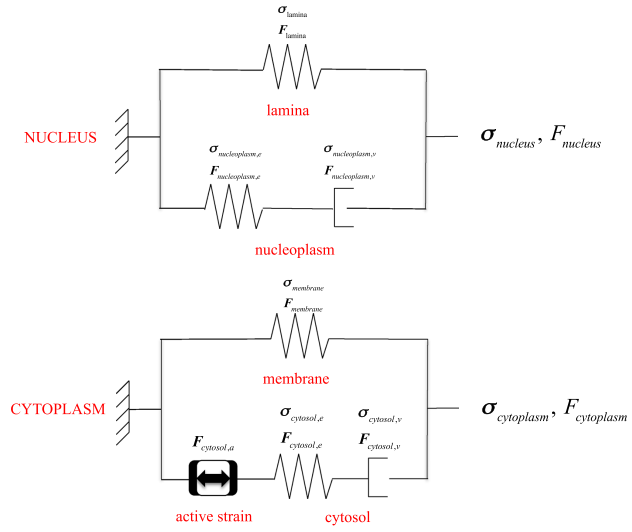
$$\mathbf{F}_{\text{cytosol}} = \mathbf{F}_{\text{cytosol},v} \mathbf{F}_{\text{cytosol},e} \mathbf{F}_{\text{cytosol},a} \quad (18)$$

where e and v stand for elastic and viscous, respectively.

The solid stress $\boldsymbol{\sigma}_{\text{cortex}}$ in the organelles can be written as

$$\boldsymbol{\sigma}_{\text{cortex}} = \frac{1}{J_{\text{cortex}}} \mathbf{F}_{\text{cortex}} \mathbf{S}_{\text{cortex}} \mathbf{F}_{\text{cortex}}^T \quad (19)$$

Fig. 8 Symbolic schemas for the standard Maxwell models used to describe the nucleus (top) and the cytoplasm (bottom) behaviours



with J_{cortex} the determinant of $\mathbf{F}_{\text{cortex}}$ and $\mathbf{S}_{\text{cortex}}$ the second Piola–Kirchhoff stress tensor, which, similarly to the nucleus (Sect. 5.2), is defined as an isotropic hyperplastic Saint Venant material as follows

$$\mathbf{S}_{\text{cortex}} = \lambda_{\text{cortex}} \text{Tr}(\mathbf{E}_{\text{cortex}}) \mathbf{I} + 2\mu_{\text{cortex}} \mathbf{E}_{\text{cortex}} \quad (20)$$

where λ_{cortex} , μ_{cortex} and $\mathbf{E}_{\text{cortex}}$ the Lamé's coefficients and the Green-Lagrange strain tensor of the solid phase, respectively.

Finally, the fluid stress σ_{cytosol} in the cytosol reads

$$\sigma_{\text{cytosol}} = 2\mu_{\text{cytosol}} \mathbf{D}_{\text{cytosol},v} \quad (21)$$

with μ_{cytosol} the viscosity of the cytosol and $\mathbf{D}_{\text{cytosol},v}$ the eulerian strain rate expressed as follows

$$2\mathbf{D}_{\text{cytosol},v} = \dot{\mathbf{F}}_{\text{cytosol},v} \mathbf{F}_{\text{cytosol},v}^{-1} + \mathbf{F}_{\text{cytosol},v}^{-T} \dot{\mathbf{F}}_{\text{cytosol},v}^T \quad (22)$$

5.4 Micro-channel geometry

As mentioned in Sect. 2.4, the micro-channel domain Ω_{channel} is modelled as two pseudo-elliptical rigid walls: a upper one (Ω_{uw}) and a lower one (Ω_{lw}). They are described through two characteristic functions as follows

$$h_{uw,i}(\mathbf{p}) = \begin{cases} 1 & \text{if } l_{uw,i} < 1 \\ 0 & \text{otherwise} \end{cases} \quad (23)$$

$$h_{lw,i}(\mathbf{p}) = \begin{cases} 1 & \text{if } l_{lw,i} < 1 \\ 0 & \text{otherwise} \end{cases}$$

where the subscript 'i' indicates the number of the channel, and $l_{uw,i}$ and $l_{lw,i}$ are two level set functions expressed as

$$l_{uw,i} = \left(\frac{x-x_0}{a} \right)^4 + \left(\frac{y-y_{uw0,i}}{b} \right)^4$$

$$l_{lw,i} = \left(\frac{x-x_0}{a} \right)^4 + \left(\frac{y+y_{lw0,i}}{b} \right)^4 \quad (24)$$

with a and b are the semi-axes of the pseudo-elliptical walls with centres $\mathbf{c}_{uw,i}(x_0, y_{uw0,i})$ and $\mathbf{c}_{lw,i}(x_0, y_{lw0,i})$. Thus, the micro-channel is the composition of the two previous characteristic functions as follows

$$\Omega_{\text{channel}} = h_{uw,i}(\mathbf{p}) + h_{lw,i}(\mathbf{p}) \quad (25)$$

The outward normals \mathbf{n}_{uw} and \mathbf{n}_{lw} to the boundary $\partial\Omega_{uw}$ and $\partial\Omega_{lw}$, respectively, given by

$$\mathbf{n}_{uw,i} = h'(l_{uw,i}) \frac{\nabla l_{uw,i}}{\|\nabla l_{uw,i}\|}$$

$$\mathbf{n}_{lw,i} = h'(l_{lw,i}) \frac{\nabla l_{lw,i}}{\|\nabla l_{lw,i}\|} \quad (26)$$

where h' indicates the Dirac function.

References

- Allena R (2013) Cell migration with multiple pseudopodia: temporal and spatial sensing models. Bull Math Biol 75:288–316. doi:10.1007/s11538-012-9806-1

- Allena R, Aubry D (2012) “Run-and-tumble” or “look-and-run”? A mechanical model to explore the behavior of a migrating amoeboid cell. *J Theor Biol* 306:15–31. doi:10.1016/j.jtbi.2012.03.041
- Bausch AR, Möller W, Sackmann E (1999) Measurement of local viscoelasticity and forces in living cells by magnetic tweezers. *Biophys J* 76:573–579
- Caille N, Thoumine O, Tardy Y, Meister J-J (2002) Contribution of the nucleus to the mechanical properties of endothelial cells. *J Biomech* 35:177–187
- Christensen RM (1991) Mechanics of composite materials. Krieger Publishing Company, NY
- Crick FHC, Hughes AFW (1950) The physical properties of cytoplasm. *Exp Cell Res* 1:37–80. doi:10.1016/0014-4827(50)90048-6
- Dahl KN, Ribeiro AJS, Lammerding J (2008) Nuclear shape, mechanics, and mechanotransduction. *Circ Res* 102:1307–1318. doi:10.1161/CIRCRESAHA.108.173989
- Drury JL, Dembo M (2001) Aspiration of human neutrophils: effects of shear thinning and cortical dissipation. *Biophys J* 81:3166–3177
- Egeblad M, Rasch MG, Weaver VM (2010) Dynamic interplay between the collagen scaffold and tumor evolution. *Curr Opin Cell Biol* 22:697–706. doi:10.1016/j.ccb.2010.08.015
- Erler JT, Weaver VM (2009) Three-dimensional context regulation of metastasis. *Clin Exp Metastas* 26:35–49. doi:10.1007/s10585-008-9209-8
- Faure-André G, Vargas P, Yuseff M-I et al (2008) Regulation of dendritic cell migration by CD74, the MHC class II-associated invariant chain. *Science* 322:1705–1710. doi:10.1126/science.1159894
- Friedl P, Wolf K (2010) Plasticity of cell migration: a multiscale tuning model. *J Cell Biol* 188:11–19. doi:10.1083/jcb.200909003
- Friedl P, Wolf K, Lammerding J (2011) Nuclear mechanics during cell migration. *Curr Opin Cell Biol* 23:55–64. doi:10.1016/j.ccb.2010.10.015
- Fukui Y, Uyeda TQP, Kitayama C, Inoué S (2000) How well can an amoeba climb? *PNAS* 97:10020–10025. doi:10.1073/pnas.97.18.10020
- Givero C, Grillo A, Preziosi L, Influence of nucleus deformability on cell entry into cylindrical structures. *Biomech Model Mechanobiol*, pp 1–22. doi:10.1007/s10237-013-0510-3
- Gracheva ME, Othmer HG (2004) A continuum model of motility in amoeboid cells. *Bull Math Biol* 66:167–193. doi:10.1016/j.bulm.2003.08.007
- Hawkins RJ, Piel M, Faure-Andre G et al (2009) Pushing off the walls: a mechanism of cell motility in confinement. *Phys Rev Lett* 102:058103. doi:10.1103/PhysRevLett.102.058103
- Hawkins RJ, Voituriez R (2010) Mechanisms of cell motion in confined geometries. *Math Model Nat Phenom* 5:84–105. doi:10.1051/mmnp/201005104
- Heuzé ML, Collin O, Terria E et al (2011) Cell migration in confinement: a micro-channel-based assay. *Methods Mol Biol* 769:415–434. doi:10.1007/978-1-61779-207-6_28
- Holzappel GA (2000) Nonlinear solid mechanics: a continuum approach for engineering, 1st edn. Wiley, London
- Iilina O, Bakker G-J, Vasaturo A et al (2011) Two-photon laser-generated microtracks in 3D collagen lattices: principles of MMP-dependent and -independent collective cancer cell invasion. *Phys Biol* 8:015010. doi:10.1088/1478-3975/8/1/015010
- Irimia D, Charras G, Agrawal N et al (2007) Polar stimulation and constrained cell migration in microfluidic channels. *Lab Chip* 7:1783–1790. doi:10.1039/b710524j
- Irimia D, Toner M (2009) Spontaneous migration of cancer cells under conditions of mechanical confinement. *Integr Biol (Camb)* 1:506–512. doi:10.1039/b908595e
- Jiang H, Sun SX (2013) Cellular pressure and volume regulation and implications for cell mechanics. *Biophys J* 105:609–619. doi:10.1016/j.bpj.2013.06.021
- Larson RG (1998) The structure and rheology of complex fluids. Oxford University Press, USA
- Lautenschlager F, Paschke S, Schinkinger S et al (2009) The regulatory role of cell mechanics for migration of differentiating myeloid cells. *Proc Natl Acad Sci* 106:15696–15701. doi:10.1073/pnas.0811261106
- Lubliner J (2008) Plasticity theory. Dover Publications, New York
- Mandel J (1972) Plasticité classique et viscoplasticité: course held at the Department of Mechanics of Solids, September–October, 1971. Springer, Berlin
- McElwain DLS (1978) A re-examination of oxygen diffusion in a spherical cell with michaelis-menten oxygen uptake kinetics. *J Theor Biol* 71:255–263. doi:10.1016/0022-5193(78)90270-9
- McElwain DLS, Callcott R, Morris LE (1979) A model of vascular compression in solid tumours. *J Theor Biol* 78:405–415. doi:10.1016/0022-5193(79)90339-4
- McElwain DLS, Ponzio PJ (1977) A model for the growth of a solid tumor with non-uniform oxygen consumption. *Math Biosci* 35:267–279. doi:10.1016/0025-5564(77)90028-1
- Mogilner A (2009) Mathematics of cell motility: have we got its number? *J Math Biol* 58:105–134. doi:10.1007/s00285-008-0182-2
- Ngalim SH, Magenau A, Zhu Y et al (2013) Creating adhesive and soluble gradients for imaging cell migration with fluorescence microscopy. *J Vis Exp*. doi:10.3791/50310
- Pesen D, Hoh JH (2005) Micromechanical architecture of the endothelial cell cortex. *Biophys J* 88:670–679. doi:10.1529/biophysj.104.049965
- Phillipson M, Heit B, Colaruso P et al (2006) Intraluminal crawling of neutrophils to emigration sites: a molecularly distinct process from adhesion in the recruitment cascade. *J Exp Med* 203:2569–2575. doi:10.1084/jem.20060925
- Provenzano PP, Inman DR, Eliceiri KW et al (2008) Collagen density promotes mammary tumor initiation and progression. *BMC Med* 6:11. doi:10.1186/1741-7015-6-11
- Rangarajan R, Zaman MH (2008) Modeling cell migration in 3D. *Cell Adhes Migr* 2:106–109
- Recho P, Putelat T, Truskinovsky L (2013) Contraction-driven cell motility. *Phys Rev Lett* 111:108102. doi:10.1103/PhysRevLett.111.108102
- Recho P, Truskinovsky L (2013) An asymmetry between pushing and pulling for crawling cells. [arXiv:1302.4002](https://arxiv.org/abs/1302.4002) [cond-mat, physics:physics, q-bio]
- Righolt CH, Raz V, Vermolen BJ et al (2010) Molecular image analysis: quantitative description and classification of the nuclear lamina in human mesenchymal stem cells. *Int J Mol Imaging*. doi:10.1155/2011/723283
- Rolli CG, Seufferlein T, Kemkemer R, Spatz JP (2010) Impact of tumor cell cytoskeleton organization on invasiveness and migration: a microchannel-based approach. *PLoS ONE* 5:e8726. doi:10.1371/journal.pone.0008726
- Ronot X, Doisy A, Tracqui P (2000) Quantitative study of dynamic behavior of cell monolayers during in vitro wound healing by optical flow analysis. *Cytometry* 41:19–30
- Sakamoto Y, Prudhomme S, Zaman MH (2011) Viscoelastic gel-strip model for the simulation of migrating cells. *Ann Biomed Eng* 39:2735–2749. doi:10.1007/s10439-011-0360-z
- Schaub S, Bohnet S, Laurent VM et al (2007) Comparative maps of motion and assembly of filamentous actin and myosin II in migrating cells. *Mol Biol Cell* 18:3723–3732. doi:10.1091/mbc.E06-09-0859
- Scianna M, Preziosi L (2013) Modeling the influence of nucleus elasticity on cell invasion in fiber networks and microchannels. *J Theor Biol* 317:394–406. doi:10.1016/j.jtbi.2012.11.003
- Scianna M, Preziosi L, Wolf K (2013) A cellular potts model simulating cell migration on and in matrix environments. *Math Biosci Eng* 10:235–261

- Stokes CL, Lauffenburger DA (1991) Analysis of the roles of microvessel endothelial cell random motility and chemotaxis in angiogenesis. *J Theor Biol* 152:377–403. doi:[10.1016/S0022-5193\(05\)80201-2](https://doi.org/10.1016/S0022-5193(05)80201-2)
- Stokes CL, Lauffenburger DA, Williams SK (1991) Migration of individual microvessel endothelial cells: stochastic model and parameter measurement. *J Cell Sci* 99(Pt 2):419–430
- Taber LA (2004) *Nonlinear theory of elasticity: applications in biomechanics*. World Scientific Pub Co Inc., Singapore
- Taylor AM, Blurton-Jones M, Rhee SW et al (2005) A microfluidic culture platform for CNS axonal injury, regeneration and transport. *Nat Methods* 2:599–605. doi:[10.1038/nmeth777](https://doi.org/10.1038/nmeth777)
- Tinevez J-Y, Schulze U, Salbreux G, et al. (2009) Role of cortical tension in bleb growth. *PNAS* *pnas.0903353106*. doi:[10.1073/pnas.0903353106](https://doi.org/10.1073/pnas.0903353106)
- Tozluoğlu M, Tournier AL, Jenkins RP et al (2013) Matrix geometry determines optimal cancer cell migration strategy and modulates response to interventions. *Nat Cell Biol* 15:751–762. doi:[10.1038/ncb2775](https://doi.org/10.1038/ncb2775)
- Tranquillo RT, Lauffenburger DA (1987) Stochastic model of leukocyte chemosensory movement. *J Math Biol* 25:229–262
- Tranquillo RT, Lauffenburger DA, Zigmond SH (1988) A stochastic model for leukocyte random motility and chemotaxis based on receptor binding fluctuations. *J Cell Biol* 106:303–309
- Vaziri A, Lee H, Mofrad MRK (2006) Deformation of the cell nucleus under indentation: mechanics and mechanisms. *J Mater Res* 21:2126–2135. doi:[10.1557/jmr.2006.0262](https://doi.org/10.1557/jmr.2006.0262)
- Wolf K, Alexander S, Schacht V et al (2009) Collagen-based cell migration models in vitro and in vivo. *Semin Cell Dev Biol* 20:931–941. doi:[10.1016/j.semcdb.2009.08.005](https://doi.org/10.1016/j.semcdb.2009.08.005)
- Zaman MH, Kamm RD, Matsudaira P, Lauffenburger DA (2005) Computational model for cell migration in three-dimensional matrices. *Biophys J* 89:1389–1397. doi:[10.1529/biophysj.105.060723](https://doi.org/10.1529/biophysj.105.060723)
- Zaman MH, Matsudaira P, Lauffenburger DA (2007) Understanding effects of matrix protease and matrix organization on directional persistence and translational speed in three-dimensional cell migration. *Ann Biomed Eng* 35:91–100. doi:[10.1007/s10439-006-9205-6](https://doi.org/10.1007/s10439-006-9205-6)
- Zaman MH, Trapani LM, Sieminski AL et al (2006) Migration of tumor cells in 3D matrices is governed by matrix stiffness along with cell-matrix adhesion and proteolysis. *Proc Natl Acad Sci USA* 103:10889–10894. doi:[10.1073/pnas.0604460103](https://doi.org/10.1073/pnas.0604460103)

2 **Mechanical Modelling of Confined Cell Migration Across**
3 **Constricted-curved Micro-channels**

4 **R. Allena^{*,†}**

5 **Abstract:** Confined migration is a crucial phenomenon during embryogenesis,
6 immune response and cancer. Here, a two-dimensional finite element model of a
7 HeLa cell migrating across constricted-curved micro-channels is proposed. The
8 cell is modelled as a continuum with embedded cytoplasm and nucleus, which are
9 described by standard Maxwell viscoelastic models. The decomposition of the de-
10 formation gradient is employed to define the cyclic active strains of protrusion and
11 contraction, which are synchronized with the adhesion forces between the cell and
12 the substrate. The micro-channels are represented by two rigid walls and exert
13 an additional viscous force on the cell boundaries. Five configurations have been
14 tested: 1) top constriction, 2) top-bottom constriction, 3) shifted top-bottom con-
15 striction, 4) embedded obstacle and 5) bending micro-channel. Additionally, for
16 the first four micro-channels both sub-cellular and sub-nuclear constrictions have
17 been obtained, while for the fifth micro-channel three types of bending have been
18 investigated ('curved', 'sharp' and 'sharper'). For each configuration, several pa-
19 rameters such as the cell behaviour, the covered distance, the migration velocity,
20 the ratio between the cell and the nucleus area as well as the cell-substrate and
21 cell-channel surfaces forces have been evaluated. The results show once more the
22 fundamental role played by mechanics of both the cell and the environment.

23 **Keywords:** Confined cell migration, Curved micro-channel, Continuum mechan-
24 ics, Computational mechanics.

25 **1 Introduction**

26 Cell migration in confinement is proper to several biological phenomena such
27 as embryogenesis, immune response and cancer [1, 2]. Although cell migration
28 on two-dimensional (2D) flat substrates has been largely investigated during the
29 last few years, the mechanical principles triggering migration of cells in three-

* Arts et Metiers ParisTech, LBM, 151 Bd de l'hôpital, 75013 Paris, France.

† Corresponding author. E-mail: rachele.allena@ensam.eu

30 dimensional (3D) confined environments such as fibres networks are still little
 31 known. In fact, in addition to the external stimuli such as attractant molecules,
 32 the geometry and the mechanical nature of the extracellular matrix (ECM) may
 33 play a critical role during *in vivo* migration [3–5]. It has been shown that the width
 34 of the ECM pores, the ECM alignment and stiffness as well as the fibres density are
 35 fundamental parameters triggering or inhibiting the cell movement [2–9]. There-
 36 fore, in order to efficiently move within the fibres network, the cell has to constantly
 37 adapt its shape and its migratory behaviour.

38 Several experimental and numerical studies can be found in the literature, which
 39 focus on specific aspects of confined migration.

40 The former employ:

- 41 • gels or lattices [9] allowing to acquire very simplified systems for which,
 42 however, many physical parameters (i.e. gel density and elasticity or local
 43 constrictions) affecting the global cell motility are difficult to handle [9–11];
- 44 • micro-structures obtained through micro-laser techniques [12] or pho-
 45 tolithography [13] for which the geometrical characteristics may be varied
 46 and tuned. Such techniques have been used to reproduce cell migration un-
 47 der confinement for cancer [14, 15] and immune [16] cells or neurons [17].

48 The latter propose Cellular Potts [18, 19], hybrid agent based finite element [20],
 49 energetic continuum [21], multi-physics [22] or purely mechanical [23] models
 50 which aim to evaluate the cell internal organization, the role of the nucleus and
 51 the migration strategy adopted by the cell according to the environment. More
 52 recently, Scianna and Preziosi [24] have presented an extension of their previous
 53 model in which migration takes place across two perpendicular micro-channels
 54 equal in width and length. In these works, the ECM is considered and represented
 55 as a regular geometry (i.e. tracks or micro-channels). Nevertheless, the ECM may
 56 be composed by fibres, which can be randomly aligned or form gaps of variable di-
 57 mensions and radius of curvature leading to more complex geometries and forcing
 58 the cell to take turns and squeeze.

59 Here, the objective of the present work is to improve the previous model proposed
 60 in [23] in order to evaluate cell migration across micro-channels presenting simul-
 61 taneously a parameterized curved shape and a constriction. The cell is modelled
 62 as a continuum with embedded cytoplasm and nucleus, which are defined by spe-
 63 cific characteristic functions and considered as viscoelastic. The cell motility is
 64 determined by the synchronization between the active strains (i.e. protrusion and
 65 contraction), which are described through the decomposition of the deformation
 66 gradient, and the viscous adhesion forces between the cell and the substrate. The

67 constricted-curved micro-channels are represented by two rigid walls, each defined
 68 by a characteristic function, and exert an additional viscous normal force on the cell
 69 boundaries. The geometrical parameters of the micro-channels have been tuned *ad*
 70 *hoc* and five configurations have been obtained.

71 In the next sections the geometry of the micro-channels (Sec. 2.1) and of the cell
 72 (Sec. 2.2) are presented as well as the cell constitutive law (Sec. 2.2) and the
 73 mechanical approach used to describe both the adhesion forces (Sec. 2.2) and the
 74 active strains (Sec. 2.3). In Sec. 3.1 and 3.2, the results are discussed by evaluating
 75 several parameters such as the cell behaviour during migration, the migration ve-
 76 locity and the cell-substrate and cell-channel surface forces. Finally, a comparison
 77 with previous models from the same author is proposed in Sec. 3.3.

78 **2 The model**

79 **2.1 Micro-channels**

80 We consider five different micro-channels $\Omega_{channel,i}$ (the subscript ‘*i*’ indicates the
 81 micro-channel number), each one represented by a upper (Ω_{uw}) and a lower (Ω_{lw})
 82 rigid walls, which are spatially arranged as follows:

- 83 1) top constriction micro-channel or $\Omega_{channel,1}$: the lower wall is straight, while the
 84 upper wall is inward convex (Fig. 1a);
- 85 2) top-bottom constriction micro-channel or $\Omega_{channel,2}$: the lower and the upper
 86 walls are inward convex (Fig. 1b);
- 87 3) shifted top-bottom constriction micro-channel or $\Omega_{channel,3}$: the lower and the
 88 upper walls are inward convex and additionally shifted along the x -axis (Fig. 1c);
- 89 4) embedded obstacle micro-channel or $\Omega_{channel,4}$: the lower and the upper walls
 90 are both outward convex and a circular obstacle is placed at the centre of the micro-
 91 channel (Fig. 1d);
- 92 5) bending micro-channel or $\Omega_{channel,5}$: the lower and the upper walls are outward
 93 and inward convex, respectively (Fig. 2a).

For each geometry, two characteristic functions are employed to describe respec-
 tively Ω_{uw} and Ω_{lw} as follows

$$\begin{aligned} h_{uw,i}(\mathbf{p}) &= \begin{cases} 1 & \text{if } l_{uw,i} < 1 \\ 0 & \text{otherwise} \end{cases} \\ h_{lw,i}(\mathbf{p}) &= \begin{cases} 1 & \text{if } l_{lw,i} < 1 \\ 0 & \text{otherwise} \end{cases} \end{aligned} \quad (1)$$

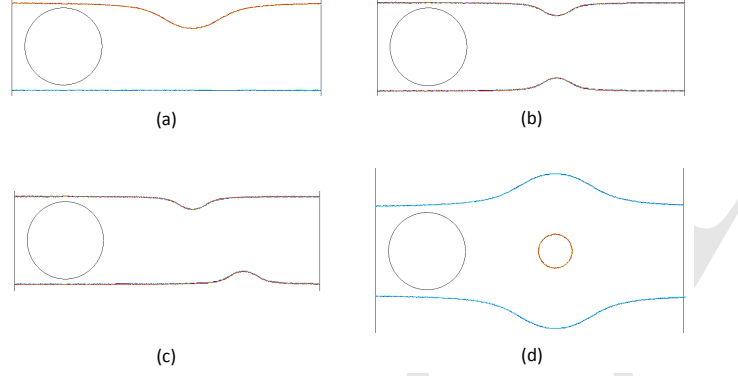


Figure 1: Geometries of the micro-channels: (a) top constriction ($\Omega_{channel,1}$), (b) top-bottom constriction ($\Omega_{channel,3}$), (c) shifted top-bottom constriction ($\Omega_{channel,3}$) and (d) embedded obstacle micro-channel ($\Omega_{channel,4}$).

where $l_{uw,i}$ and $l_{lw,i}$ are two level set functions expressed as

$$\begin{aligned}
 l_{uw,1} &= -(y - y_{0,1}) \left[(x - x_{0u,1})^2 + (y - y_{0,1})^2 + (y + y_{0,1}) \right] \\
 l_{uw,2} = l_{uw,3} &= -(y - y_{0,i}) \left[(x - x_{0u,i})^2 + (y - y_{0,i})^2 - r_{uw,i}^3 \right] \\
 l_{uw,4} &= (y - y_{0,4}) \left[(x - x_{0u,4})^2 + (y - y_{0,4})^2 - r_{uw,4}^3 \right] \\
 l_{uw,5} &= -(y - y_{0,5}) \left[(x - x_{0u,5})^j + (y - y_{0,5})^j - r_{uw,5}^k \right]
 \end{aligned} \tag{2}$$

$$\begin{aligned}
 l_{lw,1} = l_{lw,4} &= -(y + y_{0,i}) \left[(x - x_{0l,i})^2 + (y + y_{0,i})^2 - r_{lw,i}^3 \right] \\
 l_{lw,2} = l_{lw,3} &= (y + y_{0,i}) \left[(x - x_{0l,i})^2 + (y + y_{0,i})^2 - r_{lw,i}^3 \right] \\
 l_{lw,5} &= -(y + y_{0,5}) \left[(x - x_{0l,5})^j + (y + y_{0,5})^j - r_{lw,5}^k \right]
 \end{aligned} \tag{3}$$

Thus, the micro-channel $\Omega_{channel,i}$ is the sum of the two previous characteristic functions as follows

$$\Omega_{channel,i} = h_{uw,i}(\mathbf{p}) + h_{lw,i}(\mathbf{p}) \tag{4}$$

Additionally, for $\Omega_{channel,4}$ Eq. (4) is slightly modified and reads

$$\Omega_{channel,4} = h_{uw,4}(\mathbf{p}) + h_{lw,4}(\mathbf{p}) + h_{obstacle}(\mathbf{p}) \tag{5}$$

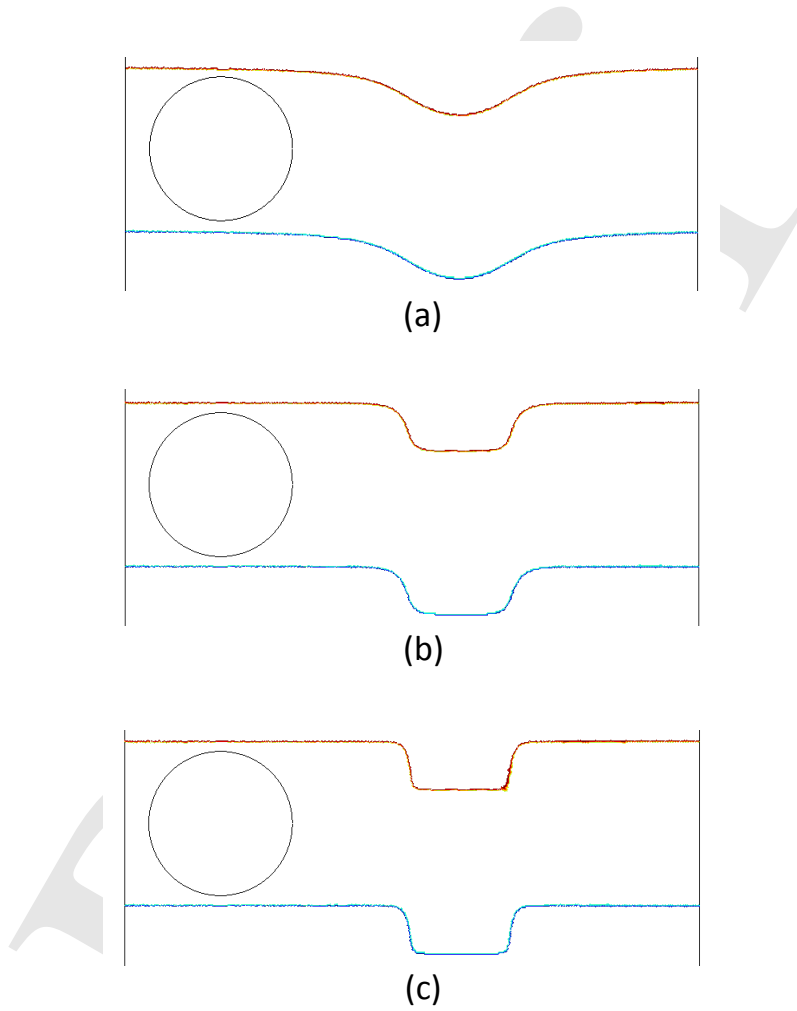


Figure 2: Geometries of $\Omega_{channel,5}$: (a) 'curved', (b) 'sharp' and (c) 'sharper' bending.

where $h_{obstacle}(\mathbf{p})$ is the characteristic function of the central circular obstacle $\Omega_{obstacle}$ expressed as

$$h_{obstacle}(\mathbf{p}) = \begin{cases} 1 & \text{if } l_{obstacle} < 1 \\ 0 & \text{otherwise} \end{cases} \quad (6)$$

94 with $l_{obstacle} = (x - x_{0,4})^2 + y^2 - r_4^2$ and r_4 the radius of the circle.

When the cell enters into the micro-channel, it is then submitted to a viscous force $\mathbf{f}_{channel}$, which is the sum of an upper ($\mathbf{f}_{uw,i}$) and a lower ($\mathbf{f}_{lw,i}$) force that read

$$\begin{aligned} \mathbf{f}_{uw,i}(\mathbf{n}_{uw,i}) &= -\mu_{channel} \frac{1}{(l_{uw,i} + 1)^8 + \alpha} \left(\frac{\partial \mathbf{u}}{\partial t}, \mathbf{n}_{uw,i} \right) \mathbf{n}_{uw,i} \quad \text{on } \partial\Omega_{uw,i} \\ \mathbf{f}_{lw,i}(\mathbf{n}_{lw,i}) &= -\mu_{channel} \frac{1}{(l_{lw,i} + 1)^8 + \alpha} \left(\frac{\partial \mathbf{u}}{\partial t}, \mathbf{n}_{lw,i} \right) \mathbf{n}_{lw,i} \quad \text{on } \partial\Omega_{lw,i} \end{aligned} \quad (7)$$

where $\mu_{channel}$ is the viscosity of the micro-channel, α is a constant and (\mathbf{a}, \mathbf{b}) defines the scalar product between two vectors \mathbf{a} and \mathbf{b} . The outward normal vectors $\mathbf{n}_{uw,i}$ and $\mathbf{n}_{lw,i}$ to the boundaries $\partial\Omega_{uw,i}$ and $\partial\Omega_{lw,i}$ of the upper and lower wall are given by

$$\begin{aligned} \mathbf{n}_{uw,i} &= h'(l_{uw,i}) \frac{\nabla l_{uw,i}}{\|\nabla l_{uw,i}\|} \\ \mathbf{n}_{lw,i} &= h'(l_{lw,i}) \frac{\nabla l_{lw,i}}{\|\nabla l_{lw,i}\|} \end{aligned} \quad (8)$$

95 where h' indicates the Dirac delta function.

Finally, for $\Omega_{channel,4}$ an additional force $\mathbf{f}_{obstacle}(\mathbf{n}_{obstacle})$ is exerted along the external boundary of the obstacle and reads

$$\mathbf{f}_{obstacle}(\mathbf{n}_{obstacle}) = -\mu_{channel} \frac{1}{(l_{obstacle} + 1)^8 + \alpha} \left(\frac{\partial \mathbf{u}}{\partial t}, \mathbf{n}_{obstacle} \right) \mathbf{n}_{obstacle} \quad (9)$$

on $\partial\Omega_{obstacle}$

96 with $\mathbf{n}_{obstacle} = h'(l_{obstacle}) \frac{\nabla l_{obstacle}}{\|\nabla l_{obstacle}\|}$.

97 2.2 Cell geometry and mechanics

At the initial time point, the cell Ω_{cell} is represented by a circle of radius r_{cell} and includes the cytoplasm ($\Omega_{cytoplasm}$) and the nucleus ($\Omega_{nucleus}$) (Fig. 3a), which are assumed to be viscoelastic and modelled by two standard Maxwell models [23, 25, 26]. The nucleus is composed by the nuclear lamina (Ω_{lamina}) and the nucleoplasm

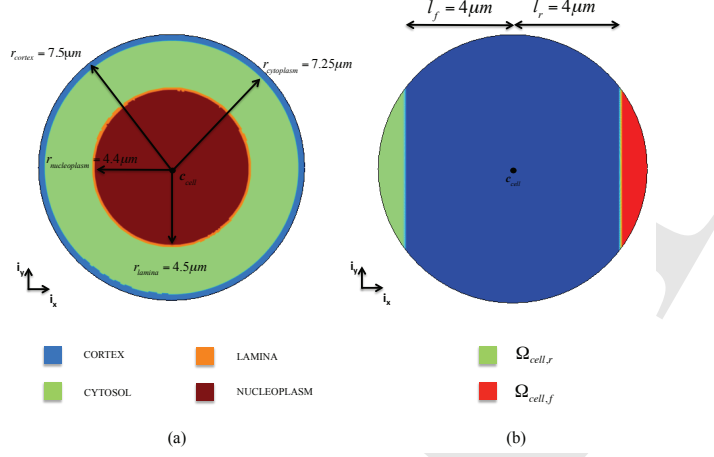


Figure 3: Geometry of the cell (a) and frontal and rear adhesion surfaces (b).

($\Omega_{nucleoplasm}$), while the cytoplasm is constituted by the cell cortex (Ω_{cortex}) and the cytosol ($\Omega_{cytosol}$). Each component is described through a characteristic function as follows

$$h_{cortex}(\mathbf{p}) = \begin{cases} 1 & \text{if } r_{cytoplasm}^2 < \|\mathbf{p} - \mathbf{c}_{cell}\|^2 < r_{cortex}^2 \\ 0 & \text{otherwise} \end{cases} \quad (10)$$

$$h_{cytosol}(\mathbf{p}) = \begin{cases} 1 & \text{if } r_{lamina}^2 < \|\mathbf{p} - \mathbf{c}_{cell}\|^2 < r_{cytosol}^2 \\ 0 & \text{otherwise} \end{cases} \quad (11)$$

$$h_{lamina}(\mathbf{p}) = \begin{cases} 1 & \text{if } r_{nucleoplasm}^2 < \|\mathbf{p} - \mathbf{c}_{cell}\|^2 < r_{lamina}^2 \\ 0 & \text{otherwise} \end{cases} \quad (12)$$

$$h_{nucleoplasm}(\mathbf{p}) = \begin{cases} 1 & \text{if } \|\mathbf{p} - \mathbf{c}_{cell}\|^2 < r_{nucleoplasm}^2 \\ 0 & \text{otherwise} \end{cases} \quad (13)$$

where $\mathbf{p} = \mathbf{x} - \mathbf{u}$, with \mathbf{x} and \mathbf{u} being respectively the actual position and the displacement, \mathbf{c}_{cell} is the cell centre and r_{cortex} , $r_{cytosol}$, r_{lamina} and $r_{nucleoplasm}$ are the external radius of the cell cortex, the cytosol, the nuclear lamina and nucleoplasm respectively (Fig. 3a). Then, the cytoplasm $\Omega_{cytoplasm}$ and the nucleus $\Omega_{nucleus}$ domains are defined by the following characteristic functions

$$\begin{aligned} h_{cytoplasm}(\mathbf{p}) &= h_{cortex}(\mathbf{p}) + h_{cytosol}(\mathbf{p}) \\ h_{nucleus}(\mathbf{p}) &= h_{lamina}(\mathbf{p}) + h_{nucleoplasm}(\mathbf{p}) \end{aligned} \quad (14)$$

The global equilibrium of the system can be expressed as

$$\rho \mathbf{a} = \text{Div}_p (J \boldsymbol{\sigma} \mathbf{F}^{-T}) + \mathbf{f}_{adh} + \mathbf{f}_{channel} \quad (15)$$

with ρ the global cell density, \mathbf{a} the acceleration, Div_p the divergence with respect to the initial position \mathbf{p} , J the determinant of the deformation gradient \mathbf{F} and \mathbf{F}^{-T} the inverse transpose of the matrix \mathbf{F} [26, 27]. \mathbf{f}_{adh} defines the viscous adhesion forces [28–31] between the cell and the substrate which are cyclically activated at the front ($\Omega_{cell,f}$) and at the back ($\Omega_{cell,r}$) of the cell (Fig. 3b), which are expressed as

$$\begin{aligned} h_{cell,f}(\mathbf{p}) &= \begin{cases} 1 & (\mathbf{p} - \mathbf{c}_{cell}, \mathbf{i}_x) > l_f \\ 0 & \text{otherwise} \end{cases} \\ h_{cell,r}(\mathbf{p}) &= \begin{cases} 1 & (\mathbf{p} - \mathbf{c}_{cell}, \mathbf{i}_x) < -l_r \\ 0 & \text{otherwise} \end{cases} \end{aligned} \quad (16)$$

98 with l_f and l_r the distances of \mathbf{c}_{cell} from the boundaries $\partial\Omega_{cell,f}$ and $\partial\Omega_{cell,r}$ re-
99 spectively (Fig. 3b).

Thus, \mathbf{f}_{adh} is the composition of a frontal ($\mathbf{f}_{adh,f}$) and a rear ($\mathbf{f}_{adh,r}$) component that read

$$\begin{aligned} \mathbf{f}_{adh,f}(\mathbf{n}_{cell}) &= -\mu_{adh} h_{sync} \left(-\frac{\partial \mathbf{F}_{cytosol,a}}{\partial t} \right) \mathbf{v} \quad \text{on } \Omega_{cell,f} \\ \mathbf{f}_{adh,r}(\mathbf{n}_{cell}) &= -\mu_{adh} h_{sync} \left(\frac{\partial \mathbf{F}_{cytosol,a}}{\partial t} \right) \mathbf{v} \quad \text{on } \Omega_{cell,r} \end{aligned} \quad (17)$$

100 with \mathbf{n}_{cell} the outward normal to the cell boundary, μ_{adh} the friction coefficient, \mathbf{v} the
101 velocity and $\mathbf{F}_{cytosol,a}$ the solid active deformation tensor defined in the next section
102 (Sec. 2.3). The characteristic function $h_{sync} \left(\mp \frac{\partial \mathbf{F}_{cytosol,a}}{\partial t} \right)$ couples the adhesion
103 forces with the active strains of protrusion and contraction [30, 31], which are
104 described in the next section.

105 2.3 Active strains

106 During migration, we observe two main phases: i) the protrusion and the adhesion
107 at the rear edge and ii) the contraction and the adhesion at the frontal edge [30].
108 Here, it is assumed that such an oscillatory movement of the cell is triggered by the
109 periodic polymerization and depolymerization of the actin filaments [32], which are
110 embedded in the cytosol. The former only occurs at the front of the cell, while the
111 latter takes place from the front towards the rear of the cell. Therefore, although not
112 submitted to any active strain, the nucleus interacts with the surrounding cytosol
113 apart from the protrusion phase [33]. Additionally, an external attractive source

114 is introduced at 0° at the right side of the micro-channel, so that the direction of
115 migration is imposed and corresponds to the horizontal axis \mathbf{i}_x .

The solid active deformation tensor $\mathbf{F}_{cytosol,a}$ [23] reads

$$\mathbf{F}_{cytosol,a} = \begin{cases} e_{a0} \sin\left(2\pi\frac{t}{T}\right) h_{cytosol,f} \mathbf{i}_x \otimes \mathbf{i}_x & \text{if } \sin\left(2\pi\frac{t}{T}\right) > 0 \\ \frac{e_{a0}}{2} \sin\left(2\pi\frac{t}{T}\right) h_{cytosol} \mathbf{i}_x \otimes \mathbf{i}_x & \text{if } \sin\left(2\pi\frac{t}{T}\right) < 0 \end{cases} \quad (18)$$

where e_{a0} is the amplitude of the active strain, t is time, T is the migration period and \otimes indicates the tensorial product. $h_{cytosol,f}$ is a characteristic function describing the portion of cytosol where the polymerization of the actin filaments takes place and reads

$$h_{cytosol,f}(\mathbf{p}) = \begin{cases} h_{cytosol} & \text{if } \mathbf{p} > \mathbf{c}_{cell} \\ 0 & \text{otherwise} \end{cases} \quad (19)$$

116 3 Results

117 COMSOL Multiphysics® 3.5a has been used to run all the simulations. As in [23],
118 the model represents a HeLa cell. The characteristic functions presented in Sec. 2.2
119 have been used to implicitly describe the cytoplasm and the nucleus components
120 in order to be able to define the parameters of the standard Maxwell models [23].
121 The radius r_{cortex} , $r_{cytosol}$, r_{lamina} and $r_{nucleoplasm}$ of the cell have been chosen equal
122 to $7.5 \mu\text{m}$ [34, 35], $7.25 \mu\text{m}$, $4.5 \mu\text{m}$ and $4.4 \mu\text{m}$ respectively, which leads to a cell
123 cortex (t_{cortex}) and a nuclear lamina (t_{lamina}) thicknesses equal to $0.25 \mu\text{m}$ [36–38]
124 and $0.1 \mu\text{m}$ [39] respectively. The nominal values of the Young moduli $E_{cortex,0}$ of
125 the cell cortex and $E_{cytosol,0}$ of the cytosol have been chosen equal to 100 Pa and 10
126 Pa [40], respectively. For the nucleus, assuming that its stiffness is mostly provided
127 by the nuclear lamina, $E_{lamina,0}$ and $E_{nucleoplasm,0}$ have been set to 3000 Pa [41,
128 42] and 25 Pa [43], respectively. Such moduli have been recalculated according
129 to a simple spatial homogenization approach [25, 44] and to the surface occupied
130 by each component in the cell to obtain E_{cortex} , $E_{cytosol}$, E_{lamina} and $E_{nucleoplasm}$. The
131 Poisson's ratios ν_{cortex} and ν_{lamina} have been set to 0.3, while $\nu_{cytosol}$ and $\nu_{nucleoplasm}$
132 to 0.4. The viscosities $\mu_{cytosol}$ and $\mu_{nucleoplasm}$ are equal to $3 \times 10^5 \text{Pa}\cdot\text{s}$ [45, 46].
133 The global cell density ρ has been set to $1000 \text{kg}/\text{m}^3$ [47] and the viscous friction
134 coefficient μ_{adh} is equal $10^8 \text{Pa}\cdot\text{s}/\text{m}$. Finally, the intensity of the active strain e_{a0}
135 and the migration period T have been chosen equal to 0.2 and 600 s respectively.
136 The geometrical and mechanical parameters of the cell have been reported in Table
137 1.

Table 1: Main geometrical and material parameters of the model.

Parameter	Description	Value	Unit	Reference
r_{cell}	Cell radius	7.5	μm	[34, 35]
r_{cortex}	Cortex radius	7.5	μm	
$r_{cytosol}$	Cytosol radius	7.25	μm	
r_{lamina}	Lamina radius	4.5	μm	
$r_{nucleoplasm}$	Nucleoplasm radius	4.4	μm	
l_{cortex}	Cortex thickness	0.25	μm	[36–38]
l_{lamina}	Lamina thickness	0.1	μm	[39]
l_f	Distance cell centre – boundary of frontal adhesion region	4	μm	
l_r	Distance cell centre – boundary of rear adhesion region	4	μm	
Ω_{cell}	Initial cell area	176.6	μm^2	
Ω_{cortex}	Initial cortex area	11.6	μm^2	
$\Omega_{cytosol}$	Initial cytosol area	101.4	μm^2	
$\Omega_{cytoplasm}$	Initial cytoplasm area	113	μm^2	
Ω_{lamina}	Initial lamina area	2.8	μm^2	
$\Omega_{nucleoplasm}$	Initial nucleoplasm area	60.8	μm^2	
$\Omega_{nucleus}$	Initial nucleus area	63.6	μm^2	
Ω_f	Initial frontal adhesion region area	31	μm^2	
Ω_r	Initial rear adhesion region area	31	μm^2	
$E_{cortex,0}$	Nominal cortex Young modulus	100	Pa	
$E_{cytosol,0}$	Nominal cytosol Young modulus	10	Pa	[40]
$E_{lamina,0}$	Nominal lamina Young modulus	3000	Pa	[41, 42]
$E_{nucleoplasm,0}$	Nominal nucleoplasm Young modulus	25	Pa	[43]
\bar{E}_{cortex}	Equivalent cortex Young modulus	15	Pa	
$\bar{E}_{cytosol}$	Equivalent cytosol Young modulus	8	Pa	
\bar{E}_{lamina}	Equivalent lamina Young modulus	196	Pa	
$\bar{E}_{nucleoplasm}$	Equivalent nucleoplasm Young modulus	23	Pa	
ν_{cortex}	Cortex Poisson ratio	0.3		
$\nu_{cytosol}$	Cytosol Poisson ratio	0.4		
ν_{lamina}	Lamina Poisson ratio	0.3		
$\nu_{nucleoplasm}$	Nucleoplasm Poisson ratio	0.4		
$\mu_{cytosol}$	Cytosol viscosity	3×10^5	Pa-s	[45, 46]
$\mu_{nucleoplasm}$	Nucleoplasm viscosity	3×10^5	Pa-s	[45, 46]
ρ	Cell density	1000	kg/m^3	[47]
e_{a0}	Amplitude of the active strain	0.8		
T	Migration period	600	s	

138 **3.1 Cell behaviour overview**

139 Here, the results obtained for $\Omega_{channel,1}$ to $\Omega_{channel,4}$ are presented. These micro-
 140 channels show a specific type of constriction (Sec. 2.1, Fig. 1a:d). Then, their
 141 geometrical parameters have been tuned (see Table 2) in order to obtain two series
 142 of simulations for which the constrictions are i) sub-cellular ($12\mu\text{m}$) and ii) sub-
 143 nuclear ($7\mu\text{m}$), respectively. For all the simulations, the total length and the viscous
 144 penalty coefficient ($\mu_{channel}$) of the micro-channels have been set to $40\mu\text{m}$ and
 145 $10^{10}\text{ Pa}\cdot\text{s}/\text{m}$, respectively. A time interval of 9000 s has been considered for micro-
 146 channels $\Omega_{channel,1}$ to $\Omega_{channel,3}$, while for $\Omega_{channel,4}$ a longer period (12000 s) has
 147 been tested. The cell behaviour has been investigated for each of the previous
 148 configurations and the main results are reported in Table 3.

149 The efficiency of the migration has been evaluated in terms of covered distance and
 150 migration velocity. For each micro-channel, whether the constriction is sub-cellular
 151 or sub-nuclear, the cell is permeative [15, 23, 24] since it is able to migrate through
 152 the micro-channel and reach the opposite side. In order to do so, the cell must
 153 squeeze or turn or both simultaneously (see Fig. 4,5). The covered distance goes
 154 from a minimal value of $43.8\mu\text{m}$ (sub-nuclear $\Omega_{channel,2}$) to a maximal value of
 155 $48.2\mu\text{m}$ (sub-cellular $\Omega_{channel,4}$). The average velocity of the cell centre of inertia
 156 is between $0.65\cdot 10^{-2}\mu\text{m}/\text{s}$ ($\Omega_{channel,1}$) and $1.05\cdot 10^{-2}\mu\text{m}/\text{s}$ ($\Omega_{channel,4}$). Some peak
 157 is observed, especially for the sub-nuclear constrictions, when the cell migrates
 158 through the micro-channel narrowing. For instance, for $\Omega_{channel,2}$ and $\Omega_{channel,4}$,
 159 the maximal values are equal to $2.6\cdot 10^{-2}\mu\text{m}/\text{s}$ and $3\cdot 10^{-2}\mu\text{m}/\text{s}$, respectively. Nev-
 160 ertheless, such values are still of the same order of magnitude of those experimen-
 161 tally observed for HeLa cells [34, 35] and, as found in [23], the velocity during the
 162 contraction phase is slightly higher than during the contraction phase.

163 For each simulation, three parameters have been defined [23]:

- 164 • $t_{contact}$ corresponds to the first contact between the cell and the upper or the
 165 lower wall of the micro-channel (or the obstacle for $\Omega_{channel,4}$);
- 166 • t_{exit} corresponds to the loss of contact between the cell and both micro-
 167 channel walls (and the obstacle for $\Omega_{channel,4}$);
- 168 • T_{entry} is the elapsed time between $t_{contact}$ and t_{exit} .

169 T_{entry} has been determined only for sub-cellular constrictions of $\Omega_{channel,2}$ and
 170 $\Omega_{channel,3}$ (2950 s and 4600 s respectively). For the other configurations in fact,
 171 the cell would certainly need more time to reacquire its initial shape. As a general
 172 remark, $t_{contact}$ is higher for sub-cellular constrictions than for sub-nuclear. This
 173 is mostly due to the fact that, in order to obtain sub-nuclear constrictions (Eqs.

Table 2: Geometrical parameters for the five micro-channels.

Parameter	Description	Value			Units
		Sub-cellular	Sub-nuclear		
$x_{0u,1}$	x-axis upper wall coordinate $\Omega_{channel,1}$	25	25		μm
$x_{0u,2}$	x-axis upper wall coordinate $\Omega_{channel,2}$	25	25		
$x_{0u,3}$	x-axis upper wall coordinate $\Omega_{channel,3}$	25	25		μm
$x_{0u,4}$	x-axis upper wall coordinate $\Omega_{channel,4}$	25	25		μm
$x_{0u,5}$	x-axis upper wall coordinate $\Omega_{channel,5}$	'curved'	'sharp'	'sharper'	μm
		25	25	25	
$x_{0l,1}$	x-axis lower wall coordinate $\Omega_{channel,1}$	25	25		μm
$x_{0l,2}$	x-axis lower wall coordinate $\Omega_{channel,2}$	25	25		
$x_{0l,3}$	x-axis lower wall coordinate $\Omega_{channel,3}$	35	35		μm
$x_{0l,4}$	x-axis lower wall coordinate $\Omega_{channel,4}$	25	25		μm
$x_{0l,5}$	x-axis lower wall coordinate $\Omega_{channel,5}$	'curved'	'sharp'	'sharper'	μm
		25	25	25	
$y_{0,1}$	y-axis coordinate $\Omega_{channel,1}$	8.5	Upper wall	Lower wall	μm
			9.5	7.5	
$y_{0,2}$	y-axis coordinate $\Omega_{channel,2}$	8.5	8.5		μm
$y_{0,3}$	y-axis coordinate $\Omega_{channel,3}$	8.5	8.5		μm
$y_{0,4}$	y-axis coordinate $\Omega_{channel,4}$	8.5	8.5		μm
$y_{0,5}$	y-axis coordinate $\Omega_{channel,5}$	'curved'	'sharp'	'sharper'	μm
		8.5	8.5	8.5	
$r_{uw,1}$	Radius upper wall $\Omega_{channel,1}$	5	10		μm
$r_{uw,2}$	Radius upper wall $\Omega_{channel,2}$	2.5	5		μm
$r_{uw,3}$	Radius upper wall $\Omega_{channel,3}$	2.5	5		μm
$r_{uw,4}$	Radius upper wall $\Omega_{channel,4}$	6.5	2.5		μm
$r_{uw,5}$	Radius upper wall $\Omega_{channel,5}$	'curved'	'sharp'	'sharper'	μm
		5	5	5	
$r_{lw,2}$	Radius lower wall $\Omega_{channel,2}$	2.5	5		μm
$r_{lw,3}$	Radius lower wall $\Omega_{channel,3}$	2.5	5		μm
$r_{lw,4}$	Radius lower wall $\Omega_{channel,4}$	6.5	2.5		μm
$r_{lw,5}$	Radius lower wall $\Omega_{channel,5}$	'curved'	'sharp'	'sharper'	μm
		5	5	5	
r_4	Radius obstacle $\Omega_{obstacle}$	3	4		μm
j	Power in Eq. [2] and [3]	'curved'	'sharp'	'sharper'	
		2	6	12	
k	Power in Eq. [2] and [3]	'curved'	'sharp'	'sharper'	
		3	7	13	
$\mu_{channel}$	Micro-channel viscosity	10^{10}	10^{10}		Pa-s/m
α		0.1			

Table 3: Main results for micro-channels $\Omega_{channel,1}$ to $\Omega_{channel,4}$.

	$\Omega_{channel,1}$		$\Omega_{channel,2}$		$\Omega_{channel,3}$		$\Omega_{channel,4}$	
	Sub-cellular	Sub-nuclear	Sub-cellular	Sub-nuclear	Sub-cellular	Sub-nuclear	Sub-cellular	Sub-nuclear
Migration behaviour	Permeative	Permeative	Permeative	Permeative	Permeative	Permeative	Permeative	Permeative
Covered distance (μm)	46.5	45.1	46.6	43.8	46.5	45.6	48.2	46.5
Average migration velocity ($\mu\text{m/s}$)	$0.65 \cdot 10^{-2}$ max $1.45 \cdot 10^{-2}$	$1.2 \cdot 10^{-2}$ max $1.98 \cdot 10^{-2}$	$0.75 \cdot 10^{-2}$ max $1.45 \cdot 10^{-2}$	$0.7 \cdot 10^{-2}$ max $2.6 \cdot 10^{-2}$	$0.75 \cdot 10^{-2}$ max $1.35 \cdot 10^{-2}$	$0.8 \cdot 10^{-2}$ max $1.7 \cdot 10^{-2}$	$0.8 \cdot 10^{-2}$ max $3 \cdot 10^{-2}$	$1.05 \cdot 10^{-2}$ max $3 \cdot 10^{-2}$
Entry time $t_{contact}$ (s)	2450	550	3650	2400	3650	2400	3000	2450
Exit time t_{exit} (s)	-	-	6600	-	8250	-	-	-
Penetration period T_{entry} (s)	-	-	2950	-	4600	-	-	-
Maximal cell area/nucleus area (during T_{entry})	3.65	3.73	3.65	3.8	3.58	3.6	3.45	3.55
Minimal cell area/nucleus area (during T_{entry})	2.55	2.24	2.57	2.28	2.63	2.41	2.41	2.21
Maximal frontal cell-substrate surface force before $t_{contact}$ and after t_{exit} [Pa]	9.5	9.5	9.5	9.7	9.5	9.5	16.2	14.5
Maximal rear cell-substrate surface force before $t_{contact}$ and after t_{exit} [Pa]	2.8	0.4	2.8	4.8	2.8	3.8	5.5	7.3
Frontal cell-substrate surface force at $t_{contact}$ [Pa]	1.7	1	8	8	8	8	8	6
Rear cell-substrate surface force at $t_{contact}$ [Pa]	2.3	1.4	2.7	2.7	2.7	2.7	2.7	2.7
Cell-channel surface force at $t_{contact}$ [Pa]	1.5	2	1	1	1	1	1.8	1.1
Maximal cell-channel surface force during T_{entry} [Pa]	4	5.3	3.8	3.7	4.6	3	6	7.8

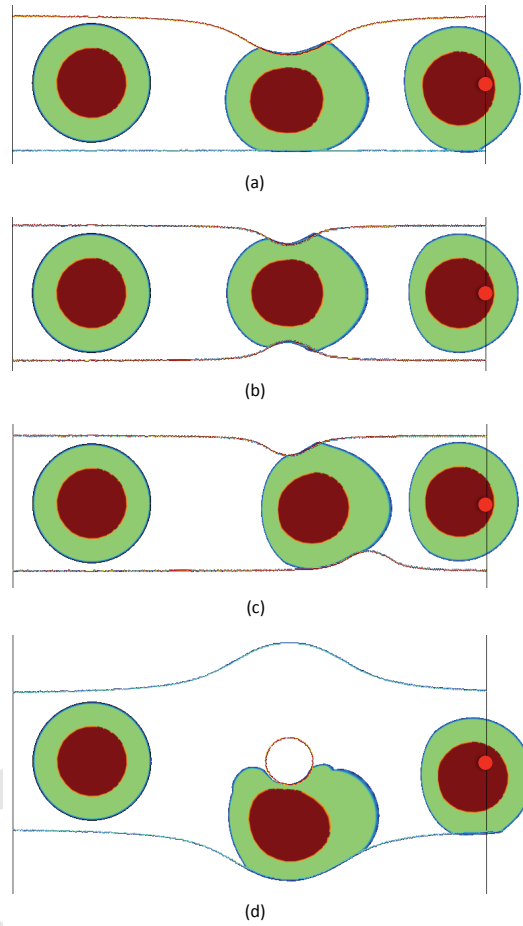


Figure 4: Migration through sub-cellular micro-channels at different time points. (a) Top constriction micro-channel (from left to right $t = 0, 5000 \text{ s}, 9000 \text{ s}$) (b) Top-bottom constriction micro-channel (from left to right $t = 0, 5000 \text{ s}, 9000 \text{ s}$) (c) Shifted top-bottom constriction micro-channel (from left to right $t = 0, 5000 \text{ s}, 9000 \text{ s}$) (d) Embedded obstacle micro-channel (from left to right $t = 0, 7300 \text{ s}, 12000 \text{ s}$) (blue= cell cortex, green = cytosol, orange = nuclear lamina, red = nucleoplasm, red circle = attractive source).

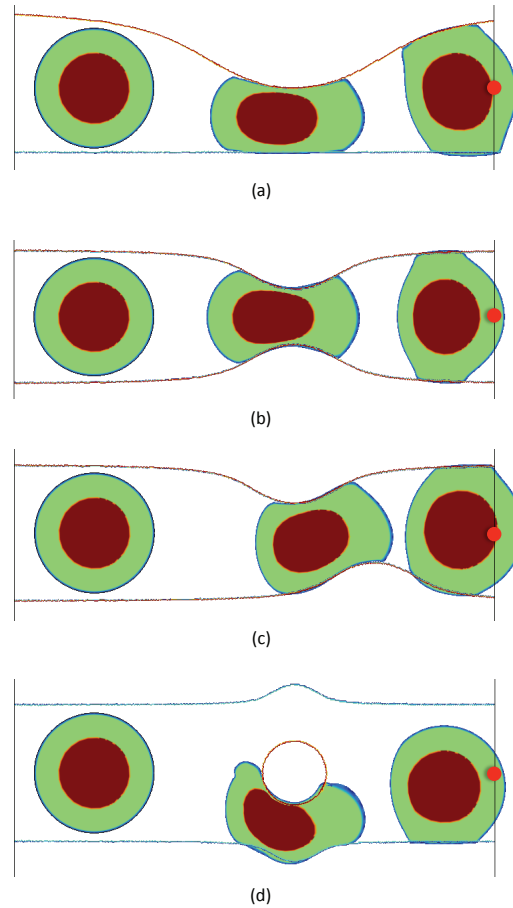


Figure 5: Migration through sub-nuclear micro-channels at different time points. (a) Top constriction micro-channel (from left to right $t = 0, 5000 \text{ s}, 9000 \text{ s}$) (b) Top-bottom constriction micro-channel (from left to right $t = 0, 5000 \text{ s}, 9000 \text{ s}$) (c) Shifted top-bottom constriction micro-channel (from left to right $t = 0, 5000 \text{ s}, 9000 \text{ s}$) (d) Embedded obstacle micro-channel (from left to right $t = 0, 7300 \text{ s}, 12000 \text{ s}$) (blue= cell cortex, green = cytosol, orange = nuclear lamina, red = nucleoplasm, red circle = attractive source).

174 (2) and (3)), the upper or the lower micro-channel walls (or both) start narrowing
 175 earlier (Fig. 1a:d), thus the cell come earlier into contact with the micro-channel.
 176 The ratio between the total cell area and the nucleus area has also been evaluated.
 177 The initial value is equal to 2.8, but, due to the protrusion and contraction phases,
 178 it oscillates between a maximal value of 3.6 and 2.6 before before $t_{contact}$ and after
 179 t_{exit} , respectively. In Table 3, the values of the ratio during the penetration period
 180 T_{entry} have been reported. For the sub-cellular constrictions, no significant varia-
 181 tions are observed. For the sub-nuclear constrictions instead, the ratio value de-
 182 crease to 2.24, 2.28, 2.41 and 2.21 respectively for $\Omega_{channel,1}$, $\Omega_{channel,2}$, $\Omega_{channel,3}$
 183 and $\Omega_{channel,4}$. For these configurations in fact, both the cytoplasm and the nucleus
 184 must squeeze in order for the cell to migrate through the narrowing region.
 185 Finally, the cell-substrate and cell-channel forces have been evaluated. Due to the
 186 asymmetry of the active strain (Sec. 2.3) and according to Eq. [17] expressing the
 187 cell-substrate surface forces, a higher force was found at the frontal edge of the cell
 188 than at the rear. Specifically, the frontal cell-substrate force is comprised between
 189 9.5 Pa and 16.2 Pa, while the rear cell-substrate force is comprised between 2.8 Pa
 190 and 7.3 Pa. As for the cell-channel surface force, it varies between a minimal value
 191 of 1 Pa at $t_{contact}$ and a maximal value of 7.8 Pa during the penetration period T_{entry} .
 192 As mentioned above, the cell shows a permeative behaviour for all the configura-
 193 tions, either sub-cellular or sub-nuclear. In fact, the three conditions defined in [23]
 194 are respected here and more specifically:

- 195 • the cell-channel force is lower than the cell-substrate force at $t_{contact}$;
- 196 • the cell is able to penetrate the micro-channel thanks to a frontal edge pro-
 197 trusion whose length is larger than half the constriction width;
- 198 • during the penetration period T_{entry} , the cell-channel force is higher than the
 199 cell-substrate force so that the cell is maintained squeezed all time.

200 3.2 Bending channel

201 In this section the results for $\Omega_{channel,4}$ are discussed and reported in Table 4. Con-
 202 trary to the previous ones, this micro-channel does not present any constriction, but
 203 the cell must turn in order to achieve the opposite side. By increasing the pow-
 204 ers in Eqs. (2) and (3), the bending angle becomes closer to a right angle. Then,
 205 three configurations have been tested: i) 'curved' (Fig. 2a) ii) 'sharp' (Fig. 2b)
 206 and iii) 'sharper' (Fig. 2c) bending. In the three cases, the cell is permeative and
 207 progresses with an average velocity of the centre of inertia which is slightly higher
 208 (between $0.8 \cdot 10^{-2} \mu\text{m/s}$ and $1.4 \cdot 10^{-2} \mu\text{m/s}$) than that found for the previous micro-
 209 channels (Sec. 3.1). Additionally, since the micro-channel induces the cell to turn

210 but not to squeeze, the ratio between the total cell area and the nucleus area does
 211 not change significantly (maximal and minimal value during T_{entry} equal to 3.65
 212 and 2.86 respectively).

Table 4: Main results for ‘curved’, ‘sharp’ and ‘sharper’ bending micro-channels.

	$\Omega_{channel,5}$ ‘curved’	$\Omega_{channel,5}$ ‘sharp’	$\Omega_{channel,5}$ ‘sharper’
Migration behaviour	Permeative	Permeative	Permeative
Covered distance (μm)	46.3	45	39.7
Average migration velocity ($\mu\text{m/s}$)	$1.4 \cdot 10^{-2}$ max $2.4 \cdot 10^{-2}$	$0.8 \cdot 10^{-2}$ max $1.4 \cdot 10^{-2}$	$0.9 \cdot 10^{-2}$ max $2.3 \cdot 10^{-2}$
Entry time $t_{contact}$ (s)	2700	2700	2700
Exit time t_{exit} (s)	7800	-	-
Penetration period T_{entry} (s)	5100	-	-
Maximal cell area/nucleus area (during T_{entry})	3.6	3.63	3.65
Minimal cell area/nucleus area (during T_{entry})	2.6	2.86	2.73
Maximal frontal cell-substrate surface force before $t_{contact}$ and after t_{exit} [Pa]	9.5	9.5	9.5
Maximal rear cell-substrate surface force before $t_{contact}$ and after t_{exit} [Pa]	2.8	2.8	2.8
Frontal cell-substrate surface force at $t_{contact}$ [Pa]	7.5	7.5	7.5
Rear cell-substrate surface force at $t_{contact}$ [Pa]	-	-	-
Cell-channel surface force at $t_{contact}$ [Pa]	1	1	1
Maximal cell-channel surface force during T_{entry} [Pa]	4.5	8.5	14.5

213 It is possible to notice that for the ‘curved’ bending (Fig. 6a), the cell comes into
 214 contact only with the upper wall of the micro-channel, while for the ‘sharp’ and
 215 ‘sharper’ bending (Fig. 6b,c respectively) the contact occurs with both the upper
 216 and the lower walls. The contact time $t_{contact}$ is the same for the three configurations
 217 and equal to 2700 s. However, the exit time t_{exit} has been determined only for the
 218 ‘curved’ bending (7800 s), while for the other two cases the cell does not loose
 219 contact with the micro-channel walls during the simulation interval.

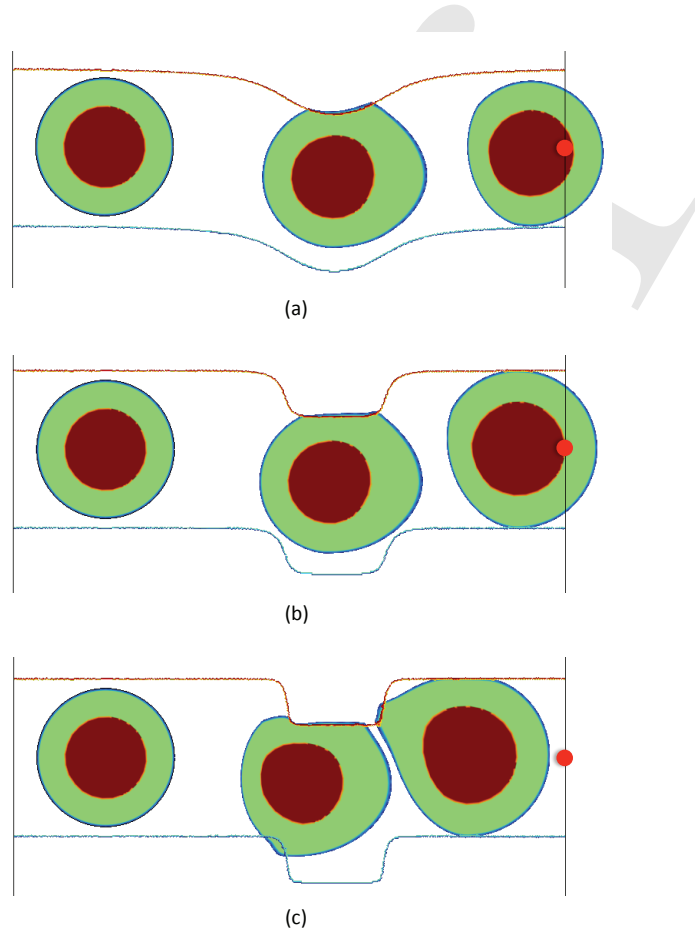


Figure 6: Migration through bending micro-channels (a) 'Curved' micro-channel (from left to right $t = 0, 5000 \text{ s}, 9000 \text{ s}$) (b) 'Sharp' micro-channel (from left to right $t = 0, 5000 \text{ s}, 9000 \text{ s}$) (c) 'Sharper' micro-channel (from left to right $t = 0, 5000 \text{ s}, 9000 \text{ s}$) (blue= cell cortex, green = cytosol, orange = nuclear lamina, red = nucleoplasm, red circle = attractive source).

220 Regarding the surface forces, the values found are very close to those of previous
 221 micro-channels especially for the maximal frontal (9.5 Pa) and rear (2.8 Pa) cell-
 222 substrate force before $t_{contact}$ and after t_{exit} . At $t_{contact}$, only the frontal cell-substrate
 223 force has been evaluated and is equal to 7.5 Pa and the cell-channel force is equal
 224 to 1Pa for the three configurations. Finally, the maximal cell-channel force during
 225 T_{entry} increases as the entry angle becomes sharper and is equal to 4.5 Pa, 8.5 Pa
 226 and 14.5 Pa respectively for the ‘curved’, ‘sharp’ and ‘sharper’ bending.

227 **3.3 Critical role of mechanics**

228 The current model represents an extension of the work proposed in [23]. In fact,
 229 the same mechanical principles are employed, but the characteristic functions used
 230 to define the micro-channels allow obtaining more complex geometries combining
 231 constriction and curved rigid walls, which induce the cell to turn or squeeze or both
 232 simultaneously in order to be permeative.

233 Let us compare the present results to those found in [30] and [23]. In [30], the cell
 234 migrates over a 2D flat substrate with slippery regions on it which inhibit the effi-
 235 cient migration. In that model, an external attractive source is introduced and the
 236 cell is equipped either with a distance or a velocity sensor, which allows detecting
 237 the slippery regions. Then, the cell is able to turn left or right and to completely or
 238 partially avoid the ‘obstacles’ in order to get to the source as fastest as possible. In
 239 some sense, the cell possesses an intrinsic will thanks to which it is able to adapt
 240 itself to the external environment. In [23], the cell migrates along the horizontal
 241 axis i_x across micro-channels of different widths leading to straight constrictions
 242 from sub-cellular to sub-nuclear dimensions. In this case, without any inherent or *a*
 243 *priori* decision, the cell adjusts its movement and shape according to the surround-
 244 ings and its behaviour (permeative, invasive or penetrating) highly depends on the
 245 nucleus ability to deform.

246 The present model includes two main aspects from the previous works, but some
 247 differences can be pointed out. First, due to the curved rigid walls of the micro-
 248 channels, the cell must turn left or right to achieve the opposite side, but no in-
 249 trinsic decision is considered. However, such behaviour is rather determined by
 250 the surrounding mechanical environment. A significant example is provided by
 251 $\Omega_{channel,4}$. In this configuration in fact, the cell turns right to avoid the central ob-
 252 stacle, but such a choice is not determined by a *a priori* decision (as it was the
 253 case in [30]), but probably triggered by some viscoelasticity effects. Second, the
 254 cell has to squeeze in order to pass through the micro-channel constrictions, but the
 255 narrowing may not be aligned with the direction of migration anymore ($\Omega_{channel,3}$
 256 and $\Omega_{channel,4}$ for instance). Therefore, according to the results, it seems that, by
 257 introducing an external attractive source only (Sec. 2.3) and without any intrinsic

258 will, the cell is still able to adapt itself to the micro-channel shape and to migrate
 259 across it. These findings demonstrate that mechanics of both the cell and the envi-
 260 ronment plays a critical role in confined migration and may, alone, provide impor-
 261 tant insights for the understanding of this phenomenon.

262 4 Conclusion

263 The work presented in this paper represents an extension of the previous model
 264 proposed in [23]. In fact, a 2D model of a HeLa cell migrating through a micro-
 265 channel is still presented. Nonetheless, five new micro-channels are tested combin-
 266 ing a curved shape and a constriction. Additionally, for micro-channel $\Omega_{channel,1}$
 267 to $\Omega_{channel,4}$, both sub-cellular ($12\mu\text{m}$) and sub-nuclear ($7\mu\text{m}$) constrictions have
 268 been obtained, while for $\Omega_{channel,5}$ three types of bending have been investigated
 269 ('curved', 'sharp' and 'sharper'). For all the configurations, the cell is able to
 270 achieve the opposite side of the micro-channel and can therefore be considered as
 271 permeative. Several parameters have been evaluated such as the covered distance,
 272 the migration velocity, the ratio between the cell area and the nucleus area as well as
 273 the cell-substrate and the cell-channel surface forces. The results confirm the fun-
 274 damental role of mechanical forces during confined migration since, without any
 275 additional chemical or molecular input but the external attractive source, the cell is
 276 able to adjust its movement and shape to the complex geometry of the environment
 277 and migrate through the constricted-curved micro-channels.

278 References

- 279 1. Nourshargh, S., Hordijk, P. L. & Sixt, M. (2010) Breaching multiple barriers:
 280 leukocyte motility through venular walls and the interstitium. *Nat Rev Mol*
 281 *Cell Biol*, 11, 366–378.
- 282 2. Friedl, P. & Wolf, K. (2010) Plasticity of cell migration: a multiscale tuning
 283 model. *J Cell Biol*, 188:11–19.
- 284 3. Su, J., Jiang, X., Welsch, R., Whitesides, G. M. & So, P. T. C (2007) Ge-
 285 ometric confinement influences cellular mechanical properties I – adhesion
 286 area dependence. *Mol Cell Biomech*, 4, 87–104.
- 287 4. Richardson WJ, van der Voort DD, Wilson E, Moore JE (2013) Differential
 288 orientation of 10T1/2 mesenchymal cells on non-uniform stretch environ-
 289 ments. *Mol Cell Biomech*, 10, 245–265.
- 290 5. Brock, A. L. & Ingber, D. E. (2005) Control of the direction of lamellipodia
 291 extension through changes in the balance between Rac and Rho activities.

- 292 *Mol Cell Biomech*, 2, 135–143.
- 293 6. Zaman, M. H., Kamm, R. D., Matsudaira, P. & Lauffenburger, D. A. (2005)
294 Computational model for cell migration in three-dimensional matrices. *Bio-*
295 *phys J*, 89, 1389–1397.
- 296 7. Zaman, M. H., Matsudaira, P. & Lauffenburger, D. A. (2007) Understand-
297 ing effects of matrix protease and matrix organization on directional per-
298 sistence and translational speed in three-dimensional cell migration. *Ann*
299 *Biomed Eng*, 35, 91–100.
- 300 8. Erler, J. T. & Weaver, V. M. (2009) Three-dimensional context regulation of
301 metastasis. *Clin Exp Metastasis*, 26, 35–49.
- 302 9. Wolf, K. et al. (2009) Collagen-based cell migration models in vitro and in
303 vivo. *Semin Cell Dev Biol*, 20, 931–941.
- 304 10. Provenzano, P. P. et al. (2008) Collagen density promotes mammary tumor
305 initiation and progression. *BMC Medicine*, 6, 11.
- 306 11. Egeblad, M., Rasch, M. G. & Weaver, V. M. (2010) Dynamic interplay be-
307 tween the collagen scaffold and tumor evolution. *Curr Opin Cell Biol*, 22,
308 697–706.
- 309 12. Ilina, O., Bakker, G-J., Vasaturo, A., Hofmann, R. M. & Friedl, P. (2011)
310 Two-photon laser-generated microtracks in 3D collagen lattices: principles
311 of MMP-dependent and -independent collective cancer cell invasion. *Phys*
312 *Biol*, 8, 015010.
- 313 13. Heuzé, M. L., Collin, O., Terriac, E., Lennon-Duménil, A-M. & Piel, M.
314 (2011) Cell migration in confinement: a micro-channel-based assay. *Methods Mol Biol*, 769, 415–434.
315
- 316 14. Irimia, D. & Toner, M. (2009) Spontaneous migration of cancer cells under
317 conditions of mechanical confinement. *Integr Biol (Camb)*, 1, 506–512.
- 318 15. Rolli, C. G., Seufferlein, T., Kemkemer, R. & Spatz, J. P. (2010) Impact of
319 Tumor Cell Cytoskeleton Organization on Invasiveness and Migration: A
320 Microchannel-Based Approach. *PLoS ONE*, 5, e8726.
- 321 16. Faure-André, G. et al. (2008) Regulation of dendritic cell migration by
322 CD74, the MHC class II-associated invariant chain. *Science*, 322, 1705–
323 1710.

- 324 17. Taylor, A. M. et al. (2005) A microfluidic culture platform for CNS axonal
325 injury, regeneration and transport. *Nat Methods*, 2, 599–605.
- 326 18. Scianna, M., Preziosi, L. (2013) Modeling the influence of nucleus elasticity
327 on cell invasion in fiber networks and microchannels. *J Theor Biol*, 317,
328 394–406.
- 329 19. Scianna, M., Preziosi, L. & Wolf, K. (2013) A Cellular Potts Model simu-
330 lating cell migration on and in matrix environments. *Math Biosci Eng*, 10,
331 235–261.
- 332 20. Tozluoğlu, M. et al. (2013) Matrix geometry determines optimal cancer cell
333 migration strategy and modulates response to interventions. *Nat Cell Biol*,
334 15, 751–762.
- 335 21. Giverso, C., Grillo, A. & Preziosi, L. Influence of nucleus deformability on
336 cell entry into cylindrical structures. *Biomech Model Mechanobiol*:1–22.
- 337 22. Mousavi, S. J., Doweidar, M. H. & Doblaré, M. (2013) Cell migration and
338 cell-cell interaction in the presence of mechano-chemo-thermotaxis. *Mol*
339 *Cell Biomech*, 10, 1–25.
- 340 23. Aubry, D., Thiam, H., Piel, M. & Allena, R. (2014) A computational me-
341 chanics approach to assess the link between cell morphology and forces dur-
342 ing confined migration. *Biomech Model Mechanobiol*.
- 343 24. Scianna, M. & Preziosi, L. (2014) A cellular Potts model for the MMP-
344 dependent and -independent cancer cell migration in matrix microtracks of
345 different dimensions. *Comput Mech*, 53, 485–497.
- 346 25. Larson, R. G. (1998) *The Structure and Rheology of Complex Fluids* (Oxford
347 University Press, USA).
- 348 26. Holzapfel, G. A. (2000) *Nonlinear Solid Mechanics: A Continuum Approach*
349 *for Engineering* (Wiley). 1st Ed.
- 350 27. Taber, L. A. (2004) *Nonlinear Theory of Elasticity: Applications in Biome-*
351 *chanics* (World Scientific Pub Co Inc).
- 352 28. Phillipson, M. et al. (2006) Intraluminal crawling of neutrophils to emigra-
353 tion sites: a molecularly distinct process from adhesion in the recruitment
354 cascade. *J Exp Med*, 203, 2569–2575.

- 355 29. Sakamoto, Y., Prudhomme, S. & Zaman, M. H. (2011) Viscoelastic gel-strip
356 model for the simulation of migrating cells. *Ann Biomed Eng*, 39, 2735–
357 2749.
- 358 30. Allena, R. & Aubry, D. (2012) “Run-and-tumble” or “look-and-run”? A
359 mechanical model to explore the behavior of a migrating amoeboid cell. *J*
360 *Theor Biol*, 306, 15–31.
- 361 31. Allena, R. (2013) Cell migration with multiple pseudopodia: temporal and
362 spatial sensing models. *Bull Math Biol*, 75, 288–316.
- 363 32. Schaub, S., Bohnet, S., Laurent, V. M., Meister, J-J. & Verkhovskiy, A. B.
364 (2007) Comparative Maps of Motion and Assembly of Filamentous Actin
365 and Myosin II in Migrating Cells. *Mol Biol Cell*, 18, 3723–3732.
- 366 33. Friedl, P., Wolf, K. & Lammerding, J. (2011) Nuclear mechanics during cell
367 migration. *Curr Opin Cell Biol*, 23, 55–64.
- 368 34. Ronot, X., Doisy, A. & Tracqui, P. (2000) Quantitative study of dynamic
369 behavior of cell monolayers during in vitro wound healing by optical flow
370 analysis. *Cytometry*, 41, 19–30.
- 371 35. Ngali, S. H. et al. (2013) Creating adhesive and soluble gradients for imag-
372 ing cell migration with fluorescence microscopy. *J Vis Exp*.
- 373 36. Pesen, D. & Hoh, J. H. (2005) Micromechanical Architecture of the Endothe-
374 lial Cell Cortex. *Biophys J*, 88, 670–679.
- 375 37. Tinevez, J-Y. et al. (2009) Role of cortical tension in bleb growth.
376 *PNAS:pnas.0903353106*.
- 377 38. Jiang, H. & Sun, S. X. (2013) Cellular Pressure and Volume Regulation and
378 Implications for Cell Mechanics. *Biophysical Journal*, 105, 609–619.
- 379 39. Righolt, C. H. et al. (2010) Molecular Image Analysis: Quantitative De-
380 scription and Classification of the Nuclear Lamina in Human Mesenchy-
381 mal Stem Cells. *International Journal of Molecular Imaging* 2011. Avail-
382 able at: <http://www.hindawi.com/journals/ijmi/2011/723283/abs/> [Accessed
383 September 4, 2013].
- 384 40. Crick, F. H. C. & Hughes, A. F. W. (1950) The physical properties of cyto-
385 plasm. *Experimental Cell Research*, 1, 37–80.

- 386 41. Caille, N., Thoumine, O., Tardy, Y. & Meister, J-J. (2002) Contribution of
387 the nucleus to the mechanical properties of endothelial cells. *J Biomech*, 35,
388 177–187.
- 389 42. Dahl, K. N., Ribeiro, A. J. S. & Lammerding, J. (2008) Nuclear Shape, Me-
390 chanics, and Mechanotransduction. *Circulation Research*, 102, 1307–1318.
- 391 43. Vaziri, A., Lee, H. & Mofrad, M. R. K. (2006) Deformation of the cell nu-
392 cleus under indentation: Mechanics and mechanisms. *Journal of Materials*
393 *Research*, 21, 2126–2135.
- 394 44. Christensen, R. M. (1991) *Mechanics of Composite Materials* (Krieger Pub-
395 lishing Company).
- 396 45. Bausch, A. R., Möller, W. & Sackmann, E. (1999) Measurement of local
397 viscoelasticity and forces in living cells by magnetic tweezers. *Biophys J*,
398 76, 573–579.
- 399 46. Drury, J. L. & Dembo, M. (2001) Aspiration of human neutrophils: effects
400 of shear thinning and cortical dissipation. *Biophys J*, 81, 3166–3177.
- 401 47. Fukui, Y., Uyeda, T. Q. P., Kitayama, C. & Inoué, S. (2000) How well can an
402 amoeba climb? *PNAS*, 97, 10020–10025.

114 is introduced at 0° at the right side of the micro-channel, so that the direction of
115 migration is imposed and corresponds to the horizontal axis \mathbf{i}_x .

The solid active deformation tensor $\mathbf{F}_{cytosol,a}$ [23] reads

$$\mathbf{F}_{cytosol,a} = \begin{cases} e_{a0} \sin\left(2\pi\frac{t}{T}\right) h_{cytosol,f} \mathbf{i}_x \otimes \mathbf{i}_x & \text{if } \sin\left(2\pi\frac{t}{T}\right) > 0 \\ \frac{e_{a0}}{2} \sin\left(2\pi\frac{t}{T}\right) h_{cytosol} \mathbf{i}_x \otimes \mathbf{i}_x & \text{if } \sin\left(2\pi\frac{t}{T}\right) < 0 \end{cases} \quad (18)$$

where e_{a0} is the amplitude of the active strain, t is time, T is the migration period and \otimes indicates the tensorial product. $h_{cytosol,f}$ is a characteristic function describing the portion of cytosol where the polymerization of the actin filaments takes place and reads

$$h_{cytosol,f}(\mathbf{p}) = \begin{cases} h_{cytosol} & \text{if } \mathbf{p} > \mathbf{c}_{cell} \\ 0 & \text{otherwise} \end{cases} \quad (19)$$

116 3 Results

117 COMSOL Multiphysics® 3.5a has been used to run all the simulations. As in [23],
118 the model represents a HeLa cell. The characteristic functions presented in Sec. 2.2
119 have been used to implicitly describe the cytoplasm and the nucleus components
120 in order to be able to define the parameters of the standard Maxwell models [23].
121 The radius r_{cortex} , $r_{cytosol}$, r_{lamina} and $r_{nucleoplasm}$ of the cell have been chosen equal
122 to $7.5 \mu\text{m}$ [34, 35], $7.25 \mu\text{m}$, $4.5 \mu\text{m}$ and $4.4 \mu\text{m}$ respectively, which leads to a cell
123 cortex (t_{cortex}) and a nuclear lamina (t_{lamina}) thicknesses equal to $0.25 \mu\text{m}$ [36–38]
124 and $0.1 \mu\text{m}$ [39] respectively. The nominal values of the Young moduli $E_{cortex,0}$ of
125 the cell cortex and $E_{cytosol,0}$ of the cytosol have been chosen equal to 100 Pa and 10
126 Pa [40], respectively. For the nucleus, assuming that its stiffness is mostly provided
127 by the nuclear lamina, $E_{lamina,0}$ and $E_{nucleoplasm,0}$ have been set to 3000 Pa [41,
128 42] and 25 Pa [43], respectively. Such moduli have been recalculated according
129 to a simple spatial homogenization approach [25, 44] and to the surface occupied
130 by each component in the cell to obtain E_{cortex} , $E_{cytosol}$, E_{lamina} and $E_{nucleoplasm}$. The
131 Poisson's ratios ν_{cortex} and ν_{lamina} have been set to 0.3, while $\nu_{cytosol}$ and $\nu_{nucleoplasm}$
132 to 0.4. The viscosities $\mu_{cytosol}$ and $\mu_{nucleoplasm}$ are equal to $3 \times 10^5 \text{Pa}\cdot\text{s}$ [45, 46].
133 The global cell density ρ has been set to $1000 \text{kg}/\text{m}^3$ [47] and the viscous friction
134 coefficient μ_{adh} is equal $10^8 \text{Pa}\cdot\text{s}/\text{m}$. Finally, the intensity of the active strain e_{a0}
135 and the migration period T have been chosen equal to 0.2 and 600 s respectively.
136 The geometrical and mechanical parameters of the cell have been reported in Table
137 1.

3.6 Influence of substrate stiffness

During migration, the cell is highly sensitive to the mechanical properties of the ECM which may affect critical processes such as adhesion (65) and polarisation (66). The latter consists of creating and maintaining an asymmetric distribution of intrinsic cellular subdomains with distinct chemical and mechanical properties. Polarity is a necessary step during cell migration and triggers the transition from a symmetric-isotropic to an asymmetric-anisotropic configuration. ECM stiffness may inhibit or induce cell polarity resulting in a mechanism called durotaxis by which the acto-myosin filaments orient in the direction of the stiffness gradient or along the stress fields generated by neighbour cells.

To investigate such phenomena, I initiated a collaboration with Benoît Ladoux who is the Principal Investigator of the Cell adhesion and mechanics Laboratory at the Institut Jacques Monod in Paris and at the Mechanobiology Institute in Singapore. Ladoux's team is interested in understanding interactions between the cell and its environment by coupling traditional molecular approaches and micro and nanotechnology related tools. In particular, they analyse single cell migration over micropatterned substrates with different rigidity and topography.

In order to reproduce this specific experimental set up and to take into account both durotaxis and polarity processes, the previous model (49) has been modified and is based on the following assumptions:

- the substrate is represented as a square which may be homogeneously soft or stiff or include a combination of both types of region. Additionally, a viscous force inhibiting cell progression is associated with the soft regions of the substrate;
- as previously (49, 50), the cell is modelled as a continuum, with initially circular shape. It is able to develop radial and cyclic active strains of protrusion and contractions which are synchronised with the adhesive forces between the cell and the substrate;
- as in (49, 50), a generalized Maxwell model is used to describe the mechanical behaviour of the cell, but here the solid elastic component is isotropic/anisotropic according to the type of substrate.

This work, which has been recently submitted for revision to Physical Biology, was partly carried out during my stays at the Mechanobiology Institute in 2013 and 2014 and will be pursued during my 'Accueil en délégation CNRS' in Ladoux's team starting from February 2016. I will present the governing equations and the results during the oral defence.

Submitted Paper:

Aubry D, Gupta M, Ladoux B, Allena R Mechanical link between durotaxis, cell polarity and anisotropy during cell migration. *Submitted with minor revisions to Physical Biology* 2015.

3.7 Conclusions and perspectives

The previous results show the progression of my research from a simple initial model of single cell migration to a more complex one allowing successful reproduction of specific experimental configurations. In fact, although the very first objective was to develop a conceptually simple model that realistically simulates cell movement, as my collaborative interactions with the biologists mentioned intensified, it became clear that more complex issues needed to be considered and the model needed to be extended accordingly. Nevertheless, the main focus of the work has always been mechanically oriented - to quantify strains and stresses and to depict the necessary conditions for a particular phenomenon to occur. Therefore, I have been able to conclude that:

- a minimal amount of adhesion between the cell and the substrate is essential throughout the migration process in order for the cell to pull or push its body forward;
- migration is much more efficient over stiff substrates than softer ones, which highly inhibit the gripping of the cell and lead to a pulsatile movement on the spot;
- during confined migration i) the cell behaviour (i.e. permeative, invasive or penetrating) is determined by close interaction between the strains and the stresses generated between the microchannel walls and the cell boundaries and ii) the nucleus being the stiffest component of the cell, a higher force has to be exerted on it in order to maintain it squeezed during the whole migration across the microchannel ;
- given the mechanical properties of the nucleus, for the cell to be permeative across sub-nuclear sized microchannels further mechanisms must occur in order to enhance the squeezing of the cellular body and the nucleus.

Although the results of the modelling to date are promising, the model has some limitations. For instance, presently the cell is considered as a solid with not well-quantified viscoelastic properties, while in actuality it behaves as a fluid with embedded elastic or viscoelastic organelles. Thus, I have started working on a more realistic description of the system, which demands a change of perspective and a questioning of the main hypotheses, but would definitely better fit the available experimental data. Additionally, key aspects such as the initial cell geometry, the perfect intra-synchronisation between the active strains and the adhesion forces or the *a priori* set intensity and duration of successive phases also require improvement or revision. Nevertheless, this is only possible in view of the current and consistent outcomes, whereas at the early stages of the work few assumptions were needed in order to move forward.

In the near future, I would like to pursue two main axes of research:

- 1) deeper exploration of the interaction between cell polarity and durotaxis over a 2D flat substrate;
- 2) investigation of the role of the nucleus during 3D confined migration within the ECM.

To pursue the first axis of research, I plan to employ two different approaches. First, I will use the finite element technique and improve the model presented in Sec. 3.6 to take into account the detailed morphology (i.e. pillar geometry and mechanical properties) of the substrate and the adhesion forces exerted by the cell on the pillars. This work is the object of the project submitted for an 'Accueil en délégation au CNRS' at the Laboratoire d'Adhésion et

Mécanique Cellulaire co-directed par Benoît Ladoux et René-Marc Mège. The main objective is to decipher the necessary mechanical conditions leading to the switch from an isotropic to an anisotropic cellular behaviour. In parallel, during my stay at the Mathematical Department at the Politecnico of Turin (Italy) last January, I have developed a discrete CellularPotts model which has already provided consistent results regarding the different behaviour of the cell over a soft or a stiff substrate. A paper is in preparation and the principal outcomes will be shown during the oral defence.

The second axis of research, which has been submitted for funding to the Agence Nationale de la Recherche, relies on the promising results obtained so far, but also on recent discoveries providing compelling evidence that the mechanical properties of the nucleus are critical for multiple cellular functions and biological phenomena (i.e. development, wound healing or immune response) and that defects in nuclear structure and organization can lead to a large number of human diseases (i.e. muscular dystrophies, cardiomyopathies or cancer). I plan to develop three essential features.

First, the migration mode in confined environments is quite different from that observed on homogenous/heterogeneous flat substrates. In fact, the usual locomotion based on the four-step mechanism mentioned earlier (i.e. i) protrusion at the front, ii) adhesion at the front, iii) contraction at the back and iv) adhesion at the back), is no longer suitable when the cell needs to adapt to the entanglement of the environment and develop non-specific adhesions (67, 68). Additionally, the complexity of the ECM requires a reduction in the number of protrusions to avoid attempting to follow multiple paths at the same time and becoming trapped in the ECM fibres (69). This alternative migration mode is also known as ‘chimneying’ because it is very similar to human climbing technique. Actually, it consists of developing a few lateral protrusions, which allow the cell to adhere to the microchannel walls by exerting forces perpendicular to the direction of migration. In order to include such aspects, I intend to modify two main features of the present model: i) the direction of the pseudopodia will now be peripheral and ii) the intensity of the active strains responsible for the pseudopodia formation will directly depend on the frictional forces generated between the cell and the microchannel walls. This aspect is the object of the Master 2 thesis of Solenne Devereaux, whom I co-supervise with Denis Aubry.

Second, migration of cells through sub-nuclear pores induces significant nuclear deformation. Four phases of locomotion have been identified: i) cell front entry with no slowdown, ii) nuclear entry and strain with high slowdown, iii) nucleus exit and iv) cell exit. The nucleus is constituted of the nucleoplasm, which is very similar to the viscous cytosol, and the rigid nuclear lamina, which is constituted by intermediate filaments encoded by Lamin A/C genes. When migrating through sub-nuclear pores, some cells (i.e. immune cells) express low level of Lamin genes whereas others (i.e. cancer cells) are able to enlarge ECM pores (70, 71). Low levels of Lamin genes lead to a short lifetime which may constitute an issue for those cells, such as dendritic cells, that must combine high migration capacity and long term viability (72). Therefore, there must exist a mechanism allowing cells with high levels of Lamin genes to contract their nucleus in order to migrate through sub-nuclear constrictions. One potential scenario involves a pressure around the nucleus inducing temporary rupture or disassembly of the Lamin A/C network while the nucleus passes through the narrow pore. From a mechanical point of view, such behaviour corresponds to a visco-plastic

constitutive law so that nucleus strains and more specifically nuclear lamina strains directly depend on the rate of the mechanical forces exerted by the ECM fibres on the cell. Therefore, a more refined description of the nucleus mechanical behaviour has to be considered which takes into account both the nucleoplasm (deformable) and the lamina (stiffer but damaging).

Third, once the two previous aspects have been addressed, 3D modelling will be required to simulate cell migration within a 3D fibre network. In the short term, the main objective will be to quantify the mechanical strains of the nucleus during confined cell migration. In the long term, the ambitious goal is to propose new mechanical therapies based on the modification of specific mechanical parameters such as the stiffness of the cell, the nucleus or the ECM. By doing so, one will be able to control the migration of the cell during various biological phenomena and therefore to prevent specific human diseases.

3.8 Bibliography

1. Charest PG, Firtel RA (2007) Big roles for small GTPases in the control of directed cell movement. *Biochem J* 401(2):377–390.
2. Krummel MF, Macara I (2006) Maintenance and modulation of T cell polarity. *Nat Immunol* 7(11):1143–1149.
3. Flaherty B, McGarry JP, McHugh PE (2007) Mathematical models of cell motility. *Cell Biochem Biophys* 49(1):14–28.
4. Smith A, et al. (2005) A talin-dependent LFA-1 focal zone is formed by rapidly migrating T lymphocytes. *J Cell Biol* 170(1):141–151.
5. Sheetz MP, Felsenfeld D, Galbraith CG, Choquet D (1999) Cell migration as a five-step cycle. *Biochem Soc Symp* 65:233–243.
6. Meili R, Alonso-Latorre B, del Alamo JC, Firtel RA, Lasheras JC (2010) Myosin II is essential for the spatiotemporal organization of traction forces during cell motility. *Mol Biol Cell* 21(3):405–417.
7. Abercrombie M (1980) The Croonian Lecture, 1978: The Crawling Movement of Metazoan Cells. *Proc R Soc Lond B Biol Sci* 207(1167):129–147.
8. Danuser G, Allard J, Mogilner A (2013) Mathematical Modeling of Eukaryotic Cell Migration: Insights Beyond Experiments. *Annu Rev Cell Dev Biol* 29:501–528.
9. DiMilla PA, Barbee K, Lauffenburger DA (1991) Mathematical model for the effects of adhesion and mechanics on cell migration speed. *Biophys J* 60(1):15–37.
10. Alt W, Dembo M (1983) A contraction-disassembly model for intracellular actin gels. *Equadiff 82*, Lecture Notes in Mathematics., eds Knobloch HW, Schmitt K (Springer Berlin Heidelberg), pp 1–9. Available at: <http://link.springer.com/chapter/10.1007/BFb0103231> [Accessed December 8, 2014].
11. Dembo M, Harlow F (1986) Cell motion, contractile networks, and the physics of interpenetrating reactive flow. *Biophys J* 50(1):109–121.
12. Alt W, Dembo M (1999) Cytoplasm dynamics and cell motion: two-phase flow models. *Math Biosci* 156(1–2):207–228.
13. Hill TL (1981) Microfilament or microtubule assembly or disassembly against a force. *Proc Natl Acad Sci U S A* 78(9):5613–5617.
14. Peskin CS, Odell GM, Oster GF (1993) Cellular motions and thermal fluctuations: the Brownian ratchet. *Biophys J* 65(1):316–324.
15. Mogilner A, Oster G (1996) Cell motility driven by actin polymerization. *Biophys J* 71(6):3030–3045.
16. Alberts JB, Odell GM (2004) In Silico Reconstitution of Listeria Propulsion Exhibits Nano-Saltation. *PLoS Biol* 2(12):e412.
17. Carlsson AE (2003) Growth Velocities of Branched Actin Networks. *Biophys J* 84(5):2907–2918.
18. Schaus TE, Borisy GG (2008) Performance of a population of independent filaments in lamellipodial protrusion. *Biophys J* 95(3):1393–1411.
19. Weichsel J, Schwarz US (2010) Two competing orientation patterns explain experimentally observed anomalies in growing actin networks. *Proc Natl Acad Sci* 107(14):6304–6309.
20. Gerbal F, Chaikin P, Rabin Y, Prost J (2000) An Elastic Analysis of Listeria monocytogenes Propulsion. *Biophys J* 79(5):2259–2275.
21. Marcy Y, Prost J, Carlier M-F, Sykes C (2004) Forces generated during

- actin-based propulsion: A direct measurement by micromanipulation. *Proc Natl Acad Sci U S A* 101(16):5992–5997.
22. Zimmermann J, Enculescu M, Falcke M (2010) Leading-edge–gel coupling in lamellipodium motion. *Phys Rev E* 82(5):051925.
 23. Lacayo CI, et al. (2012) Choosing orientation: influence of cargo geometry and ActA polarization on actin comet tails. *Mol Biol Cell* 23(4):614–629.
 24. Zhu J, Mogilner A (2012) Mesoscopic Model of Actin-Based Propulsion. *PLoS Comput Biol* 8(11):e1002764.
 25. Oster GF (1984) On the crawling of cells. *J Embryol Exp Morphol* 83:329–64.
 26. Carlier MF, Pantaloni D (1997) Control of actin dynamics in cell motility. *J Mol Biol* 269(4):459–467.
 27. Mogilner A, Oster G (1996) The Physics of Lamellipodial Protrusion. *Eur Biophys J* 25:47–53.
 28. Theriot JA, Mitchison TJ (1991) Actin microfilament dynamics in locomoting cells. *Publ Online 11 July 1991 Doi101038352126a0* 352(6331):126–131.
 29. Alt W, Tranquillo RT (1995) Basic morphogenetic system modeling shape changes of migrating cells: How to explain fluctuating lamellipodial dynamics. *J Biol Syst* 3:905–916.
 30. Lee J, Ishihara A, Jacobson K (1993) How do cells move along surfaces? *Trends Cell Biol* 3(11):366–370.
 31. Mogilner A, Rubinstein B (2005) The Physics of Filopodial Protrusion. *Biophys J* 89(2):782–795.
 32. Small JV, Rohlfes A, Mogilner A (1993) Actin and cell movement. Cell Behaviour: Adhesion and Motility. G.Jones, C. Wigley and R. Warn (Eds). *Soc Exp Biol*:57–71.
 33. Stéphanou A, Chaplain MAJ, Tracqui P (2004) A mathematical model for the dynamics of large membrane deformations of isolated fibroblasts. *Bull Math Biol* 66(5):1119–1154.
 34. Veksler A, Gov NS (2007) Phase Transitions of the Coupled Membrane-Cytoskeleton Modify Cellular Shape. *Biophys J* 93(11):3798–3810.
 35. Bereiter-Hahn J, Lüers H (1998) Subcellular tension fields and mechanical resistance of the lamella front related to the direction of locomotion. *Cell Biochem Biophys* 29(3):243–262.
 36. Oster GF, Perelson AS (1987) The physics of cell motility. *J Cell Sci Suppl* 8:35–54.
 37. Taber LA, Shi Y, Yang L, Bayly PV (2011) A poroelastic model for cell crawling including mechanical coupling between cytoskeletal contraction and actin polymerization. *J Mech Mater Struct* 6(1-4):569–589.
 38. Young J, Mitran S (2010) A numerical model of cellular blebbing: a volume-conserving, fluid-structure interaction model of the entire cell. *J Biomech* 43(2):210–220.
 39. Zhu C, Skalak R (1988) A continuum model of protrusion of pseudopod in leukocytes. *Biophys J* 54(6):1115–1137.
 40. Carlsson AE, Sept D (2008) Mathematical modeling of cell migration. *Methods Cell Biol* 84:911–937.
 41. Rubinstein B, Jacobson K, Mogilner A (2005) Multiscale two-dimensional modeling of a motile simple-shaped cell. *Multiscale Model Simul* 3:413–439.
 42. Sakamoto Y, Prudhomme S, Zaman MH (2011) Viscoelastic gel-strip model

for the simulation of migrating cells. *Ann Biomed Eng* 39(11):2735–2749.

43. Stolarska MA, Kim Y, Othmer HG (2009) Multi-scale models of cell and tissue dynamics. *Philos Trans R Soc Math Phys Eng Sci* 367(1902):3525–3553.
44. Herant M, Dembo M (2010) Form and function in cell motility: from fibroblasts to keratocytes. *Biophys J* 98(8):1408–1417.
45. Zeng X, Li S (2011) Modelling and simulation of substrate elasticity sensing in stem cells. *Comput Methods Biomech Biomed Engin* 14(5):447–458.
46. Zaman MH, Kamm RD, Matsudaira P, Lauffenburger DA (2005) Computational model for cell migration in three-dimensional matrices. *Biophys J* 89(2):1389–1397.
47. Zaman MH, et al. (2006) Migration of tumor cells in 3D matrices is governed by matrix stiffness along with cell-matrix adhesion and proteolysis. *Proc Natl Acad Sci U S A* 103(29):10889–10894.
48. Borau C, Kamm RD, García-Aznar JM (2011) Mechano-sensing and cell migration: a 3D model approach. *Phys Biol* 8(6):066008.
49. Allena R, Aubry D (2012) “Run-and-tumble” or “look-and-run”? A mechanical model to explore the behavior of a migrating amoeboid cell. *J Theor Biol* 306:15–31.
50. Allena R (2013) Cell migration with multiple pseudopodia: temporal and spatial sensing models. *Bull Math Biol* 75(2):288–316.
51. Allena R, Mouronval A-S, Aubry D (2010) Simulation of multiple morphogenetic movements in the Drosophila embryo by a single 3D finite element model. *J Mech Behav Biomed Mater* 3(4):313–323.
52. Allena R, Muñoz JJ, Aubry D (2013) Diffusion-reaction model for Drosophila embryo development. *Comput Methods Biomech Biomed Engin* 16(3):235–248.
53. Muñoz JJ, Barrett K, Miodownik M (2007) A deformation gradient decomposition method for the analysis of the mechanics of morphogenesis. *J Biomech* 40(6):1372–1380.
54. Lubarda V (2004) Constitutive theories based on the multiplicative decomposition of deformation gradient: Thermoelasticity, elastoplasticity, and biomechanics. *Appl Mech Rev* 57(2):95–109.
55. Murray JD (2003) *Mathematical Biology II: Spatial Models and Biomedical Applications* (Springer).
56. Van Haastert PJM (2010) Chemotaxis: insights from the extending pseudopod. *J Cell Sci* 123(Pt 18):3031–3037.
57. Weijer CJ (2009) Collective cell migration in development. *J Cell Sci* 122(Pt 18):3215–3223.
58. Andrew N, Insall RH (2007) Chemotaxis in shallow gradients is mediated independently of PtdIns 3-kinase by biased choices between random protrusions. *Nat Cell Biol* 9(2):193–200.
59. Bosgraaf L, Van Haastert PJM (2009) Navigation of Chemotactic Cells by Parallel Signaling to Pseudopod Persistence and Orientation. *PLoS ONE* 4(8):e6842.
60. Karsenti E (2008) Self-organization in cell biology: a brief history. *Nat Rev Mol Cell Biol* 9(3):255–262.
61. Gerish, G., Malchow, D., Hess, B. (1974) Cell communication and cyclic-amp regulation during aggregation of the slime mold, dictyostelium discoideum. *Biochem Sens Funct Ed Jaenicke Springer-Verl N Y*:279–298.
62. Zigmond SH, Levitsky HI, Kreel BJ (1981) Cell polarity: an examination of

its behavioral expression and its consequences for polymorphonuclear leukocyte chemotaxis. *J Cell Biol* 89(3):585–592.

63. Friedl P, Wolf K (2010) Plasticity of cell migration: a multiscale tuning model. *J Cell Biol* 188(1):11–19.

64. Heuzé ML, Collin O, Terriac E, Lennon-Duménil A-M, Piel M (2011) Cell migration in confinement: a micro-channel-based assay. *Methods Mol Biol Clifton NJ* 769:415–434.

65. Giannone G, et al. (2004) Periodic lamellipodial contractions correlate with rearward actin waves. *Cell* 116(3):431–443.

66. Bischofs IB, Schwarz US (2003) Cell organization in soft media due to active mechanosensing. *Proc Natl Acad Sci* 100(16):9274–9279.

67. Hawkins RJ, et al. (2009) Pushing off the Walls: A Mechanism of Cell Motility in Confinement. *Phys Rev Lett* 102(5):058103.

68. Tozluoğlu M, et al. (2013) Matrix geometry determines optimal cancer cell migration strategy and modulates response to interventions. *Nat Cell Biol* 15(7):751–762.

69. Lämmermann T, Sixt M (2009) Mechanical modes of “amoeboid” cell migration. *Curr Opin Cell Biol* 21(5):636–644.

70. Pflücke H, Sixt M (2009) Preformed portals facilitate dendritic cell entry into afferent lymphatic vessels. *J Exp Med* 206(13):2925–2935.

71. Wolf K, et al. (2013) Physical limits of cell migration: control by ECM space and nuclear deformation and tuning by proteolysis and traction force. *J Cell Biol* 201(7):1069–1084.

72. Harada T, et al. (2014) Nuclear lamin stiffness is a barrier to 3D migration, but softness can limit survival. *J Cell Biol* 204(5):669–682.

Chapter 4

Collective cell migration

Single cell migration is one of the best-studied biological phenomena due to its contribution to many *in vivo* processes. Nevertheless, cells tend to migrate collectively by staying connected as they move. The number of migrating cells may vary from a few cells (i.e. egg chamber development in *Drosophila*) to hundreds (i.e. lateral line primordium in Zebrafish) or hundreds of thousands of cells (i.e. slug development in *Dicytostelium*).

Whereas the main mechanisms of single cell migration have been largely investigated and understood (1), those in control of collective cell migration remain unclear.

As in single cell migration, the movement of the cells inside the cohort is regulated by a tight synchronisation between the cell shape changes and the adhesion forces (see Chapter 1). Nonetheless, during collective cell migration this is not a sufficient condition for efficient migration, since cells must communicate and coordinate their movement with their neighbours.

There are several distinctive hallmarks of collective cell migration. First, cells are physically and functionally connected and cell-cell junctions are maintained during the whole process. Second, as in collective animal behaviour (2), cells receive positive feedback both in space and time. The former transforms the isolated behaviour of a single cell into a mass of similar behaviours. The latter leads to adjustments in the migration frequency of single cells toward some local average. Third, in most biological models of collective migration, cells structurally modify the surrounding ECM along their path. Finally, it is still unknown whether all the cells or only a few leaders actively participate in the collective movement. In fact, the distinction between the leaders and the followers has been considered the main feature of collective migration for long time (1, 3). However, recent observations have shown that all the cells develop membrane protrusions to synchronise their movement (4–6).

4.1 Previous works

During the last few years, several computational models have been proposed in the literature. Such works can be divided into two main categories: the agent-based (AG) and the continuum models.

The AG models allow description of the population in a discrete manner and take into account specific functions such as proliferation, division, cell-cell

adhesion as well as stochastic behaviours (7–15). Among these, it is worth to specifically mentioning the work of Kabla (16) in which different aspects of collective migration are explored such as the transition from epithelial to mesenchymal cell populations, the role of population size and confinement, the transmission of signals inside the population as well as the collective or solitary invasion of a surrounding tissue. These results are interesting since the model is able to reproduce *in vivo* and *in vitro* behaviours and provides the necessary mechanical conditions for such behaviours to occur. In the same spirit and using the same numerical approach, collective cell migration has been investigated during situations of confinement such as within well-defined circles (17) or strips (18). In the first case, confinement results in a persistent and coordinated rotation of the cells and the higher the cell density, the slower the rotation. In the second case, the smaller the strip, the higher the speed of the migrating cells, whereas in wider strips large-scale vortices appeared. These findings provide a mechanical explanation on how large scale cell-cell interactions may regulate the overall behaviour of the population and confirm the existence of critical sizes leading to length scales very close to those observed in an unconfined environment.

The continuum models may describe the cohort in terms of cell density through conservation equations or as a travelling wave of cell concentration through reaction-diffusion equations (19–21) or using level set equations (22). Most of these works focus on collective migration during wound healing. There are a few other works that consider the influence of the electric field on wound closure in specific contexts such as corneal wound healing (23), tumor growth (24, 25) or ischemic dermal wounds (26).

Finally, Maini et al. (27) and Serra-Picamal et al. (28) have proposed two computational models of a wound assay and an epithelial monolayer, respectively. On one hand, Maini et al. (27) found that the frontal edge of the population starts moving as a travelling wave at constant speed after a short period of time. On the other hand, Serra-Picamal et al. (28) found that a mechanical wave progressively spans the population and results stress differentials that initiate migration of cells.

4.2 Modelling collective cell migration

In this chapter I present a modelling approach of collective cell migration, which is derived from the model of single cell migration presented in Chapter 2 and is based on the following hypotheses.

First, the cell population has been modelled as a hybrid continuum-discrete ellipse free at its outer boundaries. The ellipse includes the cellular network, which is described through a characteristic function and is constituted by approximately one hundred cells each having an initially circular shape and in contact with each other. Each cell is potentially active and able to generate a frontal and a rear adhesion region in order to adhere to the ECM in which they are embedded (Fig. 4.1).

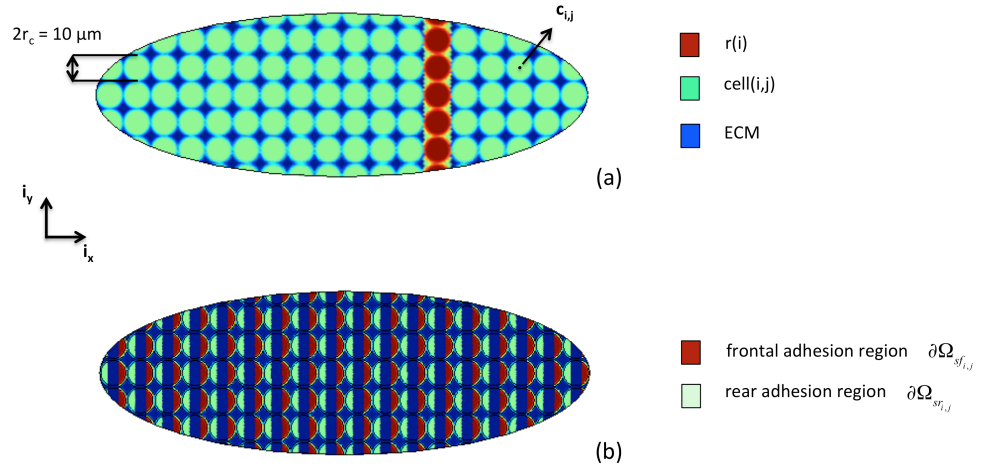


Fig. 4.1 The ellipse representing the population with the embedded cells (a) each with a frontal and a rear adhesion surface (b).

Second, as in the model of single cell migration, the mechanical behaviour of the cells is described through a standard Maxwell model (see Chapter 3), and for the ECM a Maxwell model is employed. The global equilibrium of the system is classically expressed, but, since both the cellular network and the ECM are defined by two characteristic functions, each variable (i.e. the Cauchy stress $\sigma_i(\mathbf{p})$ and the viscous strain rate $\dot{\epsilon}_i(\mathbf{p})$, where i changes according to the considered domain) is computed at each point of the continuum taking into account the contributions of the two regions (i.e. the cell network and the ECM) as follows

$$\begin{aligned}\sigma(\mathbf{p}) &= h_{ECM}(\mathbf{p})\sigma_{ECM}(\mathbf{p}) + \sum h_{cells}(\mathbf{p})\sigma_{cells}(\mathbf{p}) \\ \dot{\epsilon}_{fv}(\mathbf{p}) &= h_{ECM}(\mathbf{p})\dot{\epsilon}_{ECM_{fv}}(\mathbf{p}) + \sum h_{cells}(\mathbf{p})\dot{\epsilon}_{cells_{fv}}(\mathbf{p})\end{aligned}\quad (4.1)$$

where h_{ECM} and h_{cells} are the characteristic functions describing the ECM and the cell network, respectively and \mathbf{p} is the initial position of any particle of the system. Thus, the finite element mesh is not adapted to each sub-region of the continuum, but everything is handled via the level set functions, which allow localisation of the mechanical behaviour. The dynamic equation is first transformed into the weak form of the problem (i.e. principle of virtual work) and is then discretized by using finite elements. Accordingly, cells/ECM or cell/cell interaction forces are automatically equilibrated in a weak sense although in general, the cell boundaries intersect the finite element mesh edges. In fact, the level set functions describing the sub-regions of the system are defined independently from the finite element mesh.

Third, each active cell is intrinsically regulated by an intra-synchronization, which links the active strains of protrusion and contraction and adhesion forces between the cell and the ECM. The former are described as uniaxial cyclic deformations through the solid active strain tensor, whereas the latter are considered as viscous forces and are split into a frontal and a rear component.

Fourth, in addition to intra-synchronisation, which is a key aspect of single

cell migration (29, 30), in collective cell migration cells need to coordinate their movement in order to be as efficient as possible during the whole process. This results in what I have called inter-synchronisation, which regulates the movement of the whole population.

4.3 2D Finite element model of collective migration

As a first approach and as in previous models of single cell migration (31–35), I have decided to only focus on the mechanical aspects of collective cell migration. Such a choice is motivated by the following reasons. First, the molecular, genetic and chemical environments may vary according to the biological model one considers. However, the cell and the population movements are still governed by the Newton's law of motion (36), which provides insights into the admissibility of given movements. Second, to unveil the forces and the strains resulting from the collective migration, it is necessary to simulate the physics of the process, so that one is able to detect those constraints, which lead (or not) to an efficient migration of the population. In order to achieve such a goal, different scenarios must be tested to evaluate the mechanical interplay between intra-synchronisation (i.e. intrinsic coordination of each cell) and inter-synchronisation (i.e. coordination between the cells) and to conclude whether such configurations are realistic or not.

This work started during my post-doctoral fellowship at the Center for Genomic Regulation at Barcelona in collaboration with James Sharpe, who is the Principal Investigator of the Multicellular Systems Biology team.

Included Paper:

Allena R, Aubry D, Sharpe J (2013) On the mechanical interplay between intra- and inter-synchronization during collective cell migration: a numerical investigation. *Bull Math Biol* 75(12):2575–2599.

On the *Mechanical* Interplay Between Intra- and Inter-Synchronization During Collective Cell Migration: A Numerical Investigation

R. Allena · D. Aubry · J. Sharpe

Received: 7 May 2013 / Accepted: 19 September 2013
© Society for Mathematical Biology 2013

Abstract Collective cell migration is a fundamental process that takes place during several biological phenomena such as embryogenesis, immunity response, and tumorigenesis, but the mechanisms that regulate it are still unclear. Similarly to collective animal behavior, cells receive feedbacks in space and time, which control the direction of the migration and the synergy between the cells of the population, respectively. While in single cell migration intra-synchronization (i.e. the synchronization between the protrusion-contraction movement of the cell and the adhesion forces exerted by the cell to move forward) is a sufficient condition for an efficient migration, in collective cell migration the cells must communicate and coordinate their movement between each other in order to be as efficient as possible (i.e. inter-synchronization). Here, we propose a 2D mechanical model of a cell population, which is described as a continuum with embedded discrete cells with or without motility phenotype. The decomposition of the deformation gradient is employed to reproduce the cyclic active strains of each single cell (i.e. protrusion and contraction). We explore different modes of collective migration to investigate the mechanical interplay between intra- and inter-synchronization. The main objective of the paper is to evaluate the efficiency of the cell population in terms of covered distance and how the

Electronic supplementary material The online version of this article (doi:[10.1007/s11538-013-9908-4](https://doi.org/10.1007/s11538-013-9908-4)) contains supplementary material, which is available to authorized users.

R. Allena (✉) · J. Sharpe
EMBL-CRG Systems Biology Research Unit, Centre for Genomic Regulation (CRG), UPF,
Barcelona, Spain
e-mail: rachele.allena@ensam.eu

R. Allena
Arts et Metiers ParisTech, LBM, 151 Bd de l'hôpital, 75013 Paris, France

D. Aubry
Laboratoire MSSMat UMR CNRS 8579, Ecole Centrale Paris, 92295 Châtenay-Malabry, France

Published online: 18 October 2013

 Springer

stress distribution inside the cohort and the single cells may in turn provide insights regarding such efficiency.

Keywords Collective cell migration · Intra- and inter-synchronization · Continuum mechanics

1 Introduction

Cells can move individually or collectively. The number of migrating cells may vary from a few cells (i.e. egg chamber development in *Drosophila*) to hundreds (i.e. lateral line primordium in Zebrafish) or hundreds of thousands of cells (i.e. slug development in *Dyctyostelium*).

Although key aspects of single cell migration such as the control of protrusive activity, shape generation and interaction between the cell and the extra cellular matrix (ECM) are fairly well understood (Friedl and Gilmour 2009), the mechanisms that regulate collective cell migration are less clear.

As in single cell migration (Allena and Aubry 2012), the movement of the cells inside the population is triggered by a tight synchronization between shape changes and adhesion forces inside the cell (intra-synchronization), which results in a cyclic four (Flaherty et al. 2007) or five (Meili et al. 2010; Sheetz et al. 1999) steps process.

Nevertheless, contrarily to single cell migration, in collective cell migration the acquirement of a motility behavior by each cell does not guarantee the correct movement of the population and therefore it is not a sufficient condition. In fact, the cells inside the cohort need to communicate and to coordinate their movement with their neighbors in order to be as efficient as possible. Thus, as in collective animal behavior (Sumpter 2006), in collective cell migration we may observe positive feedbacks in space and time. Positive feedback in space builds up a collective pattern by transforming the isolated behavior of a single cell into a mass of similar behaviors. Positive feedback in time or inter-synchronization consists in small adjustments by individual cells of their own migration frequency toward that of some local average. The coupling between positive feedback in space and inter-synchronization results in a spatio-temporal wave, which regulates the collective movement and, although so far little explored, it may play a fundamental role in determining the migratory efficiency of the population.

Actually, individual cells can migrate in large populations by closely interacting over long distances or migrating as epithelial sheets where neighbor connections do not change significantly (Weijer 2009). While in the former case cells move together in a manner similar to that of single cells, in the latter case cells remain linked both physically and functionally during the movement (Friedl and Gilmour 2009). Cell-cell junctions are maintained through adherens junctions proteins, desmosomal proteins, and integrins (Friedl and Gilmour 2009; Iliina and Friedl 2009), which prevent the formation of gaps between the cells (Anand et al. 2007). These interactions limit the movement of the cells within the layer and restrict any cellular rearrangement.

Finally, it is still unclear whether all the cells or only the leader cells of the population participate to the collective migration. In fact, the distinction between leader

(located at the free boundary) and follower (located in the cell cohort) cells has been thought to be the main feature of collective cell migration (Friedl and Gilmour 2009) with the former exerting larger traction forces than the latter (Treat et al. 2009). Nevertheless, further studies have shown that both cells actually generate protrusions to coordinate the forward movement (Farooqui and Fenteany 2005; Fenteany et al. 2000; Tambe et al. 2011) and that the cell velocity is inversely proportional to the distance from the free boundary (Farooqui and Fenteany 2005).

1.1 Numerical Models of Collective Cell Migration

Numerical simulations are a powerful approach to test hypotheses about biological phenomena. For collective cell migration, we can distinguish between two categories of computational models: (i) the agent-based models (AGMs) and (ii) the continuum models (CMs). AGMs simulate the activity and the interactions of cells within a population and assess their influence on the global system by taking into account the rate of cell division, the cell proliferation, the adhesion between the cells and the substrate, the deformation energy, and the stochastic behavior of the cellular collective (Graner and Glazier 1992; Szabo et al. 2006; Vedel et al. 2013; Vicsek et al. 1995; Yamao et al. 2011).

CMs may be subdivided into two sub-categories. On the one hand, the model may be based on conservation equations of the cell density and of a mitosis-regulating chemical agent (Sherratt and Murray 1990, 1991). On the other hand, the cell layer may be represented as an incompressible fluid whose configuration is described by the density of cells and the velocity includes a growth term due to proliferation and apoptosis. Additionally, the adhesion forces of the layer sheet to the substrate and the stresses within the population are considered (Arciero et al. 2011).

A few models (McLennan et al. 2012; Yamao et al. 2011) describe the collective migration focusing on the movement of the neural crest, which occurs in the absence of extracellular signals.

Further studies have analyzed collective migration during the wound healing process. They have considered it as a free boundary problem and have taken into account the influence of physiological electric field on the wound closure in corneal wound healing (Gaffney et al. 1999), tumor growth (Chen and Friedman 2000), or ischemic dermal wounds (Xue et al. 2009).

Finally, we mention the works of Maini et al. (2004) and Serra-Picamal et al. (2012), which combine numerical and experimental approaches and may be of major interest for the present paper. Maini et al. (2004) have performed a ‘wound healing’ assay and have validated a model to assess the relationship between cell motility and proliferation. The authors have found that after a short period of time the frontal edge of the cell population moves as a traveling wave at constant speed.

Serra-Picamal et al. (2012) have discovered a mechanical wave that progressively spans a micropatterned epithelial monolayer across the cell-cell junctions and creates differentials of mechanical stress that trigger the migration of the population. Additionally, they have analyzed such a scenario through a 1D model in which the cells of the monolayer are represented by springs connected in series and are able to generate propelling forces that can be transmitted to the neighbor cells (elastic forces) or to the underneath gel substrate (viscous forces).

1.2 Objective of This Work

In the present paper, we propose a two-dimensional (2D) finite element model to simulate the collective migration of a cell population, which is based on the following hypotheses:

- the cohort is represented as a continuum with embedded discrete cells, which may have or not a motility phenotype. The cohort includes approximately hundred cells;
- as in previous works (Borisov and Svitkina 2000; Carlier and Pantaloni 1997; Condeelis 1993; Mogilner and Rubinstein 2005; Theriot and Mitchison 1991), the oscillating protrusion-contraction movement of the motile cells is assumed to be controlled by the cyclic polymerization-depolymerization process of the actin network inside the cytoskeleton;
- the decomposition of the deformation gradient (Allena et al. 2010; Lubarda 2004) is employed to take into account the active elementary deformations undergone by the motile cells (i.e. protrusion and contraction) as well as the elastic deformations generated by the interaction of the cells with the ECM (Allena 2013; Allena and Aubry 2012);
- large deformations of the motile cells are considered and the cells are able to form one pseudopod at a time at their leading edge (Allena and Aubry 2012);
- inside each motile cell the intra-synchronization between the active strains and the adhesion forces to the ECM is described (Allena 2013; Allena and Aubry 2012);
- finally, different modes of collective migration are investigated. Each one of these modes is triggered by a specific inter-synchronization between the cells resulting in different scenarios.

As in previous models of single cell migration (Carlsson and Sept 2008; Flaherty et al. 2007; Rubinstein et al. 2005; Sakamoto et al. 2011; Taber et al. 2011), we have decided here to only focus on the mechanical aspects of the phenomenon. Such a choice is motivated by the following reasons. First, the molecular, genetic, and chemical environments may vary according to the biological model one considers. However, the cell and the population movements are still governed by the Newton's law of motion (Murray 2003), which provides insights on the admissibility of given movements. Second, to unveil the forces and the strains resulting from the collective migration, we need to simulate the physics of the process, so that we are able to detect those constraints, which lead (or not) to an efficient migration of the population. In order to achieve such a goal, different scenarios must be tested to evaluate the mechanical interplay between intra- and inter-synchronization and to conclude whether such configurations are realistic or not.

2 The Model

In this section we present the general framework of the model. We first describe the 2D geometry of the cell cohort and of its constituent cells. Subsequently, we define the constitutive law for each of the component of the population, together with the

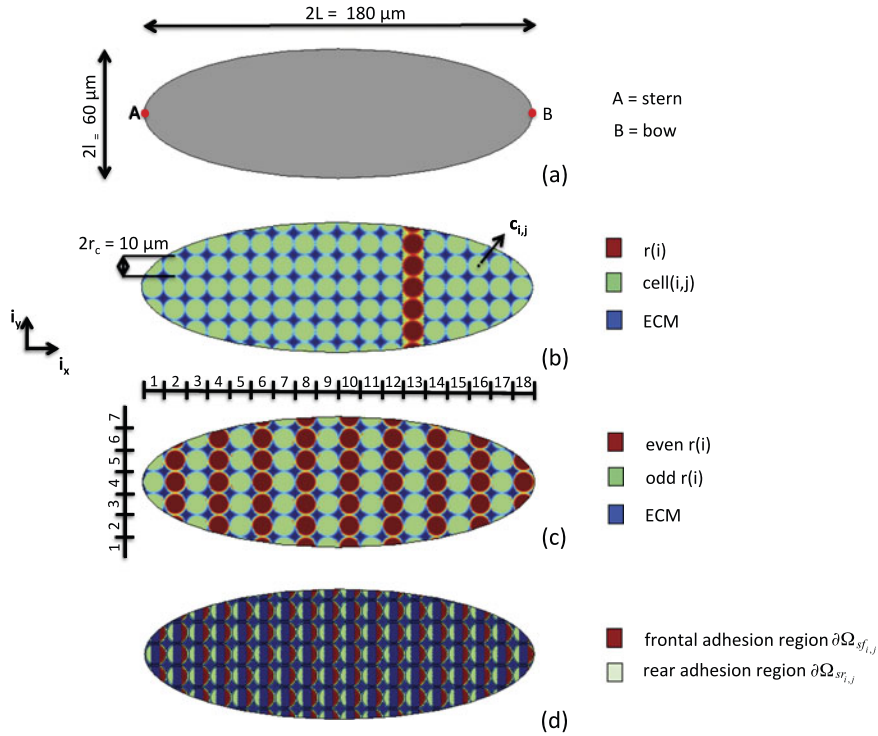


Fig. 1 (a) Geometry of the cell population. (b) Representation of the cell network $h_n(\mathbf{p})$. Each cell $c(i, j)$ (green) has a circular shape with radius r_c and centre $c_{i,j}$. (c) The ellipse is divided in cell rows $r(i)$ which are numbered from the stern to the bow of the ellipse (in red the even rows, in green the odd rows). The ECM (blue) fills the interstices between the cells. (d) Representation of the initial frontal (red) and rear (green) adhesion surfaces (Color figure online)

active deformations (protrusion and contraction) that take place during the migration process. Finally, we describe the intra- and the inter-synchronizations according to the different modes of migration adopted by the cells aggregate.

2.1 Geometry of the Cell Population

In the orthogonal frame (i_x, i_y) , the cells cohort has been modeled as a continuum and approximated by an ellipse with semi-axes L and l (Fig. 1a) free at its outer boundaries. The ellipse includes the cell network Ω_n , which is described through a characteristic function $h_n(\mathbf{p})$ (Eq. (9)) and is constituted by 106 cells. The cells are in contact with each other and embedded in the extracellular matrix (ECM) Ω_{ECM} , identified by the characteristic function $h_{ECM}(\mathbf{p})$ (Eq. (10)). Inside the cell network, we can distinguish between the active ($\Omega_{a,k}$) and the quiescent ($\Omega_{q,k}$) cells domains, which are represented through two characteristic functions $h_{a,k}(\mathbf{p})$ and $h_{q,k}(\mathbf{p})$ (Sect. 2.3.2). The number of active cells inside the population may vary according to the mode of migration adopted by the cohort (the underscript ‘ k ’ indicates such a mode (see Sect. 2.3.2)). Consequently, the quiescent cell domain $\Omega_{q,k}$ is the complementary of $\Omega_{a,k}$ with respect to Ω_n .

Each cell $c(i, j)$ inside the cohort has an initial circular shape (Fig. 1b, Eq. (12)) with radius r_c and centre $\mathbf{c}_{i,j}(c_{i,j_x}, c_{i,j_y})$, where the indices i and j indicate the position of the cell along the major and minor axes of the ellipse, respectively (Fig. 1c, Eq. (11)). For each cell, a frontal ($\partial\Omega_{sf_{i,j}}$) and a rear ($\partial\Omega_{sr_{i,j}}$) adhesion regions are defined through two characteristic functions $h_{sf_{i,j}}$ and $h_{sr_{i,j}}$, respectively (Eq. (13)), which allow the cell to adhere to the ECM. Here, we assume that the motile cells migrate along the horizontal axis \mathbf{i}_x . Additionally, the ellipse is divided into cell rows $r(i)$ (Eq. (14)), which are numbered, similarly to the single cells, from the stern (left) to the bow (right) of the ellipse (Fig. 1b).

2.2 Constitutive Model and Active Deformations

As mentioned in the previous section, three main regions constitute the mechanical system and each one of them has a specific constitutive behavior.

The first region contains the motile cells ($\Omega_{a,k}$), which actively participate to the migration process by cyclically protruding and contracting. It has been observed that a migrating cell is in general stiffer than a quiescent one (Wagh et al. 2008) and presents a gradual but significant decrease in stiffness from the front to the rear of the lamellipodia in agreement with the actin density profile (Ilina and Friedl 2009). As in our previous work (Allena 2013; Allena and Aubry 2012), we use a 2D generalized viscoelastic Maxwell model to describe the behavior of each cell which is constituted by two phases: (i) a solid-like phase (the actin filaments) where the active strains take place and (ii) a fluid-like phase, which includes some particles (the organelles, fluid-elastic) embedded into a fluid (cytoplasm, fluid-viscous). Thus, the active cells show a solid Young's modulus $E_{a,se}$ larger than the fluid-elastic Young's modulus $E_{a,fe}$ (Appendix A.2).

The second region includes the inactive (or quiescent) cells ($\Omega_{q,k}$) that follow the movement because of their connection to the active migrating cells. As for the active cells, a generalized viscoelastic 2D Maxwell model is used to reproduce their mechanical behavior. Nevertheless, the active strains (i.e. the actin filaments polymerization) do not occur in these cells, which are believed to influence the stiffness of the cell. Thus, the Young modulus $E_{q,se}$ of the solid elastic phase is considered to be much lower than $E_{a,se}$ (Soofi et al. 2009).

Finally, the third region is the one of the extracellular matrix (Ω_{ECM}) that fills the interstices between the cells (Fig. 1b). The ECM is assumed to be a viscoelastic material, with Young modulus and viscosity E_{ECM} and μ_{ECM} respectively.

Let ρ be the cells density, \mathbf{a} the acceleration, $\boldsymbol{\sigma}$ the Cauchy stress, \mathbf{F} the deformation gradient and J its determinant, then since we consider the inertial effects (Gracheva and Othmer 2004), the Newton law applied to the continuum with respect to the initial configuration \mathbf{p} is given by

$$\rho \mathbf{a} = \text{Div}_{\mathbf{p}}(J \boldsymbol{\sigma} \mathbf{F}^{-T}) + \mathbf{f}_{\text{adh}} \quad (1)$$

with $\text{Div}_{\mathbf{p}}$ the divergence with respect to the initial position, \mathbf{A}^{-T} the inverse transpose of the matrix \mathbf{A} (Holzapfel 2000; Taber 2004) and \mathbf{f}_{adh} the adhesion forces between the cell and the substrate, which will be described in the next section (Sect. 2.3.1).

The protrusion and contraction active deformations are triggered by the polymerization and depolymerization of the actin filaments and only take place in the solid phase of the active cells (Sect. 2.1). They are expressed as uniaxial cyclic deformations through the solid active strain tensor $\mathbf{F}_{a,sa}$ (Sect. A.2) as follows:

$$\mathbf{F}_{a,sa} = e_{a,k} \mathbf{i}_x \otimes \mathbf{i}_x \tag{2}$$

where $e_{a,k}$ will be defined more precisely later on for each type of collective migration adopted by the cell population.

2.3 Synchronization

In addition to intra-synchronization, which is a key aspect in single cell migration (Allena and Aubry 2012), in collective cell migration cells need to coordinate their movement (inter-synchronization) in order to be as efficient as possible during the whole process. These two fundamental aspects are described in more details in the next sections.

2.3.1 Intra-Synchronization

Single cell migration is usually described as a cyclic process occurring in four (Flaherty et al. 2007) or five (Meili et al. 2010; Sheetz et al. 1999) separate steps: (i) protrusion, (ii) frontal adhesion, (iii) contraction, (iv) rear adhesion, and (v) relaxation. Nevertheless, we have shown in Allena and Aubry (2012) that a minimal rate of adhesion at the rear and at the front of the cell is necessary during the protrusion and the contraction phases, respectively, otherwise the cell would only deform in place or slightly sliding over the surface. According to this remark, similarly to Allena and Aubry (2012), only two phases have been modeled here: (i) simultaneous protrusion of the frontal edge of the cell and adhesion at its rear edge, and (ii) simultaneous contraction of the back of the cell and adhesion at its frontal edge. Thus, we need to synchronize the adhesion forces \mathbf{f}_{adh} introduced in Eq. (1) with the active deformations that have already been defined in Sect. 2.2. Such forces are assumed to be viscous (Allena and Aubry 2012; Friedl and Wolf 2010; Phillipson et al. 2006; Sakamoto et al. 2011) and may be distinguished into a frontal (\mathbf{f}_f) and a rear (\mathbf{f}_r) force as follows:

$$\begin{aligned} \mathbf{f}_f(\mathbf{n}) &= -\mu_f h_e \left(-\frac{\partial e_{a,k}}{\partial t} \right) h_{sfi,j}(\mathbf{u}) h_{a,k}(\mathbf{p}) \frac{\partial \mathbf{u}}{\partial t} \\ \mathbf{f}_r(\mathbf{n}) &= -\mu_r h_e \left(\frac{\partial e_{a,k}}{\partial t} \right) h_{sri,j}(\mathbf{u}) h_{a,k}(\mathbf{p}) \frac{\partial \mathbf{u}}{\partial t} \end{aligned} \tag{3}$$

where \mathbf{n} is the normal vector to the boundary of the cell $c(i, j)$, μ_f , and μ_r are the friction force viscosities and \mathbf{u} is the displacement of the cell $c(i, j)$ with respect to the ECM. The characteristic function h_e is the key ingredient of the previous equations since it links the adhesion forces exerted by the cell $c(i, j)$ on the ECM with the pulsating movement of the cell $c(i, j)$. Thus, we have that: (i) when the cell protrudes (i.e. $h_e(\frac{\partial e_{a,k}}{\partial t}) = 1$), it simultaneously adheres at the back (i.e. $h_{sri,j}(\mathbf{u})$) while

(ii) when the cell contracts (i.e. $h_e(-\frac{\partial e_{a,k}}{\partial t}) = 1$), it simultaneously adheres at the front (i.e. $h_{sf_{i,j}}(\mathbf{u})$).

The characteristic function $h_{a,k}(\mathbf{p})$ defines which cells inside the cells network $h_n(\mathbf{p})$ are active. As described later on (Sect. 2.3.2), according to the mode of collective migration adopted by the cell population, all the cells or only few of them may be active. Thus, the active cells network $h_{a,k}(\mathbf{p})$ may coincide or not with the cell network $h_n(\mathbf{p})$. Consequently, the frontal ($\mathbf{f}_f(\mathbf{n})$) and the rear ($\mathbf{f}_r(\mathbf{n})$) adhesion forces are only applied in those active cells belonging to $h_{a,k}(\mathbf{p})$.

2.3.2 Inter-Synchronization

As mentioned above (Sect. 1.2), it is still unclear whether all the cells actively move forward or only the leader cells of the population migrate and pull the followers (Weijer 2009). For instance, in the lateral line primordium in Zebrafish as well as in other biological models such as Dictyostelium and Drosophila (Weijer 2009), the cells are believed to follow chemoattractant gradients that guide the collective movement. Furthermore, recent observations using epithelial monolayers have pointed out the presence of a mechanical wave that slowly spans the population and progressively transmits the forces from the leading edge to the centre of the cell sheet (Serra-Picamal et al. 2012). Accordingly, a cell can migrate only if an adjacent cell creates space, which leads to local cell unjamming, or if it pulls on the shared cell-cell junctions.

To evaluate the mechanical interplay between intra- and inter-synchronization, five different modes of collective migration of the cell population have been tested. For each one of them, the intra-synchronization inside the active cells is triggered off by a specific signal, which regulates the active strain $e_{a,k}$ inside the cells and the inter-synchronization between the cells:

- (1) strain gradient signal (or chemoattractant migration): the protrusion-contraction deformations inside the active cells are controlled by a gradient with highest intensity at the bow of the ellipse and lowest at the stern;
- (2) traveling wave with pulse signal (or worm-like migration): the migration is regulated by a wave which progressively and repeatedly covers the population and temporarily activates one by one the cell rows $r(i)$;
- (3) traveling wave with random unit step signal (or tsunami-like migration): a wave gradually spans the cell rows $r(i)$ of the ellipse and randomly activates the cells inside them that permanently acquire the motility phenotype and start migrating with their own pace which is synchronized with the one of the frontal and the rear neighbor cells;
- (4) traveling wave with gradient random unit step signal (or chemoattractant tsunami-like migration): this mode of migration is a combination of mode (1) and (3). In fact, the population movement is simultaneously triggered by a strain gradient and a traveling wave with a random unit step signal;
- (5) random signal (or random migration): the intensity and the period of the protrusion-contraction deformations inside the active cells randomly vary within the cohort. The cells migrate in a de-synchronized manner.

Each one of these migration modes requires a specific and complex inter-synchronization, which will be described in the following sections.

Strain Gradient Signal (or Chemoattractant Migration) In this mode of collective movement, all the cells inside the cohort are active so that $h_{a,1}(\mathbf{p}) = h_n(\mathbf{p})$ (Eq. (9)) and $h_{q,1}(\mathbf{p}) = 0$. Furthermore, the active cells migrate with the same intra-synchronization (i.e. they all protrude or contract simultaneously). The active deformations (protrusion and contraction) are regulated by a strain gradient. Thus, the leading cells sense more the signal than the cells in the back of the population and undergo larger strains during both the protrusion and the contraction phases. Consequently, the active deformation $e_{a,1}(\mathbf{p})$ is defined as follows:

$$e_{a,1}(\mathbf{p}) = e_{a0} \frac{(\mathbf{p} - \mathbf{p}_{\text{stern}}, \mathbf{p}_{\text{bow}} - \mathbf{p}_{\text{stern}})}{L} \sin\left(2\pi \frac{t}{T}\right) h_{a,1}(\mathbf{p}) \quad (4)$$

where e_{a0} is the amplitude of the active strain, $\mathbf{p}_{\text{stern}}$ and \mathbf{p}_{bow} are the initial position of the stern and the bow of the ellipse, respectively, and T is the duration of a migration cycle.

Traveling Wave with Pulse Signal (or Worm-Like Migration) This mode of collective migration is very similar to the one used by worms in which locomotion is triggered by waves of contraction and relaxation of alternate muscles. Here, the wave progressively and repeatedly (traveling wave) spans the cell population and temporarily (pulse signal) activates one by one the cell rows $r(i)$ (Eq. (12)), which are promptly deactivated as soon as the wave has passed by. Therefore, only one row is active at the time and the active deformation $e_{a,2}(\mathbf{p}, t)$ is expressed as

$$e_{a,2}(\mathbf{p}, t) = e_{a0} \sin\left(2\pi \frac{t}{T}\right) h_{a,2}(\mathbf{p}, t) \quad (5)$$

with $h_{a,2}(\mathbf{p}, t)$ defined in Eq. (20).

Traveling Wave with Random Unit Step Signal (or Tsunami-Like Migration) In the third mode of collective migration, a wave gradually (traveling wave) covers the cell population like a tsunami and permanently (unit step signal) ‘turns on’ one by one the rows of cells that acquire the motile phenotype and start migrating at their own pace. Three fundamental aspects have to be considered.

First, contrarily to the previous case (Sect. Traveling Wave with Pulse Signal (or Worm-Like Migration)), more than one row is active at the time now and the wave spans only once the ellipse.

Second, not all the cells inside the activated rows may acquire the motile phenotype (random unit step signal). However, some of them may remain quiescent, which leads to a random distribution of the active cells inside the population. The number of active cells in a row may vary from 1 to n_c , which is the total number of cells in a row. Such a configuration is determined by a parameter $\tau_{i,j}$, proper to each cell $c(i, j)$, which can be equal to 0 (quiescent cell) or 1 (active cell) and changes every 6 hours (Fig. 3).

Third, according to the experimental observations (Serra-Picamal et al. 2012), a cell can only move if the adjacent cell creates space or pulls on the shared cell-cell junctions. Thus, a perfect inter-synchronization between the cell $c(i, j)$ and its two

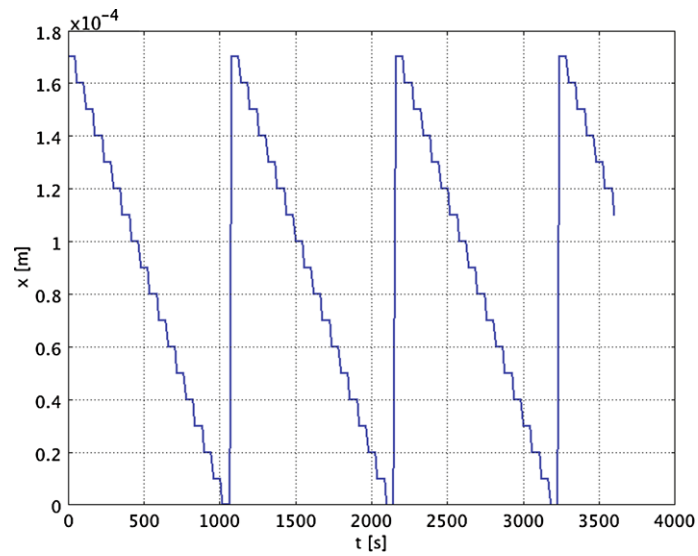
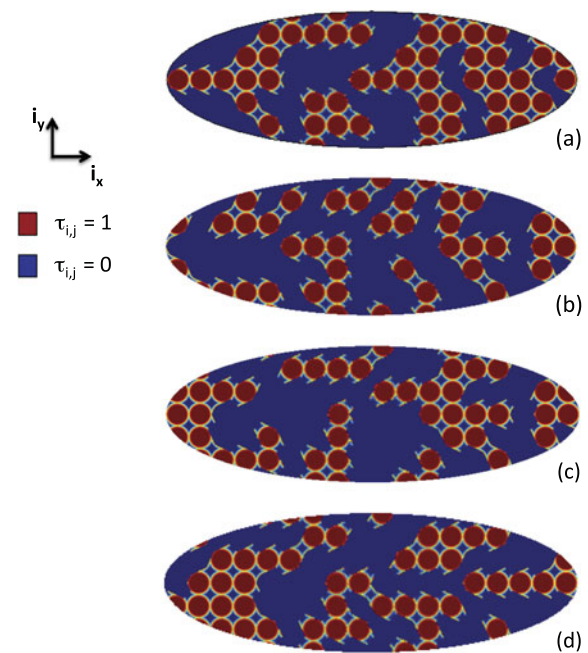


Fig. 2 Trend of the traveling wave, which defines the spatial coordinate $c_{i,j_x}(t)$ of the temporary active row for the worm-like migration (only 1 h is represented)

Fig. 3 Random distribution of the active cells network $h_{a,3}(p, t)$ between 0–6 h (a), 6 h–12 h (b), 12 h–18 h (c) and 18 h–24 h (d) for the tsunami-like migration. In red the active cells ($\tau_{i,j} = 1$) and in blue the quiescent cells ($\tau_{i,j} = 0$) (Color figure online)



adjacent cells on the same transversal coordinate j in the front ($c(i + 1, j)$) and in the back ($c(i - 1, j)$) is required. Specifically, the intra-synchronization inside the cell $c(i, j)$ must be out of phase with respect to the intra-synchronization of the

cells $c(i + 1, j)$ and $c(i - 1, j)$. Thus, when the cell $c(i + 1, j)$ protrudes, the cell $c(i, j)$ contracts and the cell $c(i - 1, j)$ protrudes; when the cell $c(i + 1, j)$ contracts, the cell $c(i, j)$ protrudes and the cell $c(i - 1, j)$ contracts. Furthermore, the inter-synchronization has to be coordinated with the wave that covers the ellipse and activates the cell rows (Eq. (23)). Therefore, a particular form of the active deformation $e_{a,3}(\mathbf{p}, t)$ is implemented as follows:

$$e_{a,3}(\mathbf{p}, t) = e_{a0} \sin\left(2\pi \frac{t - \frac{T}{2}(i_{\max} - i)}{T}\right) h_{a,3}(\mathbf{p}, t) \quad (6)$$

with $h_{a,3}(\mathbf{p}, t)$ the characteristic function describing the active cells network and defined in Eq. (22).

According to Eq. (6), the first cells to be ‘turned on’ and to deform are the ones inside the leading row of the ellipse ($i = i_{\max}$), while the other cells are gradually stimulated by the wave. After a period of $\frac{T}{2}(i_{\max} - i)$ the wave has spanned the entire length of the ellipse, thus each active cell is able to migrate at its proper pace.

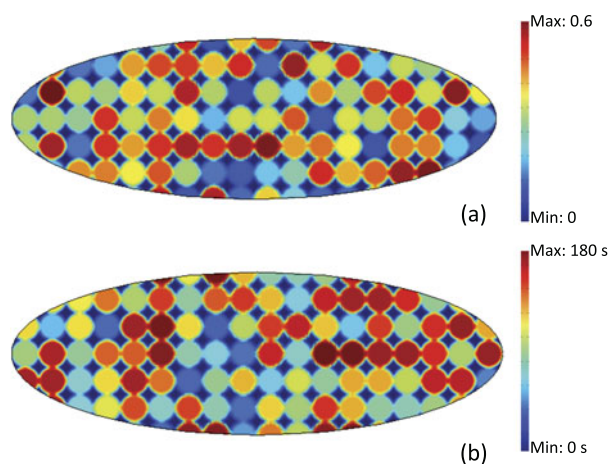
Traveling Wave with Gradient Unit Step Signal (or Chemoattractant Tsunami-Like Migration) The fourth mode of collective migration combines the strain gradient migration and the traveling wave migration. The active cells are randomly distributed inside the cohort as in the third mode of migration (Sect. Traveling Wave with Random Unit Step Signal (or Tsunami-Like Migration)), so that $h_{a,4}(\mathbf{p}) = h_{a,3}(\mathbf{p})$ (Eq. (22)), and change their configuration every 6 hours (Fig. 3). A wave progressively covers the ellipse and permanently ‘turns on’ the active cells. Therefore, the intra-synchronization proper to each cell $c(i, j)$ is out of phase with respect to the intra-synchronization of the cell $c(i + 1, j)$ and the cell $c(i - 1, j)$ on the same transversal coordinate j , as described in Sect. Traveling Wave with Random Unit Step Signal (or Tsunami-Like Migration). Furthermore, the active deformations (protrusion and contraction) are regulated by a gradient as in the first mode of migration (Sect. Strain Gradient Signal (or Chemoattractant Migration)). Accordingly, $e_{a,4}(\mathbf{p}, t)$ reads

$$e_{a,4}(\mathbf{p}, t) = e_{a0} \frac{(\mathbf{p} - \mathbf{p}_{\text{stern}}, \mathbf{p}_{\text{bow}} - \mathbf{p}_{\text{stern}})}{L} \sin\left(2\pi \frac{t - \frac{T}{2}(i_{\max} - i)}{T}\right) h_{a,4}(\mathbf{p}) \quad (7)$$

Random Signal In this mode of collective migration, all the cells inside the population are active ($h_{a,5}(\mathbf{p}) = h_n(\mathbf{p})$, Eq. (9) and $h_{q,5}(\mathbf{p}) = 0$). Nevertheless, contrarily to the first mode of migration (Sect. Strain Gradient Signal (or Chemoattractant Migration)), the cells migrate out of phase since each one of them has its own migration period T_{ij} , which ranges between 40 s and 180 s (Fig. 4b), and amplitude of the active strain e_{a0ij} , which may be comprised between 0.1 and 0.6 (Fig. 4a). Thus, $e_{a,5}(\mathbf{p}, t)$ is expressed as

$$e_{a,5}(\mathbf{p}, t) = e_{a0ij} \sin\left(2\pi \frac{t}{T_{ij}}\right) h_{a,5}(\mathbf{p}) \quad (8)$$

Fig. 4 Random values of the cyclic component $e_{a0,ij}$ of the active strain e_{a0} (a) and of the migration period T_{ij} (b) for the random migration



3 Results

The simulations were run using the finite element software COMSOL Multiphysics[®] 3.5a and reproduced an interval time of 1 day. The cell population has an initial geometry with semi-axes L and l equal to 90 μm and 30 μm , respectively (Fig. 1a). The cell network represented by $h_n(\mathbf{p})$ includes 18 cell rows ($N_c = i_{\max} = 18$, Appendix A.1) and each cell $c(i, j)$ has a radius $r_c = 5 \mu\text{m}$ (Allena 2013; Allena and Aubry 2012). The distances l_f and l_r have been fixed to 2 μm (Allena 2013; Allena and Aubry 2012), which leads to an area of 25 μm^2 covered by the adhesion surfaces $\partial\Omega_{sf_i,j}$ and $\partial\Omega_{sr_i,j}$ (Fig. 1d) and the friction force viscosities μ_f and μ_r have been set to 10^8 Pa s/m (Allena 2013; Allena and Aubry 2012). For the active cells (Sect. 2.2), the Young moduli of the solid elastic ($E_{a,se}$) and the fluid elastic ($E_{a,fe}$) phases have been chosen equal to 10^4 Pa (Allena 2013; Allena and Aubry 2012; Laurent et al. 2005) and 100 Pa (Allena 2013; Allena and Aubry 2012), respectively. The Poisson ratios $\nu_{a,se}$ and $\nu_{a,fe}$ have been set to 0.3 and 0.4, while the viscosity $\mu_{a,fv}$ of the fluid viscous phase has been set to 3×10^5 Pa s (Bausch et al. 1999; Drury and Dembo 2001). For the quiescent cells (Sect. 2.2), the Young moduli $E_{q,se}$ and $E_{q,fe}$ of the solid elastic and fluid elastic phases are equal to 400 Pa (Soofi et al. 2009) and 100 Pa (Allena 2013; Allena and Aubry 2012), respectively. The Poisson ratios $\nu_{q,se}$ and $\nu_{q,fe}$ are equal to 0.3 and 0.4, respectively, while the viscosity $\mu_{q,fv}$ of the fluid viscous phase has been set to 3×10^5 Pa s (Bausch et al. 1999; Drury and Dembo 2001). It has to be remembered that for the worm-like (Sect. Traveling Wave with Pulse Signal (or Worm-Like Migration)), the tsunami-like (Sect. Traveling Wave with Random Unit Step Signal (or Tsunami-Like Migration)) and the chemoattractant tsunami-like (Sect. Traveling Wave with Gradient Unit Step Signal (or Chemoattractant Tsunami-Like Migration)) modes of migration, the cells may switch from an active to a quiescent state or vice versa. Therefore, in these cases the Young modulus of the cells is described as a function of their state with respect to time.

Furthermore, the Young modulus E_{ECM} and the viscosity μ_{ECM} of the ECM have been fixed to 10 Pa and 3×10^5 Pa s (Bausch et al. 1999; Drury and Dembo 2001),

respectively, and the density of the cells is equal to 1000 kg/m^3 (Fukui et al. 2000). Finally, the intensity of the cyclic active strain e_{a0} and the duration of a migration cycle T have been set to 0.5 (Allena 2013; Allena and Aubry 2012) and 60 s (Allena 2013; Allena and Aubry 2012; Dong et al. 2002) respectively (except for the fifth mode of migration as described in Sect. Random Signal). e_{a0} is the same during both the protrusion and the contraction phase, although in single cell migration the contraction strain is usually smaller than the protrusion deformation (Giannone et al. 2007). The main geometrical, mechanical, and material parameters of the model are listed in Table 1.

3.1 Efficiency

As pointed out in Allena and Aubry (2012), the intra-synchronization (i.e. the synchronization between active strains and the adhesion forces) is a key factor in single cell migration. Nevertheless, it is not a sufficient condition in collective cell migration during which inter-synchronization (i.e. synchronization between the cells) is even more important. In fact, a tight synergy between the active deformations (protrusion and contraction) and the adhesion forces in each cell does not guarantee an efficient movement of the population (i.e. the cells may move in wrong directions and out of phase with respect to their neighbours). The cells need to communicate and adapt themselves in order to coordinate their movement and properly move forward together. In order to evaluate the interdependence between the intra- and the inter-synchronization, we have tested five different types of collective migration, which may reproduce realistic or unrealistic behaviors. In this section, we will analyse the efficiency (i.e. covered distance over 1 day) and discuss the reliability of each mode of migration.

In the first type of collective migration, the cell active strains are regulated by a gradient (Eq. (4)), so that the cells at the bow of the ellipse undergo larger deformations than the cells at the stern of the ellipse. Since all the cells are active and have the same intra-synchronization, they all protrude and contract simultaneously, but such a configuration induces a wrong movement of the population (Movie 1) (ESM). During protrusion, the leading cells freely and correctly deform, while the follower cells show two different behaviors. In the central region of the cohort, they are completely inhibited since their elongating leading edge hits the adhering rear edge of the cells in front of them. In the back of the cohort instead, they incorrectly deform because, due to the constriction imposed by the rear edge of the frontal neighbours, the deformation interferes with the back of the cell, which is free and, therefore, the cell elongates in the opposite direction. During contraction, the follower cells correctly move forward. However, the leading cells unsuccessfully pull their back, which is linked through the cell-cell junctions to the adhering frontal edge of the cells behind them. Thus, a contraction of the frontal edge of these cells occurs. Such a microscopic behavior leads to a global movement of the cell population very similar to the one of an accordion, which is overall poorly efficient. The cell population in fact only covers a distance of about $520 \text{ }\mu\text{m}$ after 1 day (Fig. 5, blue ellipse), with a steady state speed of about $0.006 \text{ }\mu\text{m/s}$.

The second type of collective migration reproduces the locomotion mode of worms in which alternate muscles elongate and contract. To describe such behavior,

Table 1 Geometrical, mechanical and material parameters of the model

Parameter	Description	Value	Unit	Reference
L	Major axis of the ellipse	90	μm	
l	Minor axis of the ellipse	30	μm	
N_c	Number of cells along the axis L of the ellipse	18		
$n_{c,\max}$	Maximal number of cells along the axis l of the ellipse	6		
r_c	Cell radius	5	μm	(Allena 2013; Allena and Aubry 2012)
l_f	Distance of the boundary of the frontal adhesion surface from the cell centre	2	μm	(Allena 2013; Allena and Aubry 2012)
l_r	Distance of the boundary of the rear adhesion surface from the cell centre	2	μm	(Allena 2013; Allena and Aubry 2012)
$\partial\Omega_{sf_{i,j}}$	Area of frontal adhesion region	25	μm^2	
$\partial\Omega_{sr_{i,j}}$	Area of rear adhesion region	25	μm^2	
μ_f	Friction force viscosity of the frontal adhesion surface $\partial\Omega_{sf_{i,j}}$	10^8	Pa s/m	(Allena 2013; Allena and Aubry 2012)
μ_r	Friction force viscosity of the rear adhesion surface $\partial\Omega_{sr_{i,j}}$	10^8	Pa s/m	(Allena 2013; Allena and Aubry 2012)
ρ	Cells density	1000	kg/m^3	(Fukui et al. 2000)
$E_{a,se}$	Young modulus of the solid elastic phase of the active cells	10^4	Pa	(Allena 2013; Allena and Aubry 2012; Ilina and Friedl 2009)
$\nu_{a,se}$	Poisson ratio of the solid elastic phase of the active cells	0.3		
$E_{a,fe}$	Young modulus of the fluid elastic phase of the active cells	100	Pa	(Allena 2013; Allena and Aubry 2012)
$\nu_{a,fe}$	Poisson ratio of the fluid elastic phase of the active cells	0.4		
$\mu_{a,fv}$	Viscosity of the fluid viscous phase of the active cells	3×10^5	Pa s	(Bausch et al. 1999; Drury and Dembo 2001)
$E_{q,se}$	Young modulus of the solid elastic phase of the quiescent cells	400	Pa	(Sherratt and Murray 1991)
$\nu_{q,se}$	Poisson ratio of the solid elastic phase of the active cells	0.3		
$E_{q,fe}$	Young modulus of the fluid elastic phase of the active cells	100	Pa	(Allena 2013; Allena and Aubry 2012)
$\nu_{q,fe}$	Poisson ratio of the fluid elastic phase of the active cells	0.4		
$\mu_{q,fv}$	Viscosity of the fluid viscous phase of the active cells	3×10^5	Pa s	(Bausch et al. 1999; Drury and Dembo 2001)
E_{ECM}	Young modulus of the ECM	10	Pa	
μ_{ECM}	Viscosity of the ECM	3×10^5	Pa s	(Bausch et al. 1999; Drury and Dembo 2001)

Table 1 (Continued)

Parameter	Description	Value	Unit	Reference
e_{a0}	Intensity of the cyclic active strain (for modes of migration 1, 2, 3 and 4)	0.5		(Allena 2013; Allena and Aubry 2012)
T	Duration of a migration cycle	60	s	(Allena 2013; Allena and Aubry 2012; Dong et al. 2002)

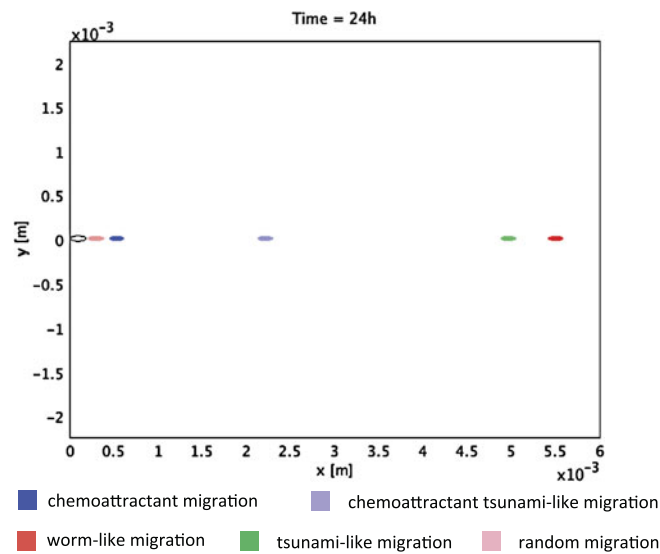


Fig. 5 The distance covered by the cell population after 24 h for the different modes of migration: chemoattractant migration (*blue*), worm-like migration (*red*), tsunami-like migration (*green*), chemoattractant tsunami-like migration (*purple*), random migration (*pink*) (Color figure online)

a traveling wave has been used to temporarily activate one by one the cell rows inside the ellipse. Each row remains active for one migration cycle T and it is promptly deactivated as soon as the wave has passed by. The cells inside the active row have the same intra-synchronization, thus they protrude and contract simultaneously (Movie 2) (ESM). Their movement correctly takes place since the cells in front and behind them during protrusion and contraction respectively, are momentarily quiescent and, therefore, easily deformable (see Sect. Traveling Wave with Pulse Signal (or Worm-Like Migration)). Nevertheless, the leading and the following cells appear to be more efficient than the cells in the central region of the ellipse. In this case, the cell population covers a total distance of $5430 \mu\text{m}$ during 1 day (Fig. 5, red ellipse), with a steady state speed of $0.06 \mu\text{m/s}$.

The third mode of collective migration is based on a complex inter-synchronization according to which a perfect coordination between the cell $c(i, j)$ and its frontal ($c(i + 1, j)$) and rear ($c(i - 1, j)$) neighbor cells is required. As experimentally observed (Serra-Picamal et al. 2012), a traveling wave progressively covers the cells

population and permanently ‘turns on’ one by one the cell rows in the ellipse. However, not all the cells in each row may be activated, thus a random distribution of the active cells is obtained. In our model, such an aspect has been taken into account by introducing a specific parameter, which allows defining the active ($\tau_{i,j} = 1$) or the quiescent ($\tau_{i,j} = 0$) cells in each row. The random configuration changes every 6 hours (Fig. 3). In Movie 3 (ESM), it is possible to observe the successive phases of the collective migration over a period of 1 hour. The inter-synchronization allows the cell $c(i, j)$ to move out of phase with respect to its frontal $c(i + 1, j)$ and rear $c(i - 1, j)$ neighbours. Thus, the active cells in the leading row ($r(18)$, Fig. 1c) are the first to be activated and to elongate. As soon as their contraction phase starts ($t = 30$ s), the active cells in the follower row ($r(17)$, Fig. 1c) elongate and so on. In this way, the accordion movement observed in the first mode of migration does not occur anymore, but all the cells belonging to the active cells network (Sect. Traveling Wave with Random Unit Step Signal (or Tsunami-Like Migration)) actively participate to the movement with their proper intra-synchronization. After 1 day, the cohort has covered a distance of 4340 μm (Fig. 5, green ellipse) at a steady state speed of 0.05 $\mu\text{m/s}$.

As mentioned above, the cyclic component e_{a0} of the active deformation is the same during both the protrusion and the contraction phase. Nevertheless, a smaller contraction with respect to the protrusion could have been considered, as it is the case in single cell migration (Giannone et al. 2007). In this case, the cell $c(i, j)$ would elongate with the same intensity of the contraction of the cell $c(i + 1, j)$, the cell $c(i - 1, j)$ would elongate with the same intensity of the contraction of the cell $c(i, j)$ and so on. Thus, the cells would adapt themselves and we would observe a ‘natural’ gradient of the active deformation.

The fourth type of migration combines the modes of movement described for the first and the third types of migration. Thus, a coupling between the chemoattractant gradient (Sect. Strain Gradient Signal (or Chemoattractant Migration)) and the traveling wave (Sect. Traveling Wave with Random Unit Step Signal (or Tsunami-Like Migration)) is implemented (Movie 4) (ESM). In this case, the population covers a distance of 2850 μm in 1 day (Fig. 5, purple ellipse; steady state speed of 0.03 $\mu\text{m/s}$).

Considering the covered distance, the modes of migration explored so far are very efficient, with the worm-like and the chemoattractant migration being the most and the least powerful respectively (Fig. 5). Nevertheless, one may wonder if such types of collective migration can be in some way related to the experimental observations. In fact, despite their efficiency, each one of the modes of migration presents ‘observed’ and ‘not observed’ features:

- in the chemoattractant migration all the cells are active (observed), but they migrate perfectly in phase (not observed);
- in the worm-like migration a wave successively activates and deactivates the rows of cells (not observed), but then only one row at the time is active (not observed) within which the cells show a behavior similar to the one of single cell migration (observed);
- in the tsunami-like migration, a wave spans the entire population and permanently activates the cells (observed) which then perfectly migrate out of phase (not observed);

- in the chemoattractant tsunami-like migration, a wave progressively activates the cells (observed) which then acquire a motility phenotype and start to migrate perfectly out of phase (not observed), but with different intensities as they felt a chemical gradient from the bow to the stern of the ellipse (observed).

Therefore, as a common feature, each mode of migration shows a perfect inter-synchronization within the population, which is regulated using specific analytical approaches. Although such a synchronization seems to be very simple to achieve from a theoretical point of view, it is much more complex to acquire in reality. In fact, cells within a population naturally tend to de-synchronize with respect to their neighbours, which leads to a random behavior of the cells inside the cohort. Given these remarks, a fifth mode of migration has been tested in which all the cells are active and the protrusion-contraction deformations are regulated by specific values of the intensity e_{a0ij} and the period $T_{a ij}$ that randomly vary within the cell cohort (Figs. 4a and b). In Movie 5 (ESM) it is possible to observe the successive phases of the collective migration over 1 h. Each cell migrates at its own pace, which results in a not necessarily coordinated movement with the neighbor cells. Thus, the overall efficiency of the population is compromised since the de-synchronization between the cells may inhibit their correct protrusion-contraction movement. Actually, the cell population only covers a distance of about 210 μm (Fig. 5, pink ellipse; steady state speed of 0.002 $\mu\text{m/s}$), which is then the smallest covered distance compared to the previous cases. Despite this apparent limitation, the random behavior represents a realistic feature of the model. Nevertheless, it is evident that, for the population to be efficient, randomness has to be coupled with a certain minimal level of inter-synchronization. This actually corresponds to what has been observed by Serrapicamal et al. (2012) according to which a mechanical wave spans the layer of cells that successively start to migrate. In practice, the cells adjust their movement according to the local stress state that is gradually developed by the migration of the nearby cells. From a theoretical point of view, this can be described by linking the active deformation e_a of each cell to the stress state of its neighbor cells. Thus, the first cells to migrate would be the ones at the leading and free edge of the ellipse and then the followers would naturally be activated because stimulated by the stresses generated around them. Therefore, a mechanotactic signal would be transmitted within the population. We are currently considering such an aspect in order to improve the present model.

3.2 Principal Stresses

Looking at principal stresses magnitudes and directions is a useful way to understand how the mechanical forces are transmitted inside and between the cells. In Table 2, we have reported the values of the average principal stresses during both protrusion and contraction for each mode of migration. Additionally, we have calculated them over the whole active cells network $\Omega_{a,k}$ and inside a leading ($c(18, 4)$ in Fig. 1c), a central ($c(10, 4)$ in Fig. 1c), and a rear ($c(1, 4)$ in Fig. 1c) cell. As expected, we observe a compression during the protrusion and a traction during the contraction. Although the stress regime may vary according to the mode of migration adopted by the cohort, few general remarks may be pointed out.

Table 2 Average principal stress calculated within the active cells network and inside a leading ($c(18, 4)$), a central ($c(10, 4)$), and a rear ($c(1, 4)$) cell during both protrusion and contraction for each mode of migration

Average principal stress	Active domain				Leading cell $c(18, 4)$		Central cell $c(10, 4)$		Follower cell $c(1, 4)$	
	Protrusion		Contraction		Protru- sion	Contraction	Protru- sion	Contraction	Protru- sion	Contraction
Mode 1	-1700 Pa		2000 Pa		-1100 Pa	3300 Pa	-1600 Pa	2000 Pa	-30 Pa	40 Pa
Mode 2	-230 Pa		-230 Pa		-200 Pa	200 Pa	-600 Pa	600 Pa	-200 Pa	200 Pa
Mode 3	Even rows	Odd rows	Even rows	Odd rows	-200 Pa	200 Pa	-500 Pa	500 Pa	-200 Pa	200 Pa
	-650 Pa		-700 Pa		650 Pa		700 Pa			
Mode 4	Even rows	Odd rows	Even rows	Odd rows	-180 Pa	190 Pa	-720 Pa	700 Pa	-16 Pa	16 Pa
	-380 Pa		-400 Pa		380 Pa		400 Pa			
Mode 5	-1200 Pa		1500 Pa		-1050 Pa	890 Pa	-3250 Pa	3210 Pa	-2900 Pa	3130 Pa

First, the first and the fifth modes of migration are the ones showing the highest concentration of stress within the active domain $\Omega_{a,k}$. Such values are too high compared to the experimental data (Serra-Picamal et al. 2012; Tambe et al. 2011; Trepats et al. 2009), which confirms the inefficiency of these migration modes (Sect. 3.1). However, values are consistent with the experimental observations (Serra-Picamal et al. 2012; Tambe et al. 2011; Trepats et al. 2009) for the second, the third and the fourth modes of migration, which are also the most efficient modes of collective movement (Sect. 3.1).

Second, in the first, second, and fifth modes of migration the principal stresses are mostly orientated along the direction of migration since all the cells inside the cohort or inside the temporarily active row migrate in phase. This is not the case in the third and fourth modes of migration, for which the active cells are randomly distributed within the cohort, and thus the mechanical stresses are transmitted within the population following such configuration (Fig. 3). Nevertheless, in the third mode of migration, few stress concentrations may be noticed at the frontal or at the rear adhesion surfaces in contact with neighbor cells.

Third, the leading ($c(18, 4)$) and the rear ($c(1, 4)$) cells show a behavior very similar to the one observed in 2D single cell migration during which the cell is only constrained by the contact with the underneath substrate, and it is free at the front and at the back. Actually, the leading cells can freely elongate during the protrusion phase since they do not have any frontal neighbor cell, while the follower cells can freely contract because they do not have to pull any further cells behind them.

As a consequence of the previous remarks, the cells inside the population ($c(10, 4)$) generate larger stresses during both protrusion and contraction compared to the leading and the follower cells. This is mostly due to the fact that, with respect to the ‘bow’ and the ‘stern’ cells, the central cells have frontal and rear neighbours, which prevent them to freely deform.

Finally and most important, whether all the cells or only few of them actively participate to the migration process, the most efficient are the ones located at the

bow of the ellipse. In fact, if we consider each cell as a propulsion-traction system, the propulsion phase is the most important since it determines the direction and the intensity of the migration. Thus, the more a cell is free to elongate during the protrusion phase, the more it will move forward during the contraction phase. This is actually the case of the leading cells, which do not have any frontal neighbours and can therefore protrude as much as they need without any constraint. Therefore, the leading cells may play a fundamental role in collective migration by providing positive feedbacks both in space (direction and intensity of the deformation) and in time (inter-synchronization) (Sect. 1.1) (Sumpter 2006).

4 Conclusions

We have proposed here a 2D mechanical model to simulate the collective movement of a cell population, which is represented as a continuum with discrete embedded cells with potential motility behavior (Sect. 2.1). The active strains (i.e. protrusion and contraction) undergone by the single cells during the migration are described through the decomposition of the deformation gradient (Sect. 2.2). Such active deformations are tightly coupled with the adhesion forces necessary to the single cells to move forward (intra-synchronization) (Sect. 2.3.1). Furthermore, the cells must communicate and coordinate their movement in order to be as efficient as possible. Therefore, inter-synchronization between the cells is required (Sect. 2.3.2). The main objective of the paper has been to evaluate the efficiency of the cell population in terms of covered distance and how the stress distribution inside the cohort and the single cells may in turn provide insights regarding such efficiency. In order to achieve this goal, we have explored five different modes of collective migration: (i) chemoattractant migration (Sect. Strain Gradient Signal (or Chemoattractant Migration)), (ii) worm-like migration (Sect. Traveling Wave with Pulse Signal (or Worm-Like Migration)), (iii) tsunami-like migration (Sect. Traveling Wave with Random Unit Step Signal (or Tsunami-Like Migration)), (iv) chemoattractant tsunami-like migration (Sect. Traveling Wave with Gradient Unit Step Signal (or Chemoattractant Tsunami-Like Migration)) and (v) random migration (Sect. Random Signal). Such an analysis has allowed us to investigate the mechanical interplay between the intra- and the inter-synchronization within the cell population (Sect. 3.1) to detect those constraints and forces leading (or not) to an efficient migration.

We have found that the most efficient modes of migration (worm-like migration, tsunami-like migration and chemoattractant tsunami-like migration) are also the ones showing the lowest stresses within the population (Sect. 3.2). Therefore, inter-synchronization and randomness are not stand-alone factors of collective cell migration, but they must be coupled. In fact, as also pointed out by Serra-Picamal et al. (2012), cells need to adjust their movement according to the local stress state, which is developed by the movement of their neighbor cells. This results in a mechanotactic signal, which progressively spans the population and stimulates the follower cells. Nevertheless, beside such a mechanotactic signal and in order to have a complete framework of the biological process, one has also to consider the complex molecular signal pathways that may control the acquirement of a motile phenotype of (at least)

the leading cells. Although here we have only focused on the mechanical aspects of the problem, we are working to improve the present model to take into account these two fundamental aspects.

Appendix

A.1 Geometry of the cell population

The cells network Ω_n is described through a characteristic function $h_n(\mathbf{p})$, which reads

$$h_n(\mathbf{p}) = \begin{cases} 1 & \text{if } \|\mathbf{p} - 2 \cdot r_c \cdot \text{round}(\mathbf{p}_x)\mathbf{i}_x - 2 \cdot r_c \cdot \text{round}(\mathbf{p}_y)\mathbf{i}_y\| < r_c^2 \\ 0 & \text{otherwise} \end{cases} \quad (9)$$

with round being the classical integer function and $\mathbf{p}(\mathbf{p}_x, \mathbf{p}_y)$ the initial position of any particle of the system.

Consequently, the ECM domain Ω_{ECM} is defined by a characteristic function as follows:

$$h_{\text{ECM}}(\mathbf{p}) = 1 - h_n(\mathbf{p}) \quad (10)$$

Each cell inside the population is indicated as $c(i, j)$ where the indices i and j vary as follows:

$$\begin{cases} 1 \leq i \leq N_c = i_{\max} \\ 1 \leq j \leq n_c(i) = n_{c,\max} \sqrt{1 - \left(\frac{2i-1}{N_c}\right)^2} \end{cases} \quad (11)$$

with $N_c = \frac{L}{r_c}$ and $n_{c,\max} = \frac{l}{r_c}$ being the number of cells along the two axes of the ellipse (Fig. 1c).

The domain $\Omega_{c_{i,j}}$ of each cell $c(i, j)$ is defined through a characteristic function as follows:

$$h_{c_{i,j}}(\mathbf{p}) = \begin{cases} 1 & \text{if } \|\mathbf{p} - \mathbf{c}_{i,j}\| < r_c^2 \\ 0 & \text{otherwise} \end{cases} \quad (12)$$

Each cell is equipped with a frontal $\partial\Omega_{sf_{i,j}}$ and a rear $\partial\Omega_{sr_{i,j}}$ adhesion region (Fig. 1d) described by two characteristic functions as

$$\begin{aligned} h_{sf_{i,j}}(\mathbf{p}) &= \begin{cases} 1 & \text{if } (\mathbf{p} - \mathbf{c}_{i,j}, \mathbf{i}_x) > l_f \\ 0 & \text{otherwise} \end{cases} \\ h_{sr_{i,j}}(\mathbf{p}) &= \begin{cases} 1 & \text{if } (\mathbf{p} - \mathbf{c}_{i,j}, \mathbf{i}_x) < l_r \\ 0 & \text{otherwise} \end{cases} \end{aligned} \quad (13)$$

where (\mathbf{a}, \mathbf{b}) defines the scalar product between two vectors, l_f and l_r are the distances of $\mathbf{c}_{i,j}$ from the frontal and rear adhesion surfaces, respectively.

The ellipse is divided into cell rows $r(i)$ (Fig. 1b), which are numbered, similarly to the single cells, from the stern (left) to the bow (right) of the ellipse ($1 \leq i \leq N_c = i_{\max}$) (Fig. 1c) and are defined through a characteristic function as

$$h_{r_i}(\mathbf{p}) = h_n(\mathbf{p}) \begin{cases} 1 & \text{if } (\mathbf{p}_x - \mathbf{c}_{i,j_x}) < r_c \\ 0 & \text{otherwise} \end{cases} \quad (14)$$

A.2 Constitutive Model of the Cells

As mentioned in Sect. 2.2, the behavior of the active and quiescent cells is described through a generalized viscoelastic 2D Maxwell model (Allena 2013; Allena and Aubry 2012). Since the cells within the cohort may undergo large rotations and deformations during their locomotion, a fully non-linear tensorial approach is required.

For the active cells, the Cauchy stress σ_a is assumed to be the sum of the solid ($\sigma_{a,s}$) and the fluid ($\sigma_{a,f}$) Cauchy stresses, while the deformation gradient \mathbf{F}_a is equal to the solid ($\mathbf{F}_{a,s}$) and the fluid ($\mathbf{F}_{a,f}$) deformation gradients.

The decomposition of the deformation gradient (Allena et al. 2010; Lubarda 2004) is used to describe the solid deformation tensor $\mathbf{F}_{a,s}$ which is then equal to

$$\mathbf{F}_{a,s} = \mathbf{F}_{a,se} \mathbf{F}_{a,sa} \quad (15)$$

where $\mathbf{F}_{a,se}$ is the elastic strain tensor responsible for the stress generation and $\mathbf{F}_{a,sa}$ is the active strain tensor responsible for the pulsating movement (protrusion-contraction) of each cell. Similarly, the fluid deformation tensor $\mathbf{F}_{a,f}$ is the multiplicative decomposition of the fluid-elastic ($\mathbf{F}_{a,fe}$) and the fluid-viscoelastic ($\mathbf{F}_{a,fv}$) gradients.

Both the solid $\sigma_{a,se}$ and the fluid-elastic $\sigma_{a,fe}$ Cauchy's stresses are given by isotropic hyperelastic models $\bar{\sigma}_{a,se}$ and $\bar{\sigma}_{a,fe}$, respectively, as

$$\begin{aligned} \sigma_{a,se} &= \bar{\sigma}_{a,se}(\mathbf{e}_{a,se}) \\ \sigma_{a,fe} &= \bar{\sigma}_{a,fe}(\mathbf{e}_{a,fe}) \end{aligned} \quad (16)$$

with $\mathbf{e}_{a,se}$ and $\mathbf{e}_{a,fe}$ the Euler–Almansi strain tensors for the solid-elastic and the fluid-elastic phases respectively. Additionally, $\sigma_{a,fe}$ has to be expressed in the actual configuration according to the multiplicative decomposition described above. Finally, the strain rate $\dot{\mathbf{e}}_{a,fv}$ is related to the deviator part of the fluid-viscous stress $\sigma_{a,fv}^D$ as follows:

$$\dot{\mathbf{e}}_{a,fv} = \frac{\sigma_{a,fv}^D}{\mu_{a,fv}} \quad (17)$$

where $\mu_{a,fv}$ is the viscosity.

For the quiescent cells, the same equations can be applied but one has to notice that the solid deformation gradient can now be written as

$$\mathbf{F}_{q,s} = \mathbf{F}_{q,se} \mathbf{F}_{q,sa} = \mathbf{F}_{q,se} \mathbf{I} \quad (18)$$

since no active strains take place in these cells (Sect. 2.2).

A.3 Numerical Implementation of the Constitutive Law

In this section, we provide the general framework of the numerical approach. For further details, we refer the reader to similar works and applications proposed by Glowinski and Pan (1992) and Vennat et al. (2010).

The cell population is modeled as a continuum (the ellipse). Each one of the three internal regions (active cells $\Omega_{a,k}$, quiescent cells $\Omega_{q,k}$, and ECM Ω_{ECM}) is represented by a level-set function ($h_{a,k}$, $h_{q,k}$, and h_{ECM} , respectively). The constitutive behavior of the active and the quiescent cells is described through a 2D generalized Maxwell model, while the ECM is described by a viscoelastic material. In the finite element formulation, the Cauchy stress σ and the viscous strain rate $\dot{\epsilon}_{fv}$ are computed at each point \mathbf{p} of the continuum taking into account the contributions of the three regions as follows:

$$\begin{aligned}\sigma(\mathbf{p}) &= h_{ECM}(\mathbf{p})\sigma_{ECM}(\mathbf{p}) + \sum h_{a,k}(\mathbf{p})\sigma_{a,k}(\mathbf{p}) + \sum h_{q,k}(\mathbf{p})\sigma_{q,k}(\mathbf{p}) \\ \dot{\epsilon}_{fv}(\mathbf{p}) &= h_{ECM}(\mathbf{p})\dot{\epsilon}_{ECM_{fv}}(\mathbf{p}) + \sum h_{a,k}(\mathbf{p})\dot{\epsilon}_{a,k_{fv}}(\mathbf{p}) + \sum h_{q,k}(\mathbf{p})\dot{\epsilon}_{q,k_{fv}}(\mathbf{p})\end{aligned}\quad (19)$$

where $\dot{\epsilon}_{ECM_{fv}}(\mathbf{p})$, $\dot{\epsilon}_{a,k_{fv}}(\mathbf{p})$, and $\dot{\epsilon}_{q,k_{fv}}(\mathbf{p})$ are the viscous strain rates for the correspondent domains. Thus, the finite element mesh is not adapted to each sub-region of the continuum, but everything is handled via the level set functions, which allow localizing the mechanical behavior.

Then such a constitutive behavior is implemented in the dynamics equation (Eq. (1)), which involves the aforementioned stress, the displacement acceleration \mathbf{a} and the adhesion forces \mathbf{f}_{adh} . This equation is first transformed into the weak form of the problem (i.e. principle of the virtual works) and it is then discretized by finite elements. Accordingly, cells/ECM or cells/cells mutual forces are automatically equilibrated in a weak sense although in general, the cell boundaries intersect the finite elements edges. In fact, the level set functions describing the sub-regions of the system are defined independently from the finite element mesh.

A.4 Traveling Wave with Pulse Signal (or Worm-Like Migration)

In this mode of migration, a traveling wave spans the cell population and successively activate and de-activate the cell rows $r(i)$. Thus, only one row is active at the time and the spatial coordinate c_{i,j_x} defining its position changes every migration cycle T (Fig. 2), so that the active cell network $h_{a,2}(\mathbf{p}, t)$ is defined as

$$h_{a,2}(\mathbf{p}, t) = h_n(\mathbf{p}) \cdot \begin{cases} 1 & \text{if } (|\mathbf{p}_x - c_{i,j_x}(t)| < r_c) \\ 0 & \text{otherwise} \end{cases}\quad (20)$$

where $c_{i,j_x}(t)$ reads

$$c_{i,j_i}(t) = (2L - r_c) - 2r_c \cdot \text{round}\left(\frac{t}{T} - 0.5\right) + 2L \cdot \text{round}\left(\frac{t}{T \cdot N_c} - 0.5\right)\quad (21)$$

In this case, also the quiescent domain $h_{q,2}$ varies in space and time as $h_{q,2}(\mathbf{p}, t) = h_n(\mathbf{p}) - h_{a,2}(\mathbf{p}, t)$.

A.5 Traveling Wave with Random Unit Step Signal (or Tsunami-Like Migration)

The characteristic function $h_{a,3}(\mathbf{p}, t)$ defining the active cells network for this mode of migration reads

$$h_{a,3}(\mathbf{p}, t) = \tau_{i,j} \cdot h_{r_i}(\mathbf{p}) \cdot h_{sw}(\mathbf{p}, t) \quad (22)$$

where $h_{sw}(\mathbf{p}, t)$ describes the progressive wave, which gradually covers the population with a velocity equal to $\frac{2t}{T}$ and is expressed as

$$h_{sw}(\mathbf{p}, t) = \begin{cases} 1 & \text{if } (2L - r_c) - \mathbf{p}_x - 2r_c \frac{2t}{T} < 0 \\ 0 & \text{otherwise} \end{cases} \quad (23)$$

Similarly to the previous case, the quiescent cells domain $h_{q,3}$ reads $h_{q,3}(\mathbf{p}, t) = h_n(\mathbf{p}) - h_{a,3}(\mathbf{p}, t)$.

References

- Allena, R. (2013). Cell migration with multiple pseudopodia: temporal and spatial sensing models. *Bull. Math. Biol.*, *75*, 288–316.
- Allena, R., & Aubry, D. (2012). “Run-and-tumble” or “look-and-run”? A mechanical model to explore the behavior of a migrating amoeboid cell. *J. Theor. Biol.*, *306*, 15–31.
- Allena, R., Mouronval, A.-S., & Aubry, D. (2010). Simulation of multiple morphogenetic movements in the *Drosophila* embryo by a single 3D finite element model. *J. Mech. Behav. Biomed. Mater.*, *3*, 313–323.
- Anand, R. J., Leaphart, C. L., Mollen, K. P., & Hackam, D. J. (2007). The role of the intestinal barrier in the pathogenesis of necrotizing enterocolitis. *Shock*, *27*, 124–133.
- Arciero, J. C., Mi, Q., Branca, M. F., Hackam, D. J., & Swigon, D. (2011). Continuum model of collective cell migration in wound healing and colony expansion. *Biophys. J.*, *100*, 535–543.
- Bausch, A. R., Möller, W., & Sackmann, E. (1999). Measurement of local viscoelasticity and forces in living cells by magnetic tweezers. *Biophys. J.*, *76*, 573–579.
- Borisy, G. G., & Svitkina, T. M. (2000). Acting machinery: pushing the envelope. *Curr. Opin. Cell Biol.*, *12*, 104–112.
- Carlier, M. F., & Pantaloni, D. (1997). Control of actin dynamics in cell motility. *J. Mol. Biol.*, *269*, 459–467.
- Carlsson, A. E., & Sept, D. (2008). Mathematical modeling of cell migration. *Methods Cell Biol.*, *84*, 911–937.
- Chen, X., & Friedman, A. (2000). A free boundary problem arising in a model of wound healing. *SIAM J. Math. Anal.*, *32*, 778.
- Condeelis, J. (1993). Life at the leading edge: the formation of cell protrusions. *Annu. Rev. Cell Biol.*, *9*, 411–444.
- Dong, C., Slattery, M. J., Rank, B. M., & You, J. (2002). In vitro characterization and micromechanics of tumor cell chemotactic protrusion, locomotion, and extravasation. *Ann. Biomed. Eng.*, *30*, 344–355.
- Drury, J. L., & Dembo, M. (2001). Aspiration of human neutrophils: effects of shear thinning and cortical dissipation. *Biophys. J.*, *81*, 3166–3177.
- Farooqui, R., & Fenteany, G. (2005). Multiple rows of cells behind an epithelial wound edge extend cryptic lamellipodia to collectively drive cell-sheet movement. *J. Cell Sci.*, *118*, 51–63.
- Fenteany, G., Janmey, P. A., & Stossel, T. P. (2000). Signaling pathways and cell mechanics involved in wound closure by epithelial cell sheets. *Curr. Biol.*, *10*, 831–838.
- Flaherty, B., McGarry, J. P., & McHugh, P. E. (2007). Mathematical models of cell motility. *Cell Biochem. Biophys.*, *49*, 14–28.
- Friedl, P., & Gilmour, D. (2009). Collective cell migration in morphogenesis, regeneration and cancer. *Nat. Rev. Mol. Cell Biol.*, *10*, 445–457.

- Friedl, P., & Wolf, K. (2010). Plasticity of cell migration: a multiscale tuning model. *J. Cell Biol.*, *188*, 11–19.
- Fukui, Y., Uyeda, T. Q. P., Kitayama, C., & Inoué, S. (2000). How well can an amoeba climb? *Proc. Natl. Acad. Sci. USA*, *97*, 10020–10025.
- Gaffney, E. A., Maini, P. K., McCaig, C. D., Zhao, M., & Forrester, J. V. (1999). Modelling corneal epithelial wound closure in the presence of physiological electric fields via a moving boundary formalism. *IMA J. Math. Appl. Med. Biol.*, *16*, 369–393.
- Giannone, G., et al. (2007). Lamellipodial actin mechanically links myosin activity with adhesion-site formation. *Cell*, *128*, 561–575.
- Glowinski, R., & Pan, T.-W. (1992). Error estimates for fictitious domain/penalty/finite element methods. *Calcolo*, *29*, 125–141.
- Gracheva, M. E., & Othmer, H. G. (2004). A continuum model of motility in ameboid cells. *Bull. Math. Biol.*, *66*, 167–193.
- Graner, F., & Glazier, J. A. (1992). Simulation of biological cell sorting using a two-dimensional extended Potts model. *Phys. Rev. Lett.*, *69*, 2013–2016.
- Holzappel, G. A. (2000). *Nonlinear solid mechanics: a continuum approach for engineering* (1st ed.). New York: Wiley.
- Ilina, O., & Friedl, P. (2009). Mechanisms of collective cell migration at a glance. *J. Cell Sci.*, *122*, 3203–3208.
- Laurent, V. M., et al. (2005). Gradient of rigidity in the lamellipodia of migrating cells revealed by atomic force microscopy. *Biophys. J.*, *89*, 667–675.
- Lubarda, V. (2004). Constitutive theories based on the multiplicative decomposition of deformation gradient: thermoelasticity, elastoplasticity, and biomechanics. *Appl. Mech. Rev.*, *57*, 95–109.
- Maini, P. K., McElwain, D. L. S., & Leavesley, D. I. (2004). Traveling wave model to interpret a wound-healing cell migration assay for human peritoneal mesothelial cells. *Tissue Eng.*, *10*, 475–482.
- McLennan, R., et al. (2012). Multiscale mechanisms of cell migration during development: theory and experiment. *Development*. Available at: <http://dev.biologists.org/content/early/2012/07/04/dev.081471> [Accessed April 27, 2013].
- Meili, R., Alonso-Latorre, B., del Alamo, J. C., Firtel, R. A., & Lasheras, J. C. (2010). Myosin II is essential for the spatiotemporal organization of traction forces during cell motility. *Mol. Biol. Cell*, *21*, 405–417.
- Mogilner, A., & Rubinstein, B. (2005). The physics of filopodial protrusion. *Biophys. J.*, *89*, 782–795.
- Murray, J. D. (2003). *Mathematical biology II: spatial models and biomedical applications*. Berlin: Springer.
- Phillipson, M., et al. (2006). Intraluminal crawling of neutrophils to emigration sites: a molecularly distinct process from adhesion in the recruitment cascade. *J. Exp. Med.*, *203*, 2569–2575.
- Rubinstein, B., Jacobson, K., & Mogilner, A. (2005). Multiscale two-dimensional modeling of a motile simple-shaped cell. *Multiscale Model. Simul.*, *3*, 413–439.
- Sakamoto, Y., Prudhomme, S., & Zaman, M. H. (2011). Viscoelastic gel-strip model for the simulation of migrating cells. *Ann. Biomed. Eng.*, *39*, 2735–2749.
- Serra-Picamal, X., et al. (2012). Mechanical waves during tissue expansion. *Nat. Phys.*, *8*, 628–634.
- Sheetz, M. P., Felsenfeld, D., Galbraith, C. G., & Choquet, D. (1999). Cell migration as a five-step cycle. *Biochem. Soc. Symp.*, *65*, 233–243.
- Sherratt, J. A., & Murray, J. D. (1990). Models of epidermal wound healing. *Proc. - Royal Soc., Biol. Sci.*, *241*, 29–36.
- Sherratt, J. A., & Murray, J. D. (1991). Mathematical analysis of a basic model for epidermal wound healing. *J. Math. Biol.*, *29*, 389–404.
- Soofi, S. S., Last, J. A., Liliensiek, S. J., Nealey, P. F., & Murphy, C. J. (2009). The elastic modulus of Matrigel™ as determined by atomic force microscopy. *J. Struct. Biol.*, *167*, 216–219.
- Sumpter, D. J. (2006). The principles of collective animal behaviour. *Philos. Trans. R. Soc. Lond. B, Biol. Sci.*, *361*, 5–22.
- Szabo, B., et al. (2006). Phase transition in the collective migration of tissue cells: experiment and model. [arXiv:q-bio/0611045](http://arxiv.org/abs/q-bio/0611045). Available at: <http://arxiv.org/abs/q-bio/0611045>. Accessed April 27, 2013.
- Taber, L. A. (2004). *Nonlinear theory of elasticity: applications in biomechanics*. Singapore: World Scientific.
- Taber, L. A., Shi, Y., Yang, L., & Bayly, P. V. (2011). A poroelastic model for cell crawling including mechanical coupling between cytoskeletal contraction and actin polymerization. *J. Mech. Mater. Struct.*, *6*, 569–589.

- Tambe, D. T., et al. (2011). Collective cell guidance by cooperative intercellular forces. *Nat. Mater.*, *10*, 469–475.
- Theriot, J. A., & Mitchison, T. J. (1991). Actin microfilament dynamics in locomoting cells. *Nature*, *352*, 126–131. Published online: 11 July 1991. doi:[101038/352126a0](https://doi.org/10.1038/352126a0).
- Trepat, X., et al. (2009). Physical forces during collective cell migration. *Nat. Phys.*, *5*, 426–430.
- Vedel, S., Tay, S., Johnston, D. M., Bruus, H., & Quake, S. R. (2013). Migration of cells in a social context. *Proc. Natl. Acad. Sci. USA*, *110*, 129–134.
- Vennat, E., Aubry, D., & Degrange, M. (2010). Collagen fiber network infiltration: permeability and capillary infiltration. *Transp. Porous Media*, *84*, 717–733.
- Vicsek, T., Czirók, A., Ben-Jacob, E., Cohen, I., & Shochet, O. (1995). Novel type of phase transition in a system of self-driven particles. *Phys. Rev. Lett.*, *75*, 1226–1229.
- Wagh, A. A., et al. (2008). Localized elasticity measured in epithelial cells migrating at a wound edge using atomic force microscopy. *Am. J. Physiol., Lung Cell. Mol. Physiol.*, *295*, L54–60.
- Weijer, C. J. (2009). Collective cell migration in development. *J. Cell Sci.*, *122*, 3215–3223.
- Xue, C., Friedman, A., & Sen, C. K. (2009). A mathematical model of ischemic cutaneous wounds. *Proc. Natl. Acad. Sci. USA*, *106*, 16782–16787.
- Yamao, M., Naoki, H., & Ishii, S. (2011). Multi-cellular logistics of collective cell migration. *PLoS ONE* *6*, e27950.

bow of the ellipse. In fact, if we consider each cell as a propulsion-traction system, the propulsion phase is the most important since it determines the direction and the intensity of the migration. Thus, the more a cell is free to elongate during the protrusion phase, the more it will move forward during the contraction phase. This is actually the case of the leading cells, which do not have any frontal neighbours and can therefore protrude as much as they need without any constraint. Therefore, the leading cells may play a fundamental role in collective migration by providing positive feedbacks both in space (direction and intensity of the deformation) and in time (inter-synchronization) (Sect. 1.1) (Sumpter 2006).

4 Conclusions

We have proposed here a 2D mechanical model to simulate the collective movement of a cell population, which is represented as a continuum with discrete embedded cells with potential motility behavior (Sect. 2.1). The active strains (i.e. protrusion and contraction) undergone by the single cells during the migration are described through the decomposition of the deformation gradient (Sect. 2.2). Such active deformations are tightly coupled with the adhesion forces necessary to the single cells to move forward (intra-synchronization) (Sect. 2.3.1). Furthermore, the cells must communicate and coordinate their movement in order to be as efficient as possible. Therefore, inter-synchronization between the cells is required (Sect. 2.3.2). The main objective of the paper has been to evaluate the efficiency of the cell population in terms of covered distance and how the stress distribution inside the cohort and the single cells may in turn provide insights regarding such efficiency. In order to achieve this goal, we have explored five different modes of collective migration: (i) chemoattractant migration (Sect. Strain Gradient Signal (or Chemoattractant Migration)), (ii) worm-like migration (Sect. Traveling Wave with Pulse Signal (or Worm-Like Migration)), (iii) tsunami-like migration (Sect. Traveling Wave with Random Unit Step Signal (or Tsunami-Like Migration)), (iv) chemoattractant tsunami-like migration (Sect. Traveling Wave with Gradient Unit Step Signal (or Chemoattractant Tsunami-Like Migration)) and (v) random migration (Sect. Random Signal). Such an analysis has allowed us to investigate the mechanical interplay between the intra- and the inter-synchronization within the cell population (Sect. 3.1) to detect those constraints and forces leading (or not) to an efficient migration.

We have found that the most efficient modes of migration (worm-like migration, tsunami-like migration and chemoattractant tsunami-like migration) are also the ones showing the lowest stresses within the population (Sect. 3.2). Therefore, inter-synchronization and randomness are not stand-alone factors of collective cell migration, but they must be coupled. In fact, as also pointed out by Serra-Picamal et al. (2012), cells need to adjust their movement according to the local stress state, which is developed by the movement of their neighbor cells. This results in a mechanotactic signal, which progressively spans the population and stimulates the follower cells. Nevertheless, beside such a mechanotactic signal and in order to have a complete framework of the biological process, one has also to consider the complex molecular signal pathways that may control the acquirement of a motile phenotype of (at least)

4.4 2D Finite element model of lateral line primordium migration

The model presented above has been extended to simulate the collective migration of lateral line primordium (LLP) in zebrafish. The previous assumptions are maintained, but here the complex signalling pathways that seem to control the population movement are considered too. In fact, reaction-diffusion equations are employed to describe the evolution in time of four main molecules whose activities are interconnected.

Thus, similarly to my previous work on *Drosophila* embryo (37), a coupling between the mechanical and molecular frameworks is introduced and occurs in two ways. First, the intensity of the active strains of protrusion and contraction depends on the concentration of a specific molecule. Second, the inter-synchronisation between the cells is regulated by the polarity of two chemokines. This leads to two main migration modes: uncoordinated and coordinated.

Besides the validation of the numerical results with respect to the experimental observations, the main objective is to evaluate the role of the leader cells and more specifically to quantify how their position inside the population may affect the whole migration.

This work is the result of a collaboration with Philip Maini from the Mathematical Institute at University of Oxford and was partially completed during my stays in Oxford in 2013.

Included Paper:

Allena R, Maini PK (2014) Reaction-diffusion finite element model of lateral line primordium migration to explore cell leadership. *Bull Math Biol* 76(12):3028–3050.

Reaction–Diffusion Finite Element Model of Lateral Line Primordium Migration to Explore Cell Leadership

R. Allena · P. K. Maini

Received: 16 April 2014 / Accepted: 5 November 2014
© Society for Mathematical Biology 2014

Abstract Collective cell migration plays a fundamental role in many biological phenomena such as immune response, embryogenesis and tumorigenesis. In the present work, we propose a reaction–diffusion finite element model of the lateral line primordium migration in zebrafish. The population is modelled as a continuum with embedded discrete motile cells, which are assumed to be viscoelastic and able to undergo large deformations. The Wnt/ β -catenin–FGF and *cxcr4b*–*cxcr7b* signalling pathways inside the cohort regulating the migration are described through coupled reaction–diffusion equations. The coupling between mechanics and the molecular scenario occurs in two ways. Firstly, the intensity of the protrusion–contraction movement of the cells depends on the *cxcr4b* concentration. Secondly, the intra-synchronization between the active deformations and the adhesion forces inside each cell is triggered by the *cxcr4b*–*cxcr7b* polarity. This influences the inter-synchronization between the cells and results in two main modes of migration: uncoordinated and coordinated. The main objectives of the work were (i) to validate our assumptions with respect to the experimental observations and (ii) to decipher the mechanical conditions leading to efficient migration of the primordium. To achieve the second goal, we will specifically focus on the role of the leader cells and their position inside the population.

Electronic supplementary material The online version of this article (doi:[10.1007/s11538-014-0043-7](https://doi.org/10.1007/s11538-014-0043-7)) contains supplementary material, which is available to authorized users.

R. Allena (✉)
Arts et Metiers ParisTech, LBM, 151 Bd de l'hôpital, 75013 Paris, France
e-mail: rachele.allena@ensam.eu

P. K. Maini
Wolfson Centre for Mathematical Biology, Mathematical Institute, University of Oxford,
Andrew Wiles Building, Woodstock Road, Oxford OX2 6GG, UK

Published online: 25 November 2014

 Springer

Keywords Collective migration · Continuum mechanics · Reaction–diffusion equation · Cell leadership

1 Introduction

Cell migration is essential for many processes in biology. In the case of single cell migration, for example, neural crest cells and immune system cells, one may observe synchronization between the protrusion–contraction movement of the cell body and the adhesion forces between the cell and the extracellular matrix (ECM), which is necessary for efficient movement (Allena and Aubry 2012). In the case of collective cell migration (e.g. gastrulation, epithelial wound healing), cells move as populations by adhering to each other via cell–cell junctions (Friedl and Gilmour 2009; Rørth 2007). While in vitro studies have led to a better understanding of the mechanisms regulating single cell migration, several fundamental aspects of collective cell migration in sheets are still ambiguous and poorly explored. Unresolved questions include, for instance, whether all the cells actively participate in the migration process or whether only the leader cells sense an external cue and, through other chemical or mechanical signals, instruct the followers (Aman and Piotrowski 2008; López-Schier 2010). Additionally, it is unclear how such a polarity between the front and the rear edges of the population is maintained and how the biomechanical signals are possibly transmitted from the leader cells to the follower cells to guarantee both the synchronization and the efficiency of the migration.

Deciphering the mechanisms controlling collective cell migration not only advances our knowledge of basic, fundamental biology, but may also be clinically relevant in cases where cell movement occurs in response to injury, or in disease, such as cancer (Friedl and Gilmour 2009; Iliina and Friedl 2009). For this purpose, the zebrafish lateral line primordium (LLP) constitutes a powerful biological model, and it has been experimentally investigated due to its simplicity and accessibility (Aman and Piotrowski 2009, 2011).

1.1 LLP Migration

The LLP is a population formed by over 100 epithelial cells that arises posterior to the ear and starts to migrate from the head to the tail of the animal along the embryonic trunk at about 20h post-egg fertilization (hpf). The LLP completes its migration at around 42 hpf, after having travelled approximately 3,000 μm (Gompel et al. 2001). During the migration, the trailing two-thirds of the cohort arrange themselves into rosettes (i.e. clusters of 20 cells) that are periodically deposited and eventually differentiate as the functional organs of the lateral line, called neuromasts (Aman and Piotrowski 2009; Anand et al. 2007).

The molecular regulation of LLP migration has been investigated in detail over recent years. Normal migration (i.e. along the embryo trunk) seems to be ensured by the polarized expression of both *cxc4b* and *cxc7b*, two chemokine receptors of the ligand *cxcl12a* (Dambly-Chaudière et al. 2007; Valentin et al. 2007), which is expressed by the cells along the migration path (David et al. 2002). In fact, *cxc4b* is mostly expressed

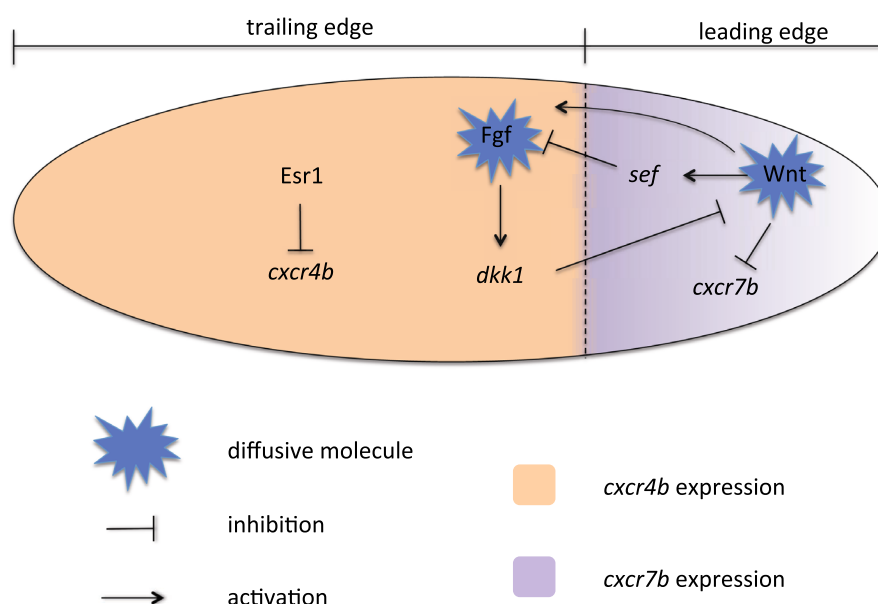


Fig. 1 Simplified LLP geometry and signalling network over the population. Wnt/ β -catenin and FGF (which are considered here as diffusive molecules) signalling is activated at the leading and trailing edge of the LLP, respectively. Such a polarity is controlled by the expression of the signalling inhibitors *dkk1* and *sef*, respectively. Simultaneously, Wnt/ β -catenin inhibits the expression of *cxcr7b* in the leading cells, while the oestrogen receptor Esr1 ensures the inhibition of *cxcr4b* expression in the trailing cells (see Sect. 1.1 for further details) (Color figure online)

in the leading cells of the LLP, while *cxcr7b* is mostly found in the trailing cells. Additionally, it has been observed that, in the absence of chemokine signalling, the cells within the LLP still migrate, but they lose their coordinated directionality (Haas and Gilmour 2006).

Aman and Piotrowski (2008) inferred that such a polarity may be controlled by a complex cell signalling network, which is based on feedback interactions between the Wnt/ β -catenin¹ and FGF² pathways that circumscribe the activation of the two chemokines to the opposite poles of the LLP (Aman and Piotrowski 2008).

This complex signalling network is represented in Fig. 1. Wnt/ β -catenin signalling is activated only in the first several rows of leader cells, where it triggers the expression of FGF3 and FGF10 ligands. Concurrently, the Wnt/ β -catenin pathway upregulates the FGF signalling inhibitor *sef* in the leading cells. Thus, FGF pathway activation is inhibited in the leading cells (even though these cells express FGF ligands), and FGF target genes are induced only in the trailing cells. In turn, FGF signalling in the back of the LLP activates the Wnt/ β -catenin inhibitor *dkk1*, which then results in the restriction of the Wnt/ β -catenin pathway to the leading cells. Finally, Wnt/ β -catenin

¹ Wnt/ β -catenin is the canonical Wnt pathway.

² FGF stands for fibroblast growth factor.

activation constrains the *cxcr7b* expression in the leading cells of the LLP, whereas *cxcr4b*, which is homogeneously distributed within the LLP at the onset of migration (Dambly-Chaudière et al. 2007; Gamba et al. 2010), is inhibited in the trailing cells via the oestrogen receptor *Esr1*, which is directly produced by Wnt (Gamba et al. 2010). This Wnt/ β -catenin–FGF feedback mechanism not only ensures the polarized expression of the two chemokine receptors, it also affects the morphogenesis of the LLP. The Wnt/ β -catenin activation restricts the FGF-dependent neurogenesis to the trailing edge resulting in an unpatterned (i.e. no rosette generation) leading edge. According to the analysis of FGF-depleted LLP which concurrently loses rosettes and stops migrating, it was deduced that rosette formation was required for migration (Lecaudey et al. 2008; Nechiporuk and Raible 2008). However, Aman and Piotrowski (Aman and Piotrowski 2008) later observed that in the absence of Wnt/ β -catenin and FGF signalling the LLP migrates normally even in the absence of rosette deposition and that the stalling in FGF-depleted LLP is due to ectopic Wnt/ β -catenin signalling and the consequent inhibition of *cxcr7b*. Therefore, the Wnt/ β -catenin and FGF pathways must be strongly coupled to guarantee forward migration as well as the periodic deposition of the rosettes. Nevertheless, it is still unclear whether all the cells actively participate in the migration process or only the leader cells sense the signal and, through other chemical or mechanical signals, instruct the followers (Aman and Piotrowski 2008). In fact, the normal migration of the LLP appears to follow a linear gradient of the chemokine stromal-derived factor 1 (SDF-1) which depends on the expression of *cxcr4b* in the leading cells (Haas and Gilmour 2006). Some experiments have shown that only a few *cxcr4b* expressed cells at the leading edge of the LLP are required to guide the movement of the population. Therefore, it has been proposed that *cxcr4b* expressing cells at the leading edge may be responsible for sensing the SDF-1 gradient, while *cxcr7b* mainly shapes the gradient across the LLP. Nonetheless, further measurements of the SDF-1 gradient throughout the population are needed to confirm such a hypothesis and the mechanism by which the cells follow the gradient is still unclear (Rørth 2007).

1.2 Objectives of the Present Work

Several models on collective cell migration can be found in the literature using either agent-based (Graner and Glazier 1992; Vedel et al. 2013; Yamao et al. 2011) or continuum approaches (Arciero et al. 2011; Sherratt and Murray 1990, 1991). Recently, Streichan et al. (2011) and Di Costanzo et al. (2014) have proposed two two-dimensional (2D) models specifically focusing on the collective migration of the LLP. The former is a discrete model in which a cell is represented as a polygon in a lattice and the tissue consists of a collection of cells. The population moves within a constant ligand distribution along a line, and as cells migrate, the frontal edge of the LLP becomes shifted to higher concentrations, while the rear edge is displaced from higher concentrations. Such an asymmetry allows the LLP to maintain a preferred direction of migration over long distances, while growing in size to deposit rosettes during migration. The latter proposes a hybrid description of the biological system, which considers both the cellular and the molecular scales. A discrete approach is used to represent the cellular

level, which includes the equation of motion and the equation of state leader–follower for each cell. A continuum approach is employed to define the molecular level and is based on the equations for the chemical signal involved. Under suitable conditions, the model is able to trigger the formation of rosettes, whose stability has been numerically evaluated and compared with experimental observations.

Contrary to these previous models (Di Costanzo et al. 2014; Streichan et al. 2011), here we propose a 2D finite element model of the LLP which only focuses on the LLP migration and does not take into account the growth of the population and rosette formation. Nonetheless, the model constitutes a significant extension of the previous one proposed by the first author in Allena et al. (2013) since it couples mechanics with molecular signalling in order to provide an exhaustive representation of the biological system.

The model is based on the following assumptions:

- as in Di Costanzo et al. (2014), a hybrid description is employed. In fact, the cell population is modelled as a continuum with embedded discrete motile cells which are assumed to be viscoelastic and able to undergo large deformations (Allena et al. 2013), while molecules are considered as continuous concentrations;
- in contrast to previous models (Di Costanzo et al. 2014; Streichan et al. 2011) where the molecular scenario inside the LLP only includes a limited number of molecules and interactions, here both the Wnt/ β -catenin–FGF and the *cxcr4b*–*cxcr7b* signalling pathways with the associated receptors and inhibitors are taken into account. Their spatiotemporal evolution is characterized by coupled reaction–diffusion equations;
- as in the previous works of the first author (Allena 2013; Allena and Aubry 2012; Allena et al. 2013), the decomposition of the deformation gradient is used to take into account both the active (i.e. protrusion and contraction) and the elastic (i.e. generated by the interactions with the ECM) deformations of the cells;
- mechanics is coupled in two ways with the molecular framework, which constitutes the main novelty of the present work. First, the intensity of the protrusion–contraction movement of the cells depends on the *cxcr4b* concentration, while the intra-synchronization (Allena et al. 2013) inside each cell (i.e. the synchronization between the protrusion–contraction movement of the cell and the adhesion forces exerted by the cell to move forward) is triggered by the *cxcr4b*–*cxcr7b* polarity. This influences the inter-synchronization (Allena et al. 2013) between the cells (i.e. the coordination between the cells) and results in two main modes of migration: uncoordinated and coordinated, which correspond, respectively, to the absence or the presence of *cxcr4b*–*cxcr7b* polarity.

For the present work, we have two main objectives: first, we want to validate, with respect to the experimental observations in the literature, our modelling assumptions on the molecular pathway interactions and its coupling with the mechanics of the LLP. In order to do so, we will consider four different mutants as described in Aman and Piotrowski (2008), and we will analyse the results in terms of migration mode, efficiency and stress distribution and compare them to the experimental observations. Second, we will try to unravel the required mechanical conditions for efficient migra-

tion of the LLP. To achieve such a goal, we will focus particularly on the role of the leader cells and their position within the population.

2 The Model

2.1 Geometry of the LLP

We model the LLP as a continuum with a free boundary approximated by an ellipse with semi-axes L and l at the onset of migration (i.e. 20 hpf) (Fig. 2a). The ellipse includes the cell network Ω_n , which is described via a characteristic function $h_n(\mathbf{p})$ (Appendix Sect. “LLP Geometry”, Eq. 8) and is constituted by 106 cells, which are in contact with each other and embedded in the extracellular matrix (ECM) Ω_{ECM} (Fig. 2b), which is also defined by a characteristic function $h_{ECM}(\mathbf{p})$ (Appendix Sect.

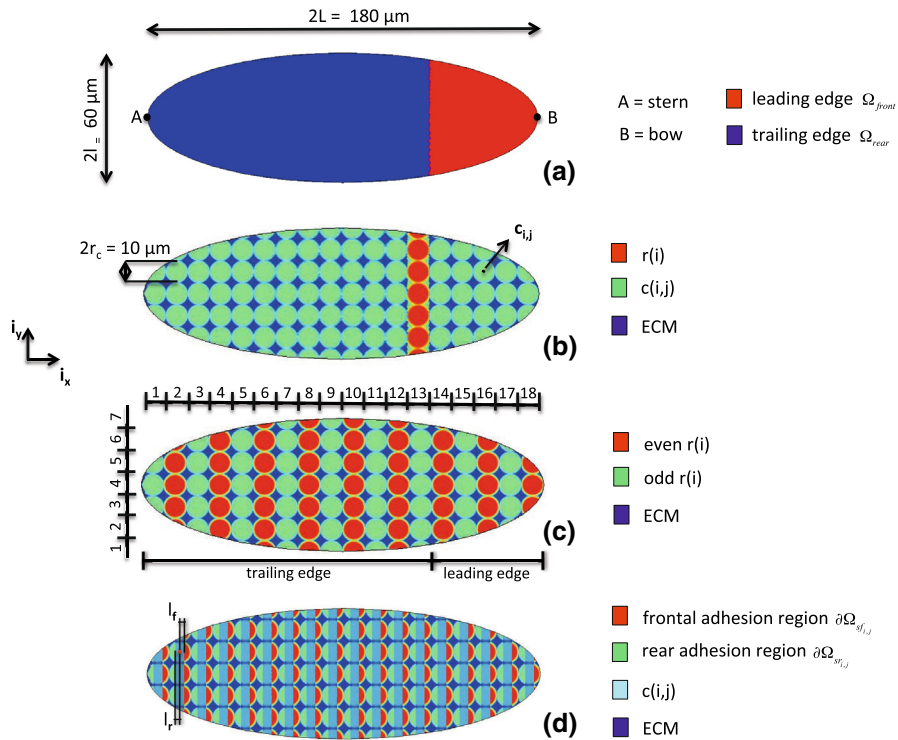


Fig. 2 **a** Simplified geometry of the LLP with the leading (red) and trailing (blue) edges. **b** Representation of the cell network $h_n(\mathbf{p})$. Each cell $c(i, j)$ (green) has a circular shape with radius r_c and centre $c_{i,j}$. **c** The elliptical shape of the LLP is divided into cell rows, $r(i)$, which are numbered from the “stern” to the “bow” of the ellipse (even rows in red, odd rows in green). The first 5 rows constitute the leading edge, while the remaining 13 rows constitute the trailing edge. The ECM (blue) fills the interstices between the cells. **d** Representation of the initial frontal ($\partial\Omega_{sf_{i,j}}$, red) and rear ($\partial\Omega_{sr_{i,j}}$, green) adhesion surfaces which are defined by the distances of the cell centre $c_{i,j}$ from the frontal (l_f) and rear (l_r) region (Color figure online)

“LLP Geometry”, Eq. 9). At the initial time step, each cell $c(i, j)$ inside the population has a circular shape (Fig. 2b, Appendix Sect. “LLP Geometry”, Eq. 11) with radius r_c and centre $c_{i,j} (c_{i,j_x}, c_{i,j_y})$, where the indices i and j indicate the position of the cell, respectively, along the major and minor axes of the ellipse (Fig. 2c, Appendix Sect. “LLP Geometry”, Eq. 10). Each cell is equipped with frontal ($\partial\Omega_{sf_{i,j}}$) and rear ($\partial\Omega_{sr_{i,j}}$) regions (Fig. 2d), which are defined through two characteristic functions $h_{sf_{i,j}}$ and $h_{sr_{i,j}}$ (Appendix Sect. “LLP Geometry”, Eq. 12) and depend on the distances l_f and l_r between the cell centre $c_{i,j}$ the corresponding regions (Fig. 2d, Appendix Sect. “LLP Geometry”, Eq. 12). These regions allow the cell to adhere to the ECM. Finally, we assume here that the cells migrate along the horizontal axis i_x .

2.2 Molecular Framework

As described in Sect. 1.1, LLP migration is controlled by a very complex interaction network of molecules and chemokines. Although a few processes and interactions remain unclear, we propose a set of four coupled reaction–diffusion equations derived from the experimental observations proposed in Aman and Piotrowski (2008, 2009, 2011) and based on the following assumptions:

- (i) we consider two molecules (Wnt-β-catenin and FGF) and two chemokines (*cxcr4b* and *cxcr7b*);
- (ii) start of polarisation of Wnt/β-catenin and *cxcr4b*–*cxcr7b* are assume to occur between the leading (Ω_{front}) and the trailing (Ω_{rear}) cells (Fig. 2a) of the LLP, which are described through two characteristic functions h_{front} and h_{rear} , respectively (Appendix Sect. “Leading and Trailing Edge of the LLP”, Eq. 14). The former includes 5 cell rows, while the latter is constituted by the remaining 13 rows;
- (iii) only Wnt/β-catenin signalling activation is considered, and it occurs in the leading edge Ω_{front} of the LLP;
- (iv) Wnt/β-catenin produces FGF and in the frontal edge Ω_{front} of the LLP simultaneously inhibits it through *sef*;
- (v) only Wnt/β-catenin and FGF are considered as diffusive molecules;
- (vi) *cxcr4b* and *cxcr7b* are homogeneously distributed throughout the LLP at the onset of migration (i.e. $cxcr4b = cxcr7b = 1$ at 20 hpf);
- (vii) *FGF*, *cxcr4b* and *cxcr7b* autoproduce themselves;
- (viii) the inhibition of *cxcr4b* in the trailing cells Ω_{rear} is directly controlled by FGF.

Therefore, the model equations take the form:

$$\frac{\partial [W]}{\partial t} = \underbrace{D_a \nabla^2 [W]}_{\text{diffusion}} + \underbrace{S_a [W] (1 - [W]) h_{front}}_{\text{signalling}} - \underbrace{R_a [W] [F] h_{rear}}_{\text{reaction by } dkk1} \quad (1)$$

$$\frac{\partial [F]}{\partial t} = \underbrace{D_b \nabla^2 [F]}_{\text{diffusion}} + \underbrace{P_b [W] (1 - [F])}_{\text{production}} - \underbrace{R_b [F] [W] h_{front}}_{\text{reaction by } sef} \quad (2)$$

$$\frac{\partial [c_4]}{\partial t} = \underbrace{P_c [c_4] (1 - [c_4])}_{\text{production}} - \underbrace{R_c [c_4] [F]}_{\text{reaction by } Fgf} \tag{3}$$

$$\frac{\partial [c_7]}{\partial t} = \underbrace{P_d [c_7] (1 - [c_7])}_{\text{production}} - \underbrace{R_d [c_7] [W]}_{\text{reaction by } Wnt} \tag{4}$$

where $[W] = \text{Wnt}/\beta\text{-catenin}$, $[F] = FGF$, $[c_4] = cxcr4b$, $[c_7] = cxcr7b$ indicate the dimensionless and normalized concentrations. D_i , P_i , R_i and S_i are the diffusion coefficients, production, reaction and signalling rates, respectively, for each molecule. Finally, Neumann boundary conditions have been applied on the continuum domain of the LLP for all the variables.

2.3 Mechanics of the Model

The cells are assumed to consist of two phases: (i) a solid-like phase (the actin filaments) where the cyclic active deformations (i.e. protrusion and contraction) take place and (ii) a fluid-like phase, which includes some particles (the organelles, fluid elastic) embedded in a fluid (cytoplasm, fluid viscous). As in previous work of the first author (Allena and Aubry 2012; Allena et al. 2013), a 2D generalized Maxwell model has been used to reproduce such a behaviour (Appendix Sect. ‘‘Constitutive Model’’). Since the cells within the cohort may undergo large rotations and deformations during their locomotion, a fully nonlinear tensorial approach is required. The ECM is assumed to be a viscoelastic material.

Newton’s law, applied to the continuum with respect to the initial configuration X , yields

$$\rho_{\text{cells}} \mathbf{a} = \text{Div}_X (\mathbf{J} \boldsymbol{\sigma} \mathbf{F}^{-T}) + \mathbf{f}_{adh} \tag{5}$$

where ρ_{cells} is the cell density, \mathbf{a} the acceleration, $\boldsymbol{\sigma}$ the Cauchy stress, \mathbf{F} the deformation gradient, \mathbf{J} its determinant, Div_X the divergence with respect to the initial position and \mathbf{F}^{-T} the inverse transpose of the matrix \mathbf{F} (Holzapfel 2000; Taber 2004). The term \mathbf{f}_{adh} defines the viscous adhesion forces between the cell and the substrate and may be decomposed into a frontal (f_f) and a rear (f_r) force as follows:

$$\begin{aligned} \mathbf{f}_f(\mathbf{n}) &= -\mu_f h_e \left(-\frac{\partial \mathbf{F}_{sa}}{\partial t} \right) h_{sf_{i,j}}(\mathbf{u}) \frac{\partial \mathbf{u}}{\partial t} \\ \mathbf{f}_r(\mathbf{n}) &= -\mu_r h_e \left(\frac{\partial \mathbf{F}_{sa}}{\partial t} \right) h_{sr_{i,j}}(\mathbf{u}) \frac{\partial \mathbf{u}}{\partial t} \end{aligned} \tag{6}$$

where \mathbf{n} is the normal vector to the boundary of the cell $c(i, j)$, μ_f and μ_r are the friction force viscosities and \mathbf{u} is the displacement of the cell $c(i, j)$ with respect to the ECM. The characteristic function h_e is the key ingredient since it links the adhesion forces exerted by the cell $c(i, j)$ on the ECM with the cyclic protrusion–contraction movement of the cell, which is expressed by \mathbf{F}_{sa} (Allena 2013; Allena and Aubry 2012) and will be defined in the next section.

2.4 Coordinated and Uncoordinated Regime of Cells

According to the literature (Dambly-Chaudière et al. 2007; Valentin et al. 2007), normal migration (i.e. coordinated movement of the cells along the trunk of the zebrafish) is determined by the polarized expression of the two chemokines *cxc4b* and *cxc7b*. If such a spatial pattern is not achieved, the cells either stall or migrate in an uncoordinated way. Thus, for the present model, we distinguish between two main modes of migration and of inter-synchronization (Allena et al. 2013):

- (i) uncoordinated migration: all the cells are active (i.e. they develop a specific inter-synchronization (Allena et al. 2013)), but they migrate at their own pace (i.e. they are not necessarily synchronized with their neighbours);
- (ii) coordinated migration: once the *cxc4b*–*cxc7b* polarization is achieved, a wave progressively covers the LLP, which activates, one by one, the rows of cells beginning at the leading row and travelling back towards the trailing edge (Haas and Gilmour 2006; Nechiporuk and Raible 2008) and the cells start migrating in a synchronized manner.

Then, the cyclic protrusion–contraction movement, which is assumed to occur in the solid phase of each cell, is expressed as a uniaxial deformation through the solid active deformation tensor \mathbf{F}_{sa} as follows

$$\mathbf{F}_{sa} = \underbrace{e_{a,uc} h_{uc} \mathbf{i}_x \otimes \mathbf{i}_x}_{\text{uncoordinated migration}} + \underbrace{e_{a,c} h_c \mathbf{i}_x \otimes \mathbf{i}_x}_{\text{coordinated migration}} \quad (7)$$

where $e_{a,c}$ and $e_{a,uc}$ describe the cyclic deformation of protrusion–contraction (Eq. 31) and \otimes indicates the tensorial product. h_c and h_{uc} are two characteristic functions which define the specific conditions on the *cxc4b* and *cxc7b* concentrations determining the switch between the uncoordinated and the coordinated migration (Appendix Sect. “Coordinated and Uncoordinated Migration”, Eq. 30).

It should be remarked that the coupling between the molecular and the mechanical frameworks of the system is here twofold since (i) the transition between the uncoordinated and the coordinated migration depends on the polarization of the two chemokines *cxc4b* and *cxc7b* and (ii) the intensity of the protrusion–contraction movement during both the coordinated and uncoordinated migration of the cells depends on the concentration of the *cxc4b* chemokine.

3 Results

The numerical simulations have been run using COMSOL Multiphysics 3.5a[®] and are shown at time intervals of 1 day. The cell population has an initial geometry with semi-axes L and l equal to 90 and 30 μm , respectively (Fig. 2a). The cell network represented by $h_n(\mathbf{p})$ includes 18 cell rows ($N_c = i_{\max} = 18$, Appendix Sect. “LLP Geometry”), and each cell $c(i, j)$ has a radius $r_c = 5 \mu\text{m}$ (Allena 2013; Allena and Aubry 2012). The distances of $\mathbf{c}_{i,j}$ from the frontal (l_f) and rear (l_r) adhesion surfaces have both been fixed to 2 μm (Allena 2013; Allena and Aubry 2012), which leads to

an area of $25 \mu\text{m}^2$ covered by the adhesion surfaces $\partial\Omega_{\text{sf},i,j}$ and $\partial\Omega_{\text{sr},i,j}$ (Fig. 2d), and the viscous coefficients μ_f and μ_r have been set to 10^8 Pa s/m (Allena 2013; Allena and Aubry 2012). The Young's moduli of the solid elastic (E_{se}) and the fluid elastic (E_{fe}) phases of the cells have been chosen equal to 10^4 Pa (Allena 2013; Allena and Aubry 2012; Laurent et al. 2005) and 100 Pa (Allena 2013; Allena and Aubry 2012), respectively. The Poisson ratios of the solid elastic (ν_{se}) and the fluid elastic (ν_{fe}) phases have been set to 0.3 and 0.4, respectively, while the viscosity μ_{fv} of the fluid viscous phase has been set to $3 \times 10^5 \text{ Pa s}$ (Bausch et al. 1999; Drury and Dembo 2001). The viscosity of the ECM has been fixed to $3 \times 10^5 \text{ Pa s}$ (Bausch et al. 1999; Drury and Dembo 2001), and the density ρ_{cells} of the cells is equal to $1,000 \text{ kg/m}^3$ (Fukui et al. 2000). The main geometrical, mechanical and material parameters of the model are listed in Table 1.

3.1 The Model Correctly Reproduces Specific Mutant Behaviour

For the first set of simulations, only the reaction–diffusion equations have been implemented in order to illustrate the ability of the model to reproduce molecule–chemokine patterns. Specifically, we have compared our numerical results to the experimental ones observed by Aman and Piotrowski (2008) who have analysed the *wild-type* (*wt*) embryo and three mutants: the *adenomatous polypolis coli* (*apc*)³ embryo, the *SU5402*⁴ embryo and the *dkk1*⁵ embryo. We describe in detail the main pattern characteristics of each one of these mutants as they have been experimentally observed (Aman and Piotrowski 2008) (Fig. 3):

- the *wt* embryo displays definite spatial polarizations for Wnt/ β -catenin and FGF as well as for *cxcr4b* and *cxcr7b*;
- the *apc* embryo presents a uniform distribution of both Wnt/ β -catenin and FGF signalling;
- the *SU5402* embryo is very similar to the *apc* embryo. In fact, *SU5402* inhibits FGF signalling, whereas Wnt/ β -catenin is still active throughout the whole LLP;
- finally, for the *dkk1* embryo, both Wnt/ β -catenin and FGF signalling are not activated. Nevertheless, *cxcr7b* and the *cxcr7b* are still present in the leading and trailing cells, respectively.

To numerically obtain the same patterns, we have first set the diffusive, signalling, production and reaction coefficients for each molecule and chemokine as they appear in Eqs. (1–4) for the *wt* embryo (see Table 2). Second, according to the previous remarks, Eqs. (1–4) have been changed and the coefficients tuned for each mutant (see Table 2 and Appendix Sect. “Description of Mutants”). In Fig. 4 (columns from 2 to 5), the normalized concentrations of the molecules and chemokines at the end of the simulations are shown for each mutant. A normalized concentration equal to 1 (red)

³ *apc* is a protein regulating Wnt/ β -catenin signalling and ensuring association with the microtubules, which is necessary for normal migration, via the C terminus.

⁴ *SU5402* is a fibroblast growth factor receptor (FGFR)-specific tyrosine kinase inhibitor.

⁵ *dkk1* is a diffusible inhibitor of the Wnt/ β -catenin pathway.

Table 1 Main geometrical, mechanical and material parameters of the model

Parameter	Description	Value	Unit	References
L	Major axis of the ellipse	90	μm	
l	Minor axis of the ellipse	30	μm	
N_c	Number of cells along the axis L of the ellipse	18		
$n_{c,\text{max}}$	Maximal number of cells along the axis l of the ellipse	6		
r_c	Cell radius	5	μm	(Allena and Aubry 2012; Allena 2013)
l_f	Distance of the boundary of the frontal adhesion surface from the cell centre	2	μm	(Allena and Aubry 2012; Allena 2013)
l_r	Distance of the boundary of the rear adhesion surface from the cell centre	2	μm	(Allena and Aubry 2012; Allena 2013)
$\partial\Omega_{\text{sf},i,j}$	Area of frontal adhesion region	25	μm^2	
$\partial\Omega_{\text{sr},i,j}$	Area of rear adhesion region	25	μm^2	
μ_f	Viscous coefficient of the frontal adhesion surface $\partial\Omega_{\text{sf},i,j}$	10^8	Pa s/m	(Allena and Aubry 2012; Allena 2013)
μ_r	Viscous coefficient of the rear adhesion surface $\partial\Omega_{\text{sr},i,j}$	10^8	Pa s/m	(Allena and Aubry 2012; Allena 2013)
E_{se}	Young's modulus of the solid elastic phase of the cells	10^4	Pa	(Allena and Aubry 2012; Allena 2013; Laurent et al. 2005)
ν_{se}	Poisson ratio of the solid elastic phase of the cells	0.3		
E_{fe}	Young's modulus of the fluid elastic phase of the cells	100	Pa	(Allena and Aubry 2012; Allena 2013)
ν_{fe}	Poisson ratio of the fluid elastic phase of the cells	0.4		
μ_{fv}	Viscosity of the fluid viscous phase of the cells	3×10^5	Pa s	(Bausch et al. 1999; Drury and Dembo 2001)
μ_{ECM}	Viscosity of the ECM	3×10^5	Pa s	(Bausch et al. 1999; Drury and Dembo 2001)
ρ_{cells}	Density of the cells	1,000	kg/m^3	(Fukui et al. 2000)

Embryo	Wnt/ β -catenin expression	FGF expression	<i>cxcr4b</i> expression	<i>cxcr7b</i> expression	Migration
<i>wt</i>					+++
<i>apc</i>					---
<i>SU5402</i>					---
<i>dkk1</i>					+++

Fig. 3 Summary of molecule and chemokine patterns and the associated migration behaviour for the four mutants tested in Aman and Piotrowski (2008) (Sect. 3.1) ('+++’ and ‘---’ indicate normal and abnormal migration, respectively; *colored region* in the LLP = molecule or chemokine expression; *white region* in the LLP = no expression of the molecule or chemokine) (Color figure online)

Table 2 Reaction–diffusion coefficients of the model

Parameter	Description	Value				Unit
		<i>wt</i>	<i>apc</i>	<i>SU5402</i>	<i>dkk1</i>	
D_a	Diffusive coefficient for Wnt/ β -catenin	$1e-11$	$1e-11$	$1e-11$	$1e-11$	m^2/s
S_a	Signalling coefficient for Wnt/ β -catenin	$8e-1$	$8e-1$	$8e-1$	$1e-3$	s^{-1}
R_a	Reaction coefficient for Wnt/ β -catenin	0.08	0.08	0.08	0.08	s^{-1}
D_b	Diffusive coefficient for Fgf	$1e-11$	$1e-11$	$1e-11$	$1e-11$	m^2/s
P_b	Production coefficient for Fgf	$8e-2$	$8e-2$	$8e-2$	$8e-2$	s^{-1}
R_b	Reaction coefficient for Fgf	$5e-1$	$5e-3$	$5e-1$	$5e-1$	s^{-1}
P_c	Production coefficient for <i>cxcr4b</i>	$0.2e-3$	$0.2e-3$	$0.2e-3$	$0.2e-3$	s^{-1}
R_c	Reaction coefficient for <i>cxcr4b</i>	$2e-4$	$2e-5$	$2e-4$	$2e-4$	s^{-1}
P_d	Production coefficient for <i>cxcr7b</i>	$0.1e-3$	$0.1e-3$	$0.1e-3$	$0.1e-3$	s^{-1}
R_d	Reaction coefficient for <i>cxcr7b</i>	$1e-4$	$1e-4$	$1e-4$	$1e-4$	s^{-1}

corresponds to the expression of the molecule or chemokine, while a value of 0 (blue) indicates that the molecule or chemokine is not expressed. Our numerical results agree with the experimental observations (Aman and Piotrowski 2008) as the same patterns for Wnt/ β -catenin, FGF, *cxcr4b* and *cxcr7b* are obtained for each mutant.

We now proceed with the implementation of the mechanical framework in the model.

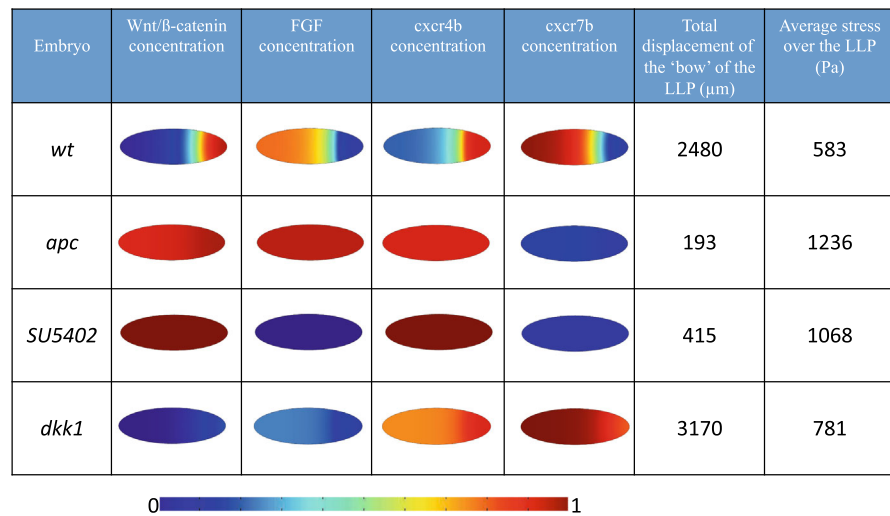


Fig. 4 Numerical results for the four mutants at the end of the simulations ($t = 1$ day) (Sect. 3.2). Columns from 2 to 5 show the molecule and chemokine normalized concentrations over the LLP, which may vary from 0 (blue) to 1 (red) (Sect. 3.1). Columns 6 and 7 show the values for the total displacement of the 'bow' of the LLP and the average stress over the whole population (Sect. 3.2) (Color figure online)

3.2 *cxcr4b*–*cxcr7b* Polarization Regulates the Efficient Migration of the LLP

According to the molecular and chemokine patterns described in Sect. 3.1, the *wt* and the mutant embryos show the following specific migration behaviour when experimentally observed (Aman and Piotrowski 2008):

- in the *wt* embryo, the LLP travels at constant speed from the head towards the tail along the trunk, which results in what is called the normal migration of the population;
- the *apc* and *SU5402* embryos show a very similar behaviour to each other. In fact, the primordium stalls due to the unpolarization of the two chemokines *cxcr4b* and *cxcr7b*, which is led by the uniform and unpolarized diffusion of Wnt/ β -catenin and FGF throughout the LLP respectively in the *apc* and the *SU5402* embryo;
- finally, in the *dkk1* embryo the LLP migration is not affected since the *cxcr4b*–*cxcr7b* spatial polarization is maintained.

Therefore, our conclusion is that for the LLP to migrate in an efficient and synchronized manner as is observed for the *wt* and the *dkk1* embryos, Wnt/ β -catenin–FGF polarity may occur (i.e. *wt* embryo) or not (i.e. *dkk1* embryo), while *cxcr4b*–*cxcr7b* polarity is a necessary condition.

In the present paper, the uncoordinated and the coordinated movements of the cells within the population have been described in Sect. 2.3. In the former case, very similar to the random migration proposed in our previous work (Allena et al. 2013), all the cells are active and migrate at their own pace, which leads to an unsynchronized migration. In the latter case, once the polarization of the two chemokines, *cxcr4b* and *cxcr7b*, is achieved, a wave progressively covers the LLP and activates one by one the

rows of cells, which start to migrate in phase. The shift between the uncoordinated and coordinated migration is observable for the *wt* and the *dkk1* embryos. In fact, *cxcr4b–cxcr7b* polarization is reached at around 22 and 23 hpf, respectively, for the former and for the latter embryo (Movies 1 and 4, respectively). However, for the *apc* and the *SU5402* embryos, the cells move in an unsynchronized manner throughout the simulation (Movies 2 and 3, respectively).

Such a cellular behaviour is also reflected in terms of distance covered and stress state inside the LLP. First, as in our previous work (Allena et al. 2013), we found a correspondence between the efficiency of the cell cohort migration and the stress distribution within the population: normal and efficient migration coincides with low stresses within the LLP. Actually, the *wt* and *dkk1* embryos are the most efficient and they migrate for 2,480 and 3,170 μm (displacement calculated at the ‘bow’ of the LLP), respectively, and the average stress has been found equal to 583 and 781 Pa, respectively (Fig. 4, columns 6 and 7). Such values are on the same order as those found experimentally by previous authors (Serra-Picamal et al. 2012; Tambe et al. 2011; Trepats et al. 2009). However, the *apc* and *SU5402* embryos only migrate a distance of 193 and 415 μm (displacement calculated at the ‘bow’ of the LLP), respectively, and the average stress is equal to 1,236 and 1,068 Pa, respectively (Fig. 4, columns 6 and 7).

Second, the switch between uncoordinated and coordinated migration coincides with the rearrangement of the principal directions of the stresses. As far as the cells migrate at their own pace, the principal stresses are oriented in different directions within the population, while they are aligned with the direction of migration as soon as the cells start coordinating their movement.

Third, while during the uncoordinated migration all the cells generate high stresses, during the coordinated migration, only the central cells are those which develop the highest stresses due to the neighbouring constrictions.

3.3 What About Cell Leadership?

According to the experimental observations in Aman and Piotrowski (2008), the polarity between *cxcr4b–cxcr7b* seems to be biochemically necessary for normal migration. By assuming this is the case, in the previous set of simulations such a polarity led to a proper inter-synchronization of all the cells within the LLP (i.e. *wt* and *dkk1* embryos, Movies 1 and 4). However, one of the main questions that has been experimentally addressed, but still remains partially unanswered, is whether all the cells, or only a few of them, sense such a polarity acting as leader cells and start migrating in a coordinated manner.

Therefore, we have numerically explored if and how, once the *cxcr4b–cxcr7b* polarity has been established, the density of coordinated cells within the LLP may affect the global behaviour of the population. To do so, a new set of simulations has been run and four configurations have been tested for which the coordinated migration involves (i) only cells in the first row (r_{18}), (ii) only cells in the first two rows (r_{18} and r_{17}), (iii) only cells in the first three rows (r_{18} , r_{17} and r_{16}) and (iv) cells inside the frontal region, Ω_{front} , of the LLP.



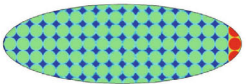
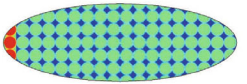
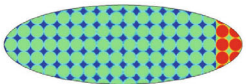
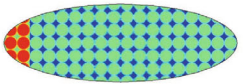
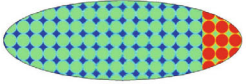
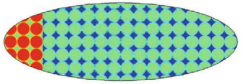
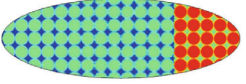
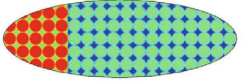
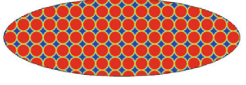
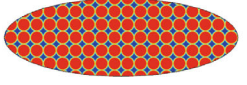
Normal polarization 		Inverse polarization 	
Coordinated cell rows in red (from right to left)	Total displacement of the 'bow' of the LLP (μm)	Coordinated cell rows in red (from left to right)	Total displacement of the 'bow' of the LLP (μm)
	553		883
	1590		2101
	1691		2266
	2494		3506
	2480 (<i>wt</i> embryo) 3170 (<i>dkk1</i> embryo)		3519

Fig. 5 Numerical results at the end of the simulations ($t=1$ day) for the case of normal (columns 1 and 2) and inverse (column 3 and 4) *cxcr4b*–*cxcr7b* polarization (Sect. 3.3). Columns 1 and 3 show in red the coordinated cell rows. In columns 2 and 4, the values of the total displacement of the 'bow' of the LLP are reported (Color figure online)

By analysing the results in terms of efficiency of the LLP (i.e. distance covered over 1 day by the 'bow' of the LLP) (column 2 in Fig. 5), we observe that when only one row of cells is coordinated, the total displacement of the population is about $553 \mu\text{m}$, which is larger than that of a continuous uncoordinated migration (193 and $415 \mu\text{m}$ for the *apc* and the *SU5402* embryos, respectively), but much smaller than that reached during normal migration ($2,480$ and $3,170 \mu\text{m}$ for the *wt* and the *dkk1* embryos, respectively). If one or two more rows also coordinate their movement, the global efficiency increases, but the total displacement of the LLP is still smaller than in the case of normal migration ($1,590$ and $1,691 \mu\text{m}$, respectively).

However, when all the cell rows inside the frontal region of the LLP are coordinated, the population is able to migrate over $2,494 \mu\text{m}$, which is very close to the displacement of the *wt* and *dkk1* embryos. Such outcomes confirm that a minimal level of inter-synchronization between the cells is necessary for the LLP to be efficient, as we have demonstrated in our previous work (Allena et al. 2013), but also that a small portion of

competent cells is required to steer the population (Kabla 2011; Vitorino and Meyer 2008).

In *in vivo* situations, leader cells are usually found at free boundaries of the population to direct the motion and to “dig up the road” within the surrounding cells. Although this second function must play a fundamental role during LLP migration, we have investigated whether the position of the leader cells may affect the global behaviour of the system. A third set of simulations has been run for which *cxcr4b*–*cxcr7b* polarity has been reversed (i.e. Ω_{front} and Ω_{rear} are reversed so that the “stern” and the “bow” of the LLP correspond to the front and rear respectively), but the direction of migration is still the same. Consequently, the leader cells are located at the “stern” of the LLP, and the synchronization of the motion occurs from the “stern” towards the “bow” of the population. As for the previous set of simulations, four configurations have been analysed for which coordinated migration involves (i) only one row of cells (r_1), (ii) two rows of cells (r_1 and r_2), (iii) three rows of cells (r_1 , r_2 and r_3) and (iv) the rows inside the Ω_{front} domain. The results are shown in column 4 of Fig. 5. Surprisingly, the same conclusions as for the second set of simulations (column 2, Fig. 5) can be drawn regarding the efficiency of the migration. In fact, from a mechanical point of view, as far as a minimal number of cells within the population are able to coordinate their movement, whether they are at the front or at the back does not influence the global effectiveness of the system (Couzin et al. 2005; Kabla 2011). As mentioned in Sect. 1.1, it has been experimentally observed that normal migration is not only triggered by *cxcr4b*–*cxcr7b* polarity, it also follows SDF-1 expression, which is controlled by *cxcr4b* at the leading edge (Haas and Gilmour 2006). Although further measurements are needed to confirm such a hypothesis, our numerical results clearly show that a further spatial signal is required for the leader cells to be located at the frontal edge of the LLP, and SDF-1 might be a good candidate. This hypothesis seems also to be plausible considering that the cells at the “bow” of the LLP might be able “to see” and sense the environment in front of them and therefore to choose and adjust their path accordingly.

Therefore, the pioneer cells would be simultaneously responsible for regulating the inter-synchronization, which is the necessary condition for normal migration, and directing migration towards the tail of the animal.

4 Conclusions

Here, we have proposed a 2D finite element model to simulate the collective migration of the LLP. The population is modelled as a continuum with embedded discrete motile cells, which are viscoelastic and able to undergo large deformations (Sect. 2.1). Both the molecular and the mechanical frameworks of the system have been considered. The former takes into account Wnt/ β -catenin and FGF signalling as well as *cxcr4b* and *cxcr7b* expression, which have been described through specific reaction–diffusion equations (Sect. 2.2). For the latter, as in the previous works of the first author (Allena 2013; Allena and Aubry 2012; Allena et al. 2013), we have employed the decomposition of the deformation gradient to describe both the active (i.e. protrusion and contraction) and the elastic (i.e. generated by the interaction with the ECM)

deformations (Sect. 2.3). Additionally, the active deformations are closely coupled with the molecular framework of the system. First, the intensity of the protrusion–contraction movement depends on the *cxcr4b* concentration. Second, the intra-synchronization between the active deformations and the adhesion forces necessary to move forward is regulated by *cxcr4b–cxcr7b* polarity. In fact, until *cxcr4b–cxcr7b* polarity is achieved, the cells migrate in an uncoordinated manner, while they start to synchronize their movement as soon as the two chemokines are correctly expressed.

In order to validate such a model, we have considered four different mutants as presented in Aman and Piotrowski (2008): the *wt*, *apc*, *SU5402* and *dkk1* embryos (Sect. 3.1). Each one of these embryos shows a specific molecular pattern, which influences the global motion of the LLP. On the one hand, the *wt* and the *dkk1* embryos migrate in a normal way due to the *cxcr4b–cxcr7b* polarity, which allows the cells to coordinate their movement. On the other hand, the *apc* and the *SU5402* embryos stall and are not very efficient in terms of distance covered. By coupling both the molecular and the mechanical frameworks, our model is able to simulate such behaviours and the results are in agreement with the experimental observations (Sect. 3.2).

By assuming that *cxcr4b–cxcr7b* polarity is the required molecular condition for normal migration, we have theoretically investigated the role of the leader cells and their position within the population. By running two new series of simulations, we have found that: (i) a small portion of coordinated cells is necessary (Allena et al. 2013) and sufficient (Vitorino and Meyer 2008) to induce the normal and efficient migration of the LLP and (ii) from a mechanical point of view, once the previous condition is ensured, the position of the leader cells inside the population does not influence the global efficiency of the LLP migration.

Therefore, the general assumption by which leader cells in the LLP are located at the frontal edge of the population can only be sustained if, besides *cxcr4b–cxcr7b* polarity, which seems to trigger the inter-synchronization, leader cells respond to a further spatial feedback in control of their position.

Such an outcome could confirm the experimental observations according to which the normal migration of the LLP appears to follow a line of the chemokine SDF-1 along the embryo trunk, which depends on the expression of *cxcr4b* in the leading edge (Haas and Gilmour 2006). Thus, cells at the front of the LLP expressing *cxcr4b* might be responsible for sensing the SDF-1 gradient and for directing migration.

The present model has two main limitations. First, no external signal, such as a SDF-1 gradient, has been considered and only molecular processes internal to the LLP have been taken into account. Therefore, the model could be extended by introducing an ordinary differential equation to control both the intensity and the direction of the external source (Allena 2013; Allena and Aubry 2012). By doing this, it would be possible to evaluate the influence of such a further spatial feedback on the global efficiency of the LLP as well as on the inter-synchronization between the cells. Second, no interaction between the LLP and the surrounding ECM and cells, which may play an important role during the whole migration, has been considered. These extensions will be presented in future research which aims to better understand how LLP is able to structurally modify its environment in order to migrate through it.

Acknowledgments This work was initiated and partially completed while Rachele Allena was a visitor to the Mathematical Institute, Oxford. The authors are grateful to Dr. Tatjana Piotrowski and Pr. Denis Aubry for useful discussions.

Appendix

LLP Geometry

The cell network Ω_n is defined by a characteristic function $h_n(\mathbf{p})$ as follows:

$$h_n(\mathbf{p}) = \begin{cases} 1 & \text{if } \|\mathbf{p} - 2 \cdot r_c \cdot \text{round}(p_x) \mathbf{i}_x - 2 \cdot r_c \cdot \text{round}(p_y) \mathbf{i}_y\| < r_c^2 \\ 0 & \text{otherwise} \end{cases} \quad (8)$$

with *round* being the classical integer function and $\mathbf{p} = (p_x, p_y)$ the initial position of any particle of the system.

The ECM domain Ω_{ECM} is identified by the characteristic function $h_{\text{ECM}}(\mathbf{p})$ which reads

$$h_{\text{ECM}}(\mathbf{p}) = 1 - h_n(\mathbf{p}). \quad (9)$$

Each cell inside the population is denoted by $c(i, j)$ where the indices i and j vary as follows:

$$\begin{cases} 1 \leq i \leq N_c = i_{\max} \\ 1 \leq j \leq n_c(i) = n_{c,\max} \sqrt{1 - \left(\frac{2i-1}{N_c}\right)^2} \end{cases} \quad (10)$$

with $N_c = \frac{L}{r_c}$, $i_{\max} = 18$ and $n_{c,\max} = \frac{l}{r_c}$ being the number of cells along the two axes of the ellipse (Fig. 2b, c).

The domain $\Omega_{c_{i,j}}$ occupied by each cell $c(i, j)$ is defined through a characteristic function as follows

$$h_{c_{i,j}}(\mathbf{p}) = \begin{cases} 1 & \text{if } \|\mathbf{p} - \mathbf{c}_{i,j}\| < r_c^2 \\ 0 & \text{otherwise} \end{cases} \quad (11)$$

Each cell is equipped with a frontal $\partial\Omega_{\text{sf}_{i,j}}$ and a rear $\partial\Omega_{\text{sr}_{i,j}}$ adhesion region (Fig. 2d) described, respectively, by two characteristic functions

$$\begin{aligned} h_{\text{sf}_{i,j}}(\mathbf{p}) &= \begin{cases} 1 & \text{if } (\mathbf{p} - \mathbf{c}_{i,j}, \mathbf{i}_x) > l_f \\ 0 & \text{otherwise} \end{cases} \\ h_{\text{sr}_{i,j}}(\mathbf{p}) &= \begin{cases} 1 & \text{if } (\mathbf{p} - \mathbf{c}_{i,j}, \mathbf{i}_x) < -l_r \\ 0 & \text{otherwise} \end{cases} \end{aligned} \quad (12)$$

where (\mathbf{a}, \mathbf{b}) defines the scalar product and l_f and l_r are the distances of $\mathbf{c}_{i,j}$ from the frontal and rear adhesion surfaces, respectively.

The ellipse is divided into cell rows $r(i)$ (Fig. 2b), which are numbered, similarly to the single cells, from the “stern” (left) to the “bow” (right) of the ellipse ($1 \leq i \leq N_c = i_{\max}$) (Fig. 2c) and are defined through a characteristic function as

$$h_{r_i}(\mathbf{p}) = h_n(\mathbf{p}) \begin{cases} 1 & \text{if } (p_x - c_{i,j_x}) < r_c \\ 0 & \text{otherwise.} \end{cases} \quad (13)$$

Leading and Trailing Edge of the LLP

The Wnt/ β -catenin–FGF network is mainly based on the spatial polarization of the LLP. We define the leading, Ω_{front} , and the trailing, Ω_{rear} , edges of the LLP through the characteristic functions h_{front} and h_{rear} , respectively, as follows:

$$h_{\text{front}} = \begin{cases} 1 & \text{if } p_x > p_{x0} \\ 0 & \text{otherwise} \end{cases} \quad h_{\text{rear}} = \begin{cases} 1 & \text{if } p_x < p_{x0} \\ 0 & \text{otherwise} \end{cases} \quad (14)$$

where p_{x0} is the axial coordinate defining the boundary between the leading and the trailing edges.

Description of Mutants

In the following, we define the reaction–diffusion equations that have been used to describe the molecular and chemokine patterns specific to each mutant as mentioned in Sect. 2.2.

– *apc* embryo

$$\frac{\partial [W]}{\partial t} = \underbrace{D_a \nabla^2 [W]}_{\text{diffusion}} + \underbrace{S_a [W] (1 - [W])}_{\text{signalling}} - \underbrace{R_a [W] [F]}_{\text{reaction by dkk1}} \quad (15)$$

$$\frac{\partial [F]}{\partial t} = \underbrace{D_b \nabla^2 [F]}_{\text{diffusion}} + \underbrace{P_b [W] (1 - [F])}_{\text{production}} - \underbrace{R_b [F] [W]}_{\text{reaction by sef}} \quad (16)$$

$$\frac{\partial [c_4]}{\partial t} = \underbrace{P_c [c_4] (1 - [c_4])}_{\text{production}} - \underbrace{R_c [c_4] [F]}_{\text{reaction by Fgf}} \quad (17)$$

$$\frac{\partial [c_7]}{\partial t} = \underbrace{P_d [c_7] (1 - [c_7])}_{\text{production}} - \underbrace{R_d [c_7] [W]}_{\text{reaction by Wnt}} \quad (18)$$

– *SU5402* embryo

$$\frac{\partial [W]}{\partial t} = \underbrace{D_a \nabla^2 [W]}_{\text{diffusion}} + \underbrace{S_a [W] (1 - [W]) h_{\text{front}}}_{\text{signalling}} - \underbrace{R_a [W] [F] h_{\text{rear}}}_{\text{reaction by dkk1}} \quad (19)$$

$$\frac{\partial [F]}{\partial t} = \underbrace{D_b \nabla^2 [F]}_{\text{diffusion}} - \underbrace{R_b [F][W] h_{\text{front}}}_{\text{reaction by sef}} \tag{20}$$

$$\frac{\partial [c_4]}{\partial t} = \underbrace{P_c [c_4] (1 - [c_4])}_{\text{production}} - \underbrace{R_c [c_4][F]}_{\text{reaction by Fgf}} \tag{21}$$

$$\frac{\partial [c_7]}{\partial t} = \underbrace{P_d [c_7] (1 - [c_7])}_{\text{production}} - \underbrace{R_d [c_7][W]}_{\text{reaction by Wnt}} \tag{22}$$

– *dkk1* embryo

$$\frac{\partial [W]}{\partial t} = \underbrace{D_a \nabla^2 [W]}_{\text{diffusion}} + \underbrace{S_a [W] (1 - [W]) h_{\text{front}}}_{\text{signalling}} - \underbrace{R_a [W][F]}_{\text{reaction by dkk1}} \tag{23}$$

$$\frac{\partial [F]}{\partial t} = \underbrace{D_b \nabla^2 [F]}_{\text{diffusion}} + P_b [W] (1 - [F]) - \underbrace{R_b [F][W] h_{\text{front}}}_{\text{reaction by sef}} \tag{24}$$

$$\frac{\partial [c_4]}{\partial t} = \underbrace{P_c [c_4] (1 - [c_4])}_{\text{production}} - \underbrace{R_c [c_4][F]}_{\text{reaction by Fgf}} \tag{25}$$

$$\frac{\partial [c_7]}{\partial t} = \underbrace{P_d [c_7] (1 - [c_7])}_{\text{production}} - \underbrace{R_d [c_7][W]}_{\text{reaction by Wnt}} \tag{26}$$

Constitutive Model

As mentioned in Sect. 2.3, the behaviour of the cells is described through a generalized viscoelastic 2D Maxwell model (Allena 2013; Allena and Aubry 2012).

The Cauchy stress, σ , is assumed to be the sum of the solid (σ_s) and the fluid (σ_f) Cauchy stresses, while the deformation gradient F is equal to the solid (F_s) and the fluid (F_f) deformation gradients.

The decomposition of the deformation gradient (Allena et al. 2010; Lubarda 2004) is used to describe the solid deformation tensor, F_s , which is then given by

$$F_s = F_{se} F_{sa} \tag{27}$$

where F_{se} is the elastic deformation tensor responsible for the stress generation and F_{sa} is the active deformation tensor responsible for the pulsating movement (protrusion–contraction) of each cell. Similarly, the fluid deformation tensor F_f is the multiplicative decomposition of the fluid elastic (F_{fe}) and the fluid viscoelastic (F_{fv}) gradients.

Both the solid σ_{se} and the fluid elastic σ_{fe} Cauchy stresses are given by isotropic hyperelastic models $\bar{\sigma}_{se}$ and $\bar{\sigma}_{fe}$, respectively, as

$$\begin{aligned} \sigma_{se} &= \bar{\sigma}_{se} (e_{se}) \\ \sigma_{fe} &= \bar{\sigma}_{fe} (e_{fe}) \end{aligned} \tag{28}$$

with e_{se} and e_{fe} the Euler–Almansi deformation tensors for the solid elastic and the fluid elastic phases, respectively. Additionally, σ_{fe} has to be expressed in the actual configuration according to the multiplicative decomposition described above. Finally, the deformation rate \dot{e}_{fv} is related to the deviator part of the fluid viscous stress σ_{fv}^D as follows:

$$\dot{e}_{fv} = \frac{\sigma_{fv}^D}{\mu_{fv}} \quad (29)$$

where μ_{fv} is the viscosity and the dot is the derivative with respect to time.

Coordinated and Uncoordinated Migration

The characteristic functions h_c and h_{uc} are expressed as follows

$$h_c = \begin{cases} 1 & \text{if } \left\{ \begin{array}{l} ([c_4] > [c_{\max}]) h_{\text{front}} \wedge ([c_4] < [c_{\min}]) h_{\text{rear}} \\ \wedge \\ ([c_7] > [c_{\max}]) h_{\text{rear}} \wedge ([c_7] < [c_{\min}]) h_{\text{front}} \end{array} \right. \\ 0 & \text{otherwise} \end{cases}$$

$$h_{uc} = \begin{cases} 1 & \text{if } \left\{ \begin{array}{l} ([c_4] < [c_{\max}]) h_{\text{front}} \wedge ([c_4] > [c_{\max}]) h_{\text{rear}} \\ \wedge \\ ([c_7] < [c_{\max}]) h_{\text{rear}} \wedge ([c_7] > [c_{\min}]) h_{\text{front}} \end{array} \right. \\ 0 & \text{otherwise} \end{cases} \quad (30)$$

with \wedge being the Boolean operator AND and c_{\max} and c_{\min} being two thresholds fixed here to 0.9 and 0.2, respectively.

The terms $e_{a,c}$ and $e_{a,uc}$ describe the cyclic deformation of protrusion–contraction, and they read

$$e_{a,c} = \frac{[c_4]}{\alpha_c} \sin\left(2\pi \frac{t - \frac{T}{2}(i_{\max} - i)}{T}\right) h_{r_i}(\mathbf{p}) h_{\text{wave}}(\mathbf{p}, t)$$

$$e_{a,uc} = \frac{[c_4]}{\alpha_{uc_{ij}}} \sin\left(2\pi \frac{t}{T_{uc_{ij}}}\right) \quad (31)$$

where t is time.

For the coordinated migration, α_c is set to 2 and T indicates the duration of a migration period which has been fixed here to 60 s (Allena and Aubry 2012; Dong et al. 2002). Additionally, a wave progressively covers the LLP from the “bow” to the “stern” to activate, one by one, the cell row $r(i)$ with a velocity equal to $\frac{2l}{T}$. The wave is expressed by the characteristic function $h_{\text{wave}}(\mathbf{p}, t)$ as follows:

$$h_{\text{wave}}(\mathbf{p}, t) = \begin{cases} 1 & \text{if } (2L - r_c) - p_x - 2r_c \frac{2t}{T} < 0 \\ 0 & \text{otherwise.} \end{cases} \quad (32)$$

For the uncoordinated migration, α_{ucij} and T_{ucij} may vary between 0 and 1 and between 60 and 120 s, respectively, for each cell $c(i, j)$.

References

- Allena R (2013) Cell migration with multiple pseudopodia: temporal and spatial sensing models. *Bull Math Biol* 75(2):288–316. doi:[10.1007/s11538-012-9806-1](https://doi.org/10.1007/s11538-012-9806-1)
- Allena R, Aubry D (2012) ‘Run-and-tumble’ or ‘look-and-run’? A mechanical model to explore the behavior of a migrating amoeboid cell. *J Theor Biol* 306:15–31. doi:[10.1016/j.jtbi.2012.03.041](https://doi.org/10.1016/j.jtbi.2012.03.041)
- Allena R, Aubry D, Sharpe J (2013) On the mechanical interplay between intra- and inter-synchronization during collective cell migration: a numerical investigation. *Bull Math Biol* 75(12):2575–2599. doi:[10.1007/s11538-013-9908-4](https://doi.org/10.1007/s11538-013-9908-4)
- Allena R, Mouronval A-S, Aubry D (2010) Simulation of multiple morphogenetic movements in the *Drosophila* embryo by a single 3D finite element model. *J Mech Behav Biomed Mater* 3(4):313–323. doi:[10.1016/j.jmbbm.2010.01.001](https://doi.org/10.1016/j.jmbbm.2010.01.001)
- Aman A, Piotrowski T (2008) Wnt/beta-catenin and Fgf signaling control collective cell migration by restricting chemokine receptor expression. *Dev Cell* 15(5):749–761. doi:[10.1016/j.devcel.2008.10.002](https://doi.org/10.1016/j.devcel.2008.10.002)
- Aman A, Piotrowski T (2009) Multiple signaling interactions coordinate collective cell migration of the posterior lateral line primordium. *Cell Adhes Migr* 3(4):365–368
- Aman A, Piotrowski T (2011) Cell–cell signaling interactions coordinate multiple cell behaviors that drive morphogenesis of the lateral line. *Cell Adhes Migr* 5(6):499–508. doi:[10.4161/cam.5.6.19113](https://doi.org/10.4161/cam.5.6.19113)
- Anand RJ, Leaphart CL, Mollen KP, Hackam DJ (2007) The role of the intestinal barrier in the pathogenesis of necrotizing enterocolitis. *Shock (Augusta, Ga)* 27(2):124–133. doi:[10.1097/01.shk.0000239774.02904.65](https://doi.org/10.1097/01.shk.0000239774.02904.65)
- Arciero JC, Mi Q, Branca MF, Hackam DJ, Swigon D (2011) Continuum model of collective cell migration in wound healing and colony expansion. *Biophys J* 100(3):535–543. doi:[10.1016/j.bpj.2010.11.083](https://doi.org/10.1016/j.bpj.2010.11.083)
- Bausch AR, Möller W, Sackmann E (1999) Measurement of local viscoelasticity and forces in living cells by magnetic tweezers. *Biophys J* 76(1 Pt 1):573–579
- Couzin ID, Krause J, Franks NR, Levin SA (2005) Effective leadership and decision-making in animal groups on the move. *Nature* 433(7025):513–516. doi:[10.1038/nature03236](https://doi.org/10.1038/nature03236)
- Dambly-Chaudière C, Cubedo N, Ghysen A (2007) Control of cell migration in the development of the posterior lateral line: antagonistic interactions between the chemokine receptors CXCR4 and CXCR7/RDC1. *BMC Dev Biol* 7:23. doi:[10.1186/1471-213X-7-23](https://doi.org/10.1186/1471-213X-7-23)
- David NB, Sapède D, Saint-Etienne L, Thisse C, Thisse B, Dambly-Chaudière C, Ghysen A (2002) Molecular basis of cell migration in the fish lateral line: role of the chemokine receptor CXCR4 and of its ligand, SDF1. *Proc Natl Acad Sci* 99(25):16297–16302. doi:[10.1073/pnas.252339399](https://doi.org/10.1073/pnas.252339399)
- Di Costanzo E, Natalini R, Preziosi L (2014) A hybrid mathematical model for self-organizing cell migration in the zebrafish lateral line. *J Math Biol*. doi:[10.1007/s00285-014-0812-9](https://doi.org/10.1007/s00285-014-0812-9)
- Dong C, Slattery MJ, Rank BM, You J (2002) In vitro characterization and micromechanics of tumor cell chemotactic protrusion, locomotion, and extravasation. *Ann Biomed Eng* 30(3):344–355
- Drury JL, Dembo M (2001) Aspiration of human neutrophils: effects of shear thinning and cortical dissipation. *Biophys J* 81(6):3166–3177
- Friedl P, Gilmour D (2009) Collective cell migration in morphogenesis, regeneration and cancer. *Nat Rev Mol Cell Biol* 10(7):445–457. doi:[10.1038/nrm2720](https://doi.org/10.1038/nrm2720)
- Fukui Y, Uyeda TQP, Kitayama C, Inoué S (2000) How well can an amoeba climb? *Proc Natl Acad Sci* 97(18):10020–10025. doi:[10.1073/pnas.97.18.10020](https://doi.org/10.1073/pnas.97.18.10020)
- Gamba L, Cubedo N, Ghysen A, Lutfalla G, Dambly-Chaudière C (2010) Estrogen receptor ESR1 controls cell migration by repressing chemokine receptor CXCR4 in the zebrafish posterior lateral line system. *Proc Natl Acad Sci* 107(14):6358–6363. doi:[10.1073/pnas.0909998107](https://doi.org/10.1073/pnas.0909998107)
- Gompel N, Cubedo N, Thisse C, Thisse B, Dambly-Chaudière C, Ghysen A (2001) Pattern formation in the lateral line of zebrafish. *Mech Dev* 105(1–2):69–77
- Graner, Glazier (1992) Simulation of biological cell sorting using a two-dimensional extended Potts model. *Phys Rev Lett* 69(13):2013–2016
- Haas P, Gilmour D (2006) Chemokine signaling mediates self-organizing tissue migration in the zebrafish lateral line. *Dev Cell* 10(5):673–680. doi:[10.1016/j.devcel.2006.02.019](https://doi.org/10.1016/j.devcel.2006.02.019)

- Holzappel GA (2000) *Nonlinear solid mechanics: a continuum approach for engineering*, 1st edn. Wiley, Hoboken
- Irina O, Friedl P (2009) Mechanisms of collective cell migration at a glance. *J Cell Sci* 122(18):3203–3208. doi:[10.1242/jcs.036525](https://doi.org/10.1242/jcs.036525)
- Kabla AJ (2011) Collective cell migration: leadership, invasion and segregation. [arXiv:1108.4286](https://arxiv.org/abs/1108.4286) [physics, q-bio]. Retrieved from <http://arxiv.org/abs/1108.4286>
- Laurent VM, Kasas S, Yersin A, Schäffer TE, Catsicas S, Dietler G, Meister J-J et al (2005) Gradient of rigidity in the lamellipodia of migrating cells revealed by atomic force microscopy. *Biophys J* 89(1):667–675. doi:[10.1529/biophysj.104.052316](https://doi.org/10.1529/biophysj.104.052316)
- Lecaudey V, Cakan-Akdogan G, Norton WHJ, Gilmour D (2008) Dynamic Fgf signaling couples morphogenesis and migration in the zebrafish lateral line primordium. *Development (Cambridge, England)* 135(16):2695–2705. doi:[10.1242/dev.025981](https://doi.org/10.1242/dev.025981)
- López-Schier H (2010) Fly fishing for collective cell migration. *Curr Opin Genet Dev* 20(4):428–432. doi:[10.1016/j.gde.2010.04.006](https://doi.org/10.1016/j.gde.2010.04.006)
- Lubarda V (2004) Constitutive theories based on the multiplicative decomposition of deformation gradient: thermoelasticity, elastoplasticity, and biomechanics. *Appl Mech Rev* 57(2):95–109
- Nechiporuk A, Raible DW (2008) FGF-dependent mechanosensory organ patterning in zebrafish. *Science (New York, NY)* 320(5884):1774–1777. doi:[10.1126/science.1156547](https://doi.org/10.1126/science.1156547)
- Rørth P (2007) Collective guidance of collective cell migration. *Trends Cell Biol* 17(12):575–579. doi:[10.1016/j.tcb.2007.09.007](https://doi.org/10.1016/j.tcb.2007.09.007)
- Serra-Picamal X, Conte V, Vincent R, Anon E, Tambe DT, Bazellieres E, Trepast X (2012) Mechanical waves during tissue expansion. *Nat Phys* 8(8):628–634
- Sherratt JA, Murray JD (1990) Models of epidermal wound healing. *Proc Biol Sci/R Soc* 241(1300):29–36. doi:[10.1098/rspb.1990.0061](https://doi.org/10.1098/rspb.1990.0061)
- Sherratt JA, Murray JD (1991) Mathematical analysis of a basic model for epidermal wound healing. *J Math Biol* 29(5):389–404
- Streichan SJ, Valentin G, Gilmour D, Hufnagel L (2011) Collective cell migration guided by dynamically maintained gradients. *Phys Biol* 8(4):045004. doi:[10.1088/1478-3975/8/4/045004](https://doi.org/10.1088/1478-3975/8/4/045004)
- Taber LA (2004) *Nonlinear theory of elasticity: applications in biomechanics*. World Scientific, Singapore
- Tambe DT, Hardin CC, Angelini TE, Rajendran K, Park CY, Serra-Picamal X, Trepast X (2011) Collective cell guidance by cooperative intercellular forces. *Nat Mater* 10(6):469–475. doi:[10.1038/nmat3025](https://doi.org/10.1038/nmat3025)
- Trepast X, Wasserman MR, Angelini TE, Millet E, Weitz DA, Butler JP, Fredberg JJ (2009) Physical forces during collective cell migration. *Nat Phys* 5(6):426–430. doi:[10.1038/nphys1269](https://doi.org/10.1038/nphys1269)
- Valentin G, Haas P, Gilmour D (2007) The chemokine SDF1a coordinates tissue migration through the spatially restricted activation of Cxcr7 and Cxcr4b. *Curr Biol* 17(12):1026–1031. doi:[10.1016/j.cub.2007.05.020](https://doi.org/10.1016/j.cub.2007.05.020)
- Vedel S, Tay S, Johnston DM, Bruus H, Quake SR (2013) Migration of cells in a social context. *Proc Natl Acad Sci* 110(1):129–134. doi:[10.1073/pnas.1204291110](https://doi.org/10.1073/pnas.1204291110)
- Vitorino P, Meyer T (2008) Modular control of endothelial sheet migration. *Genes Dev* 22(23):3268–3281. doi:[10.1101/gad.1725808](https://doi.org/10.1101/gad.1725808)
- Yamao M, Naoki H, Ishii S (2011) Multi-cellular logistics of collective cell migration. *PLoS One* 6(12):e27950. doi:[10.1371/journal.pone.0027950](https://doi.org/10.1371/journal.pone.0027950)

4.5 Conclusions and perspectives

The model of collective migration has arisen as a natural extension of the one for single cell migration. Actually, the mechanical principles are the same as for single cell migration (i.e. viscoelastic behaviour of the cell and intra-synchronisation) plus the inter-synchronisation regulating the coordination between the cells. Therefore, the very first objective of the study has been to investigate the link between the intra- and the inter-synchronisation in order to evaluate those constraints and forces leading (or not) to an efficient collective migration. By testing several migration modes, I have been able to demonstrate that the most efficient modes are those also showing a minimal degree of synchronisation between the cells and the lowest stresses inside the population. Thus, as also pointed out in (28), cells adjust their movement according to the local stress rate, which is generated by the neighbour cells and promotes local unjamming.

Although the outcomes from (38) highlighted the crucial role (once again) of mechanics, collective migration is also governed by complex molecular signals, which lead to the movement of (at least) the leader cells. Nevertheless, the molecular framework changes according to the biological model. In (39) the previous model was adapted to simulate collective migration of LLP in zebrafish. The coupling between mechanics and biology allows consideration of several chemokine-molecule pathways in control of the intra-synchronisation within the cells. Besides validation of the numerical results with respect to the experimental observations proposed in (40), the main goal was to investigate the role of leader cells in terms of how and to what extent their position inside the population might affect global migration efficiency.

In both cases (38, 39), the outcomes show the potential of the numerical approach even though a few drawbacks can be pointed out. First, the model as it is only describes the movement of the whole cell network, whereas cells may stochastically move with respect each other. Second, the population is constituted by a constant number of cells throughout the simulation, whereas in most cases (not for the LLP) proliferation takes place as the cohort migrates. To address these two specific issues, during my staying at the Department of Mathematics at Politecnico di Torino (Italy), I have started to develop a new model based on a discrete approach (i.e. Cellular Potts Model) in collaboration with Luigi Preziosi.

As a further improvement of the finite element model proposed in (38, 39), I would like to integrate a direct dependency of the cyclic active strains of protrusion-contraction of the cells on the surrounding stress state. By doing so, it will be possible to reproduce and evaluate the scenario proposed by Serra-Picamal et al. (28) according to which a mechanical wave progressively spans the population and a cell only starts to migrate if an adjacent cell creates space or pull on the cell-cell junctions.

Finally, once these aspects are taken into account, I would like to integrate the hybrid continuum/discrete description of the cell population in the model of bone modelling presented in Chapter 2.

4.6 Bibliography

1. Friedl P, Gilmour D (2009) Collective cell migration in morphogenesis, regeneration and cancer. *Nat Rev Mol Cell Biol* 10(7):445–457.
2. Sumpter DJ. (2006) The principles of collective animal behaviour. *Philos Trans R Soc B Biol Sci* 361(1465):5–22.
3. Trepap X, et al. (2009) Physical forces during collective cell migration. *Nat Phys* 5(6):426–430.
4. Tambe DT, et al. (2011) Collective cell guidance by cooperative intercellular forces. *Nat Mater* 10(6):469–475.
5. Farooqui R, Fenteany G (2005) Multiple rows of cells behind an epithelial wound edge extend cryptic lamellipodia to collectively drive cell-sheet movement. *J Cell Sci* 118(Pt 1):51–63.
6. Fenteany G, Janmey PA, Stossel TP (2000) Signaling pathways and cell mechanics involved in wound closure by epithelial cell sheets. *Curr Biol CB* 10(14):831–838.
7. Graner, Glazier (1992) Simulation of biological cell sorting using a two-dimensional extended Potts model. *Phys Rev Lett* 69(13):2013–2016.
8. Szabo B, et al. (2006) Phase transition in the collective migration of tissue cells: experiment and model. *ArXivq-Bio0611045*. Available at: <http://arxiv.org/abs/q-bio/0611045> [Accessed April 27, 2013].
9. Vedel S, Tay S, Johnston DM, Bruus H, Quake SR (2013) Migration of cells in a social context. *Proc Natl Acad Sci* 110(1):129–134.
10. Vicsek, Czirók, Ben-Jacob, Cohen, Shochet (1995) Novel type of phase transition in a system of self-driven particles. *Phys Rev Lett* 75(6):1226–1229.
11. Yamao M, Naoki H, Ishii S (2011) Multi-Cellular Logistics of Collective Cell Migration. *PLoS ONE* 6(12):e27950.
12. Bindschadler M, McGrath JL (2007) Sheet migration by wounded monolayers as an emergent property of single-cell dynamics. *J Cell Sci* 120(5):876–884.
13. Ouaknin GY, Bar-Yoseph PZ (2009) Stochastic collective movement of cells and fingering morphology: no maverick cells. *Biophys J* 97(7):1811–1821.
14. Fozard JA, Byrne HM, Jensen OE, King JR (2010) Continuum approximations of individual-based models for epithelial monolayers. *Math Med Biol* 27(1):39–74.
15. Byrne H, Drasdo D (2009) Individual-based and continuum models of growing cell populations: a comparison. *J Math Biol* 58(4-5):657–687.
16. Kabla AJ (2011) Collective Cell Migration: Leadership, Invasion and Segregation. *ArXiv11084286 Phys Q-Bio*. Available at: <http://arxiv.org/abs/1108.4286> [Accessed January 27, 2015].
17. Doxzen K, et al. (2013) Guidance of collective cell migration by substrate geometry. *Integr Biol Quant Biosci Nano Macro* 5(8):1026–1035.
18. Vedula SRK, et al. (2012) Emerging modes of collective cell migration induced by geometrical constraints. *Proc Natl Acad Sci U S A* 109(32):12974–12979.
19. Sherratt JA, Murray JD (1991) Mathematical analysis of a basic model for epidermal wound healing. *J Math Biol* 29(5):389–404.
20. Sherratt JA, Murray JD (1990) Models of epidermal wound healing. *Proc Biol Sci* 241(1300):29–36.

21. Sherratt JA (1993) Actin aggregation and embryonic epidermal wound healing. *J Math Biol* 31(7):703–716.
22. Arciero JC, Mi Q, Branca MF, Hackam DJ, Swigon D (2011) Continuum Model of Collective Cell Migration in Wound Healing and Colony Expansion. *Biophys J* 100(3):535–543.
23. Gaffney EA, Maini PK, McCaig CD, Zhao M, Forrester JV (1999) Modelling corneal epithelial wound closure in the presence of physiological electric fields via a moving boundary formalism. *IMA J Math Appl Med Biol* 16(4):369–393.
24. Chen X, Friedman A (2000) A Free Boundary Problem Arising in a Model of Wound Healing. *SIAM J Math Anal* 32(4):778.
25. Chen X, Friedman A (2003) A Free Boundary Problem for an Elliptic-Hyperbolic System: An Application to Tumor Growth. *SIAM J Math Anal* 35(4):974.
26. Xue C, Friedman A, Sen CK (2009) A mathematical model of ischemic cutaneous wounds. *Proc Natl Acad Sci* 106(39):16782–16787.
27. Maini PK, McElwain DLS, Leavesley DI (2004) Traveling wave model to interpret a wound-healing cell migration assay for human peritoneal mesothelial cells. *Tissue Eng* 10(3-4):475–482.
28. Serra-Picamal X, et al. (2012) Mechanical waves during tissue expansion. *Nat Phys* 8(8):628–634.
29. Allena R (2013) Cell migration with multiple pseudopodia: temporal and spatial sensing models. *Bull Math Biol* 75(2):288–316.
30. Allena R, Aubry D (2012) “Run-and-tumble” or “look-and-run”? A mechanical model to explore the behavior of a migrating amoeboid cell. *J Theor Biol* 306:15–31.
31. Carlsson AE, Sept D (2008) Mathematical modeling of cell migration. *Methods Cell Biol* 84:911–937.
32. Flaherty B, McGarry JP, McHugh PE (2007) Mathematical models of cell motility. *Cell Biochem Biophys* 49(1):14–28.
33. Rubinstein B, Jacobson K, Mogilner A (2005) Multiscale two-dimensional modeling of a motile simple-shaped cell. *Multiscale Model Simul* 3:413–439.
34. Sakamoto Y, Prudhomme S, Zaman MH (2011) Viscoelastic gel-strip model for the simulation of migrating cells. *Ann Biomed Eng* 39(11):2735–2749.
35. Taber LA, Shi Y, Yang L, Bayly PV (2011) A poroelastic model for cell crawling including mechanical coupling between cytoskeletal contraction and actin polymerization. *J Mech Mater Struct* 6(1-4):569–589.
36. Murray JD (2003) *Mathematical Biology II: Spatial Models and Biomedical Applications* (Springer).
37. Allena R, Muñoz JJ, Aubry D (2011) Diffusion-reaction model for Drosophila embryo development. *Comput Methods Biomech Biomed Engin*:Epub ahead of print.
38. Allena R, Aubry D, Sharpe J (2013) On the mechanical interplay between intra- and inter-synchronization during collective cell migration: a numerical investigation. *Bull Math Biol* 75(12):2575–2599.
39. Allena R, Maini PK (2014) Reaction-diffusion finite element model of lateral line primordium migration to explore cell leadership. *Bull Math Biol* 76(12):3028–3050.

40. Aman A, Piotrowski T (2008) Wnt/beta-catenin and Fgf signaling control collective cell migration by restricting chemokine receptor expression. *Dev Cell* 15(5):749–761.

